

DARK MATTER AND LONG-LIVED PARTICLES

Dugald Grant Hepburn

Royal Holloway and Bedford New college,
University of London

*Thesis submitted to
The University of London
for the degree of
Doctor of Philosophy
2022.*

Declaration of Authorship

I, Dugald Grant Hepburn, hereby declare that this thesis and the work presented in it is entirely my own. Where I have consulted the work of others, this is always clearly stated.

Abstract

This thesis explores the phenomenology of models containing a dark matter candidate, calculating the effects of constraints stemming from cosmology; collider and other experiments; and theoretical considerations.

We first consider dark matter in the “Portalino” framework. In this set-up, gauge-singlet right-handed neutrinos interact with gauge-neutral operators in the visible and dark sectors (in the visible sector, this operator is LH where L represents the left-handed leptons and H is the Higgs, with one or more analogous dark operators), and hence the two sectors are coupled via the neutrino portal. We consider scenarios with a seesaw-like mechanism setting the neutrino masses, which also suppresses the mass of the dark sector particle(s) analogous to the neutrinos (the ‘Portalino’). We determine which scenarios could lead to the observed neutrino properties, then consider a model with a single Portalino, in which the dark matter abundance is produced via freeze-out to Portalinos (either directly or via other dark states). These Portalinos decay via a small mixing with the neutrinos, so can be long-lived. We consider constraints on this model, including cosmological constraints from Portalino decays.

Supersymmetry provides a dark matter candidate, along with a solution to the hierarchy naturalness problem (i.e. why is the Higgs mass not driven up to the cut-off scale by quantum corrections?). The second set of models that we consider emerge from the Next-to-Minimally Supersymmetric Standard Model (NMSSM), i.e. the MSSM with an additional singlet superfield. We consider the limit in which the singlet is feebly coupled. This means that the singlet particles never reach thermal equilibrium, so any population of singlet particles is produced via freeze-in. Additionally, certain particles can only decay via this feeble coupling and hence are long-lived. These decays can

impact on cosmological processes such as big bang nucleosynthesis and hence constrain the model, which we explore.

Acknowledgements

I would like above all to thank my supervisor, Professor Stephen West, for his generous support and guidance throughout my time at Royal Holloway. I would also like to express my gratitude to Dr Nikolas Kauer, Dr Andrew Ho and Professor Matthias Eschrig for their advice and assistance, alongside Gill Green, Carmela Froggatt, Claire Porter and Tracy Webster who have always been extremely helpful. I would also like to take this opportunity to acknowledge the many brilliant lecturers and teachers I have had without whom I would not have reached this point, including but not limited to Mr Roberts and Dr Stephen Cowley.

I would also like to thank my friends and family who have helped me along the way – in particular Paul and Cecilia, who have been incredibly kind and generous, not least over the past couple of years, and my parents, for their love and support.

Finally, Kate – I have been very lucky to have had your company during this process. Thank you for being a constant source of joy in my life.

Contents

Declaration of Authorship	2
Abstract	3
Acknowledgements	5
Contents	6
List of Tables	10
List of Figures	11
1 Introduction	17
2 Cosmology and Particle Physics	20
2.1 Dynamics of the Universe and the Λ CDM Model	22
2.1.1 FLRW Metric and the Friedmann Equations	22
2.1.2 Radiation, Matter, Curvature and Dark Energy	23
2.1.3 The Radiation-Dominated Epoch	23
2.1.4 Effective Number of Neutrino Species	26
2.2 Big Bang Nucleosynthesis	28
2.3 Cosmic Microwave Background Radiation	31
3 Dark Matter	35
3.1 Evidence for the Existence of Dark Matter	36
3.1.1 Galaxy Rotation Curves	36
3.1.2 The Bullet Cluster	37
3.1.3 Structure Formation and the CMBR	39
3.1.4 CMB Angular Power Spectrum	41

3.2	Dark Matter Candidates	42
3.2.1	WIMPs	43
3.2.2	FIMPs, superWIMPs and WIMPzillas	44
3.2.3	Axions	45
3.2.4	(Sterile) Neutrinos	46
3.2.5	Hidden Dark Matter	48
3.2.6	MACHOs	48
3.3	Dark Matter Production	49
3.3.1	Freeze-Out	49
3.3.2	Freeze-In	56
3.4	Dark Matter Detection	57
3.4.1	Direct Detection	59
3.4.2	Indirect Detection	62
3.4.3	Collider Experiments	63
4	Supersymmetry	65
4.1	Motivation	65
4.2	Supersymmetry Generators and Superfields	67
4.3	Chiral Superfields	70
4.3.1	Chiral Superfield Lagrangian	71
4.4	Real Superfields	72
4.4.1	Generalised Gauge Transformations	73
4.4.2	Wess-Zumino Gauge	73
4.5	Gauge Theory Lagrangian	75
4.5.1	Field Strength Superfield	75
4.5.2	Fayet-Iliopoulos Term	79
4.5.3	Gauge Interactions	79
4.6	Supersymmetry Breaking	81
4.6.1	F-term Breaking	81

4.6.2	D-term Breaking	81
4.7	The Minimally Supersymmetric Standard Model	82
4.7.1	Particle Content and Lagrangian Structure	82
4.7.2	MSSM Superpotential	85
4.7.3	Soft SUSY-Breaking Terms	86
4.7.4	Auxiliary Fields	87
4.7.5	Higgs Potential and Electroweak Symmetry Breaking	90
4.7.6	The μ Problem	93
4.7.7	Other Physical States	94
5	Dark Matter and Neutrino Masses in a Portalino-like Model	95
5.1	Introduction	95
5.2	Massless States in the Portalino Framework	98
5.3	Neutrino Masses and Mixing	100
5.4	The Model	108
5.5	Full Lagrangian in Mass Eigenbasis	113
5.6	Reconstructing the PMNS Matrix	115
5.6.1	Tri-Bi-Maximal Mixing	116
5.7	Dark Matter Abundance	117
5.7.1	Direct Detection	124
5.7.2	Indirect Detection	126
5.8	Portalino Phenomenology	127
5.8.1	Portalino Decays	128
5.8.2	Portalino Decoupling	131
5.8.3	The Heavy Portalino Case	132
5.8.4	Intermediate Portalino	138
5.8.5	Light Portalino	140
5.9	Conclusions and Discussion	142

6	Freeze-in Dark Matter in the Effective MSSM	145
6.1	Introduction	145
6.2	The Effective MSSM	146
6.2.1	Minima of the Potential $V(H_u, H_d, S)$	147
6.2.2	Effective MSSM Spectrum	151
6.2.3	Higgs and Singlino Sector	151
6.2.4	Dark Matter Phenomenology Overview	153
6.3	Singlino(-like) Dark Matter	155
6.3.1	Freeze-In Abundances	157
6.3.2	Constraining the Singlino LSP Scenario	159
6.3.3	Results	164
6.4	Neutralino Dark Matter	167
6.4.1	Phenomenology	168
6.5	Conclusion	170
7	Conclusion	172
	Bibliography	175

List of Tables

4.1	Chiral superfields of the MSSM. A hat is used to denote a superfield, while a tilde marks an R-parity odd superpartner. Here we have included the conjugate of the right-handed quark and lepton superfields, so that the table only includes left-handed fields. This is also the form in which these fields will appear in the superpotential.	83
4.2	Real superfields of the MSSM. After electroweak symmetry breaking, there is as usual (along with the gluon, which is unaffected) one remaining massless gauge boson, the photon γ , along with a neutral massive gauge boson, Z , and a charged gauge boson, W^\pm	83
5.1	Charge assignments of the field content in the hidden sector under $U(1)_d$ and \mathbb{Z}_3 . All fields in the table are Standard Model singlets	109

List of Figures

2.1	Predicted abundances as a function of baryon density, together with measured abundances (yellow boxes), reproduced from [24] with permission. Predicted abundances are shown with 95% CL ranges. As can be seen, the theoretical abundances for all elements other than lithium agree with the observed abundances at the baryon density measured by Planck [11].	30
2.2	CMBR angular power spectrum, as measured by Planck, compared to the prediction from Λ CDM. The definition of D_l is given in the text. Figure reproduced from [11].	32
2.3	This figure shows the dependence of the anisotropies of the CMBR on the effective number of neutrino species N_{eff} , as explained in the text. C_l is equal to the D_l defined in the text. Reproduced from [41] with permission.	33
3.1	Composite image published by NASA/CXC/M. Weiss, using optical and gravitational lensing data from [50], and X-ray data from [51]. Optical observations are shown in yellow/orange; X-ray observations (corresponding to the intracluster medium) are superimposed in pink; and the mass density (dominated by dark matter) is superimposed in blue.	38
3.2	Comparison of the predicted matter power spectrum ($P_m(k)$ is defined in Equation 3.1.3) in the Λ CDM model and various experimental observations, reproduced from [11].	40
3.3	This figure illustrates the impact on CMBR temperature anisotropies of varying various components of the energy density. Reproduced from [40] with permission.	42

3.4	Decay of a sterile neutrino $N \rightarrow \gamma\nu_i$ (this decay is subdominant), which could give rise to the unidentified X-ray line in [105, 106]. Note that N and ν_i refer to the mostly sterile and mostly active mass eigenstates, respectively.	48
3.5	An illustration of the behaviour of the dark matter abundance in freeze-out (solid lines) and freeze-in (dashed lines) scenarios, compared to the equilibrium abundance (solid black line), reproduced from [86]. Arrows indicate increasing interaction cross-section. In freeze-out, a particle with stronger interactions remains in equilibrium for longer and hence has a more suppressed final abundance. In contrast, in freeze-in, the particle never reaches equilibrium and a particle with stronger interactions is produced in greater numbers.	57
3.6	A schematic representation of possible ways dark matter could be detected in experiments: indirect detection (dark matter annihilations or decays producing visible products); direct detection (dark matter scattering off Standard Model particles); or being produced in collider experiments.	58
3.7	Summary of spin-independent direct detection limits, with data from [146, 147, 148, 149, 150], reproduced from [146].	60
4.1	Loop diagrams with quadratic divergences contributing to the Higgs mass.	66
4.2	Process contributing to proton decay in the absence of R-parity.	84

- 5.1 **Left:** DM abundance against m_X , for $v_\phi = 2\text{ TeV}$, $m_n = 100\text{ keV}$, $\lambda_\psi = 1$, $\tilde{g} = 1$, $\lambda_\Phi = 1$, $\lambda_{H,\Phi} = 0.1$. The horizontal dotted line indicates the observed DM abundance. The first trough corresponds to the ω s-channel resonance at $m_X \approx m_\omega/2$ ($m_\omega = \frac{\tilde{g}}{2}v_\phi = 1\text{ TeV}$) and the second, shallower, trough corresponds to the ϕ s-channel resonance at $m_X \approx m_\phi/2$ ($m_\phi = \sqrt{2\lambda_\phi}v_\phi \approx 2.8\text{ TeV}$). **Middle (Right):** Relative (absolute) contributions of each channel to $(\Omega h^2)^{-1}$. The line labelled ‘Higgs Resonance’ includes several channels which are only significant near the h resonance at $m_X \approx m_h/2$. These are dominated by $X\bar{X} \rightarrow b\bar{b}$; the next largest contributions come from $X\bar{X} \rightarrow GG$, $X\bar{X} \rightarrow \tau^+\tau^-$ and $X\bar{X} \rightarrow c\bar{c}$ 119
- 5.2 DM abundance against m_X for different values of \tilde{g} (left panel) and λ_Φ (right panel). Apart from the values of \tilde{g} and λ_Φ indicated in the plots, both panels display results for parameter values as stated for the left panel of Figure 5.1. The effect of varying the values of both these parameters is seen in the position and shape of the troughs in the DM abundance (see text for details). 122
- 5.3 DM abundance against λ_X for different values of v_ϕ . All other parameters are fixed at the values stated in Figure 5.1. As can be seen, the abundance scales as approximately v_ϕ^2 . This sets an upper bound $v_\phi \lesssim 100\text{ TeV}$, above which the correct relic abundance can no longer be produced. 123

- 5.4 Portalino decoupling temperature against Portalino lifetime, for a range of Portalino masses. Marked on the plot are: the decoupling temperature as a function of lifetime, $T_{n,\text{decouple}}(\tau)$, parameterised by η (the enhancement/suppression of the Portalino-neutrino mixings); the line where the Portalino decay temperature $T_{n,\text{decay}}$ is equal to the neutrino decoupling temperature $T_{\nu,\text{decouple}}$, to the right of which the Portalino decays impact on the effective extra relativistic degrees of freedom N_{eff} ; and the region where the Portalino-neutrino mixing is larger than allowed by constraints as detailed in Section 5.8.3. The allowed region lies on the multicoloured line $T_{n,\text{decouple}}(\tau)$, between the blue box (where the model is ruled out by too large a Portalino-neutrino mixing), and the grey region (where the mixing is too small, and hence the Portalinos decay after neutrino decoupling). 133
- 5.5 Current and future bounds on heavy Portalino mixing with the electron neutrino, combined with the constraint that the Portalino must decay before neutrino decoupling. See text for details of constraints such as ‘Collider’. The line labelled $|V_{e4}(m_n)|^2$ indicates an approximate expected size of the Portalino-neutrino mixing, $|V_{e4}(m_n)|^2 \sim m_\nu/m_n$. The four lines of $T_{n,\text{decouple}}(\tau)$ from Figure 5.4 parameterised by η (for $m_n = 481 \text{ MeV}, 500 \text{ MeV}, 1 \text{ GeV}$ and 2 GeV), projected into the m_n - $|V_{e4}|^2$ plane, are also included. 136
- 5.6 Constraints on the light Portalino scenario, with the blue region ruled out by constraints on ΔN_{eff} at BBN and the grey region ruled out by Planck’s analysis of the CMB anisotropies [1]. The vertical dashed line indicates the scale of neutrino masses and is included to highlight the limitations of the model assumption that the Portalino is more massive than the neutrinos. 142

- 6.1 This plot illustrates how the lifetimes and abundances of the three long-lived particles vary with λ , for κ/λ (and all other parameters) fixed. As described in the text, we take the constraints from BBN on a particle of mass 30 GeV decaying to $\bar{b}b$, which gives a conservative bound. This limit is indicated in grey. Although these constraints assume only a single particle decaying, this is a reasonable assumption for our purposes, as explained in the text. As can be seen, the NLSP lifetime scales as λ^{-2} , while the abundance does not depend on λ , so BBN constraints on the NLSP provide a simple lower bound on λ . The singlet scalar lifetimes also scale as λ^{-2} , but their abundances scale as λ^2 . This means that BBN constraints on the scalars don't give rise to a simple upper or lower limit on λ : when λ is very small, the scalar abundances are very small, and so they don't affect BBN; when λ is very large the scalar lifetimes are very short and so again they don't affect BBN. Between these two extremes, some values of λ are ruled out, as shown. 160
- 6.2 This plot shows the allowed region in the $\kappa - \lambda$ parameter space, within the M_h^{125} benchmark (Equation 6.3.1 with NMSSM parameter values $A_\kappa = -34$ GeV and $A_\lambda = 1$ GeV. The solid black contour represents parameter points with the correct DM relic abundance. The regions ruled out by long-lived particle decays are shown labelled "BBN (NLSP/CP-odd/even)" and are coloured yellow, red and orange respectively. The blue region labelled "MSSM" is ruled out by limits on MSSM Higgs masses. In the bottom right grey region labelled "EWSB not successful" there is no EWSB and in the top left grey area labelled "Singlino not LSP" the neutralino is the LSP. See text for details. 165

6.3 This plot illustrates how the lifetimes and abundances of the three long-lived singlet particles vary with λ , for $\frac{\kappa}{\lambda}$ (and all other parameters) fixed, in the case where a neutralino is the LSP. The constraints from BBN on a particle (of mass 30 GeV) decaying to $\bar{b}b$ is also indicated in grey. As described in the text, this choice of limit gives a conservative bound. Although these limits assume only a single particle decaying, this is a reasonable assumption for our purposes, as explained in the text.169

Chapter 1

Introduction

Our standard cosmological model, the Λ CDM model, alongside the Standard Model of particle physics, provide an excellent description of the universe stretching to very high energies and very early times in the evolution of the universe.

However, there are still a number of outstanding questions still to be answered, which include the origin and identity of dark matter; how neutrinos get their masses; the hierarchy problem; the nature of dark energy or the cosmological constant; baryogenesis (the observed asymmetry between matter and anti-matter in the universe); or other more fundamental issues such as a consistent quantum theory of gravity.

This thesis will focus on dark matter: we know from astrophysical observations that some type of non-baryonic, non-luminous matter makes up about 84% of the matter in the universe, but we do not know what it is made of, and still know relatively little about its properties [1]. We focus on models in which the dark matter is ‘hidden’ to some extent, either with extremely weak interactions with the visible sector, or sitting in a hidden sector which is connected to the visible sector via a portal. Such theories often contain long-lived particles, which can have cosmologically interesting effects.

In Chapter 2, we discuss cosmology and its implications for particle physics.

We give an overview of the production of light elements in the early universe, along with the development of anisotropies in the cosmic microwave background. We review how these processes are affected by, and hence can constrain, the properties of new physics beyond the Standard Model.

Chapter 3 covers some of the evidence for the existence of dark matter, along with what this evidence can tell us about its properties. We also discuss the properties of, and motivation for, some of the most studied dark matter candidates, how they might be produced, and how they might be detected in experiments.

We review supersymmetry in Chapter 4. Supersymmetry may be able to resolve the hierarchy naturalness problem: in the Standard Model, extremely precise cancellations are required to prevent the Higgs mass from being driven up to a much higher scale, whereas these cancellations are automatic in supersymmetric theories. We explain the structure of supersymmetric theories in general, and then focus on the Minimally Supersymmetric Standard Model in particular.

Chapter 5 explores models of dark matter in the ‘Portalino’ framework. The ‘Portalino’ framework contains gauge-singlet right-handed neutrinos ν_R which mix with the Standard Model neutrinos via the coupling $\lambda_\nu LH\nu_R$ (where L contains the left-handed leptons, and H contains the Higgs fields), and also similarly mix with fermions in a hidden dark sector which are analogous to the neutrinos (which we call ‘Portalinos’). We explore the implications of this framework for neutrino properties, along with the phenomenology of the dark sector, in particular the Portalinos which can be produced in relatively large numbers and can be long-lived.

Finally, Chapter 6 examines how the correct dark matter density can be produced in an extension of the Minimally Supersymmetric Standard Model (MSSM) known as the ‘effective MSSM’. The effective MSSM consists of the

MSSM with an additional singlet superfield, containing a fermion and a complex scalar, which is extremely weakly coupled to the Higgs fields. We explore how the correct dark matter abundance can be produced via a mixture of freeze-in of singlet states and freeze-out of MSSM states.

Chapter 2

Cosmology and Particle Physics

In this Chapter, and the remainder of the thesis, natural units are used:

$$c = \hbar = k_B = 1.$$

Cosmology offers dual benefits to the development of new theories of particle physics. Firstly, there are many unsolved issues stemming from cosmology which may have a solution in particle physics, such as the origin and nature of dark matter (which we will discuss in Chapter 3), the observed matter-antimatter asymmetry, and dark energy. Secondly, the universe has expanded from an early period during which it was extremely hot and dense, so if we can make inferences about the characteristics of the early universe, we can gain insight into the properties of fundamental physics at high energies.

To set the scene, a brief history of the universe is as follows [2, 3, 4, 5, 6, 7, 8, 9, 10, 11]:

- Firstly, evidence indicates that there was an early period of accelerated expansion (‘inflation’), which explains the uniform density and temperature of the observable universe and why the universe is so spatially flat. Without inflation, most parts of the sky would never have been in contact with most other parts, and yet the temperature of the universe is observed to be extremely uniform in all directions. Inflation solves this

problem, as the entire observable universe would have come into causal contact during the inflationary epoch. Additionally, curvature should grow as the universe expands, but the universe is observed to be extremely flat, suggesting that the curvature of the early universe would have to be fine-tuned to be extremely small. Inflation can also solve this fine-tuning problem, as the universe would be extremely flat after inflation. Inflation has also been used to explain why magnetic monopoles have never been observed.

- $t \sim 20 \text{ ps}$, $T \sim 100 \text{ GeV}$ (where T is the photon temperature of the universe): electroweak symmetry breaking - particles gain mass.
- $t \sim 20 \text{ } \mu\text{s}$, $T \sim 150 \text{ MeV}$: QCD phase transition - quarks are bound into baryons and mesons.
- $t \sim 1 \text{ s}$, $T \sim \text{MeV}$: neutrinos decouple.
- $t \sim 6 \text{ s}$, $T \sim 500 \text{ keV}$: electron-positron annihilation (discussed briefly below).
- $t \sim 3 \text{ min}$, $T \sim 100 \text{ keV}$: big bang nucleosynthesis takes place - nuclei of light elements are formed.
- $t \sim 6 \times 10^4 \text{ yr}$, $T \sim 0.75 \text{ eV}$: matter-radiation equality.
- $t \sim 2.6 \times 10^5 \text{ yr}$ to $3.8 \times 10^5 \text{ yr}$, $T \sim 0.26 \text{ eV}$ to 0.33 eV : recombination occurs - electrons and protons are bound into hydrogen atoms.
- $t \sim 3.8 \times 10^5 \text{ yr}$, $T \sim 0.26 \text{ eV}$: photons decouple.
- $t \sim 1 \times 10^8 \text{ yr}$ to $4 \times 10^8 \text{ yr}$, $T \sim 2.7 \text{ meV}$ to 3 meV : reionization occurs - energetic radiation from the first sources such as stars and galaxies ionises hydrogen atoms.
- $t \sim 9 \times 10^9 \text{ yr}$, $T \sim 0.33 \text{ meV}$: dark energy-matter equality.

- $t \sim 1.38 \times 10^{10}$ yr, $T \sim 0.24$ meV: the present day.

In this chapter, we will give a brief overview of the current standard model of cosmology and then focus on two particular phenomena which can provide insight into fundamental particle physics: the abundance of light elements, and the cosmic microwave background radiation.

2.1 Dynamics of the Universe and the Λ CDM Model

2.1.1 FLRW Metric and the Friedmann Equations

At large scales, the universe is described by the Friedmann Lemaître Robertson Walker metric, which describes an isotropic and homogeneous universe [3, 2]:

$$ds^2 = dt^2 - a(t)^2 \left[\frac{dr^2}{1 - kr^2} + r^2 d\Omega^2 \right], \quad (2.1.1)$$

where $a(t)$ is the overall scaling factor of the universe, scaled to $a = 1$ at the current time, and k is the curvature. The evolution of the scaling factor can be found via the Einstein equation

$$G_{\mu\nu} = 8\pi G T_{\mu\nu}, \quad (2.1.2)$$

where the isotropic and homogeneous stress-energy tensor $T_{\mu\nu} = (\rho + P) U_\mu U_\nu - P g_{\mu\nu}$, ρ and P are the energy density and pressure of the fluid in its rest frame, and U^μ is the relative velocity of the observer with respect to the fluid. Equation 2.1.2 becomes

$$H^2 \equiv \left(\frac{\dot{a}}{a} \right)^2 = \frac{8\pi G}{3} \rho - \frac{k}{a^2}, \quad (2.1.3)$$

$$\frac{\ddot{a}}{a} = -\frac{4\pi G}{3} (\rho + 3P), \quad (2.1.4)$$

where H is the Hubble parameter that characterises the rate of expansion of the universe [3, 2].

2.1.2 Radiation, Matter, Curvature and Dark Energy

We will consider three different components which could contribute to the stress-energy tensor: radiation, matter, and dark energy. Each of these will evolve in different ways, according to the continuity equation $\nabla_\mu T^\mu_\nu = 0$, or in terms of the pressure and energy density

$$\dot{\rho} + 3\frac{\dot{a}}{a}(\rho + P) = 0. \quad (2.1.5)$$

Radiation is defined by $P = \frac{1}{3}\rho$, and so $\rho \propto a^{-4}$. Matter is defined by $P = 0$, and so $\rho \propto a^{-3}$. Dark energy is defined by $P = -\rho$, and so $\rho = \text{constant}$. The presence of dark energy is necessitated by observations of supernovae, which (at a set distance) appear dimmer than expected in a dark energy-free universe [12, 13].

Using this classification, the Hubble parameter can be written (from Equation 2.1.3) as a function of the scale factor a

$$H^2 = H_0^2 [\Omega_{r,0}a^{-4} + \Omega_{m,0}a^{-3} + \Omega_{k,0}a^{-2} + \Omega_{\Lambda,0}], \quad (2.1.6)$$

where ‘0’ denotes a parameter’s value today, $\Omega_{k,0} \equiv -\frac{k}{H_0^2}$, and the other energy densities are rescaled by the critical density $\rho_{\text{crit.}} = \frac{3H_0^2}{8\pi G}$:

$$\Omega_X = \frac{\rho_X}{\rho_{\text{crit.}}}. \quad (2.1.7)$$

2.1.3 The Radiation-Dominated Epoch

The behaviour of the different components above, combined with the fact that the universe is expanding, suggests an early universe dominated by radiation,

with matter then coming to dominate, and finally dark energy dominating at late times. The current best evidence points towards the following energy densities today [1]:

$$\Omega_\Lambda = 0.68, \quad \Omega_m = 0.32, \quad \Omega_r = 9.4 \times 10^{-5}, \quad \Omega_k < 0.003. \quad (2.1.8)$$

To analyse the evolution of the early universe, we need to define the energy density in radiation. For a single particle species, the energy density is given by

$$\rho = \frac{g}{(2\pi)^3} \int d^3\mathbf{p} f(\mathbf{p}) E(\mathbf{p}), \quad (2.1.9)$$

where g is the number of internal degrees of freedom, $E(\mathbf{p})$ is the energy

$$E(\mathbf{p}) = \sqrt{m^2 + |\mathbf{p}|^2} \quad (2.1.10)$$

(where interaction energies have been neglected under the assumption that particles in the early universe can be treated as weakly interacting), and $f(\mathbf{p})$ is the phase space distribution function, which for a particle in thermal equilibrium is given by

$$f(p, t) = \frac{1}{e^{(E-\mu)/T} \pm 1}, \quad (2.1.11)$$

where the plus sign corresponds to the Fermi-Dirac distribution for fermions, the minus sign corresponds to the Bose-Einstein distribution for bosons, and μ is the chemical potential [3]. For completeness, the number density and pressure are given by

$$n = \frac{g}{(2\pi)^3} \int d^3\mathbf{p} f(\mathbf{p}),$$

$$P = \frac{g}{(2\pi)^3} \int d^3\mathbf{p} f(\mathbf{p}) \frac{|\mathbf{p}|^2}{3E}. \quad (2.1.12)$$

Particle species whose energy density is dominated by their kinetic energy, i.e. $m \ll T$, behave as radiation. In this limit (and with $\mu \ll T$), Equations 2.1.9 and 2.1.12 become

$$\begin{aligned} n &= \frac{\zeta(3)}{\pi^2} g T^3 \begin{cases} 1, & \text{bosons} \\ \frac{3}{4}, & \text{fermions,} \end{cases} \\ \rho &= \frac{\pi^2}{30} g T^4 \begin{cases} 1, & \text{bosons} \\ \frac{7}{8}, & \text{fermions,} \end{cases} \\ P &= \frac{\rho}{3}. \end{aligned} \quad (2.1.13)$$

The corresponding relations for non-relativistic particles are

$$\begin{aligned} n &= g \left(\frac{mT}{2\pi} \right)^{\frac{3}{2}} \exp[-(m - \mu)/T], \\ \rho &= mn, \\ P &= nT. \end{aligned} \quad (2.1.14)$$

The total energy density in radiation can be written

$$\rho_r = \frac{\pi^2}{30} g_*(T) T^4 \quad (2.1.15)$$

where T is the photon temperature and g_* gives the effective number of relativistic degrees of freedom

$$g_*(T) = \sum_{\text{bosons}} g_i \left(\frac{T_i}{T} \right)^4 + \frac{7}{8} \sum_{\text{fermions}} g_i \left(\frac{T_i}{T} \right)^4 \quad (2.1.16)$$

where the sums are dominated by relativistic species with $m_i \ll T_i$. T_i refers to the temperature of particle species i , so particles in thermal equilibrium with the photons will have $T_i = T$, while particle species which are not in

thermal equilibrium with the photons (e.g. decoupled sectors such as neutrinos discussed below) may have a temperature which diverges from the photon temperature, $T_i \neq T$. If a particle remains in equilibrium while becoming non-relativistic (as the temperature T drops below its mass), its energy density becomes Boltzmann suppressed, $\rho \sim \exp(-\frac{m}{T})$, and they cease to contribute to the energy density or equivalently g_* . New physics can affect the form of $g_*(T)$ (e.g. a new particle in thermal equilibrium will contribute towards $g_*(T)$ while it is in thermal equilibrium), and hence affect the rate of expansion, which could have observable effects.

2.1.4 Effective Number of Neutrino Species

To put this idea on a firmer footing, define the effective number of neutrino species N_{eff} via the total energy density in radiation:

$$\rho_r \equiv \rho_\gamma \left[1 + \frac{7}{8} \left(\frac{4}{11} \right)^{\frac{4}{3}} N_{\text{eff}} \right]. \quad (2.1.17)$$

It is defined in this way so that, in the absence of new physics, $N_{\text{eff}} \approx 3$ (actually $N_{\text{eff}} = 3.046$ [14, 15]), as we explain below. The factor of $\frac{7}{8} \left(\frac{4}{11} \right)^{\frac{4}{3}}$ is due to the sequence of neutrino decoupling and then electron-positron annihilation.

The temperature of neutrino decoupling can be estimated very approximately by comparing the rate, Γ , of processes keeping neutrinos in equilibrium (e.g. $\nu\bar{\nu} \leftrightarrow e^+e^-$, $e^-\bar{\nu} \leftrightarrow e^-\bar{\nu}$), with the rate of expansion, H [3]

$$\frac{\Gamma}{H} \sim \frac{G_F^2 T^5}{g_*(T)^{\frac{1}{2}} T^2 / M_{Pl}} \sim \left(\frac{T}{\text{MeV}} \right)^3. \quad (2.1.18)$$

The neutrinos decouple once the expansion of the universe causes the rate of interactions Γ to drop below the rate of expansion H . The above shows that this happens at around $T_{\nu, \text{decouple}} \sim \text{MeV}$. More detailed calculations find $T_{\nu, \text{decouple}} \approx 2.3 \text{ MeV}$ [16], but for our purposes the point is that the

neutrinos decouple (mostly) before electrons and positrons annihilate (which occurs at some temperature below the electron mass).

The above means that electrons and positrons will deposit their energy (or more precisely, entropy) into the photon sector and not the decoupled neutrino sector, and hence the photons will cool more slowly than the neutrinos, leading to $\frac{T_\nu}{T_\gamma} < 1$. To calculate this ratio, consider the entropy per comoving volume s (which can be shown to be conserved - e.g. see [3]):

$$\begin{aligned} S &\equiv \frac{(\rho + P) a^3}{T}, \\ &= \frac{2\pi^2}{45} g_{*S}(T) (aT)^3, \end{aligned} \quad (2.1.19)$$

where

$$g_{*S}(T) = \sum_{\text{bosons}} g_i \left(\frac{T_i}{T} \right)^3 + \frac{7}{8} \sum_{\text{fermions}} g_i \left(\frac{T_i}{T} \right)^3. \quad (2.1.20)$$

The entropy from the electron-positron annihilations is deposited into the photons, so the ratio $\frac{T_\nu}{T_\gamma}$ can be found by comparing the entropy in the photon sector and neutrino sector, before annihilations (when photons and neutrinos share a common temperature $T_{\gamma,1} = T_{\nu,1} = T_1$) and after annihilations (when the photon and neutrino temperatures differ $T_{\gamma,2} \neq T_{\nu,2}$) - this ratio is unchanged

$$\frac{g_{*S}^\gamma(T_1)}{g_{*S}^\nu(T_1)} = \frac{g_{*S}^\gamma(T_{\gamma,2}) T_{\gamma,2}^3}{g_{*S}^\nu(T_{\nu,2}) T_{\nu,2}^3}. \quad (2.1.21)$$

The relevant degrees of freedom contributing to g_{*S}^γ are the photons ($g = 2$) and electrons ($g = 7/2$), while the only contributions to g_{*S}^ν come from the neutrinos, and so g_{*S}^ν is unchanged across this process. $g_{*S}^\gamma(T_1) = 11/2$ and $g_{*S}^\gamma(T_{\gamma,2}) = 2$ so that, after electron-positron annihilation,

$$T_\nu \approx \left(\frac{4}{11}\right)^{\frac{1}{3}} T_\gamma. \quad (2.1.22)$$

Hence, we see that N_{eff} should be approximately equal to three, the number of active neutrino species. The reason that $N_{\text{eff}} = 3.046$ rather than precisely three in the standard picture is that the neutrinos haven't completely decoupled when electron-positron annihilation begins, so some of the entropy is deposited into the neutrino sector [14, 15].

Any deviation from $N_{\text{eff}} = 3.046$ may therefore indicate the presence of new physics, and conversely, a measurement of N_{eff} close to 3.046 can constrain the form of new physics [17, 18]. Note that new physics can both raise or lower N_{eff} - for example, if an additional particle deposits entropy into the photon sector via annihilations or decays after neutrino decoupling, the photon sector's cooling will be slowed further, and the ratio $\frac{T_\nu}{T_\gamma}$ will be even smaller, hence lowering N_{eff} below three [18].

We will now consider some of the phenomena which constrain new physics via limits on N_{eff} , among other effects.

2.2 Big Bang Nucleosynthesis

After electron-positron annihilation, all particles apart from photons and neutrinos will be non-relativistic, and hence will have suppressed number density (as can be seen from Equation 2.1.14). However, there will still be some abundance of non-relativistic particles. For example, there may be an abundance of dark matter produced via freeze-out or some other mechanism (as discussed in more detail in Section 3.3). Additionally, there will be a small number density of baryons, as we will discuss below. This gives rise to the formation of light element nuclei. This process can provide a probe of particle physics [19, 20, 21, 22].

Before neutrino decoupling, protons and neutrons are held in equilibrium by weak processes such as $ne^+ \leftrightarrow p\bar{\nu}$, $n\nu \leftrightarrow pe^-$. The equilibrium value of the neutron to proton ratio is given by (c.f. Equation 2.1.14, assuming $\mu_n \approx \mu_p$ due to small chemical potentials for the electrons and neutrinos)

$$\frac{n_n}{n_p} = \left(\frac{m_n}{m_p}\right)^{\frac{3}{2}} \exp[-(m_n - m_p)/T]. \quad (2.2.1)$$

As discussed above, weak processes such as those holding neutrons and protons in equilibrium become inefficient at around $T_{\text{dec}} \sim \text{MeV}$ and hence this ratio will be frozen-out (though still affected by neutron decays) at around

$$\frac{n_n}{n_p} \approx \exp[-Q/T_{\text{dec}}], \quad (2.2.2)$$

where $Q = m_n - m_p \approx 1.3 \text{ MeV}$. This ratio then feeds into the processes that lead to the formation of light elements.

The light elements have to be formed in order, as number densities are low and so collisions involving three nuclei are very rare. Hence, protons and neutrons first form deuterium, and then helium is formed after this. As the binding energy of helium is higher than that of deuterium, almost all the neutrons are converted into helium, and so the abundance of helium is tied to the neutron to proton ratio. This is followed by the production of lithium and beryllium nuclei [22, 19, 23].

To set constraints on new physics such as ΔN_{eff} , the primordial abundances of the light elements must be calculated by solving the coupled Boltzmann equations (e.g. as carried out in [22]) and compared to the observed abundances. As shown in Figure 2.1, the observed abundances of all elements apart from lithium match the theoretical predictions (in the Standard Model) well, and so any new physics which would affect big bang nucleosynthesis, such as particles decaying during this epoch or contributing to N_{eff} , are tightly constrained [22, 19, 23, 25].

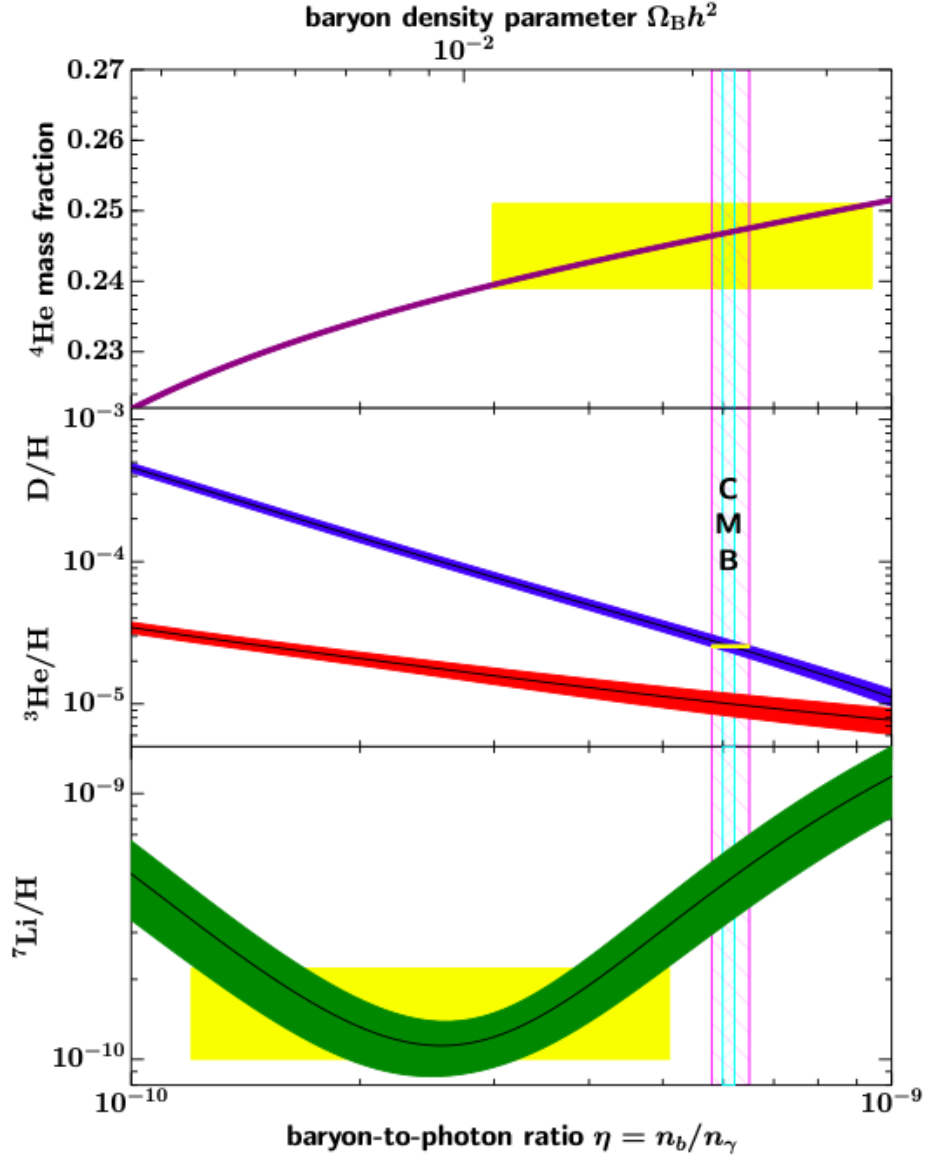


Figure 2.1: Predicted abundances as a function of baryon density, together with measured abundances (yellow boxes), reproduced from [24] with permission. Predicted abundances are shown with 95% CL ranges. As can be seen, the theoretical abundances for all elements other than lithium agree with the observed abundances at the baryon density measured by Planck [11].

For example, BBN provides a constraint on N_{eff} : if $N_{\text{eff}} > 3.046$ (i.e., there are any additional particles which are relativistic at the epoch of BBN), then the expansion rate H will be larger. This means that neutrino decoupling will

happen earlier (see Equation 2.1.18), the proton to neutron ratio will freeze-out at a higher value, and hence the helium abundance would be higher, along with other effects. A detailed recent analysis set $\Delta N_{\text{eff}} \lesssim 2.859 \pm 0.314$ [22].

As can be seen in Figure 2.1, the predicted abundance of lithium does not match its observed abundance well. Various solutions related to astrophysics or nuclear physics have been made [26, 27, 28, 29, 30, 31], but it is also possible that the discrepancy is due to new physics such as particles decaying during BBN or alterations to the gauge couplings at early times [32, 25, 33, 34, 35, 36, 37, 38, 39].

2.3 Cosmic Microwave Background Radiation

In the period after BBN has taken place, the electrons, baryons (mostly in the form of protons) and photons are strongly coupled. As the universe cools, the electrons and protons form hydrogen atoms (this is known as recombination) and so the density of free electrons drops, and the mean free path of photons increases until eventually they decouple [40, 41]. These photons then propagate unimpeded, and can be observed in the cosmic microwave background radiation (CMBR) today [40, 41, 11]. Hence, the CMBR is a snapshot of the conditions at the time of photon decoupling, and, in particular, carries information about any density and temperature fluctuations which existed at the time.

This is of great interest as some time before decoupling, matter (mostly in the form of dark matter) becomes the dominant component of the energy density of the universe, and hence primordial density fluctuations begin to grow gravitationally [41, 40, 42, 43]. However, up until decoupling, the baryons and electrons are still coupled to photons and hence subject to photon pressure. Hence, there are oscillatory density (and hence temperature) inhomogeneities

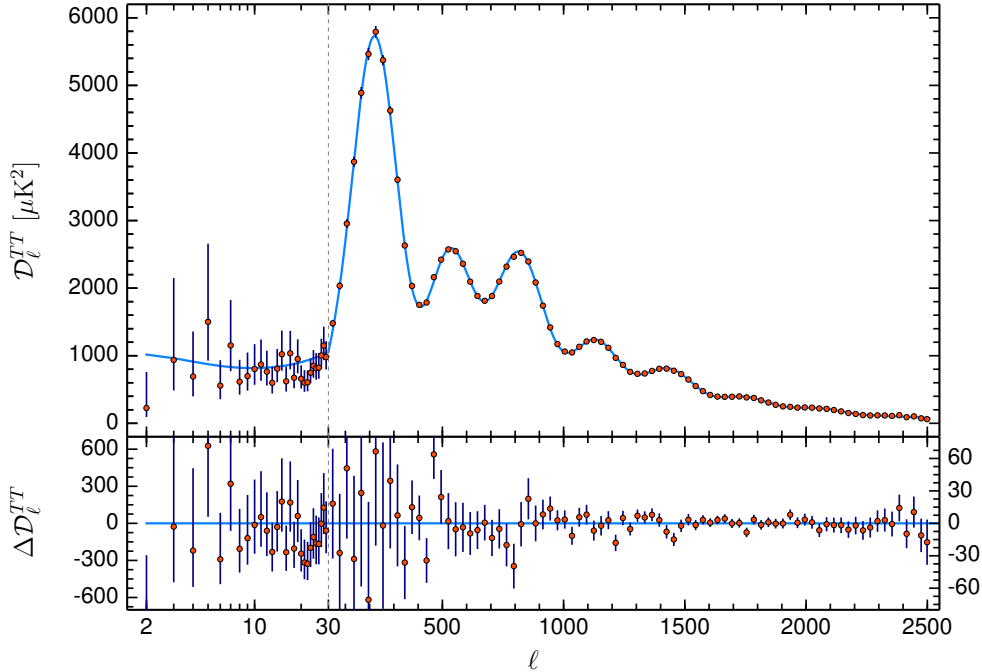


Figure 2.2: CMBR angular power spectrum, as measured by Planck, compared to the prediction from Λ CDM. The definition of D_l is given in the text. Figure reproduced from [11].

in the baryon/electron-photon fluid [41, 40, 42, 43]. At decoupling, these oscillations will stop evolving and freeze into the CMBR, with regions of higher density having higher temperature [40]. This is then encoded in the temperature anisotropies that can be observed today [11].

The angular power spectrum of the CMBR measured by Planck is displayed in Figure 2.2 [11]. In this figure, D_l is defined via the expansion of the temperature anisotropies in terms of spherical harmonics [11]

$$\frac{\delta T}{T} = \sum_{l=2}^{\infty} \sum_{m=-l}^{m=l} a_{lm} Y_{lm}(\theta, \phi), \quad (2.3.1)$$

with D_l then defined as

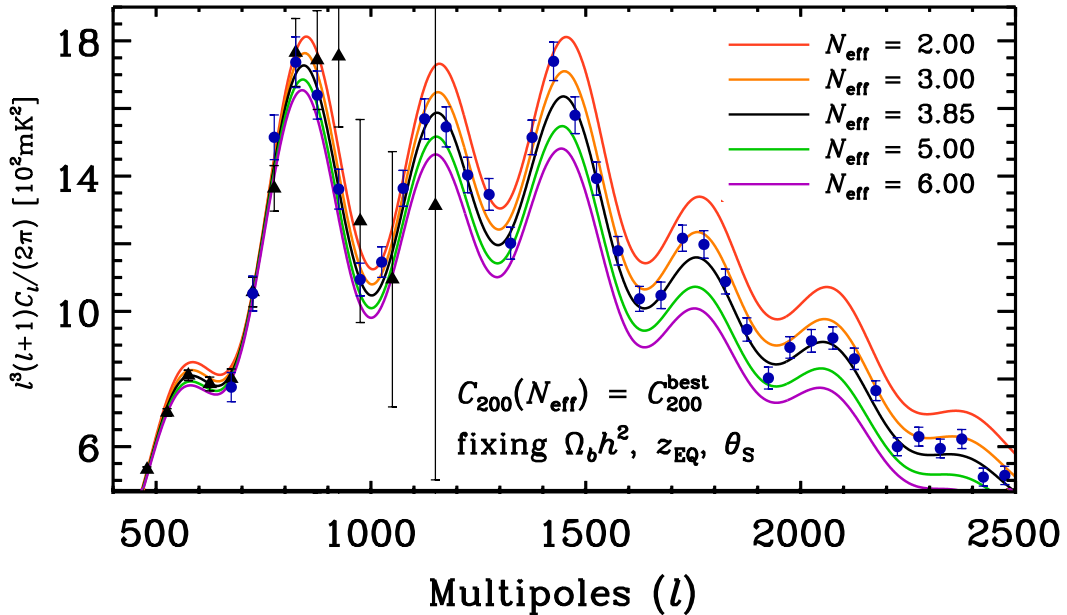


Figure 2.3: This figure shows the dependence of the anisotropies of the CMBR on the effective number of neutrino species N_{eff} , as explained in the text. C_l is equal to the D_l defined in the text. Reproduced from [41] with permission.

$$D_l \equiv \frac{1}{2l+1} \sum_{m=-l}^{m=l} |a_{lm}|^2. \quad (2.3.2)$$

As can be seen, the Λ CDM makes a very good prediction for the distribution of temperature anisotropies at photon decoupling. This provides another very strong constraint on the characteristics of physics beyond the Standard Model. For example, Figure 2.3 shows the effect on the CMBR of varying N_{eff} (note that this is reproduced from a source using the notation C_l rather than D_l , but these refer to the same quantities).

These differences again arise from the fact that increasing N_{eff} increases the expansion rate, which has two conflicting consequences. Firstly, it decreases the sound horizon, $r_s \propto H^{-1}$, which affects the position of the peaks. Secondly, it decreases the scale of Silk damping, $r_d \propto H^{-\frac{1}{2}}$. Silk damping occurs in the period shortly before decoupling, when the mean free path of photons starts to grow. As these photons propagate, they tend to diffuse energy from overdense

to underdense regions, hence smoothing perturbations on scales smaller than the Silk damping scale [41, 17, 40, 42, 43]. Figure 2.3 illustrates these two effects. By observing these effects, N_{eff} can be constrained. The latest constraint on N_{eff} from CMBR observations comes from Planck, $N_{\text{eff}} = 2.99 \pm 0.17$ [11].

The CMBR also constrains the energy density in matter and in baryons, which we will discuss in relation to dark matter in Section 3.1.4.

Chapter 3

Dark Matter

As discussed in the previous chapter, the cosmological evolution of the universe is best described by the Λ CDM model, which includes a significant fraction of its energy density in dark matter ($\sim 27\%$, or $\sim 84\%$ of the matter), some hitherto unobserved type of non-baryonic matter which is taken to be stable and neutral [1]. Dark matter has been observed via its gravitational effects, but not directly. However, various dark matter candidates have been proposed, which could also resolve other outstanding problems in particle physics. Hence, establishing the nature of dark matter is of interest not only for its own sake but also in order to further our understanding of physics at a fundamental level.

We will give an overview of the evidence for the existence of dark matter in Section 3.1, from the earliest hints in galaxy velocities to more modern evidence such as the cosmic microwave background radiation (CMBR). Section 3.2 will discuss some of the dark matter candidates which have received the most attention, including different types of WIMP dark matter, along with other options such as axions and FIMPs. Various options for the production of dark matter are covered in Section 3.3, with particular focus on freeze-out and freeze-in. Section 3.4 will review possible experimental probes of dark matter properties, which can be grouped broadly into direct detection, indirect detection and collider experiments.

3.1 Evidence for the Existence of Dark Matter

Since some form of ‘missing mass’ was first proposed by Zwicky [44], evidence for the existence of dark matter has accumulated, along with our understanding of some of its general properties. This section will cover some of the evidence pointing towards the existence of some form of dark matter, making up approximately 84% of the matter density of the universe, including galaxy rotation curves, properties of the CMBR, the Bullet cluster and gravitational lensing. It will also discuss some alternatives to dark matter, and why they are now disfavoured.

3.1.1 Galaxy Rotation Curves

The first suggestion of dark matter was made by Zwicky in 1933 [44]. This paper estimated the velocities of galaxies within the Coma galaxy cluster, along with the mass of the visible matter in the cluster. These two quantities were expected to be related by the fact that, roughly stated, the gravitational force inwards should balance with the centrifugal force. This implies that approximately

$$v \sim \sqrt{\frac{GM(r)}{r}}. \quad (3.1.1)$$

where $M(r)$ is the mass contained within the radius r . However, he found using the virial theorem that galaxy velocities implied a mass about 300 times greater than the estimate of the mass of visible matter in the cluster, and suggested this discrepancy could be explained if the majority of the mass of the cluster consisted of some kind of ‘dark matter’.

Detailed observations of galaxy rotation curves (i.e. average rotational velocities as a function of radius) were later made [45, 46, 47]. These showed that the rotational velocity is approximately constant for large values of r ,

which suggests (from Equation 3.1.1) that $M(r) \sim r$ for large r in contrast to the observed distribution of visible matter.

One possible explanation for these observations is the presence of a dark matter ‘halo’ extending out beyond the visible galaxy with $M(r) \sim r$. Other possibilities have been suggested, for example MODified Newtonian Dynamics (MOND) - e.g. moving away from proportionality of inertial and gravitational masses in the low-acceleration regime [48]. However, we will see that MOND is disfavoured by observations such as the bullet cluster, discussed below in Section 3.1.2.

3.1.2 The Bullet Cluster

Further evidence of the existence of dark matter is provided by observations of the Bullet galaxy cluster. The Bullet cluster was formed by the merger of two galaxy clusters. During the merger, galaxies in each cluster behave like nearly collisionless particles and pass through each other with very little interaction, whereas the intracluster medium (made up of superheated gas) behave like a fluid and lag behind [49]. The gas emits X-ray radiation, so the offset of galaxies and gas can be seen via comparison of optical and X-ray observations - this is shown in Figure 3.1, where the gas distribution is overlaid in pink over optical observations of the galaxies [49, 50].

The mass of the intracluster medium can be measured using X-ray observations, and is found to make up the dominant fraction of the mass of the visible matter in the clusters [52, 53]. Hence, if dark matter is not present, we would expect the mass distribution to trace the gas, while if dark matter is present we would expect the mass distribution to trace the galaxies.

The mass distribution can be mapped using weak gravitational lensing, where light from objects behind the bullet cluster is distorted by the gravitational influence of the mass contained in the bullet cluster. This distortion tends to make the distant objects appear stretched ‘around’ the centre of mass

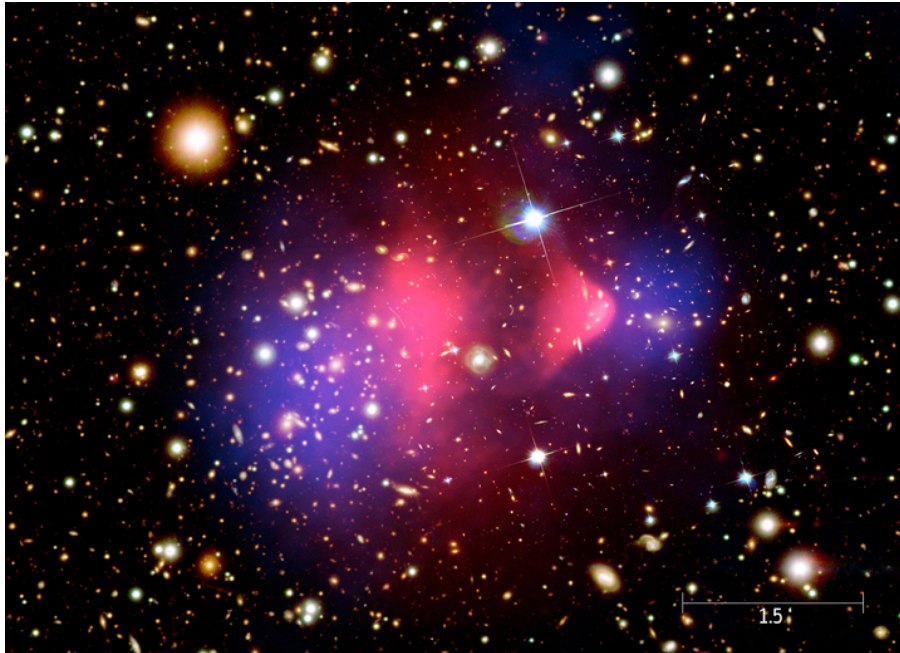


Figure 3.1: Composite image published by NASA/CXC/M. Weiss, using optical and gravitational lensing data from [50], and X-ray data from [51]. Optical observations are shown in yellow/orange; X-ray observations (corresponding to the intracluster medium) are superimposed in pink; and the mass density (dominated by dark matter) is superimposed in blue.

of the cluster. The true shape of many of these objects is unknown, so this technique requires observations of a large number of distant objects in order to accurately map the mass density. This is the approach used by [49] and [50], with the resulting mass distribution overlaid in Figure 3.1 in blue. As can be seen, the mass distribution traces the galaxies, and hence there must be non-baryonic dark matter making up the majority of the mass in the galaxy cluster. Notably, this analysis is nearly unchanged under modified theories of gravity/dynamics (there may be small changes to the gravitational lensing and hence to the precise mass distribution, but not enough to change the overall conclusion), and hence these observations are incompatible with MOND without dark matter [54]. These observations also tell us that, given

that the dark matter is closely aligned with the galaxies, it cannot have strong self-interactions - this fact has been used to set upper limits on dark matter scattering cross-sections [49, 55].

Similar observations have since been made of other galaxy cluster mergers [56].

3.1.3 Structure Formation and the CMBR

The presence (or lack) of dark matter influences how structures such as galaxies and galaxy clusters form. This is because primordial inhomogeneities in the dark matter energy density can begin to grow from matter-radiation equality onwards, whereas until decoupling baryon density inhomogeneities will still be coupled to photons and hence damped - photons will propagate from overdense regions to underdense regions, smoothing out any baryon density inhomogeneities (this is known as Silk damping) [57]. This means that baryon inhomogeneities have less time to grow than dark matter inhomogeneities, so in the absence of dark matter the initial inhomogeneities must be larger in order to produce the correct structure [11, 58, 59].

To probe the size of these inhomogeneities at recombination, we can consider the cosmic microwave background radiation (see Section 2.3 for more details). The density inhomogeneities are proportional to temperature anisotropies in the CMBR, so observations of the anisotropies can be compared to the observed large scale structure in order to infer the relative contributions of baryons and dark matter to the energy density. This was first carried out in [59] which found that dark matter was required in order to match the observed large-scale structure. Figure 3.2 shows that the expected matter power spectrum in the Λ CDM model, given the observed level of temperature anisotropy, matches the observed matter power spectrum well [11]. In this figure, $P_m(k)$ is defined in terms of the density contrast,

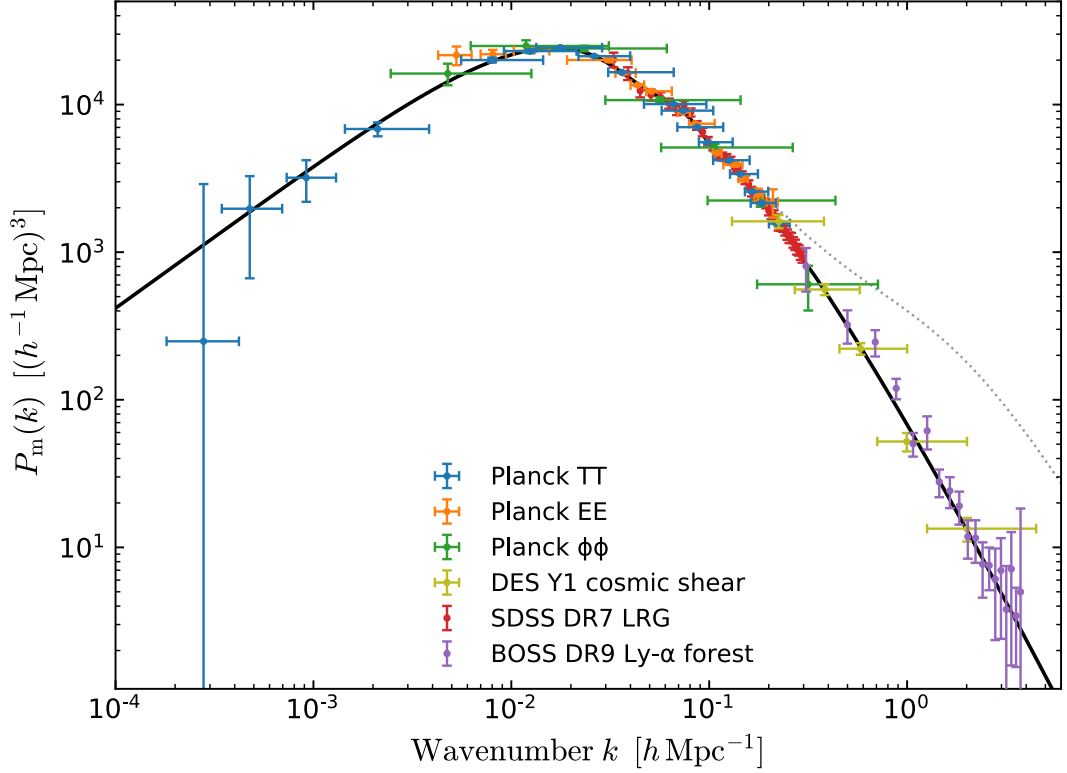


Figure 3.2: Comparison of the predicted matter power spectrum ($P_m(k)$ is defined in Equation 3.1.3) in the Λ CDM model and various experimental observations, reproduced from [11].

$$\delta(\mathbf{x}) \equiv \frac{\rho(\mathbf{x}) - \bar{\rho}}{\bar{\rho}} \quad (3.1.2)$$

where $\bar{\rho}$ is the average density. $P_m(k)$ is related to the density contrast via the Fourier transform of the autocorrelation function of the density contrast via

$$\begin{aligned} \langle \delta(\mathbf{x} + \mathbf{r}) \delta(\mathbf{x}) \rangle &\equiv \frac{1}{V} \int d^3\mathbf{x} \delta(\mathbf{x}) \delta(\mathbf{x} + \mathbf{r}) \\ &\equiv \int \frac{d^3\mathbf{k}}{(2\pi)^3} P(\mathbf{k}). \end{aligned} \quad (3.1.3)$$

Additionally, structure formation requires that the dark matter should not be too ‘hot’, i.e. its energy density should not be dominated by its kinetic

energy [60]. If all of the dark matter were hot, in the initial stage of structure formation the hot dark matter would stream from areas of higher than average density to those of lower density, reducing density perturbations on small scales [61, 62]. This means that structure tends to form in a ‘top-down’ fashion, with the largest structures forming first, then fragmenting into smaller structures [61, 62]. In order to match this to observations, these structures must have formed very recently (at a redshift of $z \lesssim 1$), which doesn’t fit with the observations (e.g. of galaxies at redshifts of $z > 1$) [60, 62].

Usually this is resolved by considering ‘cold’ dark matter (CDM) candidates, which have negligible kinetic energy (e.g. particles which decouple while non-relativistic - see Section 3.3.1), but it is also possible that dark matter could be ‘warm’, i.e. with properties somewhere between those of cold and hot dark matter [63, 64]. Such a particle could help to resolve some discrepancies between observations and predictions for structure formation on small scales in CDM models, such as the core-cusp problem [65, 66], the ‘too big to fail’ problem [67, 68] or the missing satellites problem [69, 70, 71] [72, 73, 74]. However, some suggest that such discrepancies could be explained by shortcomings in simulations or our understanding of the behaviour of CDM models [75, 76, 77].

3.1.4 CMB Angular Power Spectrum

As discussed in Section 2.3, between matter-radiation equality and decoupling, the density of baryons will oscillate as they begin to fall into gravitational wells (primarily established by dark matter), with radiation pressure then acting as a restoring force on the baryons. The dark matter and baryon abundances each affect the evolution of the oscillations in different ways (both contribute to the gravitational perturbations, but baryons experience pressure from their interactions with the photons), as illustrated in Figure 3.3, and hence estimates of each can be made from observations of the CMBR [40].

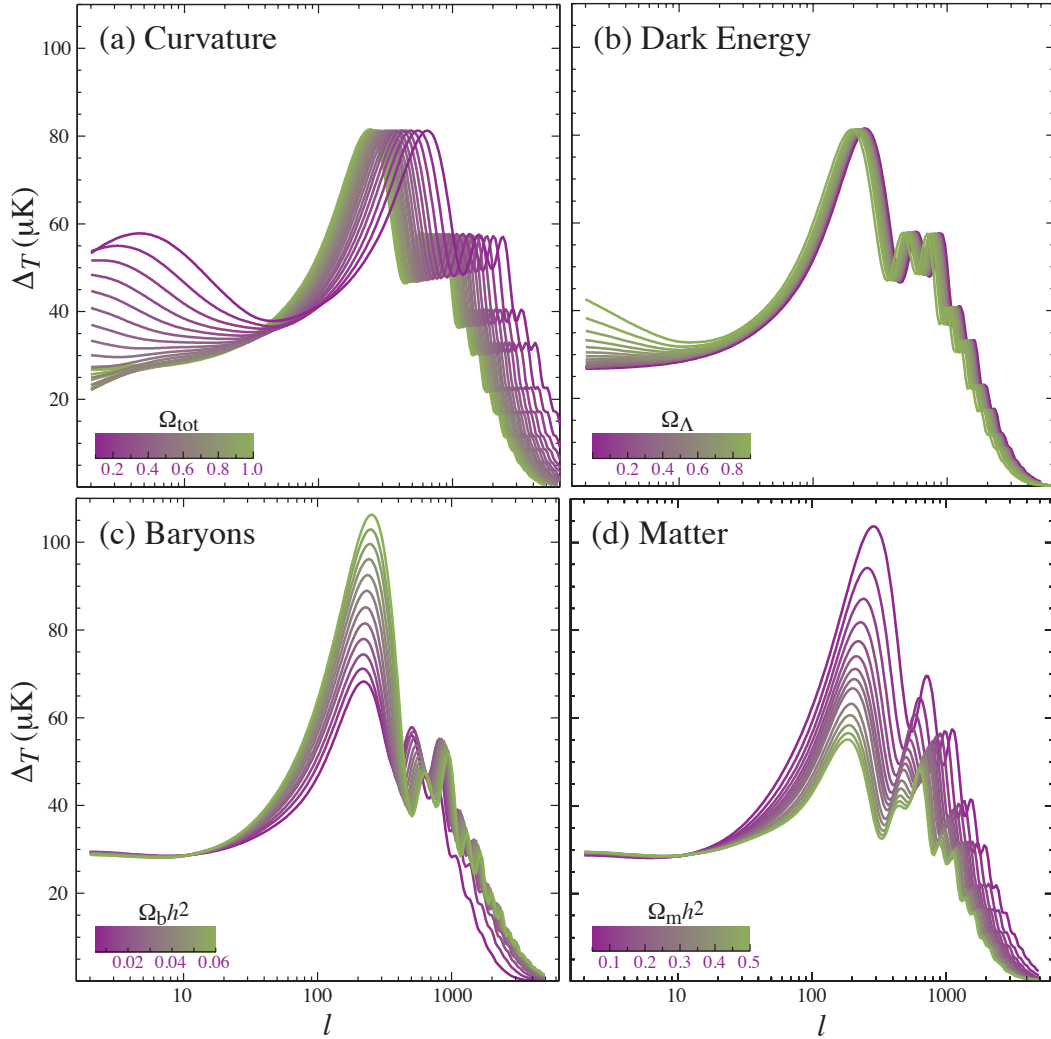


Figure 3.3: This figure illustrates the impact on CMBR temperature anisotropies of varying various components of the energy density. Reproduced from [40] with permission.

3.2 Dark Matter Candidates

Having summarised the evidence for the existence of dark matter, we will now give a brief overview of some of the candidates which could make up dark matter. As discussed above, we would generally like a dark matter candidate to be stable, non-baryonic, cold (in the sense described in Section 3.1.3), electrically neutral, and able to be produced with the correct abundance. There are exceptions, such as particles which are unstable but with lifetimes much longer

than the age of the universe, or warm dark matter which has non-negligible kinetic energy, as discussed in Section 3.1.3 (sterile neutrinos provide an example of a dark matter candidate which can decay with a very long lifetime, and also can be warm [78]).

3.2.1 WIMPs

Weakly interacting massive particles (WIMPs) tend to have masses around the weak scale and weak strength interactions. They can be produced in approximately the correct abundance by freeze-out - this is dubbed the ‘WIMP miracle’ (discussed in Section 3.3.1). Some examples are:

Neutralinos in supersymmetric theories with R-parity. For example, the Minimally Supersymmetric Standard Model (MSSM) contains two neutral fermionic ‘gauginos’ (superpartners to gauge bosons - in particular, the neutral gauginos are superpartners to the B and W_3 bosons), and two neutral fermionic ‘higgsinos’ (superpartners to the Higgs bosons), which can mix (after electroweak symmetry breaking). If the lightest neutralino is the lightest superpartner in the model, it will be stabilised by R-parity, and hence offers a stable WIMP candidate. This is discussed further in Chapter 4.

Kaluza-Klein excitations in models with extra dimensions. In particular, models with universal extra dimensions (UED) contain ‘towers’ of Kaluza-Klein states with masses $m_n \propto n/R$, where R is the compactification scale of the extra dimensions [79]. Many UED theories have a symmetry called Kaluza-Klein parity, under which the Kaluza-Klein states with n odd are charged. This stabilises the lightest $n = 1$ Kaluza-Klein state, which could be the WIMP candidate. Within each UED model, a particular compactification scale is required to reproduce the correct DM relic abundance, for example in minimal UED, the required range is $1.25 \text{ TeV} \lesssim R^{-1} \lesssim 1.5 \text{ TeV}$ [80], which is in tension

with collider searches [81, 82].

Little Higgs theories explain the lightness of the Higgs boson by identifying the Higgs boson with a pseudo-Goldstone boson associated with a broken global symmetry. Such theories can contain stable scalar particles with the correct abundance [83, 84]. However, little Higgs models tend to predict a Higgs mass around $m_h \sim 500$ GeV, and fine-tuning is required to produce the correct value [85].

3.2.2 FIMPs, superWIMPs and WIMPzillas

All of the above particles are in thermal equilibrium in the early universe, and are produced via freeze-out (see Section 3.3.1). However, it is possible that dark matter may have such feeble interactions that it would *never* have been in thermal equilibrium. Such a particle could still be produced via these feeble interactions. Some examples are:

Freeze-in massive particles (FIMPs) as described in Section 3.3.2. Such a particle is not in thermal equilibrium (and is assumed to have a negligible abundance) in the early universe, and is produced via processes such as decays of particles in the thermal bath, or number-changing scattering processes [86]. This abundance is then ‘frozen-in’ once the relevant particles drop out of equilibrium.

SuperWIMPs are extremely weakly interacting particles produced by late decays of frozen-out WIMPs. The relic abundance of the superWIMP is given by $\Omega_{SW} h^2 = \frac{m_{SW}}{m_{WIMP}} \Omega_{WIMP}^{\text{no decay}} h^2$, where $\Omega_{WIMP}^{\text{no decay}} h^2$ would be the relic abundance of the frozen-out WIMP if it didn’t decay. Usually the mass of the superWIMP is taken to be of the same scale as the WIMP mass, so the superWIMP inherits approximately the right relic abundance from the WIMP abundance [87].

WIMPzillas are extremely heavy particles (with masses $10^{12} \text{ GeV} \lesssim m \lesssim 10^{15} \text{ GeV}$), produced with an extremely small number density (e.g. gravitationally) [88].

The presence of feeble interactions such as those found in theories with FIMPs, superWIMPs and WIMPzillas can lead to relatively long-lived particles. Such particles may lead to interesting signals such as displaced vertices at colliders, as well as effects on cosmological observables such as abundances of light elements [86].

3.2.3 Axions

Axions are motivated by the strong CP problem: the Standard Model Lagrangian can contain a CP-violating term

$$\mathcal{L} \supset \frac{\bar{\theta} g_3^2}{32\pi^2} F_{\mu\nu} \tilde{F}^{\mu\nu}, \quad (3.2.1)$$

where $\tilde{F}_{\mu\nu}$ is the antisymmetrised gluon field strength $\tilde{F}^{\mu\nu} = \epsilon^{\mu\nu\rho\sigma} F_{\rho\sigma}$. This term contributes to the electric dipole moment of the neutron, $d_e \sim \bar{\theta} \times 10^{-16} e \cdot \text{cm}$ [89]. The measured value of d_e is $d_e = (0.0 \pm_{\text{stat}} 1.1 \pm_{\text{sys}} 0.2) \times 10^{-26} e \cdot \text{cm}$ [90], implying that $\bar{\theta} \lesssim 10^{-10}$, which presents a fine-tuning problem for the Standard Model.

Axions are introduced to resolve this problem: a new pseudoscalar field a is introduced with a coupling

$$\mathcal{L} \supset \frac{a g_3^2}{32\pi^2 f_a} F_{\mu\nu} \tilde{F}^{\mu\nu}, \quad (3.2.2)$$

where f_a is the axion decay constant. The total $\bar{\theta}$ parameter then becomes dynamical, with the vacuum energy minimised with $\bar{\theta}$ very small [89]. The axion mass and interactions both decrease with increasing decay constant f_a [91, 92, 93].

In particular, axions couple to photons at loop-level, which gives rise to constraints such as those from stellar cooling and supernovae, which imply that axions must be very light ($m_a \lesssim 10 \text{ meV}$) [94]. Such a light axion will also be very weakly interacting and long-lived, so could be dark matter. Axion dark matter requires a non-thermal production mechanism, as the abundance of such a light axion would be too small if thermally produced [95]. Additionally, it would be hot dark matter. Axions can be produced non-thermally via mechanisms such as ‘vacuum realignment’ (where the axion field takes a different value in the early universe compared to now, and the change in axion field generates an axion abundance), or production from decays of topological defects [96].

3.2.4 (Sterile) Neutrinos

Among the first particles put forward as a dark matter candidate were the active (i.e. Standard Model) neutrinos. Neutrinos decouple while relativistic, hence with an appreciable number density - the neutrinos have abundance [97]

$$\Omega_\nu h^2 \approx \sum_i \frac{m_{\nu_i}}{94 \text{ eV}}. \quad (3.2.3)$$

However, the neutrino masses are limited by the KATRIN tritium beta decay experiment, which sets an upper bound on the effective neutrino mass [98, 99]

$$m_\nu^{\text{eff}} \equiv \left(\sum_i |U_{ei}|^2 m_i^2 \right)^{\frac{1}{2}} \lesssim 0.8 \text{ eV}, \quad (3.2.4)$$

where U_{ei} is the mixing of the electron neutrino with the i th mass eigenstate. This effectively constrains all three active neutrino masses, as the neutrino masses must have splittings $\Delta m^2 \approx 2.5 \times 10^{-3} \text{ eV}^2$ and $\Delta m^2 \approx 7.4 \times 10^{-5} \text{ eV}^2$ in order to explain solar and atmospheric neutrino oscillations [100, 101, 102].

Contributions from additional light neutrinos are also tightly constrained by observations of the CMBR. Hence, neutrinos can only provide a subdominant contribution to the dark matter abundance ($\Omega_\nu h^2 \sim 10^{-5}$) [1].

‘Sterile’ neutrinos are a related dark matter candidate. Sterile neutrinos are uncharged under all Standard Model gauge interactions, and hence can provide a mass term for the neutrinos via the Higgs mechanism - schematically

$$\mathcal{L} \supset -\lambda_\nu H \bar{\nu}_L \nu_S + \text{h.c.} \rightarrow -m_\nu \nu_h \bar{\nu}_L \nu_S - \lambda_\nu h \bar{\nu}_L \nu_S + \text{h.c.} \quad (3.2.5)$$

where ν_L represents the active neutrinos. (Clearly this set-up requires a very small value of λ_ν in order to obtain the correct neutrino masses - this can be avoided e.g. by including a Majorana mass for the singlet, ν_S , which can give rise to a see-saw mechanism [103, 104].)

Generally, a sterile neutrino will mix with the active neutrinos. It will therefore inherit the active neutrino interactions, suppressed by the size of the active-sterile mixing. They can therefore provide a dark matter candidate, if produced with the correct abundance. Sterile neutrinos don’t tend to reach thermal equilibrium but can be produced by neutrino oscillations, e.g. via the Dodelson-Widrow mechanism [64].

Sterile neutrinos with keV masses received attention after observations of an unidentified X-ray emission line at 3.55 keV, which could be caused by the decay of a sterile neutrino with mass around 7.1 keV (see Figure 3.4) [105, 106]. However, the interpretation that this X-ray line stems from keV sterile neutrinos making up all of the dark matter is in tension with non-observation of this line in other contexts, such as observations of dwarf spheroidal galaxies [107, 108, 109]. Recent surveys of Milky Way dwarf satellite galaxies (whose formation is suppressed by WDM) also seem to rule out this interpretation [110].

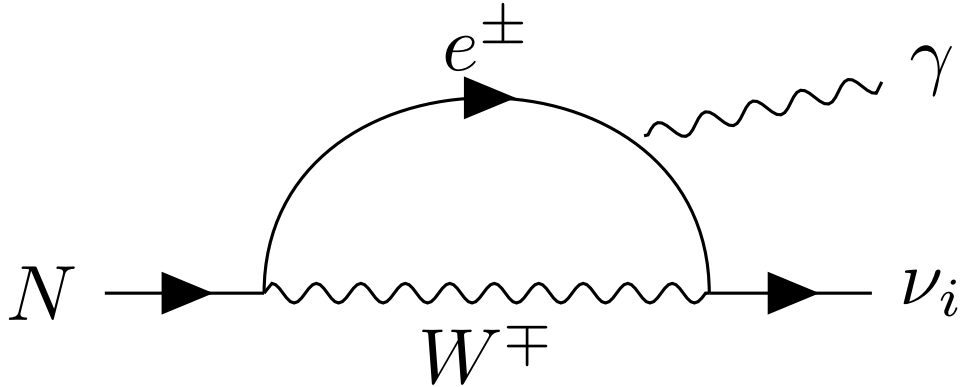


Figure 3.4: Decay of a sterile neutrino $N \rightarrow \gamma \nu_i$ (this decay is subdominant), which could give rise to the unidentified X-ray line in [105, 106]. Note that N and ν_i refer to the mostly sterile and mostly active mass eigenstates, respectively.

3.2.5 Hidden Dark Matter

Most dark matter candidates presented here have some direct interactions with Standard Model particles. However, it is possible that this is not the case, and the dark matter sits in a hidden sector which is only connected to the visible sector via some ‘portal’ (or no portal at all) [111, 112]. Portals are characterised by Standard Model operators coupled to singlet (dark sector) operators. Such a Standard Model operator must be a gauge singlet, and requires mass dimension less than 4 (to allow a renormalizable coupling with singlet operators). Various such portals have been suggested, such as the Higgs portal, neutrino portal, kinetic mixing portal, or axion portal [113, 114, 115, 116, 117, 118, 119, 120, 121, 122, 123, 124, 125, 126].

3.2.6 MACHOs

Non-luminous massive compact halo objects (MACHOs) such as primordial black holes (PBHs) have also been proposed as a dark matter candidate [127, 128]. Such objects would be detectable via gravitational lensing: as a MACHO

passes between the earth and a star, the star's brightness would appear to increase and then decrease [129]. Searches for such microlensing events have found too few for dark matter to be entirely composed of MACHOs in the mass range $10^{-7}M_{\odot} \lesssim m \lesssim 10M_{\odot}$ [130, 131]. After the observation of gravitational waves, by the Laser Interferometer Gravitational-Wave Observatory (LIGO), of the merger of two black holes with masses around $30M_{\odot}$, there was further interest in PBHs as dark matter, with masses in the range $20M_{\odot} \lesssim m \lesssim 100M_{\odot}$ [132, 133]. However, such an interpretation seems to be in tension with CMB distortion constraints [134, 135].

3.3 Dark Matter Production

As discussed in Section 3.1.4, the dark matter abundance is estimated by Planck to be $\Omega h^2 = 0.12 \pm 0.0012$ [1]. We will focus on two main mechanisms to produce this abundance - freeze-out and freeze-in - however there are a number of other possible mechanisms such as gravitational production [111]; late decays of frozen-out particles [87]; production from topological defects [95, 136]; or mechanisms specific to the dark matter candidate, such as Dodelson-Widrow production of neutrinos [64] or primordial black holes produced by density perturbations in the early universe [128].

3.3.1 Freeze-Out

Freeze-out is based on the assumption that dark matter is formed of a particle species which is in thermal equilibrium in the early universe - it has interaction rate $\Gamma \gg H$, where H is the expansion rate of the universe ($H = \frac{\dot{a}}{a}$ where a is the scale factor in the FRW metric - see Section 2.1.1). We are interested in the dark matter phase space distribution function $f(x^\mu, p^\mu)$, which is proportional to the density of dark matter particles per unit comoving volume:

$$n = \frac{g}{(2\pi)^3} \int d^3p f, \quad (3.3.1)$$

where g is the number of internal degrees of freedom.

For a particle species in equilibrium, the distribution function is given by

$$f(p, t) = \frac{1}{e^{(E-\mu)/T} \pm 1}, \quad (3.3.2)$$

as discussed in Section 2.1.3 (the plus sign gives the distribution for fermions, the minus sign gives the distribution for bosons, and μ is the chemical potential) [3]. From 3.3.2, if the dark matter remains in thermal equilibrium until a temperature much less than the particle mass, the number density of the dark matter will be exponentially suppressed, $\rho_{\text{DM}} \sim \exp(-\frac{m}{T})$. If the dark matter remained in equilibrium until the present day, its density would be negligible. However, this does not occur in freeze-out - the interaction rate is proportional to the density of states taking part in the interaction, so once the dark matter number density drops below a certain level the interactions will become very rare ($\Gamma \ll H$) and the dark matter will leave equilibrium (see Figure 3.5). Once $H \gg \Gamma$, the dark matter density can be well approximated by neglecting interactions and only considering the effect of the expansion of the universe, $\rho_{\text{DM}} \propto a^{-3}$.

The above explains the qualitative behaviour of the dark matter density. In order to make a quantitative estimate of the dark matter abundance, we must calculate the evolution of the phase space distribution through decoupling. Our analysis here will follow that of [3].

The evolution of the phase space distribution is given by the Boltzmann equation

$$\hat{\mathbf{L}}[f] = \mathbf{C}[f] \quad (3.3.3)$$

where $\hat{\mathbf{L}}$ is the Liouville operator, given in general relativity by

$$\hat{\mathbf{L}} = p^\mu \frac{\partial}{\partial x^\alpha} - \Gamma_{\beta\gamma}^\alpha p^\beta p^\gamma \frac{\partial}{\partial p^\alpha}, \quad (3.3.4)$$

and \mathbf{C} is the collision operator [3].

Under the assumption that the universe is spatially homogeneous and isotropic, the distribution function should only be a function of E and t . Hence, 3.3.3 simplifies to

$$E \frac{\partial f}{\partial t} - H |\mathbf{p}|^2 \frac{\partial f}{\partial E} = \mathbf{C} [f]. \quad (3.3.5)$$

Integrating across $\frac{g}{(2\pi)^3} \int d^3p$ (after taking out a factor of E), this can be rewritten in terms of the number density $n(t)$,

$$\frac{dn}{dt} + 3Hn = \frac{g}{(2\pi)^3} \int \frac{d^3p}{E} \mathbf{C} [f]. \quad (3.3.6)$$

Labelling the dark matter as X , the term involving the collision operator for a single process $X + a + b + \dots \leftrightarrow i + j + \dots$ is [3]

$$\begin{aligned} \frac{g}{(2\pi)^3} \int \frac{d^3p_X}{E} \mathbf{C} [f] = & \int d\Pi_X d\Pi_a \dots d\Pi_i \dots \\ & \left\{ (2\pi)^4 \delta^4(p_X + p_a + \dots - p_i - \dots) \right. \\ & [|\mathcal{M}|_{i+j+\dots \leftrightarrow X+a+\dots}^2 f_i \dots (1 \pm f_X) (1 \pm f_a) \dots \\ & \left. - |\mathcal{M}|_{X+a+\dots \leftrightarrow i+\dots}^2 f_X f_a \dots (1 \pm f_i) \dots] \right\}, \quad (3.3.7) \end{aligned}$$

where f_y is the phase space distribution function of the particle y ($y = X, a, b, \dots, i, j, \dots$), the matrix elements squared $|\mathcal{M}|^2$ are averaged over final and initial spins and include all symmetry factors, and

$$d\Pi_y = \frac{g_y}{(2\pi)^3} \frac{d^3 p_y}{2E_y}. \quad (3.3.8)$$

Assuming CP -invariance, which is a reasonable assumption for all models which we will consider, $|\mathcal{M}|_{i+j+\dots\leftrightarrow X+a+\dots}^2 = |\mathcal{M}|_{X+a+\dots\leftrightarrow i+\dots}^2$, so write both as $|\mathcal{M}|^2$. Additionally, we assume that all species obey Maxwell-Boltzmann statistics, which means that the distribution functions for all species in equilibrium are given by $f_y(E_y) = \exp[-(E_y - \mu_y)/T]$, and $(1 \pm f_y) \approx 1$. Hence, Equation 3.3.6 becomes

$$\begin{aligned} \frac{dn_X}{dt} + 3Hn_X = \int d\Pi_X d\Pi_a \dots d\Pi_i \dots \\ \left\{ (2\pi)^4 \delta^4(p_X + p_a + \dots - p_i - \dots) \right. \\ \left. |\mathcal{M}|^2 (f_i f_j \dots - f_X f_a \dots) \right\}. \end{aligned} \quad (3.3.9)$$

This equation has a physical interpretation: the first term on the left-hand side is the total change in the X number density; the second term on the left-hand side is the change due to expansion of the universe; and the term on the right-hand side is the change due to number changing interactions. It can be further simplified by introducing variables

$$x \equiv \frac{m_X}{T}, \quad Y \equiv \frac{n_X}{s}, \quad (3.3.10)$$

where s is the entropy density $s \equiv S/a^3$. The conservation of entropy, $\frac{d}{dt}(a^3 s) = 0$, implies that $\dot{n}_X + 3Hn_X = sY_X$. Freeze-out occurs long before radiation-matter equality so during radiation domination, and during this epoch

$$t \approx 0.301 g_*^{-\frac{1}{2}} \frac{m_P l}{T^2},$$

$$H \approx 1.67 g_*^{\frac{1}{2}} \frac{T^2}{m_{Pl}}. \quad (3.3.11)$$

Hence, Equation 3.3.9 can finally be written

$$\begin{aligned} \frac{dY}{dx} = & -\frac{x}{H(m)s} \int d\Pi_X d\Pi_a \dots d\Pi_i \dots \\ & \left\{ (2\pi)^4 \delta^4(p_X + p_a + \dots - p_i - \dots) \right. \\ & \left. |\mathcal{M}|^2 (f_X f_a \dots - f_i f_j \dots) \right\}. \end{aligned} \quad (3.3.12)$$

Now we will specialise to the case of a stable particle, X , freezing out via a $2 \leftrightarrow 2$ process $X\bar{X} \leftrightarrow \chi\bar{\chi}$, where χ is in thermal equilibrium with zero chemical potential, and with no asymmetry between χ and $\bar{\chi}$. In this case, and under the delta function $\delta^4(p_X + p_{\bar{X}} - p_\psi - p_{\bar{\psi}})$, we can simplify $(f_X f_{\bar{X}} - f_\psi f_{\bar{\psi}})$ as

$$f_\psi f_{\bar{\psi}} = e^{-(E_\psi + E_{\bar{\psi}})/T} = e^{-(E_X + E_{\bar{X}})/T} = f_X^{\text{Eq}} f_{\bar{X}}^{\text{Eq}}, \quad (3.3.13)$$

where f^{Eq} indicates the distribution function if the X s were in equilibrium, and Equation 3.3.12 becomes

$$\frac{dY}{dx} = -\frac{x \langle \sigma_{X\bar{X} \rightarrow \chi\bar{\chi}} v \rangle s}{H(m)} (Y^2 - Y_{\text{Eq}}^2), \quad (3.3.14)$$

where $\langle \cdot \rangle$ indicates the thermal average. We can take the leading order behaviour of $\langle \sigma v \rangle$ in v ($v \approx 0.3$ during freeze-out, so often it is necessary to consider multiple terms in this expansion, but we will consider only one for simplicity), $\langle \sigma v \rangle \propto v^p$. Hence, define $\langle \sigma v \rangle = \sigma_0 x^{-n}$ ($v \sim T^{-\frac{1}{2}}$), with $n = 0$ for s -wave annihilation ($p = 0$), $n = 1$ for p -wave ($p = 2$) and so on. In this case, Y obeys

$$\frac{dY}{dx} = -\lambda x^{-n-2} (Y^2 - Y_{\text{Eq}}^2), \quad (3.3.15)$$

where

$$\lambda \approx 0.264 \frac{g_{*S}}{g_*^{\frac{1}{2}}} m_{Pl} m \sigma_0, \quad (3.3.16)$$

and, for a cold relic (i.e. dark matter that is non-relativistic during decoupling),

$$Y_{\text{Eq}} \approx 0.145 \frac{g_{*S}}{g_*} x^{\frac{3}{2}} e^{-x}. \quad (3.3.17)$$

This can be solved approximately; write

$$\Delta \equiv Y - Y_{\text{Eq}}, \quad (3.3.18)$$

which obeys

$$\Delta' = -Y'_{\text{Eq}} - \lambda x^{-n-2} \Delta (2Y_{\text{Eq}} + \Delta), \quad (3.3.19)$$

where $'$ indicates differentiation with respect to x . After freeze-out, Y diverges very rapidly from Y_{Eq} , so $\Delta \gg Y_{\text{Eq}}$, and 3.3.19 can be approximated as

$$\Delta' = -\lambda x^{-n-2} \Delta^2. \quad (3.3.20)$$

Integrating this from freeze-out, $x = x_f$ (and $\Delta \approx 0$), to $x = \infty$ to find the final abundance, $Y_\infty = \Delta_\infty$, we find

$$Y_\infty \approx \frac{n+1}{\lambda} x_f^{n+1} \quad (3.3.21)$$

We can then find x_f by considering the period just before freeze-out, during which Δ' will be small, so that

$$\Delta \approx -\frac{Y'_{\text{Eq}} x^{n+2}}{\lambda (2Y_{\text{Eq}} + \Delta)}. \quad (3.3.22)$$

Now defining x_f by the requirement that at $x = x_f$, Δ and Y_{Eq} should be of comparable size: write $\Delta(x_f) = cY_{\text{Eq}}(x_f)$, then using the behaviour of Y_{eff} given in Equation 3.3.17 along with the fact that $x > 1$ just before freeze-out, the approximate solution to 3.3.22 near freeze-out will be given by

$$\Delta \approx \frac{x_f^{n+1}}{(2+c)\lambda}, \quad (3.3.23)$$

so that the freeze-out requirement $\Delta(x_f) = cY_{\text{Eq}}(x_f)$ has approximate solution

$$x_f \approx \log[(2+c)\lambda ac] - \left(n + \frac{1}{2}\right) \log\{\log[(2+c)\lambda ac]\}, \quad (3.3.24)$$

where $a \approx 0.145 \frac{g}{g_{*S}}$. This only depends logarithmically on c , but $c(c+2) = n+1$ gives the best fit to numerical results. This gives a freeze-out temperature characterised by

$$x_f \approx \log \left[0.038 (n+1) \left(\frac{g}{g_{*S}} \right) m_{Pl} m \sigma_0 \right] - \left(n + \frac{1}{2} \right) \log \left\{ \log \left[0.038 (n+1) \left(\frac{g}{g_{*S}} \right) m_{Pl} m \sigma_0 \right] \right\}, \quad (3.3.25)$$

and final yield

$$Y_\infty \approx \frac{3.79 (n+1) x_f^{n+1}}{\left(g_{*S} / g_*^{\frac{1}{2}} \right) m_{Pl} m \sigma_0}. \quad (3.3.26)$$

The abundance is related to Y_∞ by

$$\Omega_X h^2 = \frac{8\pi G s_0}{3 (H/h)^2} m_X Y_\infty \approx \frac{m_X}{3.6 \times 10^{-9} \text{ GeV}} Y_\infty. \quad (3.3.27)$$

This gives rise to suggestions of the so-called ‘WIMP miracle’: a weakly-interacting particle with mass around the electroweak scale can give very approximately $\Omega_X h^2 \sim 0.1$ [137].

There are situations in which 3.3.26 is no longer valid (in addition to situations in which the assumptions stated no longer hold): for example, if there are other states which are nearly degenerate with the dark matter state [138]. In this case, the two (or more) states will freeze-out nearly simultaneously, so additional processes such as $X\bar{X}' \leftrightarrow \chi_1\bar{\chi}_2$ (where X' is the near-degenerate state) become important, altering the final abundance. The approximation also breaks down if the annihilation is taking place near a pole in the cross-section. In this case the Taylor expansion in v can lose validity, and the cross-section can be resonantly enhanced, suppressing the relic abundance significantly [138].

3.3.2 Freeze-In

Freeze-in is a production mechanism for a particle (or particles) that have such feeble couplings that they never reach thermal equilibrium - again, call this particle X . It is based on the essential assumption that the abundance of the particle X is negligible in the early universe (e.g. due to inflation) [86]. Such a particle will be produced via processes such as decays of bath particles ψ_i , $\psi_i \rightarrow X + \dots$, or scattering processes such as $\psi_i\psi_j \rightarrow \psi_3X$. This production will occur until the temperature drops below the mass of the relevant bath particles, $T \lesssim m_{\psi_i}$, at which point the abundance of the bath particles (and hence the production rate) will become exponentially suppressed. At this point, the X abundance will ‘freeze-in’ - see Figure 3.5.

Clearly, the behaviour of the freeze-in abundance is very different to that of freeze-out. The primary differences are that in contrast to freeze-out, the freeze-in abundance increases as the relevant coupling λ increases (for $\lambda \sim 10^{-12}$, very approximately), and that freeze-in production primarily occurs

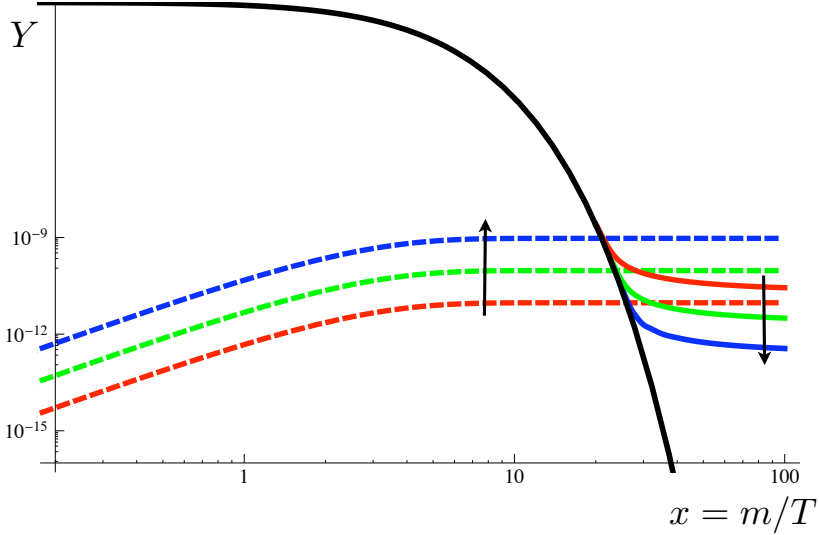


Figure 3.5: An illustration of the behaviour of the dark matter abundance in freeze-out (solid lines) and freeze-in (dashed lines) scenarios, compared to the equilibrium abundance (solid black line), reproduced from [86]. Arrows indicate increasing interaction cross-section. In freeze-out, a particle with stronger interactions remains in equilibrium for longer and hence has a more suppressed final abundance. In contrast, in freeze-in, the particle never reaches equilibrium and a particle with stronger interactions is produced in greater numbers.

around temperatures characterised by $x_{\text{FI}} \sim 2 - 5$, compared to freeze-out which mostly occurs around $x_{\text{FO}} \sim 20 - 40$ [86].

3.4 Dark Matter Detection

So far, dark matter has only been observed via its gravitational interactions, however many dark matter candidates will have (weak) non-gravitational interactions.

For example, a WIMP X is required to take part in annihilations, such

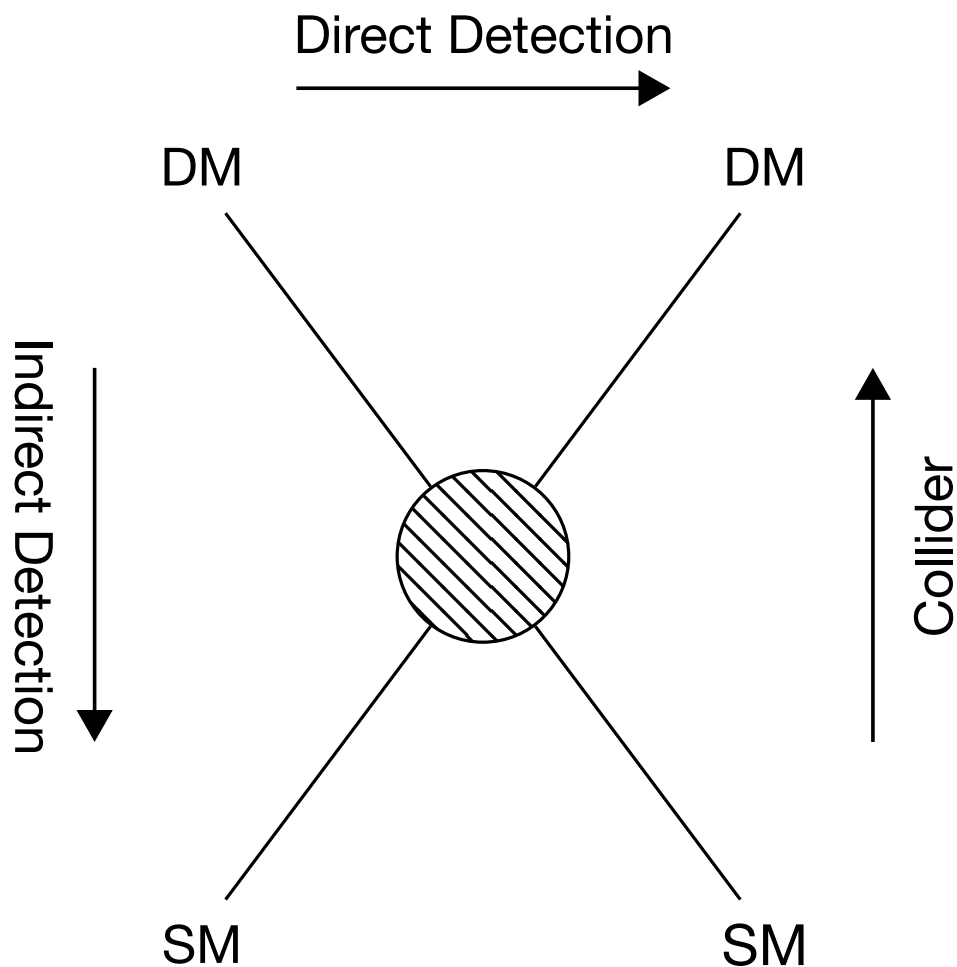


Figure 3.6: A schematic representation of possible ways dark matter could be detected in experiments: indirect detection (dark matter annihilations or decays producing visible products); direct detection (dark matter scattering off Standard Model particles); or being produced in collider experiments.

as $X\bar{X} \rightarrow \bar{\chi}\chi$ in order to have the correct freeze-out abundance (see Section 3.3.1). Such an annihilation cross-section can also give rise to observable processes today - for example, this same annihilation could take place (possibly in a suppressed manner, though it could be at the same level or even enhanced) in dark matter halos or between dark matter gravitationally trapped within nearby objects such as the sun, with observable products - this is an example of indirect detection [139, 140, 141]. Other processes, such as sterile neutrino

decay, may also give rise to indirect detection signals [106, 105].

Alternatively, dark matter may scatter off Standard Model particles (usually nuclei), and such a scattering process may be detectable in experiments - this is known as direct detection [142, 137, 143]. Experiments aiming to detect dark matter interacting via processes other than scattering with nuclei may also fall in to this category, such as the Axion Dark Matter eXperiment (ADMX), which aims to detect resonant scattering of axions in a magnetic field leading to conversion to photons [144, 145].

The final broad category of experiments to detect dark matter are collider experiments, in which dark matter may be produced or give rise to signals in collisions of Standard Model particles. Figure 3.6 illustrates some of the possibilities for detection of dark matter in terrestrial experiments.

3.4.1 Direct Detection

If dark matter is present, as expected, then the earth's velocity relative to the galaxy would induce a dark matter 'wind'. This dark matter could then scatter off Standard Model particles, if they share interactions.

In particular, if the dark matter has interactions with quarks then it could scatter off nuclei, with possibly detectable effects (typically this scattering is characterised by a recoil energy of approximately $\mathcal{O}(10 \text{ keV})$, for a dark matter mass $m_{DM} \sim 100 \text{ GeV}$) [142, 151]. The scattering may be detected via phonons, scintillation or ionisation [146, 152]. Such phenomena can also be triggered by many other effects such as cosmic rays and radiation, so direct detection experiments tend to be situated underground to reduce these backgrounds [153, 154].

Given that the recoil energy is much lower than the masses of the weak gauge and Higgs bosons, direct detection can be treated via a low-energy effective operators such as $\bar{X}X\bar{q}q$ or $\bar{X}\gamma_\mu\gamma_5X\bar{q}\gamma^\mu\gamma_5q$ [155, 156]. The first set of interactions will result in a total nuclear cross-section which depends only on

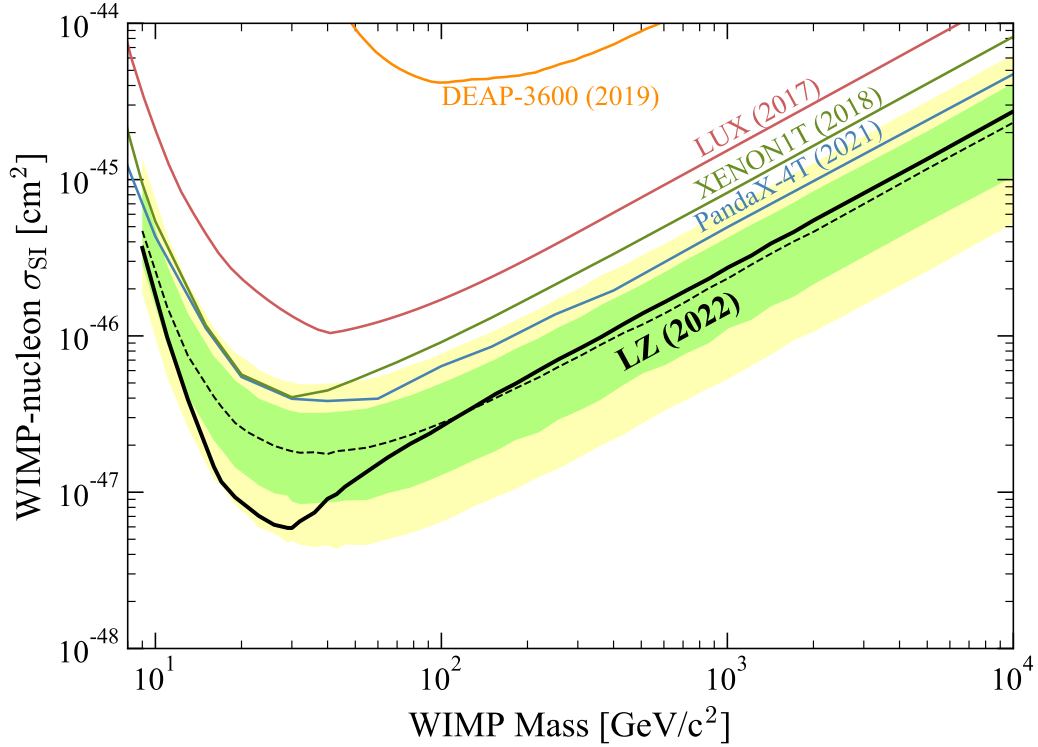


Figure 3.7: Summary of spin-independent direct detection limits, with data from [146, 147, 148, 149, 150], reproduced from [146].

the nuclear mass (‘spin-independent’), while the second set will result in a total nuclear cross-section which depends on the net nuclear spin (‘spin-dependent’) [156].

The scattering cross-sections can be written as

$$\begin{aligned}\sigma_{SI}^{Z,A} &= \frac{4m_r^2}{\pi} [Zf_p + (A - Z)f_n]^2, \\ \sigma_{SD}^{Z,A} &= \frac{32m_r^2}{\pi} \left(\frac{J+1}{J} \right) G_F^2 (a_p \langle S_p \rangle + a_n \langle S_n \rangle),\end{aligned}\quad (3.4.1)$$

where m_r is the reduced WIMP-nucleon mass; Z is the atomic number (i.e. charge) of the nucleus; A is the atomic mass number (i.e. number of nucleons) of the nucleus; J is the spin of the nucleus; S_N is the nucleon spin ($N = n, p$); and f_N and a_N are the WIMP-nucleon effective couplings [157, 158]. The f_N and a_N will be dependent on the form of the interaction. For example, for a

coupling

$$\mathcal{L} \supset \sum_i \alpha_{3i} \bar{X} X \bar{q}_i q_i \quad (3.4.2)$$

the WIMP-nucleon couplings can be approximated by

$$\frac{f_N}{m_N} = \sum_{q=u,d,s} f_{T_q}^N \frac{\alpha_{3q}}{m_q} + \frac{2}{27} f_{T_G}^N \sum_{q=c,b,t} \frac{\alpha_{3q}}{m_q} \quad (3.4.3)$$

where the $f_{T_q}^N$ can be determined via QCD calculations or estimated from experimental data, and $f_{T_G}^N = 1 - \sum_{q=u,d,s} f_{T_q}^N$ [137, 156, 158, 159, 160, 161].

Various direct detection experiments have reported dark matter signals [162, 163, 164, 165, 166, 167, 168], however many of these are not in good agreement with each other and are in tension with more sensitive experiments [169, 146, 147, 148, 149, 150].

There are two particularly interesting anomalies: the first is the DAMA/LIBRA experiment, which reports a 13.7σ annual modulation of events which is consistent with the presence of a ~ 10 GeV WIMP [162, 163, 164]. However, this is strongly in tension with many more sensitive experiments, including experiments using the same tellium-doped sodium iodide (NaI(Tl)) target as DAMA/LIBRA, which rules out a dark matter interpretation of the result [146, 147, 148, 149, 150, 170, 171, 172].

The second case was the XENON1T experiment, which observed an excess of electron recoil events around $2 - 3$ keV, which they suggested could be explained by solar axions, an enhanced neutrino magnetic moment, bosonic dark matter or by decays of trace quantities of tritium (though the solar axion and neutrino magnetic moment explanations were both in strong tension with astrophysical constraints) [173, 174, 175, 176, 177, 178, 179, 180]. Other explanations were put forward, such as axion dark matter with suppressed coupling to photons, boosted dark matter, or new light mediators of interactions between dark and visible sectors [177, 178, 181, 182, 183]. However, the

XENONnT experiment subsequently observed no excess, thereby ruling out any "new physics" interpretation of the data [184].

The strongest spin-independent direct detection limits are shown in Figure 3.7.

3.4.2 Indirect Detection

An alternative to searching for dark matter interacting with Standard Model particles is to try to detect the products of dark matter annihilations or decays. These products depend on the model but can include energetic neutrinos, gamma rays, or charged particles. Gamma rays can be observed directly by space-based telescopes, or via Cherenkov light produced by the gamma rays interacting with the earth's atmosphere by earth-based telescopes - many such experiments have been carried out, or are currently underway [185, 186, 187, 188]. High-energy neutrinos can scatter off matter on earth, converting into a high-energy charged lepton. The lepton then emits Cherenkov radiation, which can be detected [189, 190]. Neutrino observatories such as IceCube and Super-Kamiokande are carrying out searches for high-energy neutrinos [191, 192, 193]. Cosmic rays such as high-energy positrons or antiprotons could also provide evidence for dark matter [194, 195, 196, 197]. Cosmic ray searches are complicated by the fact that charged particles are deflected by magnetic fields, and there are considerable astrophysical uncertainties on their propagation [198, 199, 200].

There have been numerous anomalies reported which could be interpreted as indirect detection of dark matter [201, 202, 203, 199, 196, 204, 205, 206]. Many of these have turned out instead to be due to astrophysical or other background effects rather than dark matter [207, 208, 209, 210, 211, 212]. However, there are still some outstanding signals which could be due to dark matter, such as those from the Fermi Gamma-Ray Space Telescope (FGST) Large Area Telescope (LAT), which has observed an excess of GeV gamma

rays from around the Galactic Centre which would be consistent with dark matter annihilations [213, 214, 215, 216, 217, 218, 219, 220, 221, 222], though this too could be explained by other effects, such as millisecond pulsars or transient cosmic ray outbursts [223, 224, 225, 226, 222].

3.4.3 Collider Experiments

The final broad category of experiments which can probe dark matter properties is collider experiments. Collider signatures of dark matter are model dependent, but there are some possible signals which would be common to many different forms of dark matter.

One of the most common collider searches for dark matter is to look for collisions in which the products have missing transverse momentum. This could indicate that dark matter has been directly produced and then left without interacting further [227, 228]. The simplest such searches are ‘mono-X’ searches, where dark matter is produced (usually in a pair) alongside a single Standard Model particle or jet.

Other collider signals could indicate dark matter physics less directly: for example, if there is a mediator via which Standard Model particles interact with dark matter, this could also affect Standard Model-Standard Model interactions [229, 230, 231].

Particle colliders can also probe branching ratios of particles such as the Higgs which may decay to dark matter or particles which interact with the dark matter, hence constraining dark matter properties [227, 232, 233].

Some theories of dark matter, such as FIMPs or hidden sector dark matter, can contain new particles which may travel a short distance before decaying within the detector volume [86, 234, 235, 236]. Therefore, searches for displaced jets or vertices can also constrain certain types of dark matter [237, 238].

Clearly, many of the above signals wouldn't necessarily equate to the discovery of dark matter - for example, a particle propagating out of the detector without decaying only requires a lifetime $\tau \gtrsim 1 \times 10^{-7}$ sec, whereas dark matter is required to be stable over timescales greater than the age of the universe [239, 240].

Chapter 4

Supersymmetry

4.1 Motivation

Our primary motivation for working with supersymmetry is its resolution of the hierarchy naturalness problem. In the Standard Model, the hierarchy naturalness problem stems from the quantum corrections to the Higgs mass. For example, if the Higgs couples to a fermion, Ψ , with coupling $-\lambda_\Psi H \bar{\Psi} \Psi$, then the Higgs mass will receive corrections from diagrams such as that shown on the left-hand of Figure 4.1, contributing

$$\Delta^\Psi m_H^2 \sim -\frac{|\lambda_\Psi|^2}{8\pi^2} \Lambda^2 \quad (4.1.1)$$

where Λ is the cutoff scale (and hence at least as large as the scale of ‘new’ physics), along with similar corrections from all other fermions with which the Higgs couples. Similarly, if the Higgs couples to a boson, ϕ , with coupling $-\lambda_\phi |H|^2 |\phi|^2$, then diagrams such as that shown on the right-hand of Figure 4.1 will give corrections

$$\Delta^\phi m_H^2 \sim \frac{|\lambda_\phi|^2}{16\pi^2} \Lambda^2 \quad (4.1.2)$$

along with similar corrections from all other bosons with coupling with the Higgs. Hence we might expect that, in the absence of precise cancellation

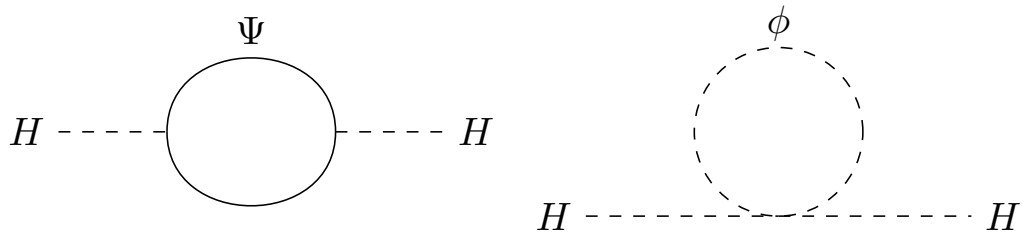


Figure 4.1: Loop diagrams with quadratic divergences contributing to the Higgs mass.

between quantum corrections, the Higgs mass will be pushed up to the scale of new physics (e.g. m_{Pl}), but this isn't what we observe.

Supersymmetry resolves this by introducing a symmetry which relates fermions to bosons:

$$Q_\alpha |B\rangle = |F\rangle, \quad Q_\alpha |F\rangle = |B\rangle \quad (4.1.3)$$

where $|B\rangle, |F\rangle$ are bosonic and fermionic states respectively, and Q_α is (one of) the generator(s) of this new symmetry. A supersymmetric theory will resolve the hierarchy naturalness problem, as supersymmetry predicts precise relationships between the fermionic and bosonic couplings λ_Ψ and λ_ϕ , leading to cancellation of quadratic divergences in fermionic and bosonic corrections to the Higgs mass ¹ [242, 243, 244, 245].

Additionally, supersymmetric theories predict gauge coupling unification at some 'grand unification' energy, and often contain a stable, neutral particle which could play the role of dark matter [243, 246, 247].

¹Note also that although a supersymmetric theory will contain many extra bosons as 'superpartners' to the known fermionic states (and vice versa), these bosons having masses much smaller than the cutoff scale does not give rise to new naturalness problems. This is because the bosonic and fermionic partners will have equal masses, and the relatively small fermion masses are technically natural (in the sense of 't Hooft [241]) and hence so are the boson masses.

4.2 Supersymmetry Generators and Superfields

The Poincaré group corresponds to the symmetries of Minkowski space. The Poincaré group is generated by P^μ (which generate translations) and $M^{\mu\nu}$ (which generate Lorentz transformations), with commutators given by

$$\begin{aligned} [P^\mu, P^\nu] &= 0, \\ [M^{\mu\nu}, P^\rho] &= i(\eta^{\nu\rho}P^\mu - \eta^{\mu\rho}P^\nu), \\ [M^{\mu\nu}, M^{\rho\sigma}] &= i(\eta^{\nu\rho}M^{\mu\sigma} + \eta^{\mu\sigma}M^{\nu\rho} - \eta^{\nu\sigma}M^{\mu\rho} - \eta^{\mu\rho}M^{\nu\sigma}), \end{aligned} \quad (4.2.1)$$

which can be shown by comparing the infinitesimal Lorentz transformation of the generators treated as Lorentz vectors/tensors, i.e. $P^\mu \rightarrow \Lambda_\nu^\mu P^\nu$, $M^{\mu\nu} \rightarrow \Lambda_\rho^\mu \Lambda_\sigma^\nu M^{\rho\sigma}$, to their transformations as operators, i.e. $P^\mu \rightarrow U^\dagger P^\mu U$, $M^{\mu\nu} \rightarrow U^\dagger M^{\mu\nu} U$ where $U = \exp\left(\frac{i}{2}\omega_{\mu\nu}M^{\mu\nu}\right)$.

As mentioned above, supersymmetry is defined by extending the Poincaré algebra to include an additional spinor generator Q_α and its conjugate $\bar{Q}_{\dot{\alpha}}$ (we use dotted indices to indicate spinors transforming in the conjugate representation of $SL(2, \mathbb{C})$). This effectively extends our space from Minkowski space, with coordinates $\{x^\mu\}$, to superspace, with coordinates $\{x^\mu, \theta^\alpha, \bar{\theta}_{\dot{\alpha}}\}$, where θ^α and $\bar{\theta}_{\dot{\alpha}}$ are (spinors of) anti-commuting Grassman variables.

Multiple spinor generators can be included, but we will only consider the case with a single spinor generator in the algebra. This is known as $N = 1$ or simple supersymmetry. These generators have (anti-)commutators

$$\begin{aligned} [Q_\alpha, P^\mu] &= [\bar{Q}_{\dot{\alpha}}, P^\mu] = 0, \\ [Q_\alpha, M^{\mu\nu}] &= (\sigma^{\mu\nu})_\alpha^\beta Q_\beta, \\ \{Q_\alpha, Q_\beta\} &= 0, \\ \{Q_\alpha, \bar{Q}_{\dot{\alpha}}\} &= 2(\sigma^\mu)_{\alpha\dot{\beta}} P_\mu, \end{aligned} \quad (4.2.2)$$

where $\sigma^\mu = (I, \sigma_i)$, $\bar{\sigma}^\mu = (I, -\sigma_i)$ (σ_i are the Pauli sigma matrices); and $\sigma^{\mu\nu} = \frac{i}{4} (\sigma^\mu \bar{\sigma}^\nu - \sigma^\nu \bar{\sigma}^\mu)$ are the generators of $SL(2, \mathbb{C})$. These (anti-)commutation relations can be found in a similar way to those of the Poincaré algebra.

To construct supersymmetric theories, we define superfields which are functions of $\{x^\mu, \theta^\alpha, \bar{\theta}_{\dot{\alpha}}\}$. As $\theta^\alpha \theta^\beta \theta^\gamma = 0$ (and similarly for $\bar{\theta}_{\dot{\alpha}}$), a scalar superfield² $S(x^\mu, \theta^\alpha, \bar{\theta}_{\dot{\alpha}})$ has a finite Taylor expansion in $\theta^\alpha, \bar{\theta}_{\dot{\alpha}}$, given by

$$\begin{aligned} S(x, \theta, \bar{\theta}) = & \phi(x) + \theta\psi(x) + \bar{\theta}\bar{\chi}(x) + (\theta\theta)M(x) + (\bar{\theta}\bar{\theta})N(x) \\ & + (\theta\sigma^\mu\bar{\theta})V_\mu(x) + (\theta\theta)(\bar{\theta}\bar{\lambda}(x)) + (\bar{\theta}\bar{\theta})(\theta\rho(x)) \\ & + (\theta\theta)(\bar{\theta}\bar{\theta})D(x) \end{aligned} \quad (4.2.3)$$

where the product of two spinors is defined as $\theta\psi = \epsilon^{\alpha\beta}\theta_\beta\psi_\alpha = \theta^\alpha\psi_\alpha$, $\bar{\theta}\bar{\chi} = \epsilon_{\dot{\alpha}\dot{\beta}}\bar{\theta}^{\dot{\beta}}\bar{\chi}^{\dot{\alpha}} = \bar{\theta}_{\dot{\alpha}}\bar{\chi}^{\dot{\alpha}}$ ($\epsilon^{\alpha\beta} = -\epsilon_{\alpha\beta} = i\sigma_2$ is used to raise and lower spinor indices).

Note that $(\theta\sigma^\mu\bar{\theta})(\theta\sigma^\nu\bar{\theta}) = \frac{1}{2}(\theta\theta)(\bar{\theta}\bar{\theta})\eta^{\mu\nu}$ so that terms such as $(\theta\sigma^\mu\bar{\theta})(\theta\sigma^\nu\bar{\theta})B_{\mu\nu}(x) = \frac{1}{2}(\theta\theta)(\bar{\theta}\bar{\theta})B_\mu^\mu$ can be absorbed into the D -term.

Under a superspace translation generated by $U = \exp(i\epsilon Q + i\bar{\epsilon}\bar{Q})$, the superfield transforms as [248]

$$\begin{aligned} S(x^\mu, \theta, \bar{\theta}) \rightarrow & S(x^\mu + i\theta\sigma^\mu\bar{\epsilon} - i\epsilon\sigma^\mu\bar{\theta}, \theta + \epsilon, \bar{\theta} + \bar{\epsilon}) \\ = & S(x^\mu, \theta, \bar{\theta}) + (i\epsilon Q + i\bar{\epsilon}\bar{Q})S + \dots, \end{aligned} \quad (4.2.4)$$

where Q, \bar{Q} are the following representations of the generators Q, \bar{Q} :

$$\begin{aligned} Q_\alpha = & -i\frac{\partial}{\partial\theta^\alpha} - (\sigma^\mu\bar{\theta})_\alpha\frac{\partial}{\partial x^\mu}, \\ \bar{Q}_{\dot{\alpha}} = & i\frac{\partial}{\partial\bar{\theta}^{\dot{\alpha}}} + (\theta\sigma^\mu)_{\dot{\alpha}}\frac{\partial}{\partial x^\mu}. \end{aligned} \quad (4.2.5)$$

²We can consider superfields in other representations of Poincaré, but we will primarily be interested in scalar superfields.

Substituting 4.2.3 into 4.2.4 gives the transformation of the individual component fields in the superfield, for example the only scalar terms are given by

$$\begin{aligned}
\delta S &= \epsilon^\alpha \frac{\partial}{\partial \theta^\alpha} S - \epsilon_{\dot{\alpha}} \frac{\partial}{\partial \bar{\theta}^{\dot{\alpha}}} S + \dots \\
&= \epsilon^\alpha \frac{\partial}{\partial \theta^\alpha} \theta^\beta \psi_\beta - \bar{\epsilon}_{\dot{\alpha}} \frac{\partial}{\partial \bar{\theta}^{\dot{\alpha}}} \bar{\theta}_{\dot{\beta}} \bar{\chi}^{\dot{\beta}} + \dots \\
&= \epsilon \psi + \bar{\epsilon} \bar{\chi} + \dots
\end{aligned} \tag{4.2.6}$$

(Grassmann differentiation is defined as $\frac{\partial \theta^\alpha}{\partial \theta^\beta} = \delta^\alpha_\beta$, $\frac{\partial \bar{\theta}^{\dot{\alpha}}}{\partial \bar{\theta}^{\dot{\beta}}} = \delta^{\dot{\alpha}}_{\dot{\beta}}$ and so $\frac{\partial \bar{\theta}^{\dot{\alpha}}}{\partial \theta^\beta} = \epsilon_{\dot{\alpha}\beta} \epsilon^{\dot{\alpha}\gamma} \frac{\partial \bar{\theta}^{\dot{\beta}}}{\partial \theta^\gamma} = -\delta^{\dot{\alpha}}_\beta$, which we've used on the third line.) Hence the scalar $\phi(x)$ transforms as $\delta\phi = \epsilon\psi + \bar{\epsilon}\bar{\chi}$. Transformation of all component fields can be found in a similar way, and are given by

$$\begin{aligned}
\delta\phi &= \epsilon\psi + \bar{\epsilon}\bar{\chi}, \\
\delta\psi_\alpha &= 2\epsilon_\alpha M + (\sigma^\mu \bar{\epsilon})_\alpha (i\partial_\mu \phi + V_\mu), \\
\delta\bar{\chi}^{\dot{\alpha}} &= 2\bar{\epsilon}^{\dot{\alpha}} N - (\epsilon\sigma^\mu)^{\dot{\alpha}} (i\partial_\mu \phi - V_\mu), \\
\delta M &= \bar{\epsilon}\bar{\lambda} - \frac{i}{2} (\partial_\mu \psi) \sigma^\mu \bar{\epsilon}, \\
\delta N &= \epsilon\rho + \frac{i}{2} \epsilon\sigma^\mu (\partial_\mu \bar{\chi}), \\
\delta V_\mu &= \epsilon\sigma_\mu \bar{\lambda} + \rho\sigma_\mu \bar{\epsilon} + \frac{i}{2} [(\partial^\nu \psi) \sigma_\mu \bar{\sigma}_\nu \epsilon - \bar{\epsilon}\bar{\sigma}_\nu \sigma_\mu \partial^\nu \bar{\chi}], \\
\delta\rho_\alpha &= 2\epsilon_\alpha D - \frac{i}{2} (\sigma^\nu \bar{\sigma}^\mu)_\alpha \partial_\mu V_\nu + i(\sigma^\mu \bar{\epsilon})_\alpha \partial_\mu N, \\
\delta\bar{\lambda}^{\dot{\alpha}} &= 2\bar{\epsilon}^{\dot{\alpha}} D + \frac{i}{2} (\bar{\sigma}^\nu \sigma^\mu)^{\dot{\alpha}} \partial_\mu V_\nu + i(\bar{\sigma}^\mu \epsilon)^{\dot{\alpha}} \partial_\mu N, \\
\delta D &= \frac{i}{2} \partial_\mu (\epsilon\sigma^\mu \bar{\lambda} - \rho\sigma^\mu \bar{\epsilon}).
\end{aligned} \tag{4.2.7}$$

We are interested in superfields which are irreducible representations of the SUSY algebra. Two such superfields are chiral superfields and real superfields [248].

4.3 Chiral Superfields

Chiral superfields are defined by $\bar{\mathcal{D}}_{\dot{\alpha}}\Phi = 0$ where $\bar{\mathcal{D}}_{\dot{\alpha}} = -\frac{\partial}{\partial\theta^{\dot{\alpha}}} - i\theta^{\alpha}\sigma_{\alpha\dot{\alpha}}^{\mu}\frac{\partial}{\partial x^{\mu}}$. This is a well-defined condition (it survives a supersymmetry transformation) - this is because $\bar{\mathcal{D}}_{\dot{\alpha}}$ anti-commutes with \mathcal{Q}_{α} and $\bar{\mathcal{Q}}_{\dot{\alpha}}$, so that

$$\bar{\mathcal{D}}_{\dot{\alpha}}(\delta\Phi) = \bar{\mathcal{D}}_{\dot{\alpha}}(i\epsilon\mathcal{Q} + i\bar{\epsilon}\bar{\mathcal{Q}})\Phi = (i\epsilon\mathcal{Q} + i\bar{\epsilon}\bar{\mathcal{Q}})\bar{\mathcal{D}}_{\dot{\alpha}}\Phi = 0. \quad (4.3.1)$$

To expand a chiral superfield in terms of component fields, firstly shift to the coordinate $y^{\mu} = x^{\mu} + i\theta\sigma^{\mu}\bar{\theta}$, so that the supercovariant derivatives become $\bar{\mathcal{D}}_{\dot{\alpha}} = \bar{\partial}_{\dot{\alpha}}$ and $\mathcal{D}_{\alpha} = \frac{\partial}{\partial\theta^{\alpha}} + 2i\sigma_{\alpha\dot{\alpha}}^{\mu}\bar{\theta}^{\dot{\alpha}}\frac{\partial}{\partial x^{\mu}}$. Then $\bar{\partial}_{\dot{\alpha}}\Phi(y, \theta, \bar{\theta}) = 0$, so that

$$\Phi(y, \theta, \bar{\theta}) = \phi(y) + \sqrt{2}\theta\psi(y) + (\theta\theta)F(y). \quad (4.3.2)$$

Hence, a chiral superfield can be interpreted physically as representing a complex scalar field ϕ and a fermion ψ . There is also the field F , however as we shall see it does not propagate - i.e. it is an auxiliary field. Equation 4.3.2 can be rewritten in terms of $\{x, \theta, \bar{\theta}\}$ using the Taylor expansion

$$\begin{aligned} f(x^{\mu} + i\theta\sigma^{\mu}\bar{\theta}) &= f(x) + i(\theta\sigma^{\mu}\bar{\theta})\frac{\partial f(x)}{\partial x^{\mu}} - (\theta\sigma^{\mu}\bar{\theta})(\theta\sigma^{\nu}\bar{\theta})\frac{\partial^2 f(x)}{\partial x^{\mu}\partial x^{\nu}} \\ &= f(x) + i(\theta\sigma^{\mu}\bar{\theta})\frac{\partial f(x)}{\partial x^{\mu}} - \frac{1}{2}(\theta\theta)(\bar{\theta}\bar{\theta})\frac{\partial^2 f(x)}{\partial x^{\mu}\partial x_{\mu}}, \end{aligned} \quad (4.3.3)$$

where the spinor identity $(\theta\sigma^{\mu}\bar{\theta})(\theta\sigma^{\nu}\bar{\theta}) = \frac{1}{2}(\theta\theta)(\bar{\theta}\bar{\theta})\eta^{\mu\nu}$ has been used for the final term. Hence

$$\begin{aligned} \Phi(x, \theta, \bar{\theta}) &= \phi(x) + \sqrt{2}\theta\psi(x) + (\theta\theta)F(x) + i\theta\sigma^{\mu}\bar{\theta}\partial_{\mu}\phi(x) \\ &\quad + i\sqrt{2}(\theta\sigma^{\mu}\bar{\theta})\theta\partial_{\mu}\psi - \frac{1}{4}(\theta\theta)(\bar{\theta}\bar{\theta})\partial_{\mu}\partial^{\mu}\phi(x) \\ &= \phi(x) + \sqrt{2}\theta\psi(x) + (\theta\theta)F(x) + i\theta\sigma^{\mu}\bar{\theta}\partial_{\mu}\phi(x) \end{aligned}$$

$$-\frac{i}{\sqrt{2}}(\theta\theta)\partial_\mu\psi(x)\sigma^\mu\bar{\theta}-\frac{1}{4}(\theta\theta)(\bar{\theta}\bar{\theta})\partial_\mu\partial^\mu\phi(x), \quad (4.3.4)$$

using the spinor identity $\theta^\alpha\theta^\beta = -\frac{1}{2}\epsilon^{\alpha\beta}$.

Comparing to 4.2.7, the components of Φ transform as

$$\begin{aligned} \delta\phi &= \sqrt{2}\epsilon\psi, \\ \delta\psi^\alpha &= i\sqrt{2}(\sigma^\mu\bar{\epsilon})^\alpha\partial_\mu\phi + \sqrt{2}\epsilon^\alpha F, \\ \delta F &= i\sqrt{2}\bar{\epsilon}\bar{\sigma}^\mu\partial_\mu\psi. \end{aligned} \quad (4.3.5)$$

For reference, the conjugate of a chiral superfield will be an anti-chiral superfield satisfying $\mathcal{D}_\alpha\Phi^\dagger = 0$, as Φ^\dagger will only be a function of y^* and $\bar{\theta}$, which satisfy $\mathcal{D}_\alpha y^* = \mathcal{D}_\alpha\bar{\theta} = 0$ and so $\mathcal{D}_\alpha\Phi^\dagger = 0$. Φ^\dagger is written

$$\begin{aligned} \Phi^\dagger(x, \theta, \bar{\theta}) &= \phi^\dagger(x) + \sqrt{2}\bar{\theta}\bar{\psi}(x) + (\bar{\theta}\bar{\theta})F^\dagger(x) - i\theta\sigma^\mu\bar{\theta}\partial_\mu\phi^\dagger(x) \\ &+ \frac{i}{\sqrt{2}}(\bar{\theta}\bar{\theta})\theta\sigma^\mu\partial_\mu\bar{\psi}(x) - \frac{1}{4}(\theta\theta)(\bar{\theta}\bar{\theta})\partial_\mu\partial^\mu\phi^\dagger(x). \end{aligned} \quad (4.3.6)$$

4.3.1 Chiral Superfield Lagrangian

The most general Lagrangian for a chiral superfield is given by [248, 249]

$$\mathcal{L} = \Phi^\dagger\Phi|_D + (W(\Phi)|_F + \text{h.c.}), \quad (4.3.7)$$

where $W(\Phi)$ is a holomorphic function (and hence is a chiral superfield). $\Phi^\dagger\Phi|_D$ indicates the ‘D-term’ of $\Phi^\dagger\Phi$, i.e. the coefficient of $(\theta\theta)(\bar{\theta}\bar{\theta})$ in the component expansion of $\Phi^\dagger\Phi$, and hence this term is invariant under a supersymmetry transformation as δD is a total derivative for the D -term of any superfield (see 4.2.7). Similarly $W(\Phi)|_F$ is the ‘F-term’ of $W(\Phi)$, i.e. the coefficient of $(\theta\theta)$ in the component expansion of $W(\Phi)$. δF is a total derivative for the F -term of any chiral superfield (see 4.3.5) and so this term is also invariant under a supersymmetry transformation.

We can write this in terms of the component fields ϕ , ψ and F . Firstly expand $W(\Phi)$

$$W(\Phi) = W(\phi) + (\Phi - \phi) \frac{\partial W}{\partial \phi} + \frac{1}{2} (\Phi - \phi)^2 \frac{\partial^2 W}{\partial \phi^2}, \quad (4.3.8)$$

so that

$$W(\Phi)|_F = W(\phi)|_F + F \frac{\partial W}{\partial \phi} - \frac{1}{2} \psi \psi \frac{\partial^2 W}{\partial \phi^2}. \quad (4.3.9)$$

Similarly

$$\Phi^\dagger \Phi|_D = \partial_\mu \phi^\dagger \partial^\mu \phi - i \bar{\psi} \bar{\sigma}^\mu \partial_\mu \psi + F^\dagger F. \quad (4.3.10)$$

Neither $W(\Phi)|_F$ nor $\Phi^\dagger \Phi|_D$ contain any kinetic terms for F , so it can be eliminated using the Euler-Lagrange equations

$$F + \frac{\partial W^*}{\partial \phi^*} = 0. \quad (4.3.11)$$

Hence, $F = -\frac{\partial W^*}{\partial \phi^*}$ can be substituted back into the Lagrangian, to obtain \mathcal{L} in terms of ϕ and ψ alone

$$\mathcal{L} = \partial_\mu \phi^\dagger \partial^\mu \phi - i \bar{\psi} \bar{\sigma}^\mu \partial_\mu \psi - \left| \frac{\partial W}{\partial \phi} \right|^2 - \left(\frac{1}{2} \psi \psi \frac{\partial^2 W}{\partial \phi^2} + \text{h.c.} \right). \quad (4.3.12)$$

4.4 Real Superfields

A real (or vector) superfield V is defined by $V^\dagger = V$. It can be written

$$V(x, \theta, \bar{\theta}) = C(x) + \theta \chi(x) + \bar{\theta} \bar{\chi}(x) + i(\theta\theta) M(x) - i(\bar{\theta}\bar{\theta}) M^\dagger(x) + \theta \sigma^\mu \bar{\theta} A_\mu(x)$$

$$\begin{aligned}
& + (\theta\theta) \bar{\theta} \left(\bar{\lambda}(x) + \frac{i}{2} \bar{\sigma}^\mu \partial_\mu \chi(x) \right) + (\bar{\theta}\bar{\theta}) \theta \left(\lambda(x) + \frac{i}{2} \sigma^\mu \partial_\mu \bar{\chi}(x) \right) \\
& + \frac{1}{2} (\theta\theta) (\bar{\theta}\bar{\theta}) \left(D(x) - \frac{1}{2} \partial^\mu \partial_\mu C(x) \right), \tag{4.4.1}
\end{aligned}$$

(where the inclusion of terms such as $\frac{i}{2} \bar{\sigma}^\mu \partial_\mu \chi(x)$ alongside $\lambda(x)$ are included to simplify gauge transformations).

This superfield appears to contain real scalar fields C and D , a complex scalar field M , two fermions λ and χ , and a gauge field A_μ , but we will show below that all but λ , A_μ and D can be removed by a generalised gauge transformation. Physically, a real superfield can be interpreted as containing a gauge field A_μ plus a Weyl fermion (gaugino/gluino) λ , plus D which, as with F above, is an auxiliary field which will not propagate.

4.4.1 Generalised Gauge Transformations

Standard gauge transformations can be generalised to superfields. A real superfield transforms under a generalised gauge transformation as

$$e^{2V} \rightarrow e^{-2i\Lambda^\dagger} e^{2V} e^{2i\Lambda}, \tag{4.4.2}$$

where Λ is a chiral superfield (Λ can be expanded in terms of T^A , the generators of the Lie algebra associated with the gauge group, as $\Lambda = \Lambda^A T^A$). Using the Baker-Cambell-Hausdorff formula $e^X e^Y = e^{X+Y+\frac{1}{2}[X,Y]}$, this can be written

$$V \rightarrow V + i(\Lambda - \Lambda^\dagger) - i[V, \Lambda + \Lambda^\dagger] + \dots \tag{4.4.3}$$

If the gauge symmetry is abelian, $[T^A, T^B] = 0$ and so this simplifies to $V \rightarrow V + i(\Lambda - \Lambda^\dagger)$.

4.4.2 Wess-Zumino Gauge

The gauge can be chosen to simplify the expression for V above. We will show this first for the case where the gauge symmetry is abelian, before extending

to the non-abelian case.

In the abelian case, the real superfield transforms as $V \rightarrow V + i(\Lambda - \Lambda^\dagger)$. Λ is chiral, so $i(\Lambda - \Lambda^\dagger)$ can be expanded in components as

$$\begin{aligned}
i(\Lambda - \Lambda^\dagger) = & -2\text{Im}(\omega) + i\sqrt{2}\theta\rho - i\sqrt{2}\bar{\theta}\bar{\rho} + i(\theta\theta)G - i(\bar{\theta}\bar{\theta})G^\dagger \\
& - 2\theta\sigma^\mu\bar{\theta}\partial_\mu\text{Re}(\omega) - \frac{1}{\sqrt{2}}(\theta\theta)\bar{\theta}\bar{\sigma}^\mu\partial_\mu\rho + \frac{1}{\sqrt{2}}(\bar{\theta}\bar{\theta})\theta\sigma^\mu\partial_\mu\bar{\rho} \\
& + \frac{1}{2}(\theta\theta)(\bar{\theta}\bar{\theta})\partial_\mu\partial^\mu\text{Im}(\omega), \tag{4.4.4}
\end{aligned}$$

where ω , ρ and G are respectively the complex scalar, fermion and auxiliary components of Λ . This gives the gauge transformations of the components of V as

$$\begin{aligned}
C & \rightarrow C - 2\text{Im}(\omega), \\
\chi & \rightarrow \chi + i\sqrt{2}\rho, \\
M & \rightarrow M + G, \\
A_\mu & \rightarrow A_\mu - 2\partial_\mu\text{Re}(\omega), \tag{4.4.5}
\end{aligned}$$

with λ and D unchanged. Hence, we can choose ω , ρ and G to set $C = M = 0$, $\chi = 0$, leaving only λ , A_μ and D as discussed above:

$$V(x, \theta, \bar{\theta}) = \theta\sigma^\mu\bar{\theta}A_\mu(x) + (\theta\theta)\bar{\theta}\bar{\lambda}(x) + (\bar{\theta}\bar{\theta})\theta\lambda(x) + \frac{1}{2}(\theta\theta)(\bar{\theta}\bar{\theta})D(x). \tag{4.4.6}$$

This choice of gauge is known as Wess-Zumino gauge. (This gauge choice isn't preserved by supersymmetry transformations, but a gauge transformation can be performed after any supersymmetry transformation to bring the superfield back into Wess-Zumino gauge.)

If the symmetry is non-abelian, the gauge transformation of V is given by $V \rightarrow V'$ where

$$V' = V + i(\Lambda - \Lambda^\dagger) - i[V, \Lambda + \Lambda^\dagger] + \dots \quad (4.4.7)$$

If we define $V'' = V - i[V, \Lambda + \Lambda^\dagger] + \dots = V' - i(\Lambda - \Lambda^\dagger)$, this is also a real superfield (trivially, as $V''^\dagger = V'^\dagger - \{i(\Lambda - \Lambda^\dagger)\}^\dagger = V' - i(\Lambda - \Lambda^\dagger) = V''$). Hence $V' = V'' + i(\Lambda - \Lambda^\dagger)$, where V'' is a real superfield. But as we showed above, a shift of the form $V + i(\Lambda - \Lambda^\dagger)$ can be used to set $C = M = 0$, $\chi = 0$. Hence, for a non-abelian gauge symmetry, we can again choose a gauge transformation to bring the real superfield V into Wess-Zumino gauge.

4.5 Gauge Theory Lagrangian

4.5.1 Field Strength Superfield

The field strength can also be generalised to the supersymmetric case. The field strength superfield is defined as

$$W_\alpha = -\frac{1}{8}\bar{\mathcal{D}}^2(e^{-2V}\mathcal{D}_\alpha e^{2V}). \quad (4.5.1)$$

This is a chiral spinor superfield (as $\bar{\mathcal{D}}_\alpha\bar{\mathcal{D}}^2 = 0$) and transforms as $W_\alpha \rightarrow e^{-2i\Lambda}W_\alpha e^{2i\Lambda}$ under a generalised gauge transformation

$$\begin{aligned} W_\alpha &\rightarrow -\frac{1}{8}\bar{\mathcal{D}}^2\left(e^{-2i\Lambda}e^{-2V}e^{2i\Lambda^\dagger}\mathcal{D}_\alpha\left(e^{-2i\Lambda^\dagger}e^{2V}e^{2i\Lambda}\right)\right) \\ &= -\frac{1}{8}e^{-2i\Lambda}\bar{\mathcal{D}}^2\left(e^{-2V}e^{2i\Lambda^\dagger}e^{-2i\Lambda^\dagger}\mathcal{D}_\alpha\left(e^{2V}e^{2i\Lambda}\right)\right) \\ &= -\frac{1}{8}e^{-2i\Lambda}\bar{\mathcal{D}}^2\left(e^{-2V}\mathcal{D}_\alpha e^{2V}\right)e^{2i\Lambda} - \frac{1}{8}e^{-2i\Lambda}\bar{\mathcal{D}}^2\mathcal{D}_\alpha e^{2i\Lambda}, \end{aligned} \quad (4.5.2)$$

where we have used $\mathcal{D}_\alpha\Lambda^\dagger = 0$ and $\bar{\mathcal{D}}_\alpha\Lambda = 0$ at each stage. We will show that the remaining term is zero, $-\frac{1}{8}e^{-2i\Lambda}\bar{\mathcal{D}}^2\mathcal{D}_\alpha e^{2i\Lambda} = 0$:

$$\bar{\mathcal{D}}^2\mathcal{D}_\alpha e^{2i\Lambda} = [-\bar{\mathcal{D}}_\alpha\mathcal{D}_\alpha\bar{\mathcal{D}}^{\dot{\alpha}} + \bar{\mathcal{D}}^{\dot{\alpha}}\{\mathcal{D}_\alpha, \bar{\mathcal{D}}_{\dot{\alpha}}\}]e^{2i\Lambda}$$

$$\begin{aligned}
&= 2i\bar{\mathcal{D}}^{\dot{\alpha}}(\sigma^{\mu})_{\alpha\dot{\alpha}}\partial_{\mu}e^{2i\Lambda} \\
&= 2i(\sigma^{\mu})_{\alpha\dot{\alpha}}\partial_{\mu}\bar{\mathcal{D}}^{\dot{\alpha}}e^{2i\Lambda} = 0,
\end{aligned} \tag{4.5.3}$$

where we've used the anticommutator $\{\mathcal{D}_{\alpha}, \bar{\mathcal{D}}_{\dot{\alpha}}\} = -2i(\sigma^{\mu})_{\alpha\dot{\alpha}}\partial_{\mu}$, and the fact that $\bar{\mathcal{D}}_{\dot{\alpha}}\Lambda = 0$.

Hence, as claimed the field strength superfield transforms under gauge transformations as

$$W_{\alpha} \rightarrow e^{-2i\Lambda}W_{\alpha}e^{2i\Lambda}. \tag{4.5.4}$$

We will break the field strength down into its components. Shift to the coordinate $y^{\mu} = x^{\mu} + i\theta\sigma^{\mu}\bar{\theta}$. The real superfield in Wess-Zumino gauge, in terms of y , is given by

$$\begin{aligned}
V &= \theta\sigma^{\mu}\bar{\theta}A_{\mu}(y) + (\theta\theta)(\bar{\theta}\bar{\lambda}(y)) + (\bar{\theta}\bar{\theta})(\theta\lambda(y)) \\
&\quad + \frac{1}{2}(\theta\theta)(\bar{\theta}\bar{\theta})(D(y) - i\partial_{\mu}A^{\mu}(y)),
\end{aligned} \tag{4.5.5}$$

where $A_{\mu}(x)$ has been Taylor expanded as $A_{\mu}(x) = A_{\mu}(y, \theta, \bar{\theta}) - i\theta\sigma^{\nu}\bar{\theta}\frac{\partial A_{\mu}}{\partial y^{\nu}} - (\theta\sigma^{\nu}\bar{\theta})(\theta\sigma^{\rho}\bar{\theta})\frac{\partial^2 A_{\mu}}{\partial y^{\nu}\partial y^{\rho}}$, and the third term is $\sim (\theta\theta)(\bar{\theta}\bar{\theta})$ and hence vanishes when multiplied by $\theta\sigma^{\mu}\bar{\theta}$. Similarly only the leading term in the Taylor expansions of λ and D survive in the expression for $V(y, \theta, \bar{\theta})$. Also, we have used the Fierz identity $(\theta\sigma^{\mu}\bar{\theta})(\theta\sigma^{\nu}\bar{\theta}) = \frac{1}{2}\eta^{\mu\nu}(\theta\theta)(\bar{\theta}\bar{\theta})$ to rewrite $(\theta\sigma^{\mu}\bar{\theta})(\theta\sigma^{\nu}\bar{\theta})\frac{\partial A_{\mu}}{\partial y^{\nu}} = \frac{1}{2}(\theta\theta)(\bar{\theta}\bar{\theta})\partial_{\mu}A^{\mu}$.

Clearly $V^3 = 0$, so $e^{\pm 2V} = 1 \pm 2V + 2V^2$, and additionally terms such as $V^2\mathcal{D}_{\alpha}V = 0$ and so W_{α} can be expanded as

$$W_{\alpha} = -\frac{1}{4}\bar{\mathcal{D}}_{\dot{\alpha}}[\mathcal{D}_{\alpha}V + 2(\mathcal{D}_{\alpha}V)V - 2V(\mathcal{D}_{\alpha}V)]. \tag{4.5.6}$$

This can be evaluated in terms of components - first evaluate $\mathcal{D}_{\alpha}V$:

$$\begin{aligned}
\mathcal{D}_\alpha V &= (\sigma^\mu \bar{\theta})_\alpha A_\mu(y) + 2\theta_\alpha (\bar{\theta} \bar{\lambda}(y)) + (\bar{\theta} \bar{\theta}) \lambda_\alpha(y) \\
&\quad + \theta_\alpha (\bar{\theta} \bar{\theta}) D(y) - i\theta_\alpha (\bar{\theta} \bar{\theta}) \partial_\mu A^\mu(y) \\
&\quad + 2i (\sigma^\nu \bar{\theta})_\alpha [\theta \sigma^\mu \bar{\theta} \partial_\nu A_\mu + (\theta \theta) \bar{\theta}_{\dot{\alpha}} \partial_\nu \bar{\lambda}^{\dot{\alpha}}] \\
&= (\sigma^\mu \bar{\theta})_\alpha A_\mu(y) + 2\theta_\alpha (\bar{\theta} \bar{\lambda}(y)) + 2(\bar{\theta} \bar{\theta}) \lambda_\alpha(y) \\
&\quad + \theta_\alpha (\bar{\theta} \bar{\theta}) D(y) - i\theta_\alpha (\bar{\theta} \bar{\theta}) \partial_\mu A^\mu(y) \\
&\quad - i(\bar{\theta} \bar{\theta}) \left[\epsilon^{\dot{\beta} \dot{\gamma}} \theta^{\dot{\beta}} (\sigma^\mu)_{\beta \dot{\gamma}} (\sigma^\nu)_{\alpha \dot{\beta}} \partial_\nu A_\mu + (\theta \theta) (\sigma^\nu)_{\alpha \dot{\alpha}} \partial_\nu \bar{\lambda}^{\dot{\alpha}} \right], \quad (4.5.7)
\end{aligned}$$

where the final term has been rewritten using $\bar{\theta}^{\dot{\alpha}} \bar{\theta}^{\dot{\beta}} = \frac{1}{2} \epsilon^{\dot{\alpha} \dot{\beta}} (\bar{\theta} \bar{\theta})$. Hence

$$\begin{aligned}
(\mathcal{D}_\alpha V) V - V (\mathcal{D}_\alpha V) &= \left[(\sigma^\mu)_{\alpha \dot{\alpha}} \bar{\theta}^{\dot{\alpha}} \bar{\theta}_{\dot{\beta}} (\theta \theta) - 2\theta^\beta (\sigma^\mu)_{\beta \dot{\alpha}} \bar{\theta}^{\dot{\alpha}} \theta_\alpha \bar{\theta}_{\dot{\beta}} \right] \left(A_\mu \bar{\lambda}^{\dot{\beta}} - \bar{\lambda}^{\dot{\beta}} A_\mu \right) \\
&\quad + \left[(\sigma^\mu)_{\alpha \dot{\alpha}} \bar{\theta}^{\dot{\alpha}} \theta^\beta (\sigma^\nu)_{\beta \dot{\beta}} \bar{\theta}^{\dot{\beta}} \right] (A_\mu A_\nu - A_\nu A_\mu) \\
&= -(\theta \theta) (\bar{\theta} \bar{\theta}) (\sigma^\mu)_{\alpha \dot{\beta}} \left(A_\mu \bar{\lambda}^{\dot{\beta}} - \bar{\lambda}^{\dot{\beta}} A_\mu \right) \\
&\quad - i(\bar{\theta} \bar{\theta}) (\sigma^{\mu\nu} \theta)_\alpha (A_\mu A_\nu - A_\nu A_\mu), \quad (4.5.8)
\end{aligned}$$

where the $\sigma^{\mu\nu} = \frac{i}{4} (\sigma^\mu \bar{\sigma}^\nu - \sigma^\nu \bar{\sigma}^\mu)$ emerges after exploiting the fact that

$$\begin{aligned}
&\left[(\sigma^\mu)_{\alpha \dot{\alpha}} \bar{\theta}^{\dot{\alpha}} \theta^\beta (\sigma^\nu)_{\beta \dot{\beta}} \bar{\theta}^{\dot{\beta}} \right] (A_\mu A_\nu - A_\nu A_\mu) \\
&= \left[(\sigma^{[\mu})_{\alpha \dot{\alpha}} \bar{\theta}^{\dot{\alpha}} \theta^\beta (\sigma^{\nu]})_{\beta \dot{\beta}} \bar{\theta}^{\dot{\beta}} \right] (A_\mu A_\nu - A_\nu A_\mu), \quad (4.5.9)
\end{aligned}$$

where $\dots^{[\mu} \dots^{\nu]}$ indicates anti-symmetrisation over μ and ν . Hence

$$\begin{aligned}
W_\alpha &= -\frac{1}{4} \bar{\partial}_{\dot{\alpha}} \bar{\partial}^{\dot{\alpha}} \left\{ (\sigma^\mu \bar{\theta})_\alpha A_\mu(y) + 2\theta_\alpha (\bar{\theta} \bar{\lambda}(y)) + (\bar{\theta} \bar{\theta}) \lambda_\alpha(y) \right. \\
&\quad + \theta_\alpha (\bar{\theta} \bar{\theta}) D(y) - i\theta_\alpha (\bar{\theta} \bar{\theta}) \partial_\mu A^\mu(y) \\
&\quad - i(\bar{\theta} \bar{\theta}) \left[\epsilon^{\dot{\beta} \dot{\gamma}} \theta^{\dot{\beta}} (\sigma^\mu)_{\beta \dot{\gamma}} (\sigma^\nu)_{\alpha \dot{\beta}} \partial_\nu A_\mu + (\theta \theta) (\sigma^\nu)_{\alpha \dot{\alpha}} \partial_\nu \bar{\lambda}^{\dot{\alpha}} \right] \\
&\quad \left. - 2(\theta \theta) (\bar{\theta} \bar{\theta}) (\sigma^\mu)_{\alpha \dot{\beta}} \left(A_\mu \bar{\lambda}^{\dot{\beta}} - \bar{\lambda}^{\dot{\beta}} A_\mu \right) \right\}
\end{aligned}$$

$$\begin{aligned}
& \left. - 2i (\bar{\theta}\theta) (\sigma^{\mu\nu}\theta)_\alpha (A_\mu A_\nu - A_\nu A_\mu) \right\} \\
= & \lambda_\alpha(y) + \theta_\alpha D(y) - i\theta_\alpha \partial_\mu A^\mu(y) \\
& - i\epsilon^{\dot{\beta}\dot{\gamma}}\theta^\beta (\sigma^\mu)_{\beta\dot{\gamma}} (\sigma^\nu)_{\alpha\dot{\beta}} \partial_\nu A_\mu - i(\theta\theta) (\sigma^\nu)_{\alpha\dot{\alpha}} \partial_\nu \bar{\lambda}^{\dot{\alpha}} \\
& - 2(\theta\theta) (\sigma^\mu)_{\alpha\dot{\beta}} \left(A_\mu \bar{\lambda}^{\dot{\beta}} - \bar{\lambda}^{\dot{\beta}} A_\mu \right) - 2i (\sigma^{\mu\nu}\theta)_\alpha (A_\mu A_\nu - A_\nu A_\mu), \quad (4.5.10)
\end{aligned}$$

using the fact that $\bar{\partial}_{\dot{\alpha}}\bar{\partial}^{\dot{\alpha}}(\bar{\theta}\theta) = -2\bar{\partial}_{\dot{\alpha}}\bar{\theta}^{\dot{\alpha}} = -4$. We can simplify the ∂A terms using the fact that $\eta^{\mu\nu}\delta_\alpha^\beta = \frac{1}{2}(\sigma^\mu\bar{\sigma}^\nu + \sigma^\nu\bar{\sigma}^\mu)_\alpha^\beta$ and hence

$$\begin{aligned}
& - i\theta_\alpha \partial_\mu A^\mu(y) - i\epsilon^{\dot{\beta}\dot{\gamma}}\theta^\beta (\sigma^\mu)_{\beta\dot{\gamma}} (\sigma^\nu)_{\alpha\dot{\beta}} \partial_\nu A_\mu \\
= & - i \left[\frac{1}{2}\theta_\beta (\sigma^\mu\bar{\sigma}^\nu + \sigma^\nu\bar{\sigma}^\mu)_\alpha^\beta + \theta_\beta (\sigma^\mu\bar{\sigma}^\nu)_\alpha^\beta \right] \partial_\nu A_\mu \\
= & (\theta\sigma^{\mu\nu})_\alpha (\partial_\mu A_\nu - \partial_\nu A_\mu). \quad (4.5.11)
\end{aligned}$$

W_α can therefore be simplified to

$$\begin{aligned}
W_\alpha(y, \theta) = & \lambda_\alpha(y, \theta) + \theta_\alpha D(y) + (\sigma^{\mu\nu}\theta)_\alpha F_{\mu\nu}(y) \\
& - i(\theta\theta) (\sigma^\mu)_{\alpha\dot{\alpha}} \mathcal{D}_\mu \bar{\lambda}^{\dot{\alpha}}(y), \quad (4.5.12)
\end{aligned}$$

where $F_{\mu\nu} = \partial_\mu A_\nu - \partial_\nu A_\mu - 2i(A_\mu A_\nu - A_\nu A_\mu)$ and $\mathcal{D}_\mu \bar{\lambda}^{\dot{\alpha}}(y) = \partial_\mu \bar{\lambda}^{\dot{\alpha}} - 2i(A_\mu \bar{\lambda}^{\dot{\alpha}} - \bar{\lambda}^{\dot{\alpha}} A_\mu)$.

Because the field strength is a chiral superfield and transforms as $W_\alpha \rightarrow e^{-2i\Lambda} W_\alpha e^{2i\Lambda}$, kinetic terms for the gauge fields (and gauginos) can be included in the Lagrangian via the following term:

$$\mathcal{L} \supset \tau \text{Tr} [W_\alpha W^\alpha] \Big|_F + \text{h.c.}, \quad (4.5.13)$$

where τ is the gauge coupling. This term can be written in components as

$$\mathcal{L} \supset 2i\tau \text{Tr} [\lambda\sigma^\mu \mathcal{D}_\mu \bar{\lambda}] + \tau \text{Tr} [D^2] + \frac{1}{2}\tau \text{Tr} [F_{\mu\nu} F^{\mu\nu}]$$

$$+ \frac{i}{2} \tau \text{Tr} \left[F_{\mu\nu} \tilde{F}^{\mu\nu} \right] + h.c., \quad (4.5.14)$$

where we've used the cyclic property of the trace and the identity $\text{Tr} \left[\sigma^{\mu\nu} \sigma^{\rho\delta} \right] = \eta^{\mu\rho} \eta^{\nu\delta} - \eta^{\mu\delta} \eta^{\nu\rho} + i \epsilon^{\mu\nu\rho\delta}$, and the dual field strength is defined as $\tilde{F}_{\mu\nu} = \frac{1}{2} \epsilon^{\mu\nu\rho\delta} F_{\rho\delta}$.

4.5.2 Fayet-Iliopoulos Term

For completeness, we mention that for abelian gauge symmetries, it is also possible to include an additional term proportional to the D - term of the gauge superfield V , given by

$$\mathcal{L} \supset \xi V|_D = \frac{1}{2} \xi D \quad (4.5.15)$$

in Wess-Zumino gauge. We will discuss the possible consequences of this term in the context of the MSSM in Section 4.7.

4.5.3 Gauge Interactions

Chiral superfields can transform in any representation of the gauge group. Such a chiral superfield transforms under a generalised gauge transformation as

$$\Phi \rightarrow e^{-2i\Lambda^A T_R^A} \Phi \quad (4.5.16)$$

where T_R^A are the relevant generators of the representation of the Lie algebra. This means that the Kähler potential $\Phi^\dagger \Phi|_D$ must be modified to the following in order to define a gauge-invariant action

$$\mathcal{L} \supset \Phi^\dagger e^{2V^A T_R^A} \Phi, |_D. \quad (4.5.17)$$

We can evaluate this in terms of the component fields, again exploiting the fact that $e^{2V} = 1 + 2V + 2V^2$ (where the gauge group indices A are implicit):

$$\begin{aligned}
\mathcal{L} \supset & \partial_\mu \phi^\dagger \partial^\mu \phi - i \bar{\psi} \bar{\sigma}^\mu \partial_\mu \psi + F^\dagger F + \phi^\dagger D \phi \\
& + 2 \left\{ \left(\phi^\dagger + \sqrt{2} \bar{\theta} \bar{\psi} - i \theta \sigma^\mu \bar{\theta} \partial_\mu \phi^\dagger \right) \right. \\
& \quad \left(\theta \sigma^\mu \bar{\theta} A_\mu + (\theta \theta) (\bar{\theta} \bar{\lambda}) + (\bar{\theta} \bar{\theta}) (\theta \lambda) + \frac{1}{2} (\theta \theta) (\bar{\theta} \bar{\theta}) D \right) \\
& \quad \left. \left(\phi + \sqrt{2} \theta \psi + i \theta \sigma^\mu \bar{\theta} \partial_\mu \phi \right) \right\} \Big|_D \\
& + 2 \left\{ \phi^\dagger (\theta \sigma^\mu \bar{\theta}) A_\mu (\theta \sigma^\nu \bar{\theta} A_\nu) \right\} \Big|_D \\
= & \mathcal{D}_\mu \phi^\dagger \mathcal{D}^\mu \phi - i \bar{\psi} \bar{\sigma}^\mu \mathcal{D}_\mu \psi + F^\dagger F + \phi^\dagger D \phi \\
& - \sqrt{2} \phi^\dagger (\lambda \psi) - \sqrt{2} (\bar{\lambda} \bar{\psi}) \phi, \tag{4.5.18}
\end{aligned}$$

where $\mathcal{D}^\mu X = \partial_\mu X - i A_\mu X$ for $X = \phi, \psi$.

Similarly to the F -field above, there are no kinetic terms for D and so it can be eliminated. Gathering the D -field terms together, we obtain

$$\mathcal{L} \supset \tau D^A D^B \text{Tr} [T^A T^B] + D^A \sum_{\Phi} \Phi^\dagger T^A \Phi. \tag{4.5.19}$$

Hence the value of the D -field is given by

$$D^A = -\frac{1}{\tau} (M^{-1})^{AB} \sum_{\Phi} \Phi^\dagger T^A \Phi, \tag{4.5.20}$$

where $M^{AB} = 2 \text{Tr} [T^A T^B]$, and so the D -field contribution to the Lagrangian is given by

$$\mathcal{L} \supset -\tau D^A D^B \text{Tr} [T^A T^B], \tag{4.5.21}$$

with the value of D^A as given above.

4.6 Supersymmetry Breaking

Because we have not observed any superpartners to any Standard Model particles, with identical mass and gauge couplings, we can see that supersymmetry is not respected by the vacuum state that we occupy in reality. Hence supersymmetry (if it exists) must be broken. Supersymmetry is broken if $Q_\alpha|0\rangle \neq 0$, which is equivalent to the vacuum having non-zero energy.

4.6.1 F-term Breaking

As can be seen from Equation 4.3.12, the scalar potential has F-term contributions

$$V \supset \sum_i F_i^* F_i, \quad (4.6.1)$$

and so if the vacuum expectation value $\langle F_i \rangle \neq 0$, for some F_i , the vacuum will have non-zero energy and supersymmetry will be broken.

This can also be seen by considering the supersymmetry transformation of a chiral superfield in the ground state of the theory:

$$\begin{aligned} \phi &\rightarrow \phi + \sqrt{2}(\epsilon\psi), \\ \psi &\rightarrow \psi + \sqrt{2}(\epsilon F) + i\sqrt{2}\sigma^\mu\bar{\epsilon}\partial_\mu\phi, \\ F &\rightarrow F + i\sqrt{2}\bar{\epsilon}\bar{\sigma}^\mu\partial_\mu\psi \end{aligned} \quad (4.6.2)$$

from which it is clear that if $\langle F \rangle \neq 0$ then $\delta\psi \neq 0$ and supersymmetry is not respected by the vacuum.

4.6.2 D-term Breaking

Similarly to the F-term case, the scalar potential has D-term contributions (see Equation 4.5.21)

$$V \supset \sum_i \tau_i D_i^a D_i^b \text{Tr} [T_i^a T_i^b], \quad (4.6.3)$$

and so supersymmetry will also be broken if any D_i gains an expectation value.

This can similarly be seen by considering the supersymmetry transformation of a real superfield in the ground state of the theory:

$$\begin{aligned} V_\mu &\rightarrow V_\mu + \epsilon \sigma_\mu \bar{\lambda} + \lambda \sigma_\mu \bar{\epsilon}, \\ \lambda &\rightarrow \lambda + \epsilon D + \frac{i}{2} (\bar{\sigma}^\nu \sigma^\mu \bar{\epsilon}) \partial_\mu V_\nu, \\ D &\rightarrow D + i \partial_\mu (\epsilon \sigma^\mu \bar{\lambda} - \lambda \sigma^\mu \bar{\epsilon}), \end{aligned} \quad (4.6.4)$$

and, analogously to the F-term case above, if $\langle D \rangle \neq 0$ then $\delta\lambda \neq 0$ and supersymmetry is clearly broken.

4.7 The Minimally Supersymmetric Standard Model

4.7.1 Particle Content and Lagrangian Structure

The MSSM is formed by assigning all SM fermions to chiral superfields - containing the SM fermion along with a scalar (sfermion) superpartner - and all SM vector fields to real superfields - containing the SM vector field along with a fermion (gaugino) superpartner. The chiral superfields have $SU(3) \times SU(2)_L \times U(1)_Y$ charges corresponding to their respective fermion components' SM values, e.g. the superfields containing the left-handed leptons (or equivalently the left-handed leptons and their scalar partners, the sleptons) have charges $(\mathbf{1}, \mathbf{2}, \frac{1}{2})$ - they are uncharged under $SU(3)_C$, transform in the fundamental representation of $SU(2)_L$ and have $U(1)$ hypercharge $Y = \frac{1}{2}$.

In addition, the MSSM has chiral Higgs superfields \hat{H}_u and \hat{H}_d (we will use hats to indicate superfields) which each contain a Higgs scalar along with a

Superfield	Spin- $\frac{1}{2}$	Spin-1	$SU(3)_C \times SU(2)_L \times U(1)_Y$
	Quarks	Squarks	
\hat{Q} (x3 generations)	Q	\tilde{Q}	$(\mathbf{3}, \mathbf{2}, \frac{1}{6})$
\hat{U}_R^c (x3 generations)	U_R^c	\tilde{U}_R^c	$(\bar{\mathbf{3}}, \mathbf{1}, -\frac{2}{3})$
\hat{D}_R^c (x3 generations)	D_R^c	\tilde{D}_R^c	$(\bar{\mathbf{3}}, \mathbf{1}, \frac{1}{3})$
	Leptons	Sleptons	
\hat{L} (x3 generations)	L	\tilde{L}	$(\mathbf{1}, \mathbf{2}, -\frac{1}{2})$
\hat{E}_R^c (x3 generations)	E_R^c	\tilde{E}_R^c	$(\mathbf{1}, \mathbf{1}, 1)$
	Higgsinos	Higgs	
\hat{H}_u	\tilde{H}_u	H_u	$(\mathbf{1}, \mathbf{2}, \frac{1}{2})$
\hat{H}_d	\tilde{H}_d	H_d	$(\mathbf{1}, \mathbf{2}, -\frac{1}{2})$

Table 4.1: Chiral superfields of the MSSM. A hat is used to denote a superfield, while a tilde marks an R-parity odd superpartner. Here we have included the conjugate of the right-handed quark and lepton superfields, so that the table only includes left-handed fields. This is also the form in which these fields will appear in the superpotential.

Superfield	Spin- $\frac{1}{2}$	Spin-1	$SU(3)_C \times SU(2)_L \times U(1)_Y$
	Gauginos	Gauge Bosons	
\hat{g}	\tilde{g} Gluino	g Gluon	$(\mathbf{8}, \mathbf{1}, 0)$
\hat{B}	\tilde{B} Bino	B B Boson	$(\mathbf{1}, \mathbf{3}, \frac{1}{6})$
\hat{W}	$\tilde{W}^0, \tilde{W}^\pm$ Wino	W^0, W^\pm W Boson	$(\mathbf{1}, \mathbf{1}, 0)$

Table 4.2: Real superfields of the MSSM. After electroweak symmetry breaking, there is as usual (along with the gluon, which is unaffected) one remaining massless gauge boson, the photon γ , along with a neutral massive gauge boson, Z , and a charged gauge boson, W^\pm .

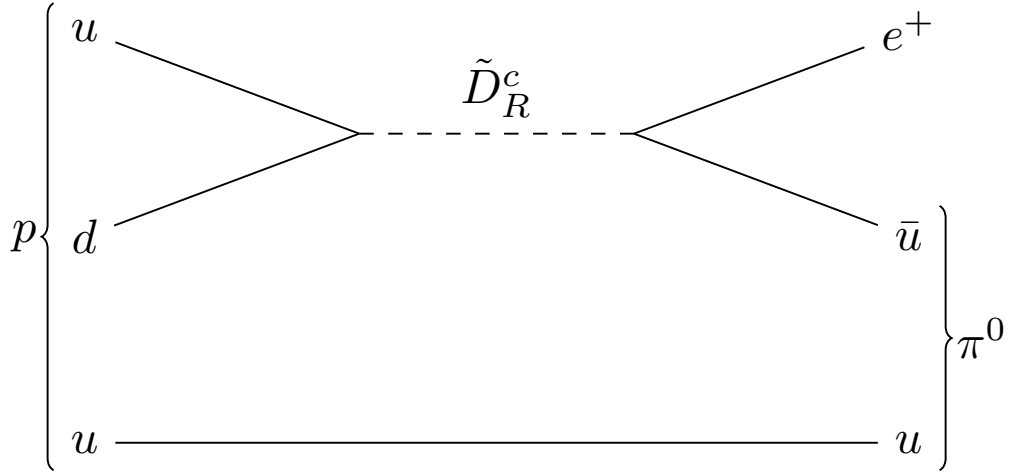


Figure 4.2: Process contributing to proton decay in the absence of R-parity.

fermion superpartner - a Higgsino. They have charges $(\mathbf{1}, \mathbf{2}, \pm\frac{1}{2})$, i.e. they are both uncharged under $SU(3)$, transform in the fundamental representation of $SU(2)_L$, but have opposite $U(1)$ hypercharges to avoid a chiral Y^3 anomaly due to the Higgsino hypercharges. The particle content of the MSSM is summarised in Tables 4.1 and 4.2.

Finally, the MSSM has an additional \mathbb{Z}_2 symmetry, R-parity, which is defined for a particle of spin s as

$$P_R = (-1)^{3(B-L)+2s}. \quad (4.7.1)$$

This enforces baryon number, B, and lepton number, L, conservation, and thereby forbids terms such as $(\hat{L} \cdot \hat{Q}) \hat{D}_R^c$ and $\hat{U}_R^c \hat{D}_R^c \hat{D}_R^c$ in the superpotential - where \hat{L} contains the left-handed parts of the (s)lepton fields, \hat{Q} contains the left-handed parts of the (s)quark fields, and \hat{D}_R^c, \hat{U}_R^c contains the conjugate of the right-handed parts of the down, up (s)quark fields (so that e.g. \hat{D}_R^c transforms in the antifundamental representation of $SU(3)_C$ and with hypercharge $Y = \frac{1}{3}$ i.e. as $(\bar{\mathbf{3}}, \mathbf{1}, \frac{1}{3})$). Such a term would allow very rapid proton decay, as shown in Figure 4.2.

Hence the MSSM lagrangian will include:

A superpotential containing gauge invariant combinations of the chiral superfields. Comparing to Equation 4.3.12, it can be seen that this will contain interactions between the components of the chiral superfields, i.e. (s)fermion-(s)fermion, (s)fermion-Higgs(ino) and Higgs(ino)-Higgs(ino) interactions, and in particular much of the the Higgs potential.

Interaction terms $\Phi e^{2V} \Phi|_D$ for each chiral superfield. This will contain kinetic terms for the (s)fermions and Higgs(ino)s, and interactions between the (s)fermions/Higgs(ino)s and the gauge bosons/gauginos.

A field strength for each real superfield. This will contain kinetic terms for the gauge and gaugino fields.

Soft SUSY-breaking terms which contain gaugino and slepton masses, sfermion-Higgs interactions and further contributions to the Higgs potential

(No) Fayet-Iliopoulos term - we will show that an FI term would break colour and charge.

4.7.2 MSSM Superpotential

The MSSM superpotential is given by

$$\begin{aligned}
 W = & h_u \left(\hat{Q} \cdot \hat{H}_u \right) \hat{U}_R^c + h_d \left(\hat{Q} \cdot \hat{H}_d \right) \hat{D}_R^c \\
 & + h_e \left(\hat{H}_d \cdot \hat{L} \right) \hat{E}_R^c + \mu \left(\hat{H}_u \cdot \hat{H}_d \right), \tag{4.7.2}
 \end{aligned}$$

where e.g. $\left(\hat{Q} \cdot \hat{H}_u \right) = \epsilon^{\alpha\beta} \hat{Q}_\alpha \left(\hat{H}_u \right)_\beta$ is the gauge invariant way of combining $SU(2)$ indices - $\epsilon^{\alpha\beta} \hat{Q}_\alpha$ transforms in the antifundamental representation. Alternatively this can be seen by considering how this combination transforms under a generalised gauge transformation:

$$\begin{aligned}
\epsilon^{\alpha\beta} \hat{Q}_\alpha \left(\hat{H}_u \right)_\beta &\rightarrow \epsilon^{\alpha\beta} \hat{Q}'_\alpha \left(\hat{H}'_u \right)_\beta \\
&= \epsilon^{\alpha\beta} \left(e^{\Lambda^A \sigma^A} \right)_{\alpha\gamma} \hat{Q}_\gamma \left(e^{\Lambda^B \sigma^B} \right)_{\beta\delta} \left(\hat{H}_u \right)_\delta \\
&= \left[\left(e^{\Lambda^A \sigma^A} \right)^T \epsilon \left(e^{\Lambda^B \sigma^B} \right) \right]_{\gamma\delta} \hat{Q}_\gamma \left(\hat{H}_u \right)_\delta, \tag{4.7.3}
\end{aligned}$$

as the $SU(2)$ generators are given by $T^A = \frac{i\sigma^A}{2}$. Then exploiting the fact that $\epsilon^{-1} \sigma_A^T \epsilon = -\sigma_A$, we can rewrite

$$\begin{aligned}
\epsilon^{\alpha\beta} \hat{Q}'_\alpha \left(\hat{H}'_u \right)_\beta &= \left[\epsilon e^{-\Lambda^A \sigma^A} \left(e^{\Lambda^B \sigma^B} \right) \right]_{\gamma\delta} \hat{Q}_\gamma \left(\hat{H}_u \right)_\delta \\
&= \epsilon^{\gamma\delta} \hat{Q}_\gamma \left(\hat{H}_u \right)_\delta, \tag{4.7.4}
\end{aligned}$$

and so this combination is indeed gauge invariant.

4.7.3 Soft SUSY-Breaking Terms

Regardless of the mechanism of supersymmetry breaking, its effects at low energy can be parameterised as

$$\begin{aligned}
\mathcal{L}_{\text{soft}} &= -m_{H_u}^2 H_u^\dagger H_u - m_{H_d}^2 H_d^\dagger H_d - (B\mu (H_u \cdot H_d) + \text{h.c.}) \\
&\quad - m_Q^2 \tilde{Q}^\dagger \tilde{Q} - m_L^2 \tilde{L}^\dagger \tilde{L} - m_u^2 \tilde{U}_R^{c\dagger} \tilde{U}_R^c - m_d^2 \tilde{D}_R^{c\dagger} \tilde{D}_R^c - m_e^2 \tilde{E}_R^{c\dagger} \tilde{E}_R^c \\
&\quad - \left(A_u \left(\hat{Q} \cdot \hat{H}_u \right) \hat{U}_R^c + A_d \left(\hat{Q} \cdot \hat{H}_d \right) \hat{D}_R^c + A_e \left(\hat{H}_d \cdot \hat{L} \right) \hat{E}_R^c + \text{h.c.} \right) \\
&\quad - \frac{1}{2} \left(M_1 \tilde{B} \tilde{B} + M_2 \tilde{W} \tilde{W} + M_3 \tilde{g} \tilde{g} \right), \tag{4.7.5}
\end{aligned}$$

where \tilde{X} denotes the superpartner of the particle X , so that e.g. \tilde{Q} are the (left-handed parts of the) squarks, $H_{u,d}$ are the scalar part of the Higgs superfields, and $\tilde{B}, \tilde{W}, \tilde{g}$ are the gauginos.

All of these terms are assumed to stem from some SUSY-breaking mechanism, and so each of these mass parameters should be around the same scale M_{SUSY} .

4.7.4 Auxiliary Fields

To find the superpotential in terms of the physical fields, the auxiliary fields $F_{H_u, H_d, \dots}$ and $D_{A, W, \dots}$ must be eliminated.

Both the gauge interaction terms and the superpotential will contain terms involving the F -fields. Grouping these together we obtain

$$\begin{aligned}
\mathcal{L}_F = & \sum_{\Phi} F_{\Phi}^{\dagger} F_{\Phi} \\
& + \left[h_u \left(\tilde{Q} \cdot F_{H_u} \right) \tilde{U}_R^c + \mu \left(F_{H_u} \cdot H_d \right) \right. \\
& \quad + h_d \left(\tilde{Q} \cdot F_{H_d} \right) \tilde{D}_R^c + h_e \left(F_{H_d} \cdot \tilde{L} \right) \tilde{E}_R^c + \mu \left(H_u \cdot F_{H_d} \right) \\
& \quad + h_u \left(F_Q \cdot H_u \right) \tilde{U}_R^c + h_d \left(F_Q \cdot H_d \right) \tilde{D}_R^c \\
& \quad + h_u \left(\tilde{Q} \cdot H_u \right) F_{U_R} + h_d \left(\tilde{Q} \cdot H_d \right) F_{D_R} \\
& \quad \left. + h_e \left(H_d \cdot F_L \right) \tilde{E}_R^c + h_e \left(H_d \cdot \tilde{L} \right) F_{E_R} + \text{h.c.} \right], \tag{4.7.6}
\end{aligned}$$

Hence we can solve for each F -field to eliminate it from the Lagrangian

$$\begin{aligned}
(F_{H_u})_{\alpha} &= \epsilon^{\alpha\beta} \left(h_u \tilde{Q} \tilde{U}_R^c - \mu \tilde{H}_d \right)_{\beta}^*, \\
(F_{H_d})_{\alpha} &= \epsilon^{\alpha\beta} \left(h_d \tilde{Q} \tilde{D}_R^c + \mu \tilde{H}_u - h_e \tilde{L} \tilde{E}_R^c \right)_{\beta}^*, \\
(F_Q)_{\alpha} &= -\epsilon^{\alpha\beta} \left(h_u H_u \tilde{U}_R^c + h_d H_d \tilde{D}_R^c \right)_{\beta}^*, \\
F_{U_R} &= \left(h_u \tilde{Q} \cdot H_u \right)^*, \\
F_{D_R} &= \left(h_d \tilde{Q} \cdot H_d \right)^*, \\
(F_L)_{\alpha} &= \epsilon^{\alpha\beta} \left(h_e H_d \tilde{E}_R^c \right)_{\beta}^*, \\
F_{E_R} &= \left(h_e H_d \cdot \tilde{L} \right)^*. \tag{4.7.7}
\end{aligned}$$

The F -field contributions to the scalar potential will then be given by

$$\mathcal{L}_F = - \sum_{\Phi} F_{\Phi}^{\dagger} F_{\Phi} \tag{4.7.8}$$

and in particular we will get the following contributions towards the Higgs potential

$$\mathcal{L}_F = -|\mu|^2 \left(H_u^\dagger H_u + H_d^\dagger H_d \right) + \dots, \quad (4.7.9)$$

where the ellipsis contains contributions to the scalar potential for the squarks and sleptons.

D -field terms are contained in the gauge field strength along with the gauge interactions. Grouping these together, we obtain

$$\begin{aligned} \mathcal{L}_D = & \frac{1}{2g_1^2} D_B^2 + D_B \sum_{\phi} Y_{\phi} \phi^\dagger \phi \\ & + \frac{1}{2g_2^2} D_W^A D_W^A + \frac{1}{2} D_W^A \sum_{\phi \in SU(2)} \phi^\dagger \sigma^A \phi, \end{aligned} \quad (4.7.10)$$

where $\sum_{\phi \in SU(2)}$ means the sum over all scalar fields ϕ in the fundamental representation of $SU(2)_L$, and using the fact that $\text{Tr} [\sigma^A \sigma^B] = 2\delta^{AB}$. Hence the D-fields are given by

$$\begin{aligned} D_B &= -g_1^2 \sum_{\phi} Y_{\phi} \phi^\dagger \phi, \\ D_W^A &= -\frac{g_2^2}{2} \sum_{\phi \in SU(2)_L} \phi^\dagger \sigma^A \phi. \end{aligned} \quad (4.7.11)$$

The D-field contributions to the scalar potential are given by

$$\mathcal{L}_D = -\frac{1}{2g_1^2} D_B^2 - \frac{1}{2g_2^2} D_W^A D_W^A. \quad (4.7.12)$$

The second term can be evaluated using the Pauli matrix identity $\sum_A (\sigma^A)_{\alpha\beta} (\sigma^A)_{\gamma\delta} = 2\delta_{\alpha\delta}\delta_{\beta\gamma} - \delta_{\alpha\beta}\delta_{\gamma\delta}$ and so

$$\begin{aligned}\mathcal{L}_D = & -\frac{g_1^2}{2} \left(\sum_{\phi} Y_{\phi} \phi^{\dagger} \phi \right)^2 \\ & -\frac{g_2^2}{8} \sum_{\phi_{i,j} \in SU(2)_L} \left[2 \left(\phi_i^{\dagger} \phi_j \right)^2 - \left(\phi_i^{\dagger} \phi_i \right) \left(\phi_j^{\dagger} \phi_j \right) \right],\end{aligned}\quad (4.7.13)$$

and in particular it will contain contributions towards the Higgs potential

$$\begin{aligned}\mathcal{L}_D = & -\frac{g_1^2 + g_2^2}{8} \left[\left(H_u^{\dagger} H_u \right)^2 + \left(H_d^{\dagger} H_d \right)^2 - 2 \left(H_u^{\dagger} H_u \right) \left(H_d^{\dagger} H_d \right) \right] \\ & -\frac{g_2^2}{2} |H_u^{\dagger} H_d|^2 + \dots,\end{aligned}\quad (4.7.14)$$

along with further contributions to the scalar potential for the squarks and sleptons (which are contained in the ellipsis).

To see that the presence of a $U(1)$ Fayet-Iliopoulos term breaks colour and/or charge, note that in this case the $U(1)$ D -field would be modified to

$$D_B = -\xi - g_1^2 \sum_{\phi} Y_{\phi} \phi^{\dagger} \phi, \quad (4.7.15)$$

and so the scalar potential would be given by

$$V = \sum_{\Phi} F_{\Phi}^{\dagger} F_{\Phi} + \frac{1}{2g_1^2} D_B^2 + \frac{1}{2g_2^2} D_W^A D_W^A \geq 0. \quad (4.7.16)$$

The minimum at $V = 0$ requires a non-zero vev for (at least) one of the squark or lepton fields, and hence breaks colour and/or charge. This is because $V = 0$ only occurs for $D_B = 0$, which necessitates a non-zero vev for one of the scalar fields. However, this cannot be either of the Higgs fields, as the F -field contributions $F_{H_{u,d}}^{\dagger} F_{H_{u,d}}$ contain Higgs masses $|\mu|^2 \left(H_u^{\dagger} H_u + H_d^{\dagger} H_d \right)$. Hence the MSSM does not contain an FI term.

4.7.5 Higgs Potential and Electroweak Symmetry Breaking

The SUSY-breaking terms combine with the contributions from the superpotential, gauge interactions and gauge field strength to give the Higgs potential

$$\begin{aligned}
V(H_u, H_d) = & (|\mu|^2 + m_{H_u}^2) H_u^\dagger H_u + (|\mu|^2 + m_{H_d}^2) H_d^\dagger H_d + (B\mu (H_u \cdot H_d) + \text{h.c.}) \\
& + \frac{g_1^2 + g_2^2}{8} \left[(H_u^\dagger H_u)^2 + (H_d^\dagger H_d)^2 \right. \\
& \left. - 2 (H_u^\dagger H_u) (H_d^\dagger H_d) \right] + \frac{g_2^2}{2} |H_u^\dagger H_d|^2, \quad (4.7.17)
\end{aligned}$$

or, in terms of charged and neutral components

$$\begin{aligned}
V(H_u, H_d) = & (|\mu|^2 + m_{H_u}^2) (|H_u^+|^2 + |H_u^0|^2) + (|\mu|^2 + m_{H_d}^2) (|H_d^-|^2 + |H_d^0|^2) \\
& + (B\mu (H_u^+ H_d^- - H_u^0 H_d^0) + \text{h.c.}) \\
& + \frac{g_1^2 + g_2^2}{8} \left[(|H_u^+|^2 + |H_u^0|^2) - (|H_d^-|^2 + |H_d^0|^2) \right]^2 \\
& + \frac{g_2^2}{2} |H_u^{+*} H_d^0 + H_u^{0*} H_d^-|^2. \quad (4.7.18)
\end{aligned}$$

We can take $B\mu$ to be real and positive by redefinition of H_u and H_d . To simplify this further, we can $SU(2)$ rotate away the charged component of one of the Higgs vevs, so we can take $\langle H_u^+ \rangle = 0$. This then also sets $H_d^- = 0$ at the minimum (assuming a minimum exists - we will explore the necessary conditions for existence of a minimum below) - this follows from $\frac{\partial V}{\partial H_u^+} = H_d^- \left[B\mu + \frac{g_2^2}{2} (H_u^0 H_d^0)^* \right]$ combined with the fact that the combination $H_u^0 H_d^0$ must be real and positive at the minimum. Exploiting the realness of $H_u^0 H_d^0$ at the minimum again, we can also $U(1)$ rotate both phases away from H_u^0 and H_d^0 at the minimum (as they have opposite hypercharges) to make them both real and positive. Hence the potential simplifies to

$$V(H_u, H_d) = (|\mu|^2 + m_{H_u}^2) (H_u^0)^2 + (|\mu|^2 + m_{H_d}^2) (H_d^0)^2$$

$$-2B\mu H_u^0 H_d^0 + \frac{g_1^2 + g_2^2}{8} \left((H_u^0)^2 - (H_d^0)^2 \right)^2 + \dots, \quad (4.7.19)$$

where the ellipsis contains terms which are zero at the minimum.

Firstly, we consider the necessary conditions for electroweak symmetry breaking (EWSB) to occur. For $B\mu = 0$ or very small, $H_u^0 = H_d^0 = 0$ is a minimum of the potential and EWSB does not occur, so we can set a lower bound on $B\mu$ above which $H_u^0 = H_d^0 = 0$ is no longer a minimum

$$(B\mu)^2 \gtrsim (|\mu|^2 + m_{H_u}^2) (|\mu|^2 + m_{H_d}^2). \quad (4.7.20)$$

There is also an upper bound on $B\mu$, stemming from the requirement that the potential must be bounded below (in particular, for $|H_u| = |H_d|$):

$$B\mu \lesssim 2|\mu|^2 + m_{H_u}^2 + m_{H_d}^2. \quad (4.7.21)$$

Assuming these are satisfied, we define $\langle H_{u,d}^0 \rangle = v_{u,d}$, $v^2 = v_u^2 + v_d^2$ and $\tan \beta = \frac{v_u}{v_d}$. (By comparison to Standard Model EWSB, we must have $v^2 \sim 174 \text{ GeV}$ in order to obtain the correct gauge boson masses.) We can then use the minimisation condition to relate v^2 and $\tan \beta$ to $m_{H_{u,d}}^2$:

$$\begin{aligned} (|\mu|^2 + m_{H_u}^2) - B\mu \cot \beta - \frac{g_1^2 + g_2^2}{4} v^2 \cos 2\beta &= 0, \\ (|\mu|^2 + m_{H_d}^2) - B\mu \tan \beta + \frac{g_1^2 + g_2^2}{4} v^2 \cos 2\beta &= 0, \end{aligned} \quad (4.7.22)$$

which gives

$$\begin{aligned} \sin 2\beta &= \frac{2B\mu}{2|\mu|^2 + m_{H_u}^2 + m_{H_d}^2}, \\ v^2 &= \frac{2|m_{H_u}^2 - m_{H_d}^2|}{(g_1^2 + g_2^2) \sqrt{1 - \sin^2 2\beta}} - \frac{2(2|\mu|^2 + m_{H_u}^2 + m_{H_d}^2)}{g_1^2 + g_2^2}, \end{aligned} \quad (4.7.23)$$

where the fact that $(\cos 2\beta > 0) \Leftrightarrow (m_{H_u}^2 > m_{H_d}^2)$ - which can be seen from the minimisation equations above - has been used.

After EWSB, the neutral components can be rewritten as

$$H_{u,d}^0 = v_{u,d} + \frac{h_{u,dR}^0 + ih_{u,dI}^0}{\sqrt{2}}, \quad (4.7.24)$$

and note that as $B\mu$ is real there will be no mixing between CP-even and CP-odd parts, but there will be mixing within the CP-odd, CP-even, and charged states separately. The mass terms are given by

$$\begin{aligned} \mathcal{L} \supset & -\frac{1}{2} \begin{pmatrix} h_{uR}^0 & h_{dR}^0 \end{pmatrix} M_{\text{CP-even}}^2 \begin{pmatrix} h_{uR}^0 \\ h_{dR}^0 \end{pmatrix} \\ & -\frac{1}{2} \begin{pmatrix} h_{uI}^0 & h_{dI}^0 \end{pmatrix} M_{\text{CP-odd}}^2 \begin{pmatrix} h_{uI}^0 \\ h_{dI}^0 \end{pmatrix} \\ & - \begin{pmatrix} H_u^+ & H_d^{-*} \end{pmatrix}^* M_{\text{charged}}^2 \begin{pmatrix} H_u^+ \\ H_d^{-*} \end{pmatrix}, \end{aligned} \quad (4.7.25)$$

where

$$\begin{aligned} (M_{\text{CP-even}}^2)_{11} &= |\mu|^2 + m_{H_u}^2 + \left(\frac{g_1^2 + g_2^2}{4}\right) (3v_u^2 - v_d^2), \\ (M_{\text{CP-even}}^2)_{12} &= -B\mu - \left(\frac{g_1^2 + g_2^2}{2}\right) v_u v_d, \\ (M_{\text{CP-even}}^2)_{22} &= |\mu|^2 + m_{H_d}^2 + \left(\frac{g_1^2 + g_2^2}{4}\right) (3v_d^2 - v_u^2), \\ (M_{\text{CP-odd}}^2)_{11} &= |\mu|^2 + m_{H_u}^2 + \left(\frac{g_1^2 + g_2^2}{2}\right) (v_u^2 - v_d^2), \\ (M_{\text{CP-odd}}^2)_{12} &= B\mu, \\ (M_{\text{CP-odd}}^2)_{22} &= |\mu|^2 + m_{H_d}^2 - \left(\frac{g_1^2 + g_2^2}{2}\right) (v_u^2 - v_d^2), \\ (M_{\text{charged}}^2)_{11} &= |\mu|^2 + m_{H_u}^2 + \frac{g_1^2}{4} (v_u^2 - v_d^2) + \frac{g_2^2}{4} (v_u^2 + v_d^2), \\ (M_{\text{charged}}^2)_{12} &= B\mu + \frac{g_2^2}{2} v_u v_d, \\ (M_{\text{charged}}^2)_{22} &= |\mu|^2 + m_{H_d}^2 - \frac{g_1^2}{4} (v_u^2 - v_d^2) + \frac{g_2^2}{4} (v_u^2 + v_d^2), \end{aligned} \quad (4.7.26)$$

or rewriting in order to make the presence of Goldstone modes clearer

$$\begin{aligned}
M_{\text{CP-even}}^2 &= \begin{pmatrix} B\mu \cot \beta + \left(\frac{g_1^2+g_2^2}{2}\right) v_u^2 & -B\mu - \left(\frac{g_1^2+g_2^2}{2}\right) v_u v_d \\ -B\mu - \left(\frac{g_1^2+g_2^2}{2}\right) v_u v_d & B\mu \tan \beta + \left(\frac{g_1^2+g_2^2}{2}\right) v_d^2 \end{pmatrix}, \\
M_{\text{CP-odd}}^2 &= B\mu \begin{pmatrix} \cot \beta & 1 \\ 1 & \tan \beta \end{pmatrix}, \\
M_{\text{charged}}^2 &= \left(B\mu + \frac{g_2^2}{2} v_u v_d\right) \begin{pmatrix} \cot \beta & 1 \\ 1 & \tan \beta \end{pmatrix}. \tag{4.7.27}
\end{aligned}$$

This makes clear that $M_{\text{CP-odd}}^2$ and M_{charged}^2 each have a massless eigenvalue - these are the Goldstone modes which are absorbed into the massive gauge bosons W^\pm, Z . Also, it shows that β is the mixing angle for the charged and CP-odd states. Hence the remaining degrees of freedom are three neutral scalars (two CP-even, $h_{1,2}$, and one CP-odd, A), and a charged scalar (H^\pm). The eigenvalues of the mass matrices above give the masses of these states

$$\begin{aligned}
m_A^2 &= \frac{2B\mu}{\sin 2\beta}, \\
m_{H^\pm}^2 &= \frac{2B\mu}{\sin 2\beta} + \frac{g_2^2 v^2}{2}, \\
m_{h_{1,2}}^2 &= \frac{1}{2} \left[m_A^2 + m_Z^2 \pm \sqrt{(m_A^2 + m_Z^2)^2 - 4m_A^2 m_Z^2 \cos^2 2\beta} \right]. \tag{4.7.28}
\end{aligned}$$

The mass of the lighter CP-even scalar ($m_{h_1}^2$) is bounded above, as $m_{h_1}^2 \rightarrow m_Z^2 \cos^2 2\beta$ for $m_A^2 \rightarrow \infty$, hence at tree-level $m_{h_1} < m_Z$. Hence radiative corrections are important for obtaining the correct Higgs mass. Including radiative corrections, an upper bound of $m_{h_1} \lesssim 135$ GeV is obtained [250, 251, 252].

4.7.6 The μ Problem

From Equations 4.7.20 and 4.7.21, we see that μ must be around the scale of M_{SUSY} . However, there is no explanation within the MSSM of why this might arise, as they appear to be unrelated scales, and μ might be expected to take

a more natural value such as zero, M_{GUT} or M_{Pl} . This is known as the μ problem of the MSSM.

One solution to the μ problem is found in the Next-to-Minimally Supersymmetric Standard Model (NMSSM) - it introduces an additional singlet superfield \hat{S} which has a term $\lambda\hat{S}(\hat{H}_u \cdot \hat{H}_d)$ in the superpotential. This singlet then gains a vacuum expectation value v_s , giving rise to an effective μ term in the Lagrangian $\mu_{\text{eff}}H_u \cdot H_d$, where $\mu_{\text{eff}} = \lambda v_s$. This vev is set by soft SUSY-breaking terms, and so μ_{eff} would be expected to be around M_{SUSY} , as required. Other solutions have also been proposed, such as within theories of supergravity [253]. The NMSSM will be discussed in Chapter 6.

4.7.7 Other Physical States

The remaining gauge eigenstates are not necessarily the physical states (i.e. mass eigenstates) of the theory. After EWSB, states of the same spin which have the same remaining unbroken gauge charges can mix.

The first set of states which can mix are the neutral higgsinos and gauginos (\tilde{W}^0, \tilde{B}), which mix to form four ‘neutralinos’. Similarly, the charged higgsinos and winos (\tilde{W}^\pm) all have charge ± 1 and so mix to form two ‘charginos’.

Squarks and sleptons can also mix with other squarks or sleptons with the same charges, however these mixings contribute to flavour changing neutral currents (FCNCs) which are tightly constrained, and hence so too are these mixings [254].

Gluginos are the only remaining state, and don’t participate in any mixing, as no other state gauge transforms in the same way.

The lightest particle with R-parity -1 will be stable - this is often taken to be the lightest neutralino, which as a neutral, stable, weakly interacting particle offers a good WIMP dark matter candidate.

Chapter 5

Dark Matter and Neutrino Masses in a Portalino-like Model

5.1 Introduction

The question of how the dark sector interacts with the visible sector, if it does at all, underpins the uncertainty surrounding the nature and origin of Dark Matter (DM). As discussed in Section 3.2.5, many proposals have been made for how a connection can be established through so called “portals”, including the Higgs portal see e.g. [113, 114, 115], through the Kinetic mixing portal [122, 123, 124, 125], neutrino portal [119, 117, 120, 121], axion portal [126], or perhaps there is no portal at all in which case the dark sector evolves independently but may still have observable effects [111].

In this chapter we focus on the neutrino portal, and in particular examine a model inspired by the Portalino scenario in which a singlet fermion field connects gauge neutral fermion operators from the Standard Model (SM) and hidden sector [255].

In a simple realisation of the Portalino framework introduced in [255] the SM is supplemented by two additional gauge singlet fermions and a complex scalar singlet. One of the fermion states plays the role of the right-handed neutrino, ν_R , and couples to the gauge invariant combination of the SM Higgs and Lepton doublets generating a Dirac like neutrino mass term after electroweak

symmetry breaking. This right-handed neutrino state also couples to a second gauge invariant operator composed of the second singlet fermion, which we call ψ , and the complex scalar field, call it Φ . If there is a dark $U(1)$ under which Φ and ψ both transform, then we can construct Yukawa interactions that lead to Dirac Masses after the spontaneous symmetry breaking of the dark $U(1)$ such that

$$\mathcal{L} \supset \lambda_1 \nu_R^\dagger H_0 \nu_L + \lambda_2 \nu_R^\dagger \Phi \psi = m_d \nu_R^\dagger (\sin \theta \nu_L + \cos \theta \psi), \quad (5.1.1)$$

where H_0 is the neutral component of the SM Higgs doublet, and the linear combination of ψ and ν_L forms a massive Dirac state with ν_R . As ψ has vector interactions with the dark gauge sector the light neutrino (zero) mass eigenstate, $\nu = \cos \theta \nu_L - \sin \theta \psi$ inherits these interactions, albeit suppressed by a factor of $\sin \theta$. As pointed out in [255], this scenario is a specific version of a Z' model in which the only interactions between the new hidden sector $U(1)$ and the SM is via the neutrinos.¹

Introducing DM into the hidden sector is straightforward. For example, in [255] a Yukawa interaction involving the scalar state Φ and a new Dirac fermion, call it X , was included. The dark sector dominantly interacts with the neutrino sector, potentially leading to the X DM states freezing-out via annihilation to neutrinos. This removes, or greatly suppresses, the usual modes for probing DM in direct and indirect detection experiments, allowing for models that consider a wider range of potentially viable DM masses. On the other hand, this makes the model harder to probe.

The simple model outlined above however requires modification in order to include neutrino masses. There are a number of choices we can make to do this. One possibility is to add a Majorana mass term for the ψ field leading to a model along the lines of the inverse see-saw model, see e.g. [256]. In [257], it

¹Although, given the introduction of a new scalar field, the Higgs portal also connects the two sectors.

was suggested that it may be possible to produce non-zero neutrino masses in a Zee-type model including two Higgs doublets via a $(l_i h)(h l_j)$ term generated at loop level.

An alternative is to change particle content by introducing further singlet fermion fields. In this chapter, we focus on a minimal extension with two more right-handed neutrinos and introduce associated large Majorana mass terms for these states. This set-up generates masses for two of the three generations of light neutrinos, with the heavy Majorana masses suppressing the mass scale of these two mass eigenstates through a seesaw-like mechanism. Without the heavy Majorana masses, the light neutrinos will be Dirac states with Dirac neutrino masses of $\mathcal{O}(\lambda_\nu v_h)$. Although with sufficiently small Yukawa couplings this is in principle a viable model, we choose instead to adopt the Majorana case.

The introduction of the large Majorana mass scale leads to small mixing angles in this combined neutrino-hidden state sector, which in turn generates suppressed couplings for the more massive hidden sector states. This leads to relatively long lifetimes for these states, giving rise to interesting cosmological implications and constraints on the model.

We first calculate the possible number of massless neutrino-like states included in a model in the Portalino framework in Section 5.2. This allows us to classify the number of singlet states and ψ -fermions which can give rise to physically realistic models. We then explicitly calculate the masses of the physical states for the case where there are 3 singlet states and a single ψ , along with the mixing between these states in Section 5.3. In Section 5.4 we describe a dark matter model within the Portalino framework, including the detailed properties of the putative DM candidate. The full Lagrangian of the model, specifying the interactions of the mass eigenstates, is given in Section 5.5. In Section 5.6 we outline the model's predictions for neutrino

masses and mixings, and how the experimentally observed values can be accommodated. In Section 5.7 we specify the viable parameter space capable of generating the correct DM abundance. We explore the phenomenology of – and constraints on – the new hidden sector states, which can have lifetimes up to and exceeding the age of the universe, in Section 5.8.

5.2 Massless States in the Portalino Framework

The Portalino framework is characterised by the presence of an additional n_R right-handed neutrinos $\nu_{R\alpha}$ and n_ψ Weyl fermions ψ_α , alongside the three left-handed neutrinos $\nu_{l\alpha}$. There will be mass terms between the ν_l and ν_R ; between the ψ and ν_R ; and additionally we include Majorana masses for the ν_R as discussed in the Introduction. This will be the most general set of masses allowed in our model, as discussed below in Section 5.4.

We are interested in cases with at most one massless neutrino-like state. This is because the neutrino masses must have splittings $\Delta m^2 \approx 2.5 \times 10^{-3} \text{ eV}^2$ and $\Delta m^2 \approx 7.4 \times 10^{-5} \text{ eV}^2$ in order to explain solar and atmospheric neutrino oscillations, hence ruling out models with two or more massless active neutrinos [100, 101, 102].

To calculate the number of massless states, we consider the general mass matrix for these states. It can be written (in the basis $\{\nu_l, \psi, \nu_R\}$)

$$M = \begin{pmatrix} 0_{n_\psi+3} & M_d^T \\ M_d & M_\psi & M_R \end{pmatrix}, \quad (5.2.1)$$

where M_d is an $n_R \times 3$ matrix, M_ψ is an $n_R \times n_\psi$ matrix, and M_R is an $n_R \times n_R$ matrix. If M_R is invertible and the combined sub-matrix

$$M_l = (M_d \quad M_\psi) \quad (5.2.2)$$

has maximal rank (i.e. rank equal to $\min(n_\psi + 3, n_R)$), then this matrix will have $\text{Nullity}(M) = \min(3 - n_R + n_\psi, 0)$ (as we will show briefly below). Hence, such a model would contain $\min(3 - n_R + n_\psi)$ massless neutrino-like states. If M_l is not of maximal rank, there may be up to $n_R - 1$ additional massless states.

To see the above, consider a massless eigenvector of M , which can be written

$$\chi_i = \begin{pmatrix} \mathbf{u} \\ \mathbf{w} \end{pmatrix}, \quad (5.2.3)$$

where \mathbf{u} is a $(3 + n_\psi)$ -vector, and \mathbf{w} is an n_R -vector, and they obey

$$\begin{aligned} M_l^T \mathbf{w} &= 0, \\ M_l \mathbf{u} + M_R \mathbf{w} &= 0. \end{aligned} \quad (5.2.4)$$

\mathbf{w} is in the kernel of M_l^T , and if M_l is of maximal rank, then the kernel has dimension $(n_R - \min(n_\psi + 3, n_R))$. If $n_R \leq n_\psi + 3$, this is equal to zero, and so $\mathbf{w} = 0$. Then \mathbf{u} is in the kernel of M_l , which has dimension $(n_\psi + 3) - \min(n_\psi + 3, n_R) = n_\psi + 3 - n_R$. Whereas, if $n_R > n_\psi + 3$, there are $(n_R - n_\psi - 3)$ linearly independent solutions to $M_l^T \mathbf{w} = 0$. \mathbf{u} must then satisfy $M_l \mathbf{u} = -M_R \mathbf{w}$, so

$$M_l \mathbf{u} \in (M_R \text{Ker}(M_l^T)) \cap \text{Image}(M_l), \quad (5.2.5)$$

which implies $M_l \mathbf{u} = \mathbf{0}$ (as $\text{Image}(M_l) = (\text{Ker}(M_l^T))^\perp$). But for $n_R > n_\psi + 3$, the kernel of M_l is only the zero vector, so $\mathbf{u} = \mathbf{0}$, which means that $\mathbf{w} = \mathbf{0}$ also, and there are no non-zero eigenvectors. Hence, $\text{Nullity}(M) = \min(3 - n_R + n_\psi, 0)$ for M_l and M_R of maximal rank.

If M_l is not of maximal rank (e.g. if the rows are linearly dependent due to a symmetry of the theory), then there are additional massless states. Assuming M_l is non-zero, it can have rank in the range

$$\text{Rank}(M_l) = \min(n_r, n_\psi + 3), \min(n_r, n_\psi + 2), \dots, 2, 1. \quad (5.2.6)$$

The same argument as above implies

$$M_l \mathbf{u} \in (M_R \text{Ker}(M_l^T)) \cap \text{Image}(M_l), \quad (5.2.7)$$

and so again $M_l \mathbf{u} = \mathbf{0}$ and $\mathbf{w} = \mathbf{0}$. Hence, in this case $\text{Nullity}(M)$ is of the same dimension as $\text{Ker}(M_l)$, which is given by $\text{Nullity}(M_l) = n_\psi + 3 - \text{Rank}(M_l)$ and so

$$\begin{aligned} \text{Nullity}(M_l) = & \max(n_\psi + 3 - n_R, 0), \max(n_\psi + 4 - n_R, 0), \dots \\ & \dots, n_\psi + 1, n_\psi + 2. \end{aligned} \quad (5.2.8)$$

Hence the number of massless states will be in this range, and will depend on the linear dependence in the mass matrices M_d and M_ψ . However, given that a physically realistic model cannot have more than a single massless neutrino, we can see from the above that we will require $n_\psi + 3 \leq n_R + 1$. In the next section, we consider the minimal physically viable case which includes a Portalino state, i.e. $n_\psi = 1$ and $n_R = 3$ (with M_l of maximal rank).

5.3 Neutrino Masses and Mixing

Before considering a model which includes a dark matter candidate, we would like to understand the structure of the mass eigenstates which emerge from the neutrino-singlet- ψ sector. We will focus on the minimal physically viable case

that includes a Portalino state, i.e. $n_\psi = 1$ and $n_R = 3$ (with M_l of maximal rank). The mass eigenstates and mixings of this seven-by-seven system can be evaluated by diagonalising the mass matrix of the system, which is given by

$$M = \begin{pmatrix} 0 & M_d^T \\ M_d & \mathbf{M}_\psi \\ M_d & \mathbf{M}_\psi & M_R \end{pmatrix}, \quad (5.3.1)$$

where M_d and M_R are 3×3 matrices and \mathbf{M}_ψ is a three vector, each with entries of order m_d , m_R and m_ψ respectively.

First it is noted that the mass matrix, M , has a zero eigenvalue, m_{ν_1} , with eigenvector

$$\mathbf{e}_1 = N \begin{pmatrix} -M_d^{-1} \mathbf{M}_\psi \\ 1 \\ 0 \\ 0 \\ 0 \end{pmatrix}, \quad (5.3.2)$$

where $N = 1/\sqrt{1 + \|M_d^{-1} \mathbf{M}_\psi\|^2}$. We define an orthonormal basis which includes this zero eigenvector:

$$\begin{aligned} \mathbf{e}_1, \quad \mathbf{e}_2 &= \begin{pmatrix} \mathbf{x}_1 \\ 0 \\ 0 \\ 0 \\ 0 \end{pmatrix}, \quad \mathbf{e}_3 = \begin{pmatrix} \mathbf{x}_2 \\ 0 \\ 0 \\ 0 \\ 0 \end{pmatrix}, \\ \mathbf{e}_4 &= \frac{N}{\|M_d^{-1} \mathbf{M}_\psi\|} \begin{pmatrix} M_d^{-1} \mathbf{M}_\psi \\ \|M_d^{-1} \mathbf{M}_\psi\|^2 \\ 0 \\ 0 \\ 0 \end{pmatrix}, \quad (\mathbf{e}_i)_j = \delta_{ij}, \end{aligned} \quad (5.3.3)$$

where $\mathbf{x}_{1,2}$ are chosen such that $\mathbf{x}_{1,2}^T M_d^{-1} \mathbf{M}_\psi = \mathbf{x}_1^T \mathbf{x}_2 = 0$ and $\|\mathbf{x}_{1,2}\|^2 = 1$.

After rotating away the zero eigenstate, we obtain a 7×7 matrix with a non-zero 6×6 sub-matrix with a seesaw-type structure:

$$P^{-1}MP = \begin{pmatrix} \mathbf{0}_{4,4} & \mathbf{0}_{1,3} \\ \mathbf{0}_{3,1} & M_D^T & M_R \end{pmatrix}, \quad (5.3.4)$$

where for the sake of clarity we have indicated the dimensions of the zero matrices (e.g. $\mathbf{0}_{n,m}$ is a $n \times m$ zero matrix) and where

$$M_D = \begin{pmatrix} \mathbf{x}_1^T M_d^T \\ \mathbf{x}_2^T M_d^T \\ \frac{\mathbf{M}_\psi^T}{N \|M_d^{-1} \mathbf{M}_\psi\|} \end{pmatrix}, \quad (5.3.5)$$

and

$$P = \begin{pmatrix} -NM_d^{-1} \mathbf{M}_\psi & \mathbf{x}_1 & \mathbf{x}_2 & \frac{NM_d^{-1} \mathbf{M}_\psi}{\|M_d^{-1} \mathbf{M}_\psi\|} & \mathbf{0}_{4,3} \\ N & 0 & 0 & N \|M_d^{-1} \mathbf{M}_\psi\| & \\ & & \mathbf{0}_{3,4} & & I_3 \end{pmatrix}. \quad (5.3.6)$$

The resulting matrix can be approximately block diagonalised, assuming the hierarchy $m_d, m_\psi \ll m_R$ (below, we will further assume $m_d \ll m_\psi \ll m_R$ - this will be discussed in more detail in the next section):

$$Q^{-1}P^{-1}MPQ = \begin{pmatrix} \mathbf{0}_{1,1} & \mathbf{0}_{1,6} \\ \mathbf{0}_{6,1} & M' \end{pmatrix} \quad (5.3.7)$$

where

$$M' = \begin{pmatrix} -M_D M_R^{-1} M_D^T + \mathcal{O}(M_D^3 M_R^{-2}) & \mathbf{0}_{3,3} \\ \mathbf{0}_{3,3} & M_R + \mathcal{O}(M_D) \end{pmatrix}, \quad (5.3.8)$$

$$Q = \begin{pmatrix} \mathbf{0}_{1,1} & \mathbf{0}_{1,6} \\ \mathbf{0}_{6,1} & Q' \end{pmatrix}, \quad (5.3.9)$$

and

$$\begin{aligned}
Q' = & \begin{pmatrix} I_3 - \frac{1}{2}M_D M_R^{-1} M_R^{-1} M_D^T & M_D M_R^{-1} \\ -M_R^{-1} M_D^T & I_3 - \frac{1}{2}M_R^{-1} M_D^T M_D M_R^{-1} \end{pmatrix} \\
& + \begin{pmatrix} \mathcal{O}(M_D^3 M_R^{-3}) & \mathcal{O}(M_D^3 M_R^{-3}) \\ \mathcal{O}(M_D^3 M_R^{-3}) & \mathcal{O}(M_D^3 M_R^{-3}) \end{pmatrix}. \tag{5.3.10}
\end{aligned}$$

We note that the eigenvalues of the M_R mass matrix will approximately correspond to the masses of the three heavy neutrino states, labelled N_i in Section 5.4.

The remaining three mass eigenvalues contained within the central 3×3 mass matrix block in Equation 5.3.7 are identified as the remaining two light neutrino masses, along with the Portalino mass, m_n , in Section 5.4. The explicit form of this mass matrix is given by

$$-M_D M_R^{-1} M_D^T = - \begin{pmatrix} c & d & f \\ d & e & b \\ f & b & a \end{pmatrix}, \tag{5.3.11}$$

where

$$\begin{aligned}
a &= \frac{\mathbf{M}_\psi^T M_R^{-1} \mathbf{M}_\psi}{N^2 \|M_d^{-1} \mathbf{M}_\psi\|^2} \\
b &= \frac{\mathbf{x}_2^T M_d^T M_R^{-1} \mathbf{M}_\psi}{N \|M_d^{-1} \mathbf{M}_\psi\|} \\
c &= \mathbf{x}_1^T M_d^T M_R^{-1} M_d \mathbf{x}_1 \\
d &= \mathbf{x}_1^T M_d^T M_R^{-1} M_d \mathbf{x}_2 \\
e &= \mathbf{x}_2^T M_d^T M_R^{-1} M_d \mathbf{x}_2 \\
f &= \frac{\mathbf{M}_\psi^T M_R^{-1} M_d \mathbf{x}_1}{N \|M_d^{-1} \mathbf{M}_\psi\|}. \tag{5.3.12}
\end{aligned}$$

We use the remaining freedom to choose \mathbf{x}_1 (or equivalently \mathbf{x}_2) to aid in further diagonalising. For example, choose $\mathbf{x}_1 \propto (M_d^T M_R^{-1} \mathbf{M}_\psi) \times (M_d^{-1} \mathbf{M}_\psi)$ (note that if this is zero then $M_d^T M_R^{-1} \mathbf{M}_\psi \propto M_d^{-1} \mathbf{M}_\psi$ and hence we can choose

\mathbf{x}_1 and \mathbf{x}_2 such that the 1, 3 part is already block diagonalised - so assume this isn't the case), then

$$-M_D M_R^{-1} M_D^T = - \begin{pmatrix} c & d & 0 \\ d & e & b \\ 0 & b & a \end{pmatrix}, \quad (5.3.13)$$

where

$$\begin{aligned} a &= \frac{\mathbf{M}_\psi^T M_R^{-1} \mathbf{M}_\psi}{N^2 \|M_d^{-1} \mathbf{M}_\psi\|^2} = \mathcal{O}\left(\frac{m_\psi^2}{m_R}\right), \\ b &= \frac{\mathbf{M}_\psi^T M_R^{-1} M_d \mathbf{x}_2}{N \|M_d^{-1} \mathbf{M}_\psi\|} = \mathcal{O}\left(\frac{m_d m_\psi}{m_R}\right), \\ c &= \mathbf{x}_1^T M_d^T M_R^{-1} M_d \mathbf{x}_1 = \mathcal{O}\left(\frac{m_d^2}{m_R}\right), \\ d &= \mathbf{x}_1^T M_d^T M_R^{-1} M_d \mathbf{x}_2 = \mathcal{O}\left(\frac{m_d^2}{m_R}\right), \\ e &= \mathbf{x}_2^T M_d^T M_R^{-1} M_d \mathbf{x}_2 = \mathcal{O}\left(\frac{m_d^2}{m_R}\right), \end{aligned} \quad (5.3.14)$$

where we have used the definitions in Equation 5.4.9 to write the leading order behaviour of these expressions assuming the hierarchy of masses $m_d \ll m_\psi \ll m_R$ mentioned above. Utilising this hierarchy further, we can apply a rotation, R_{24} , to the mass matrix in Equation 5.3.13 such that

$$\begin{aligned} -R_{24}^{-1} M_D M_R^{-1} M_D^T R_{24} &= - \begin{pmatrix} c & d & 0 \\ d & e - \frac{|b|^2}{a} & 0 \\ 0 & 0 & a + \frac{|b|^2}{a} \end{pmatrix} \\ &+ \mathcal{O}\left(\frac{m_d^3}{m_R m_\psi}\right), \end{aligned} \quad (5.3.15)$$

where

$$R_{24} = \begin{pmatrix} 1 & 0 & 0 \\ 0 & \cos \theta_{24} & \sin \theta_{24} \\ 0 & \sin \theta_{24} & \cos \theta_{24} \end{pmatrix}, \quad \theta_{24} = -\frac{|b|}{a} + \mathcal{O}\left(\frac{m_d^3}{m_\psi^3}\right). \quad (5.3.16)$$

This leaves a final 2×2 matrix to diagonalise. All elements are of the same order, and \mathbf{x}_2 is already fixed by the orthogonality constraints. A final rotation

leaves the system diagonal:

$$\begin{aligned}
-R_{23}^{-1}R_{24}^{-1}M_D M_R^{-1}M_D^T R_{24}R_{23} &= -\begin{pmatrix} m_{\nu_2} & 0 & 0 \\ 0 & m_{\nu_3} & 0 \\ 0 & 0 & m_n \end{pmatrix} \\
&+ \mathcal{O}\left(\frac{m_d^3}{m_R m_\psi}\right)
\end{aligned} \tag{5.3.17}$$

where

$$\begin{aligned}
R_{23} &= \begin{pmatrix} \cos \theta_{23} & \sin \theta_{23} & 0 \\ -\sin \theta_{23} & \cos \theta_{23} & 0 \\ 0 & 0 & 1 \end{pmatrix}, \\
\cos \theta_{23} &= \frac{\text{sign}(d)}{\sqrt{2}} \sqrt{1 - \frac{\left(c + \frac{|b|^2}{a} - e\right)}{\sqrt{\left(c + \frac{|b|^2}{a} - e\right)^2 + 4|d|^2}}}, \\
\sin \theta_{23} &= \frac{1}{\sqrt{2}} \sqrt{1 + \frac{\left(c + \frac{|b|^2}{a} - e\right)}{\sqrt{\left(c + \frac{|b|^2}{a} - e\right)^2 + 4|d|^2}}}.
\end{aligned} \tag{5.3.18}$$

The three masses, $m_{\nu_{1,2}}$ and m_n read

$$\begin{aligned}
m_{\nu_1} &= \frac{1}{2} \left(c + e - \frac{|b|^2}{a} - \sqrt{\left(c + \frac{|b|^2}{a} - e\right)^2 + 4|d|^2} \right) = \mathcal{O}\left(\frac{m_d^2}{m_R}\right), \\
m_{\nu_2} &= \frac{1}{2} \left(c + e - \frac{|b|^2}{a} + \sqrt{\left(c + \frac{|b|^2}{a} - e\right)^2 + 4|d|^2} \right) = \mathcal{O}\left(\frac{m_d^2}{m_R}\right), \\
m_n &= a + \frac{|b|^2}{a} = \mathcal{O}\left(\frac{m_\psi^2}{m_R}\right).
\end{aligned} \tag{5.3.19}$$

Summarising the above, the 7×7 unitary matrix that diagonalises the mass matrix, M , is given to leading order by

$$V = \begin{pmatrix} i & 0 & 0 \\ 0 & iI_3 & 0 \\ 0 & 0 & I_3 \end{pmatrix} PQ \begin{pmatrix} 1 & 0 & 0 \\ 0 & R_{24} & 0 \\ 0 & 0 & I_3 \end{pmatrix} \begin{pmatrix} 1 & 0 & 0 \\ 0 & R_{23} & 0 \\ 0 & 0 & I_3 \end{pmatrix} \begin{pmatrix} -i & 0 & 0 \\ 0 & -iI_3 & 0 \\ 0 & 0 & I_3 \end{pmatrix}$$

$$= (\mathbf{V}_1 \quad \mathbf{V}_2 \quad \mathbf{V}_3 \quad \mathbf{V}_4 \quad \mathbf{V}_5 \quad \mathbf{V}_6 \quad \mathbf{V}_7), \quad (5.3.20)$$

where explicitly

$$\begin{aligned} \mathbf{V}_1 &= \begin{pmatrix} -NM_d^{-1}\mathbf{M}_\psi \\ N \\ 0_{3,1} \end{pmatrix}, \\ \mathbf{V}_2 &= \begin{pmatrix} c_{23}\mathbf{x}_1 - s_{23}c_{24}\mathbf{x}_2 \\ -s_{23}s_{24}N\|M_d^{-1}\mathbf{M}_\psi\| \\ c_{23}M_R^{-1}M_d\mathbf{x}_1 + s_{23}c_{24}M_R^{-1}M_d\mathbf{x}_2 + s_{23}s_{24}\frac{M_R^{-1}\mathbf{M}_\psi}{N\|M_d^{-1}\mathbf{M}_\psi\|} \end{pmatrix}, \\ \mathbf{V}_3 &= \begin{pmatrix} s_{23}\mathbf{x}_1 + c_{23}c_{24}\mathbf{x}_2 \\ c_{23}s_{24}N\|M_d^{-1}\mathbf{M}_\psi\| \\ -s_{23}M_R^{-1}M_d\mathbf{x}_1 + c_{23}c_{24}M_R^{-1}M_d\mathbf{x}_2 + c_{23}s_{24}\frac{M_R^{-1}\mathbf{M}_\psi}{N\|M_d^{-1}\mathbf{M}_\psi\|} \end{pmatrix}, \\ \mathbf{V}_4 &= \begin{pmatrix} \frac{c_{24}NM_d^{-1}\mathbf{M}_\psi}{\|M_d^{-1}\mathbf{M}_\psi\|} - s_{24}\mathbf{x}_2 \\ c_{24}N\|M_d^{-1}\mathbf{M}_\psi\| \\ c_{24}\frac{M_R^{-1}\mathbf{M}_\psi}{N\|M_d^{-1}\mathbf{M}_\psi\|} \end{pmatrix}, \\ (\mathbf{V}_5 \quad \mathbf{V}_6 \quad \mathbf{V}_7) &= \begin{pmatrix} A \\ -i\mathbf{M}_\psi^T M_R^{-1} \\ I_3 - \frac{1}{2}M_R^{-1}M_D^T M_D M_R^{-1} \end{pmatrix}, \end{aligned} \quad (5.3.21)$$

where

$$\begin{aligned} A &= -i(\mathbf{x}_1)(M_R^{-1}M_d\mathbf{x}_1)^T - i(\mathbf{x}_2)(M_R^{-1}M_d\mathbf{x}_2)^T \\ &\quad - i\frac{(M_d^{-1}\mathbf{M}_\psi)(M_R^{-1}\mathbf{M}_\psi)^T}{\|M_d^{-1}\mathbf{M}_\psi\|^2} \end{aligned} \quad (5.3.22)$$

and $c_{23} = \cos\theta_{23}$ etc. The order of the terms in the mixing matrix V are

$$V \sim \begin{pmatrix} (U(\nu_L))^T & \frac{m_d}{m_\psi}\mathbf{U}(n\nu_L) & \frac{m_d}{m_R}(U(N\nu_L))^T \\ \frac{m_d}{m_\psi}(\mathbf{U}(\nu_\psi))^T & U(n\psi) & \frac{m_\psi}{m_R}(\mathbf{U}(N\psi))^T \\ \frac{m_d}{m_R}(U(\nu_R))^T & \frac{m_\psi}{m_R}\mathbf{U}(n\nu_R) & (U(N\nu_R))^T \end{pmatrix}, \quad (5.3.23)$$

where the U matrices tend to have $\mathcal{O}(1)$ entries. Explicitly

$$\begin{aligned}
U^{(\nu\nu)} &= \begin{pmatrix} -N (M_d^{-1} \mathbf{M}_\psi)^T \\ c_{23} \mathbf{x}_1^T - s_{23} c_{24} \mathbf{x}_2^T \\ s_{23} \mathbf{x}_1^T + c_{23} c_{24} \mathbf{x}_2^T \end{pmatrix}, \\
\frac{m_d}{m_\psi} \mathbf{U}^{(\nu\psi)} &= \begin{pmatrix} N \\ -s_{23} s_{24} N \|M_d^{-1} \mathbf{M}_\psi\| \\ c_{23} s_{24} N \|M_d^{-1} \mathbf{M}_\psi\| \end{pmatrix}, \\
\frac{m_d}{m_R} U^{(\nu\nu_R)} &= \begin{pmatrix} 0_{1,3} \\ c_{23} \mathbf{x}_1^T M_d^T M_R^{-1} + s_{23} c_{24} \mathbf{x}_2^T M_d^T M_R^{-1} + s_{23} s_{24} \frac{M_R^{-1} \mathbf{M}_\psi}{N \|M_d^{-1} \mathbf{M}_\psi\|} \\ -s_{23} \mathbf{x}_1^T M_d^T M_R^{-1} + c_{23} c_{24} \mathbf{x}_2^T M_d^T M_R^{-1} + c_{23} s_{24} \frac{M_R^{-1} \mathbf{M}_\psi}{N \|M_d^{-1} \mathbf{M}_\psi\|} \end{pmatrix}, \\
\frac{m_d}{m_\psi} \mathbf{U}^{(n\nu)} &= \frac{c_{24} N M_d^{-1} \mathbf{M}_\psi}{\|M_d^{-1} \mathbf{M}_\psi\|} - s_{24} \mathbf{x}_2, \\
U^{(n\psi)} &= c_{24} N \|M_d^{-1} \mathbf{M}_\psi\|, \quad \frac{m_\psi}{m_R} \mathbf{U}^{(n\nu_R)} = s_{24} \frac{M_R^{-1} \mathbf{M}_\psi}{N \|M_d^{-1} \mathbf{M}_\psi\|}, \\
\frac{m_d}{m_R} U^{(N\nu)} &= -i \frac{(M_R^{-1} \mathbf{M}_\psi) (M_d^{-1} \mathbf{M}_\psi)^T}{\|M_d^{-1} \mathbf{M}_\psi\|^2} \\
&\quad - i (M_R^{-1} M_d \mathbf{x}_1) (\mathbf{x}_1)^T - i (M_R^{-1} M_d \mathbf{x}_2) (\mathbf{x}_2)^T, \\
\frac{m_\psi}{m_R} \mathbf{U}^{(N\psi)} &= -i M_R^{-1} \mathbf{M}_\psi, \quad U^{(N\nu_R)} = I_3 - \frac{1}{2} M_R^{-1} M_D^T M_D M_R^{-1} \quad (5.3.24)
\end{aligned}$$

Once the three very heavy states are integrated out, the model would resemble a 3+1 model (i.e. a model with three active neutrinos plus one sterile neutrino) when only considering the neutral lepton sector alone. However, the Portalino model will have certain characteristic features when considered in the overall context of a dark matter model, with important implications for direct and indirect detection, as we shall see below. The PMNS plus mixing with Portalino matrix, once again assuming there is no contribution from the charged lepton sector, is then defined via

$$\begin{pmatrix} \nu_e \\ \nu_\mu \\ \nu_\tau \\ \psi \end{pmatrix} \approx V_{\text{PMNS}}^{4 \times 4} \begin{pmatrix} \nu_1 \\ \nu_2 \\ \nu_3 \\ n \end{pmatrix} + \text{mixing with singlet states}, \quad (5.3.25)$$

where

$$V_{\text{PMNS}}^{4 \times 4} = \begin{pmatrix} -NM_d^{-1}\mathbf{m}_n & c_{23}\mathbf{X}_1 - s_{23}c_{24}\mathbf{X}_2 & s_{23}\mathbf{X}_1 + c_{23}c_{24}\mathbf{X}_2 & \frac{c_{24}NM_d^{-1}\mathbf{m}_n}{\|M_d^{-1}\mathbf{m}_n\|} - s_{24}\mathbf{X}_2 \\ N & -s_{23}s_{24}N\|M_d^{-1}\mathbf{m}_n\| & c_{23}s_{24}N\|M_d^{-1}\mathbf{m}_n\| & c_{24}N\|M_d^{-1}\mathbf{m}_n\| \end{pmatrix}.$$

As noted in Equation 5.3.25, the neutrinos and Portalino will also have small mixings with the singlet states - for the neutrinos these will be $\mathcal{O}\left(\frac{m_d}{m_R}\right)$ and for the Portalino these will be $\mathcal{O}\left(\frac{m_n}{m_R}\right)$.

5.4 The Model

We now expand the model to include a dark matter candidate within a dark sector. This model consists of the Standard Model supplemented by a number of SM singlet fields. These include three generations of right-handed neutrino, ν_{R_α} ($\alpha = 1, 2, 3$), a complex scalar, Φ , and three Weyl fermions, ψ , X_L and X_R . The X_L , X_R fields will combine to form a Dirac fermion state and will be our DM candidate. We further introduce a new abelian gauge symmetry, $U(1)_d$, under which Φ , ψ and X_R transform each with charge 1/2.

The right-handed neutrinos, X_L , and all other Standard Model states are uncharged under the new symmetry. Additionally, X_L and X_R have the same charge under a separate \mathbb{Z}_3 symmetry, with all other states uncharged, thereby stabilising the dark matter candidate. A summary of these charges is displayed in Table 5.1.

Field	$\nu_{R\alpha}$	Φ	ψ	X_L	X_R
$U(1)_d$	0	1/2	1/2	0	1/2
\mathbb{Z}_3	1	1	1	$e^{\frac{2\pi i}{3}}$	$e^{\frac{2\pi i}{3}}$

Table 5.1: Charge assignments of the field content in the hidden sector under $U(1)_d$ and \mathbb{Z}_3 . All fields in the table are Standard Model singlets

This choice of charges avoids chiral anomalies ($\Sigma Y^3 = \Sigma Y = 0$), and forbids any additional mass terms beyond those included in the model below - in particular, a Majorana mass term $\sim X_L^T X_L$ is forbidden by the \mathbb{Z}_3 symmetry. (All fields other than X_L and ν_R carry gauge charges, and so Majorana masses for these fields would break gauge invariance.)

Given this particle content and charge assignment, the Lagrangian for the model reads

$$\begin{aligned}
\mathcal{L} = & \left(-\sqrt{2}\lambda_{\alpha\beta}^\nu L_\alpha^\dagger H \nu_{R\beta} - \sqrt{2}\lambda_\alpha^\psi \psi^\dagger \Phi \nu_{R\alpha} + \frac{i}{2} M_{R\alpha\beta} \nu_{R\alpha}^T \sigma_2 \nu_{R\beta} \right. \\
& \left. -\sqrt{2}\lambda_X X_R^\dagger \Phi X_L + \text{h.c.} \right) \\
& + \mu_H^2 |H|^2 - \lambda_H |H|^4 + \mu_\Phi^2 |\Phi|^2 - \lambda_\Phi |\Phi|^4 - \lambda_{H,\Phi} |H|^2 |\Phi|^2 + \dots, \quad (5.4.1)
\end{aligned}$$

where the ellipsis represents the Standard Model Lagrangian terms and all kinetic terms for the new states including all relevant gauge interactions with the $U(1)_d$ gauge boson, ω_μ , and we specify that $\mu_\Phi^2, \mu_H^2 > 0$. In principle, we may expect a kinetic mixing term that mixes the field strengths of the new $U(1)_d$ and the Standard Model hypercharge $U(1)_Y$. We assume for simplicity that this term is sufficiently small that it does not impact the phenomenology of the model. (Following [258], the leading contribution to the loop-induced kinetic mixing arises from a 3-loop diagram and is hence extremely suppressed.)

The form of the potential leads to the spontaneous breaking of $SU(2)_L \times U(1)_Y \rightarrow U(1)_{\text{em}}$ and $U(1)_d$ to nothing. We parameterise both Φ and H in terms of excitations, ϕ' and h' respectively, around the corresponding vacuum

expectation values, expressed in the unitary gauge as $H = \frac{1}{\sqrt{2}} \begin{pmatrix} 0 \\ v_h + h' \end{pmatrix}$ and $\Phi = \frac{1}{\sqrt{2}} (v_\phi + \phi')$, where the expectation values are given by

$$v_h^2 = \frac{2\mu_H^2\lambda_\Phi - \mu_\Phi^2\lambda_{H,\Phi}}{4\lambda_H\lambda_\Phi - \lambda_{H,\Phi}^2}, \quad v_\phi^2 = \frac{2\mu_\Phi^2\lambda_H - \mu_H^2\lambda_{H,\Phi}}{4\lambda_\Phi\lambda_H - \lambda_{H,\Phi}^2}. \quad (5.4.2)$$

The Lagrangian after spontaneous symmetry breaking reads

$$\begin{aligned} \mathcal{L} = & \left(-M_{d\alpha\beta}\nu_{l\alpha}^\dagger\nu_{R\beta} - M_{\psi\alpha}\psi^\dagger\nu_{R\alpha} + \frac{i}{2}M_{R\alpha\beta}\nu_{R\alpha}^T\sigma_2\nu_{R\beta} - m_X X_R^\dagger X_L + \text{h.c.} \right) \\ & + \left(-\lambda_{\alpha\beta}^\nu\nu_{l\alpha}^\dagger\nu_{R\beta}h' - \lambda_\alpha^\psi\psi^\dagger\phi'\nu_{R\alpha} - \lambda_X X_R^\dagger\phi'X_L + \text{h.c.} \right) - V(h', \phi') + \dots, \end{aligned} \quad (5.4.3)$$

where $M_{d\alpha\beta} = \lambda_{\alpha\beta}^\nu v_h$, $M_{\psi\alpha} = \lambda_\alpha^\psi v_\phi$, $m_X = \lambda_X v_\phi$, and where we have assumed λ_X is real. The scalar potential now reads

$$\begin{aligned} V(h', \phi') = & \lambda_H v_h^2 h'^2 + \lambda_\Phi v_\phi^2 \phi'^2 + \lambda_{H,\Phi} v_h v_\phi h' \phi' \\ & + \lambda_H v_h h'^3 + \frac{\lambda_H}{4} h'^4 + \lambda_\Phi v_\phi \phi'^3 + \frac{\lambda_\Phi}{4} \phi'^4 \\ & + \frac{\lambda_{H,\Phi} v_h}{2} h' \phi'^2 + \frac{\lambda_{H,\Phi} v_\phi}{2} h'^2 \phi' + \frac{\lambda_{H,\Phi}}{4} h'^2 \phi'^2. \end{aligned} \quad (5.4.4)$$

The ellipsis in Equation 5.4.3 again include the rest of the Standard Model Lagrangian with the addition of all the BSM kinetic terms and interactions of the states charged under $U(1)_d$ with the associated gauge boson, ω , whose mass is given by $m_\omega = (v_\phi \tilde{g})/2$ after symmetry breaking.

The scalar sector is diagonalised via the rotation defined by

$$\begin{pmatrix} h \\ \phi \end{pmatrix} = \begin{pmatrix} \cos \theta & \sin \theta \\ -\sin \theta & \cos \theta \end{pmatrix} \begin{pmatrix} h' \\ \phi' \end{pmatrix}, \quad \text{where} \quad \tan 2\theta = -\frac{\lambda_{H,\Phi} v_h v_\phi}{\lambda_\Phi v_\phi^2 - \lambda_H v_h^2}. \quad (5.4.5)$$

The couplings of the SM gauge bosons to the Higgs are very close to that predicted by the SM and consequently the mixing angle θ must be small – in the region of interest ($v_\phi \gtrsim \text{TeV}$), the limit is approximated by [116, 118]

$$|\sin \theta| \lesssim \frac{0.3}{\sqrt{1 + \log\left(\frac{m_\phi}{\text{TeV}}\right)}}. \quad (5.4.6)$$

This can be achieved by insisting $v_\phi \gg v_h$ and by assuming that the coupling $\lambda_{H,\phi}$ is moderately suppressed compared with the other dimensionless couplings in the scalar potential. Suppressing $\lambda_{H,\phi}$ also has the effect of shutting off the Higgs Portal as a channel for DM annihilation, see Section 5.7 for details. The $v_\phi \gg v_h$ hierarchy is also necessary for achieving light neutrinos with phenomenologically viable masses.

In this limit, the mass eigenstates read

$$m_h^2 = 2\lambda_H v_h^2 \left(1 - \frac{\lambda_{H,\Phi}^2}{4\lambda_\Phi \lambda_H} + \mathcal{O} \left(\left(\frac{\lambda_{H,\Phi} v_h}{\lambda_\Phi v_\phi} \right)^2 \right) \right), \quad (5.4.7)$$

$$m_\phi^2 = 2\lambda_\Phi v_\phi^2 \left(1 + \left(\frac{\lambda_{H,\Phi} v_h}{\lambda_\Phi v_\phi} \right)^2 + \mathcal{O} \left(\left(\frac{\lambda_{H,\Phi} v_h}{\lambda_\Phi v_\phi} \right)^2 \frac{\lambda_H v_h^2}{\lambda_\Phi v_\phi^2} \right) \right). \quad (5.4.8)$$

Moving to the fermionic content of the model, the first two mass mixing terms of Equation 5.4.3 encode the Portalino-like mixing, as detailed in Equation 5.1.1. The picture is necessarily complicated by the Majorana mass term for ν_R fields, and this is what leads to non-zero light neutrino masses. In this work, we do not propose a full flavour model. Instead, we assume that there are no significant hierarchies within the components of $\lambda_{\alpha\beta}^\nu$, λ_α^ψ or $M_{R\alpha}$. Under this assumption, we define

$$\lambda_{\alpha\beta}^\nu \equiv \lambda^\nu F_{\alpha\beta}^\nu \equiv \frac{m_d}{v_u} F_{\alpha\beta}^\nu, \quad \lambda_\alpha^\psi \equiv \lambda^\psi F_\alpha^\psi \equiv \frac{m_\psi}{v_\phi} F_\alpha^\psi, \quad M_{R\alpha\beta} \equiv m_R F_{R\alpha\beta} \quad (5.4.9)$$

where the parameters without indices, which we define to be real, will be used to indicate the typical size of the entries of each term leaving the precise flavour dependence to the objects labelled F .

In order to obtain the correct mass spectrum, we require that the ν_R Majorana mass is much larger than its mixing with either ψ or the active neutrinos ν_L , and that the mixing with ψ is much larger than the mixing with ν_L , that is $\lambda^\nu v_h \ll \lambda^\psi v_\phi \ll m_R$ or equivalently, $m_d \ll m_\psi \ll m_R$.

Given this hierarchy of scales, the mass matrix mixing the states ψ, ν_l and ν_R can be approximately diagonalised via the following transformations

$$\begin{aligned}
\nu_i &\sim U_{i\alpha}^{(\nu\nu_i)} \begin{pmatrix} \nu_{l\alpha} \\ i\sigma_2\nu_{l\alpha}^* \end{pmatrix} + \frac{m_d}{m_\psi} U_i^{(\nu\psi)} \begin{pmatrix} \psi \\ i\sigma_2\psi^* \end{pmatrix} + \frac{m_d}{m_R} U_{i\alpha}^{(\nu\nu_R)} \begin{pmatrix} -i\sigma_2\nu_{R\alpha}^* \\ \nu_{R\alpha} \end{pmatrix}, \\
n &\sim \frac{m_d}{m_\psi} U_\alpha^{(n\nu_i)} \begin{pmatrix} \nu_{l\alpha} \\ i\sigma_2\nu_{l\alpha}^* \end{pmatrix} + U^{(n\psi)} \begin{pmatrix} \psi \\ i\sigma_2\psi^* \end{pmatrix} + \frac{m_\psi}{m_R} U_\alpha^{(n\nu_R)} \begin{pmatrix} -i\sigma_2\nu_{R\alpha}^* \\ \nu_{R\alpha} \end{pmatrix}, \\
N_i &\sim \frac{m_d}{m_R} U_{i\alpha}^{(N\nu_i)} \begin{pmatrix} \nu_{l\alpha} \\ i\sigma_2\nu_{l\alpha}^* \end{pmatrix} + \frac{m_\psi}{m_R} U_i^{(N\psi)} \begin{pmatrix} \psi \\ i\sigma_2\psi^* \end{pmatrix} + U_{i\alpha}^{(N\nu_R)} \begin{pmatrix} -i\sigma_2\nu_{R\alpha}^* \\ \nu_{R\alpha} \end{pmatrix},
\end{aligned} \tag{5.4.10}$$

where $i, \alpha = 1, 2, 3$ and in the above the definitions in Equation 5.4.9 have been used to factor out the leading order behaviour while the various factors of U contain all the detailed flavour mixing. The explicit form of the U factors are given in the previous section, in Equation 5.3.24.

To leading order the three light neutrinos, ν_i , have masses

$$m_{\nu_1} = 0, \quad m_{\nu_{2,3}} \sim \frac{m_d^2}{m_R}, \tag{5.4.11}$$

and the three heavy neutrinos, N_i , have masses

$$m_{N_i} \sim m_R. \tag{5.4.12}$$

The field n , which we choose to call the Portalino², has a mass suppressed relative to the mass scale m_ψ given by

$$m_n \sim \frac{m_\psi^2}{m_R}. \tag{5.4.13}$$

These mass eigenstates will inherit one another's interactions due to the mixing between states, as detailed in the next Section.

²It is not entirely clear which of our states is the analogue of the Portalino from the earlier example outlined in Equation 5.1.1, where ν_R was the Portalino. It should perhaps, morally speaking, be the fields N_i that should take on the Portalino title, given that their largest component comes from the ν_R fields. We prefer however to adopt the naming conventions from neutrino mass models where the N_i s are the heavy neutrinos, the ν_i are the light neutrinos, leaving the n field which we will refer to as the Portalino.

5.5 Full Lagrangian in Mass Eigenbasis

In this Section we detail the dominant contributions to interactions in the mass eigenbasis Lagrangian. For some components, more than one term is included if the dominant contribution depends on relative sizes of couplings. The full Lagrangian in the mass eigenstate basis reads

$$\mathcal{L} = \mathcal{L}_{\text{matter-scalar}} + \mathcal{L}_{\text{gauge-matter}} + \mathcal{L}_{h-\phi},$$

where

$$\begin{aligned} \mathcal{L}_{\text{matter-scalar}} \supset & -\frac{m_d}{m_R} \cos \theta \left(\frac{U_{\alpha i}^{(\nu\nu_l)} \lambda_{\alpha\beta}^\nu U_{\beta j}^{(\nu\nu_R)}}{2} \right) \bar{\nu}_i \nu_j h \\ & - \left[\frac{m_d}{m_R} \cos \theta \left(\frac{U_\alpha^{(n\nu_l)} \lambda_{\alpha\beta}^\nu U_\beta^{(n\nu_R)}}{2} \right) \right. \\ & \quad \left. + \frac{m_\psi}{m_R} \sin \theta \left(\frac{U^{(n\psi)} \lambda_\alpha^\psi U_\alpha^{(n\nu_R)}}{2} \right) \right] \bar{n} n h \\ & - \left[\frac{m_d}{m_R} \cos \theta \left(\frac{U_{\alpha i}^{(N\nu_l)*} \lambda_{\alpha\beta}^{\nu*} U_{\beta j}^{(N\nu_R)*}}{2} \right) \right. \\ & \quad \left. + \frac{m_\psi}{m_R} \sin \theta \left(\frac{U_i^{(N\psi)*} \lambda_\alpha^{\psi*} U_{\alpha j}^{(N\nu_R)*}}{2} \right) \right] \bar{N}_i N_j h \\ & - \frac{m_\psi}{m_R} \cos \theta \left(\frac{U_{\alpha i}^{(\nu\nu_l)} \lambda_{\alpha\beta}^\nu U_\beta^{(n\nu_R)}}{2} \right) \bar{\nu}_i n h \\ & - \cos \theta \left(\frac{U_{\alpha i}^{(\nu\nu_l)} \lambda_{\alpha\beta}^\nu U_{\beta j}^{(N\nu_R)}}{2} \right) \bar{\nu}_i N_j h \\ & - \left[\frac{m_d}{m_\psi} \cos \theta \left(\frac{U_\alpha^{(n\nu_l)} \lambda_{\alpha\beta}^\nu U_{\beta i}^{(N\nu_R)}}{2} \right) \right. \\ & \quad \left. + \sin \theta \left(\frac{U^{(n\psi)} \lambda_\alpha^\psi U_{\alpha i}^{(N\nu_R)}}{2} \right) \right] \bar{n} N_i h \\ & - \left[\frac{m_d^2}{m_R m_\psi} \cos \theta \left(\frac{U_i^{(\nu\psi)} \lambda_\alpha^\psi U_{\alpha j}^{(\nu\nu_R)}}{2} \right) \right. \\ & \quad \left. - \frac{m_d}{m_R} \sin \theta \left(\frac{U_{\alpha i}^{(\nu\nu_l)} \lambda_{\alpha\beta}^\nu U_{\beta j}^{(\nu\nu_R)}}{2} \right) \right] \bar{\nu}_i \nu_j \phi \end{aligned}$$

$$\begin{aligned}
& - \frac{m_\psi}{m_R} \cos \theta \left(\frac{U^{(n\psi)} \lambda_\alpha^\psi U_\alpha^{(n\nu_R)}}{2} \right) \bar{n} n \phi \\
& - \frac{m_\psi}{m_R} \cos \theta \left(\frac{U_i^{(N\psi)*} \lambda_\alpha^{\psi*} U_{\alpha j}^{(N\nu_R)*}}{2} \right) \bar{N}_i N_j \phi \\
& - \left[\frac{m_d}{m_R} \cos \theta \left(\frac{U_i^{(\nu\psi)} \lambda_\alpha^\psi U_\alpha^{(n\nu_R)}}{2} \right) \right. \\
& \quad - \frac{m_d}{m_R} \cos \theta \left(\frac{U^{(n\psi)} \lambda_\alpha^\psi U_{\alpha i}^{(\nu' n\nu_R)}}{2} \right) \\
& \quad \left. - \frac{m_\psi}{m_R} \sin \theta \left(\frac{U_{\alpha i}^{(\nu\nu_i)} \lambda_{\alpha\beta}^\nu U_\beta^{(n\nu_R)}}{2} \right) \right] \bar{\nu}_i n \phi \\
& - \left[\frac{m_d}{m_\psi} \cos \theta \left(\frac{U_i^{(\nu\psi)} \lambda_\alpha^\psi U_{\alpha j}^{(N\nu_R)}}{2} \right) \right. \\
& \quad \left. - \sin \theta \left(\frac{U_{\alpha i}^{(\nu\nu_i)} \lambda_{\alpha\beta}^\nu U_{\beta j}^{(N\nu_R)}}{2} \right) \right] \bar{\nu}_i N_j \phi \\
& - \cos \theta \left(\frac{U^{(n\psi)} \lambda_\alpha^\psi U_{\alpha i}^{(N\nu_R)}}{2} \right) \bar{n} N_i \phi + \text{h.c.} \\
& - \lambda_X \cos \theta \bar{X} X \phi + \lambda_X \sin \theta \bar{X} X h, \tag{5.5.1}
\end{aligned}$$

$$\begin{aligned}
\mathcal{L}_{\text{gauge-matter}} \supset & \frac{g}{\sqrt{2}} \left[\left(U_{\alpha i}^{(\nu\nu_i)} \bar{\nu}_i + \frac{m_d}{m_\psi} U_\alpha^{(n\nu_i)} \bar{n} + \frac{m_d}{m_R} U_{\alpha j}^{(N\nu_i)} \bar{N}_j \right) \right. \\
& \quad \left. \times \gamma^\mu \frac{1}{2} (1 - \gamma^5) e_\alpha W_\mu^+ + \text{h.c.} \right] \\
& - \frac{\sqrt{g^2 + g'^2}}{2} \left[\left(U_{\alpha i}^{(\nu\nu_i)} \bar{\nu}_i + \frac{m_d}{m_\psi} U_\alpha^{(n\nu_i)} \bar{n} + \frac{m_d}{m_R} U_{\alpha j}^{(N\nu_i)} \bar{N}_j \right) \gamma^\mu \frac{1}{2} \gamma^5 \right. \\
& \quad \left. \times \left(U_{\alpha i}^{(\nu\nu_i)*} \nu_i + \frac{m_d}{m_\psi} U_\alpha^{(n\nu_i)*} n + \frac{m_d}{m_R} U_{\alpha j}^{(N\nu_i)*} N_j \right) Z_\mu \right] \\
& + \frac{\tilde{g}}{2} \left[\left(\frac{m_d}{m_\psi} U_i^{(\nu\psi)} \bar{\nu}_i + U^{(n\psi)} \bar{n} + \frac{m_\psi}{m_R} U_j^{(N\psi)} \bar{N}_j \right) \gamma^\mu \frac{1}{2} \gamma^5 \right. \\
& \quad \left. \times \left(\frac{m_d}{m_\psi} U_i^{(\nu\psi)*} \nu_i + U^{(n\psi)*} n + \frac{m_\psi}{m_R} U_j^{(N\psi)*} N_j \right) \omega_\mu \right] \\
& - \frac{\tilde{g}}{4} \bar{X} \gamma^\mu (1 + \gamma^5) X \omega_\mu \\
& + \left(\frac{g^2}{2} W_\mu^+ W^{-\mu} + \left(\frac{g^2 + g'^2}{4} \right) Z_\mu Z^\mu \right)
\end{aligned}$$

$$\begin{aligned}
& \times \left(\cos \theta v_h h + \frac{\cos^2 \theta}{2} h^2 - \cos \theta \sin \theta h \phi \right. \\
& \quad \left. - \sin \theta v_h \phi + \frac{\sin^2 \theta}{2} \phi^2 \right) \\
& + \frac{\tilde{g}^2}{4} \omega_\mu \omega^\mu \left(\cos \theta v_\phi \phi + \frac{\cos^2 \theta}{2} \phi^2 + \cos \theta \sin \theta h \phi \right. \\
& \quad \left. + \sin \theta v_\phi h + \frac{\sin^2 \theta}{2} h^2 \right), \tag{5.5.2}
\end{aligned}$$

and

$$\begin{aligned}
\mathcal{L}_{h-\phi} \supset & \left(\lambda_H v_h \cos \theta - \frac{\lambda_{H,\Phi} v_\phi}{2} \sin \theta \right) \cos^2 \theta h^3 + \frac{\lambda_H}{4} \cos^4 \theta h^4 \\
& + \lambda_\Phi v_\phi \cos^3 \theta \phi^3 + \frac{\lambda_\Phi}{4} \cos^4 \theta \phi^4 + \frac{\lambda_{H,\Phi} v_\phi}{2} \cos^3 \theta h^2 \phi \\
& + \left(\frac{\lambda_{H,\Phi} v_h}{2} \cos \theta - 3 \lambda_\Phi v_\phi \sin \theta + \lambda_{H,\Phi} v_\phi \sin \theta \right) \cos^2 \theta h \phi^2 \\
& + \left(\lambda_H - \frac{\lambda_{H,\Phi}}{2} \right) \cos^3 \theta \sin \theta h^3 \phi + \frac{\lambda_{H,\Phi}}{4} \cos^4 \theta h^2 \phi^2 \\
& - \left(\lambda_\Phi - \frac{\lambda_{H,\Phi}}{2} \right) \cos^3 \theta \sin \theta h \phi^3. \tag{5.5.3}
\end{aligned}$$

5.6 Reconstructing the PMNS Matrix

In Section 5.3 the full masses and mixings of the $(\nu_{l\alpha}, \psi, \nu_{R\alpha})$ system were calculated and presented as approximate analytic expressions following the hierarchy in masses scales $m_d \ll m_\psi \ll m_R$. As stated above, we are assuming that there are no significant hierarchies between the flavours of the individual masses.

Due to the additional states mixing with the left-handed neutrinos, the PMNS matrix will no longer be unitary. Assuming no mixing in the charged lepton sector, the PMNS matrix is determined by the mixing in the extended neutrino sector only. The allowed 3σ ranges on the entries of the PMNS matrix (once the assumption of unitary is dropped) are [259]

$$|V| = \begin{pmatrix} 0.76 \rightarrow 0.85 & 0.50 \rightarrow 0.60 & 0.13 \rightarrow 0.16 \\ 0.21 \rightarrow 0.54 & 0.42 \rightarrow 0.70 & 0.61 \rightarrow 0.79 \\ 0.18 \rightarrow 0.58 & 0.38 \rightarrow 0.72 & 0.40 \rightarrow 0.78 \end{pmatrix}. \quad (5.6.1)$$

In addition to the constraints on the mixing, the masses of the light neutrinos must fall within the following ranges (the lightest neutrino is massless in this model) – assuming normal ordering [260]:

$$m_2 \in [8.2 \text{ meV}, 9.0 \text{ meV}], m_3 \in [49.0 \text{ meV}, 50.9 \text{ meV}]. \quad (5.6.2)$$

A flavour model for the structure of $\lambda^\nu, \lambda^\psi$ and M_R is beyond the scope of this work, and without such a model the task of finding values for the components of these matrices that satisfy the mixing and mass constraints is an under-constrained problem. However, for interest, we briefly present a simple form of the mass matrices $M_{d\alpha\beta}$ and $M_{\psi\alpha}$ which can lead to a good approximation of the observed neutrino mixing.

5.6.1 Tri-Bi-Maximal Mixing

Neutrino mixing can be reasonably well approximated as a deviation from tri-bi-maximal mixing, which is given by [261]

$$U_{\text{TBM}} = \begin{pmatrix} \sqrt{\frac{2}{3}} & \frac{1}{\sqrt{3}} & 0 \\ -\frac{1}{\sqrt{6}} & \frac{1}{\sqrt{3}} & \frac{1}{\sqrt{2}} \\ \frac{1}{\sqrt{6}} & -\frac{1}{\sqrt{3}} & \frac{1}{\sqrt{2}} \end{pmatrix}. \quad (5.6.3)$$

This can be obtained if M_d takes the following form

$$M_d = (\alpha \mathbf{M}_\psi \quad \mathbf{M}_d \quad \alpha \mathbf{M}_\psi + \mathbf{M}_d). \quad (5.6.4)$$

where $\alpha = \mathcal{O}\left(\frac{m_d}{m_n}\right)$, and \mathbf{M}_ψ and \mathbf{M}_d are otherwise unconstrained. This also has the side effect of introducing an additional massless neutrino-like state,

due to the additional linear dependence in the mass matrix (as discussed in Section 5.2). However, this isn't a problem, as tri-bi-maximal mixing is only an approximation of the actual neutrino mixing, and so some perturbation from this structure is required. These perturbations will also restore a non-zero (but possibly suppressed – c.f. Equation 5.6.2) mass to the second neutrino.

5.7 Dark Matter Abundance

We move now to the DM phenomenology of this model. In our numerical analysis below, we have used micrOMEGAs [262] to compute the freeze-out abundance for a range of parameter values. We can eliminate a number of parameters in favour of the measured values of the Higgs mass, m_h , and the masses of the Standard Model gauge bosons. The DM phenomenology is not sensitive to the relative sizes of the neutrino masses and mixings. In order to ensure that we consider parameter values that can reproduce light neutrino masses, we set $(\frac{m_d}{m_\psi})^2 m_n = 20 \text{ meV}$ in order to fix λ_ν . This mass sets the scale for the light neutrinos, the precise masses and mixings are determined by other flavour parameters that do not play a leading role in the determination of the DM abundance. In order to numerically calculate the DM abundance we do need to input some structure by hand, and we assume a simple parameterised form of the components of the full 7×7 neutrino mixing matrix, which is as follows:

$$\begin{aligned}
 U^{(\nu\nu_l)} &= \sqrt{\left(1 - \left(\frac{m_d}{m_\psi}\right)^2\right) \left(1 - \left(\frac{m_\psi}{m_R}\right)^2\right)} N_{\text{PMNS}}^\dagger, \\
 \mathbf{U}^{(\nu\psi)} &= \frac{1}{\sqrt{3}} \begin{pmatrix} 1 \\ 1 \\ 1 \end{pmatrix} \eta, \\
 U^{(\nu\nu_R)} &= \frac{1}{\sqrt{3}} \begin{pmatrix} 1 & 1 & 1 \\ 1 & 1 & 1 \\ 1 & 1 & 1 \end{pmatrix}, \quad \mathbf{U}^{(n\nu_l)} = \frac{1}{\sqrt{3}} \begin{pmatrix} 1 \\ 1 \\ 1 \end{pmatrix} \eta,
 \end{aligned}$$

$$\begin{aligned}
U^{(m_\psi)} &= \sqrt{\left(1 - \left(\frac{m_d}{m_\psi}\right)^2\right) \left(1 - \left(\frac{m_\psi}{m_R}\right)^2\right)}, & \mathbf{U}^{(n\nu_R)} &= \frac{1}{\sqrt{3}} \begin{pmatrix} 1 \\ 1 \\ 1 \end{pmatrix}, \\
U^{(N\nu_l)} &= \frac{1}{\sqrt{3}} \begin{pmatrix} 1 & 1 & 1 \\ 1 & 1 & 1 \\ 1 & 1 & 1 \end{pmatrix}, & \mathbf{U}^{(N\psi)} &= \frac{1}{\sqrt{3}} \begin{pmatrix} 1 \\ 1 \\ 1 \end{pmatrix}, \\
U^{(N\nu_R)} &= \sqrt{\left(1 - \left(\frac{m_d}{m_\psi}\right)^2\right) \left(1 - \left(\frac{m_\psi}{m_R}\right)^2\right)} I_3,
\end{aligned}$$

where N_{PMNS} is the experimentally observed PMNS matrix [101], and η parameterises our ignorance of the underlying flavour structure – the mixing between the Portalino and neutrinos can vary from the first order approximations described by Equation 5.4.10 depending on the underlying flavour parameters. To account for this in a simplified manner, we include an overall scaling parameter η in all of the Portalino-neutrino mixings and neglect any further details of the flavour structure, as they do not have a significant impact on the phenomenology of the model.

The remaining relevant masses and couplings are determined, at least to leading order, by seven parameters: v_ϕ , λ_ψ , λ_Φ , $\lambda_{H,\Phi}$, m_n , \tilde{g} , and m_X .

In the left-hand panel of Figure 5.1 we demonstrate how the DM abundance behaves as a function of the DM mass, m_X , with other parameters fixed at $v_\phi = 2 \text{ TeV}$, $m_n = 100 \text{ keV}$, $\lambda_\psi = 1$, $\tilde{g} = 1$, $\lambda_\Phi = 1$, $\lambda_{H,\Phi} = 0.1$ (unless stated otherwise these are the parameter values used in all plots in this section).

The horizontal dotted line in Figure 5.1 indicates the observed DM abundance. In the middle and right-hand panel of Figure 5.1 we show the absolute and relative contributions of different DM annihilation channels to $(\Omega h^2)^{-1}$ respectively.

For $m_X < m_\omega$ the dominant annihilation process is $X\bar{X} \rightarrow nn$, which proceeds via s-channel exchange of the hidden sector gauge boson, ω . For $m_X > m_\omega$, DM annihilation into pairs of ω gauge bosons is kinetically possible and becomes the dominant channel for $m_X \sim m_\phi/2$ and above.

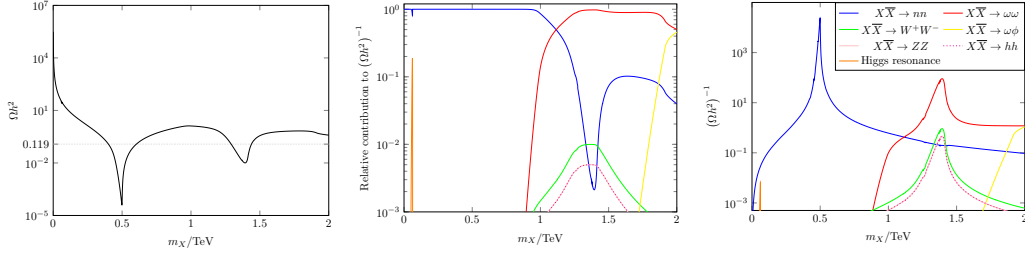


Figure 5.1: **Left:** DM abundance against m_X , for $v_\phi = 2 \text{ TeV}$, $m_n = 100 \text{ keV}$, $\lambda_\psi = 1$, $\tilde{g} = 1$, $\lambda_\Phi = 1$, $\lambda_{H,\Phi} = 0.1$. The horizontal dotted line indicates the observed DM abundance. The first trough corresponds to the ω s-channel resonance at $m_X \approx m_\omega/2$ ($m_\omega = \frac{\tilde{g}}{2}v_\phi = 1 \text{ TeV}$) and the second, shallower, trough corresponds to the ϕ s-channel resonance at $m_X \approx m_\phi/2$ ($m_\phi = \sqrt{2\lambda_\phi}v_\phi \approx 2.8 \text{ TeV}$). **Middle (Right):** Relative (absolute) contributions of each channel to $(\Omega h^2)^{-1}$. The line labelled ‘Higgs Resonance’ includes several channels which are only significant near the h resonance at $m_X \approx m_h/2$. These are dominated by $X\bar{X} \rightarrow b\bar{b}$; the next largest contributions come from $X\bar{X} \rightarrow GG$, $X\bar{X} \rightarrow \tau^+\tau^-$ and $X\bar{X} \rightarrow c\bar{c}$.

These annihilation cross-sections expanded in powers of relative velocity, v , read

$$\sigma(X\bar{X} \rightarrow nn)v \approx \frac{\tilde{g}^4 m_X^2 |U^{n\psi}|^4}{128\pi \left[(4m_X^2 - m_\omega^2)^2 + \Gamma_\omega^2 m_\omega^2 \right]} \quad (5.7.1)$$

$$\begin{aligned} \sigma(X\bar{X} \rightarrow \omega\omega)v &\approx \frac{\tilde{g}^4 (m_X^2 - m_\omega^2)^{3/2}}{256\pi m_\omega^2 m_X (2m_X^2 - m_\omega^2)} + \frac{v^2 \tilde{g}^2 F(m_X, m_\omega, \tilde{g}, \lambda_X, \theta)}{\left[(4m_X^2 - m_\phi^2)^2 + m_\phi^2 \Gamma_\phi^2 \right]} \\ &\equiv \frac{\tilde{g}^4 (m_X^2 - m_\omega^2)^{3/2}}{256\pi m_\omega^2 m_X (2m_X^2 - m_\omega^2)} \\ &\quad + \frac{v^2 \tilde{g}^2 \sqrt{m_X^2 - m_\omega^2}}{6144\pi m_X \left[(4m_X^2 - m_\phi^2)^2 + m_\phi^2 \Gamma_\phi^2 \right] (m_\omega^3 - 2m_\omega m_X^2)^4} \\ &\quad \times \left[2K_1 \lambda_X m_\omega (m_\omega^2 - 2m_X^2)^2 + 18K_2 \lambda_X^2 m_\omega^2 (m_\omega^2 - 2m_X^2)^4 \right. \\ &\quad \left. + \tilde{g}^2 K_4 \left((m_\phi^2 - 4m_X^2)^2 + m_\phi^2 \Gamma_\phi^2 \right) \right. \\ &\quad \left. + 8K_3 \tilde{g} \lambda_X m_\omega m_X (m_\phi^2 - 4m_X^2) (m_\omega^2 - 2m_X^2)^2 \right], \quad (5.7.2) \end{aligned}$$

where Γ_ω and Γ_ϕ are the total decay width of ω and ϕ respectively and

$$\begin{aligned}
K_1 &= 3K_2\lambda_X(4\cos 2\theta + \cos 4\theta)m_\omega(m_\omega^2 - 2m_X^2)^2 \\
&\quad + 4K_3\cos 2\theta\tilde{g}m_X(m_\phi^2 - 4m_X^2) \\
K_2 &= 4m_X^4 - 4m_\omega^2m_X^2 + 3m_\omega^4, \\
K_3 &= 10m_\omega^4m_X^2 - 24m_\omega^2m_X^4 + m_\omega^6 + 16m_X^6, \\
K_4 &= 3m_\omega^8m_X^2 - 84m_\omega^6m_X^4 + 152m_\omega^4m_X^6 \\
&\quad - 80m_\omega^2m_X^8 + 7m_\omega^{10} + 32m_X^{10}.
\end{aligned} \tag{5.7.3}$$

The $\mathcal{O}(v^2)$ term in Equation 5.7.2 includes the s-channel diagram with ϕ in the intermediate state, that, although p -wave, will dominate the $\sigma(X\bar{X} \rightarrow \omega\omega)$ around $m_X \sim m_\phi/2$. The s-wave term in Equation 5.7.2 comes from a diagram with X in the t-channel.

Looking more closely at the left panel in Figure 5.1, the structure of the plot is dominated by two resonances, one in each of the channels described above: the first with an on-shell ω in the s-channel appearing at $m_X \sim m_\omega/2$, and the second with an on-shell ϕ appearing at $m_X \sim m_\phi/2$.

The middle and right panels of Figure 5.1 demonstrate over what mass range the two processes dominantly contribute to the determination of the DM abundance. In the middle panel, we plot the relative contributions of all channels with more than a 1% contribution, and it is clear that the hidden sector/Portalino only channels dominate.

There are some contributions from SM model channels, all of which are enabled by the Higgs Portal via the mixing between the SM Higgs and hidden sector ϕ . For example, contributions from the W^+W^- , ZZ , hh final state channels are present due to resonant s-channel exchange of the ϕ field. The size of these SM channel contributions is ultimately controlled by the parameter $\lambda_{H,\phi}$. Suppressing this parameter or even setting it to zero shuts off the Higgs Portal and removes the contributions from the SM channels in Figure 5.1. On one hand, this may be desirable as it means the DM abundance is determined

entirely by hidden sector/Portalino physics. The usually close link in freeze-out models between the annihilation process determining the abundance and the predicted signal rate in direct and indirect DM detection experiments is then decoupled. There are however still potential constraints on this model from the phenomenology of the Portalinos described in Section 5.8 and potential signals from indirect detection described in Section 5.7.2.

Conversely, if the Higgs Portal is activated by increasing the size of $\lambda_{H,\phi}$ the role of the SM states in both generating the DM abundance (mainly around the ϕ resonance) and in constraining the model become more important and can lead to interesting signals, for example in indirect detection signals where the DM states are annihilating to SM final states. These processes are however p-wave and therefore velocity suppressed and do not trouble current limits.

For sufficiently large masses, the process $X\bar{X} \rightarrow \phi\omega$ can play a role, with a modest dip in the abundance towards $m_X \sim 2$ TeV. At smaller masses, the Higgs s-channel resonance can also contribute but only in a very narrow range, as can be seen in the middle panel of Figure 5.1. This latter channel is again only present due to the Higgs Portal and will be reduced if $\lambda_{H,\phi}$ is further suppressed below the value of 0.1 used here.

In Figure 5.2, we demonstrate the dependence of the DM abundance on \tilde{g} (left panel) and λ_ϕ (right panel). In particular, we examine the way in which these parameters determine the position and shape of the troughs in the abundance. With reference to the left panel, \tilde{g} modifies the abundance in three ways. For $m_X < 1.25$ TeV, the process $X\bar{X} \rightarrow nn$ dominates the determination of the abundance. With the cross-section for this process going as $\sim \tilde{g}^4$, reducing the value of \tilde{g} increases the abundance, which can be seen in the left panel of Figure 5.2.

A second variation arises due to the fact that the value of \tilde{g} determines the mass of the vector boson ω for fixed v_ϕ and hence shifts the position of the resonance in m_X and in turn shifts where the trough appears in the abundance.

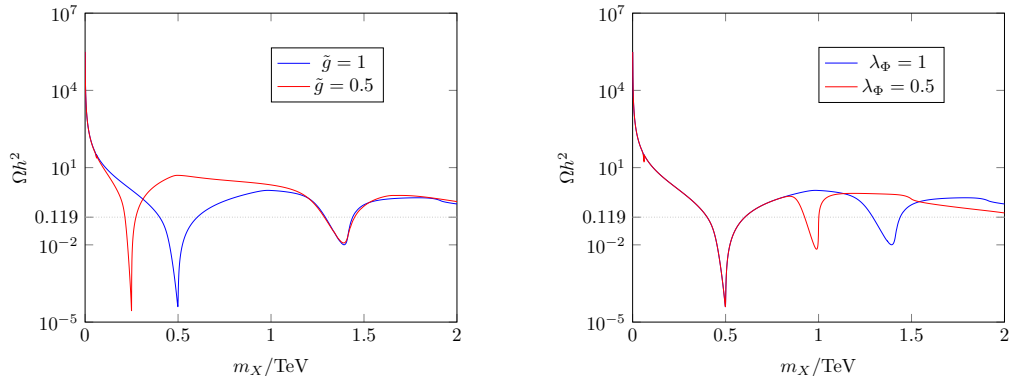


Figure 5.2: DM abundance against m_X for different values of \tilde{g} (left panel) and λ_Φ (right panel). Apart from the values of \tilde{g} and λ_Φ indicated in the plots, both panels display results for parameter values as stated for the left panel of Figure 5.1. The effect of varying the values of both these parameters is seen in the position and shape of the troughs in the DM abundance (see text for details).

Decreasing the value of \tilde{g} therefore shifts the trough in the abundance to lower DM masses.

Finally, the width of the trough/resonance depends on \tilde{g} via the decay rate of ω . A smaller value of \tilde{g} decreases Γ_ω producing a more narrow trough/resonance. The second trough remains largely unchanged.

In the right panel of Figure 5.2, the dependence of the DM abundance on λ_Φ is demonstrated. The first trough is unchanged as this is dominantly determined by the nn final state channel, but the decrease in λ_Φ shifts the second trough to lower m_X due to the decrease in m_ϕ . The width of the ϕ resonance/trough is narrower for smaller λ_X .

We note that the modest dip in the abundance at large m_X is no longer visible in the left panel of Figure 5.2 when \tilde{g} is decreased. The reason is that the $X\bar{X} \rightarrow \omega\omega$ annihilation process will dominate in this mass range due to having a dominant contribution that goes like $\tilde{g}^2\lambda_X$ compared with the leading contribution for the $\omega\phi$ channel, which goes like \tilde{g}^4 . In the left panel of Figure 5.2 however, the dip is clearly visible and appears at a lower value of m_X for $\lambda_\Phi = 0.5$ owing to the reduced value of m_ϕ .

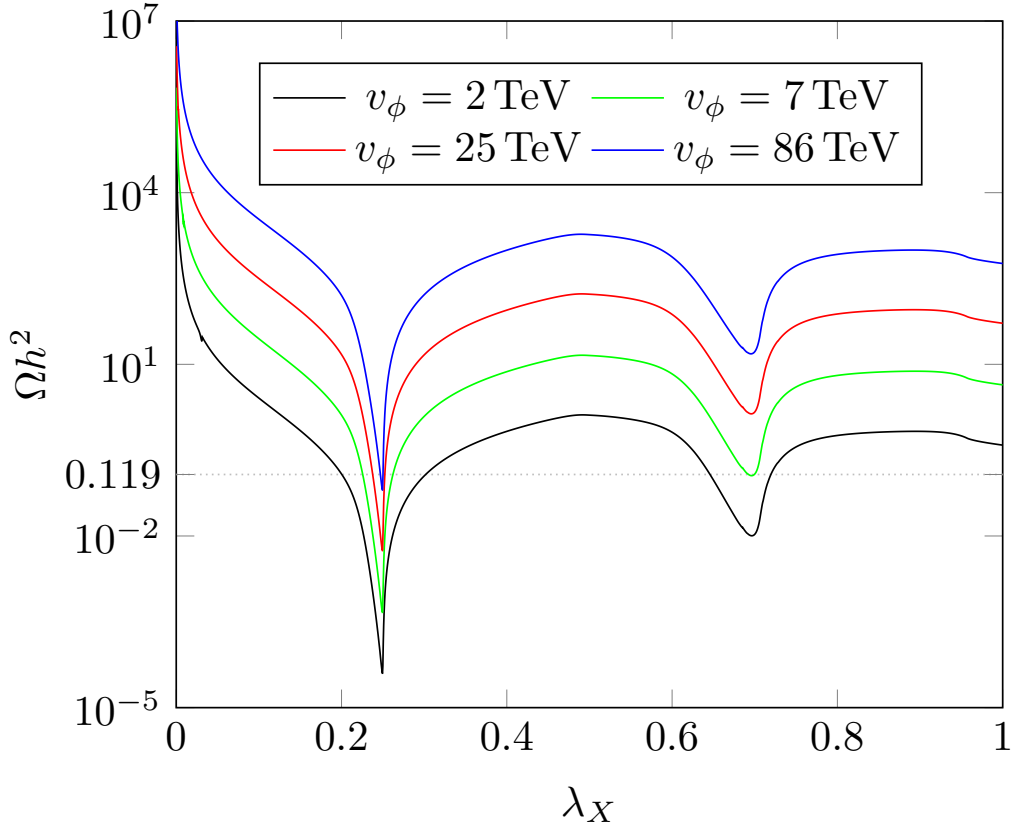


Figure 5.3: DM abundance against λ_X for different values of v_ϕ . All other parameters are fixed at the values stated in Figure 5.1. As can be seen, the abundance scales as approximately v_ϕ^2 . This sets an upper bound $v_\phi \lesssim 100$ TeV, above which the correct relic abundance can no longer be produced.

For fixed $\tilde{g}, \lambda_X, \lambda_\psi$, increasing v_ϕ increases the masses of the hidden sector states. The DM abundance can still be generated, but only via the peak in the resonant nn annihilation channel. This is shown in Figure 5.3.

Finally, we summarise the dependence on the remaining free parameters. For fixed v_ϕ the DM abundance doesn't depend on $\lambda_\nu, \lambda^\psi$ or m_n , as can be seen from Equations 5.7.1. There is a degeneracy in these parameters, whereby a change in one can be compensated by another with no effect on the DM abundance. In Section 5.8, however, we show that there are constraints on the Portalino that constrain these parameters of the model.

In summary, we have shown that it is relatively straightforward to reconstruct the correct DM abundance in this model with the X states freezing-out dominantly via the annihilation channels: $X\bar{X} \rightarrow nn$ and $X\bar{X} \rightarrow \omega\omega$. There is an important question, however, about the fate of the Portalino, n , states. It is expected that there is a significant number density of these states left after the DM states have frozen-out and all other dark sector states have decayed. The Portalino states are unstable with long lifetimes and may potentially disrupt, for example, Big Bang Nucleosynthesis (BBN) or the Cosmic Microwave Background Radiation (CMBR) as they decay to SM particles. Constraints coming from the Portalino phenomenology are discussed in the Section 5.8.

5.7.1 Direct Detection

Direct DM detection signals can be generated if the Higgs portal is active, that is, if the parameter $\lambda_{H,\Phi}$ is non-zero. The dominant contribution to the direct detection signal comes from Higgs exchange with scattering cross-section per nucleon approximately given by [143]

$$\sigma \sim \frac{m_r^2}{2\pi} \left(\frac{\lambda_X \sin 2\theta}{v_h m_h^2} \right)^2 f_p^2, \quad (5.7.4)$$

where m_r is the reduced mass of the DM-proton given by $m_r = m_X m_p / (m_X + m_p)$ and we have assumed that the interactions with protons and neutrons are the same with

$$f_p = m_p \left[\sum_{u,d,s} f_{T_q} + \frac{6}{27} f_{T_G} \right] \sim 0.30 m_p, \quad (5.7.5)$$

where, following [156], we have used $(f_{T_u}, f_{T_d}, f_{T_s}, f_{T_G}) = (0.018, 0.027, 0.037, 0.917)$.

Assuming a small mixing angle θ and applying $\lambda_\Phi v_\phi^2 \gg \lambda_H v_h^2$ to $\tan(2\theta)$ in Equation 5.4.5, we find

$$\sigma \sim 5 \times 10^{-46} \text{ cm}^{-2} \left(\frac{\lambda_{H,\Phi}}{0.1} \right)^2 \left(\frac{2 \text{ TeV}}{v_\phi} \right)^4 \left(\frac{m_X}{2 \text{ TeV}} \right)^2 \left(\frac{1}{\lambda_\Phi} \right)^2. \quad (5.7.6)$$

This value is just below the constraint from LUX-ZEPLIN (LZ), [146], at 2 TeV. For smaller values of m_X , the direct detection limit decreases linearly with decreasing mass (until around 30 GeV where it flattens off) in contrast, the predicted cross-section from Equation 5.7.6 with fixed values of $\lambda_{H,\Phi}$, v_ϕ and λ_Φ decreases with m_X^2 . As a result, masses below 2 TeV are allowed for $\lambda_{H,\Phi}$, v_ϕ and λ_Φ fixed at values from Equation 5.7.6.

To get a more general understanding of the direct detection limits, Equation 5.7.6 can be compared to a linear approximation of the LZ bound (which holds for $m_X \gtrsim 40$ GeV) and reads

$$\sigma_{\max} \sim 5.5 \times 10^{-46} \text{ cm}^{-2} \left(\frac{m_X}{2 \text{ TeV}} \right). \quad (5.7.7)$$

Using this, we can write

$$m_X \lesssim 2.2 \text{ TeV} \left(\frac{0.1}{\lambda_{H,\Phi}} \right)^2 \left(\frac{v_\phi}{2 \text{ TeV}} \right)^4 \left(\frac{\lambda_\Phi}{1} \right)^2. \quad (5.7.8)$$

Focusing now on parameter values where the observed DM abundance is correctly reproduced in the model, it is clear from Figure 5.1 that we need to be near one of the troughs corresponding to the ω or ϕ resonances. These occur at $m_X = m_\omega/2$ and $m_X = m_\phi/2$ respectively, or equivalently at $m_X/v_\phi = \tilde{g}/2$ and $m_X/v_\phi = \sqrt{\lambda_\phi/2}$. Comparing these to Equation 5.7.8, the troughs will be allowed by direct detection limits if

$$\lambda_{H,\Phi} \lesssim 0.15 \lambda_\Phi \tilde{g}^{-1/2} \left(\frac{v_\phi}{2 \text{ TeV}} \right)^{\frac{3}{2}} \quad (\omega \text{ resonance}), \quad (5.7.9)$$

$$\lambda_{H,\Phi} \lesssim 0.12 \lambda_\Phi^{3/4} \left(\frac{v_\phi}{2 \text{ TeV}} \right)^{\frac{3}{2}} \quad (\phi \text{ resonance}). \quad (5.7.10)$$

In summary, direct detection can play a role in limiting the allowed parameter space of the model, but it is always possible to suppress the predicted signal by reducing the size of $\lambda_{H,\Phi}$. Reducing this parameter has no significant impact on whether the correct abundance can be achieved.

5.7.2 Indirect Detection

As outlined above, there are two DM mass regions of interest corresponding to resonant annihilation processes in which the model can generate the observed DM relic abundance. For DM masses around $m_\omega/2$ the resonant annihilation into nn pairs dominates and for masses around $m_\phi/2$ the resonant annihilation into $\omega\omega$ pairs dominates.

The ω states decay quickly into nn pairs and as a result for DM states with masses around the ϕ resonance, DM annihilation results in the production of four high energy n states.

Portalinos can decay via virtual SM gauge bosons as $n \rightarrow \nu_i Z$ or $l^- W^+$, with the Z and W decaying either hadronically or leptonically and can therefore lead to indirect DM signals. The mean lifetime of the Portalinos can be long (see Section 5.8) and may travel significant distances before decaying.

Resonant DM annihilation into nn final states is an s-wave process and is therefore DM velocity independent. This means that the DM annihilation rate in the Galactic centre or Dwarf Spheroidal galaxies will be the same as that during freeze-out.

Indirect detection limits on Gamma rays from annihilation in the DM mass range we consider here are currently at least an order of magnitude away from the typical freeze-out value, see for example [186] and [187] for the scenario where DM dominantly annihilates into τ or b pairs, which best matches (in a very conservative way) the case where the Portalinos produced in the DM annihilations can decay leptonically or hadronically respectively.

For neutrinos final states, the limits from IceCube [191] and ANTARES [193] are again at least an order of magnitude above the typical value required for successful freeze-out and so do not constrain the model.

The projected limits from [188] will potentially probe this model. A dedicated study of the detailed indirect detection signal rates is required to understand this in detail, but is beyond the scope of this work.

Now moving to the DM mass range where the ϕ resonance dominates, the resonant part of the annihilation cross-section to $\omega\omega$ is p-wave and with the velocity in astrophysical environments, such as the galactic centre, at $v \sim 10^{-3}$ (or lower in Dwarf Spheroidal Galaxies), the indirect detection signals coming from such a process will be velocity suppressed and hence play no role in constraining this mass region.

There is an s-wave contribution to the $\omega\omega$ channel, but this is not resonant with an annihilation rate well below the “standard” freeze-out result and as such does not lead to tensions with indirect detection.

For the lighter Portalino case, it will be the Portalinos themselves that can travel all the way to the Earth. Neutrino search experiments potentially be capable of detecting Portalinos e.g. IceCube [191] and ANTARES [193], but with reduced sensitivity as the Portalinos will have a coupling to the SM suppressed by $\sqrt{m_\nu/m_n}$ compared with neutrino interactions and for light Portalinos of around an eV this ratio is $\sim 10^{-2}$, although even lighter Portalinos could increase this to order one. One interesting feature is that these Portalino states will be highly boosted particles and will be mono-energetic in the case of DM annihilations to nn pairs, the energy of each Portalino being equal to the DM mass, which in our model means they are produced with TeV energies providing an intriguing target for neutrino telescopes.

5.8 Portalino Phenomenology

The Portalino mass and dark sector masses are all related to v_ϕ and so the scale of the Portalino mass can be linked to the dark sector masses. In particular, the mass of the DM particle X can be written in terms of the Portalino mass

as

$$\begin{aligned}
m_X &= \lambda_X v_\phi = \left(\frac{\lambda^\nu \lambda_X}{\lambda^\psi} \right) \left(\frac{m_n}{m_\nu} \right)^{\frac{1}{2}} v_h \\
&\approx 500 \text{ GeV} \left(\frac{\lambda_X}{0.25} \right) \left(\frac{m_n}{\text{GeV}} \right)^{\frac{1}{2}} \left(\frac{1}{\lambda^\psi} \right) \left(\frac{\lambda^\nu}{3.6 \times 10^{-5}} \right). \tag{5.8.1}
\end{aligned}$$

Comparing with Figure 5.1, the correct DM abundance can be produced even in scenarios with a relatively heavy Portalino. Note though that this does require a relatively small value of λ_ν . This is due to the fact that increasing the Portalino mass m_n in Equation 5.4.13 while holding v_ϕ (m_ψ) constant is only possible via decreasing the Majorana mass m_R . In turn, a decrease in m_R necessitates a smaller value of λ_ν in order to obtain the correct neutrino mass scale in Equation 5.4.11.

Beyond the phenomenological role Portalinos play in indirect detection, their presence in the Early Universe may also lead to significant constraints due to their potentially very long lifetime. The decay modes for the Portalino are to: SM neutrinos; a neutrino plus neutral meson; a neutrino plus charged lepton pair; or a charged lepton plus charged meson, the first two via a SM Z boson and the latter two via the SM W^\pm .

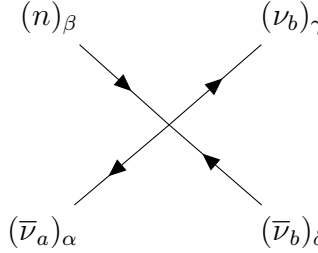
5.8.1 Portalino Decays

The lifetime of the Portalino can be parameterised as

$$\tau_n = \frac{2048\pi^3 C(m_n)}{5\eta^2 G_F^2 m_\nu} \frac{1}{m_n^4} \approx \eta^{-2} C(m_n) \left(\frac{\text{GeV}}{m_n} \right)^4 3 \text{ s}, \tag{5.8.2}$$

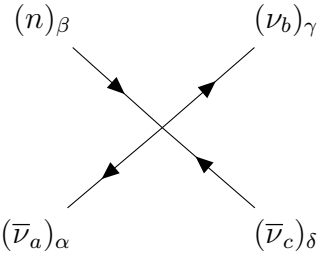
where $C(m_n)$ accounts for the different decay modes possible for a given mass m_n . The value of $C(m_n)$ ranges from ~ 1 for $m_n < 2m_e$ to ~ 0.01 for a Portalino mass just below the W^\pm mass. As discussed above, the factor of η parameterises our ignorance of the underlying flavour model. The decay width is calculated in calcHEP, but we can calculate an approximate lifetime

for $m_n < 2m_e$, in which case the only decay channel at tree-level is $n \rightarrow 3\nu$ [263]. The partial width can then be calculated in the effective field theory with W^\pm, Z integrated out, so that this process is characterised by the vertex



$$= -\frac{G_F \eta}{4\sqrt{2}} \left(\frac{m_\nu}{m_n}\right)^{\frac{1}{2}} [\gamma^\mu \gamma^5]_{\alpha\beta} [\gamma_\mu \gamma^5]_{\gamma\delta}. \quad (5.8.3)$$

Note that two of the neutrinos are of the same type (ν_b) – if you have three distinct neutrinos, the vertex is suppressed by an additional factor of $\left(\frac{m_\nu}{m_n}\right)$. This is because the general vertex is



$$= -\frac{G_F \eta}{4\sqrt{2}} (U^\dagger)_{al_1} U_{l_1 n} (U^\dagger)_{bl_2} U_{l_2 c} [\gamma^\mu \gamma^5]_{\alpha\beta} [\gamma_\mu \gamma^5]_{\gamma\delta}, \quad (5.8.4)$$

(where $l_1, l_2 = 1, 2, 3$ - corresponding to e, μ, τ). To evaluate the $(U^\dagger)_{al_1} U_{l_1 n} (U^\dagger)_{bl_2} U_{l_2 c}$ factor, we use the unitarity of U :

$$(U^\dagger)_{il} U_{lj} = (U^\dagger U)_{ij} - (U^\dagger)_{iD} U_{Dj} = \delta_{ij} - (U^\dagger)_{iD} U_{Dj} \quad (5.8.5)$$

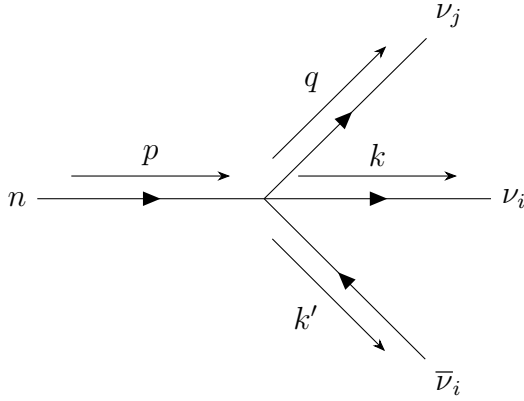
where $D = 4, 5, 6, 7$ corresponds to the dark/BSM particles (the Portalino and 3 heavy singlets). Using the fact that the neutrino mixing with the Portalino is suppressed ($V \sim \eta \left(\frac{m_\nu}{m_n}\right)^{\frac{1}{2}}$), and that the Portalino mixing with itself is approximately 1, this means that

$$(U^\dagger)_{bl_2} U_{l_2c} = \delta_{bc} + \mathcal{O}\left(\frac{m_\nu}{m_n}\right), \quad (5.8.6)$$

and

$$(U^\dagger)_{al_1} U_{l_1n} \approx \left(\frac{m_\nu}{m_n}\right)^{\frac{1}{2}}, \quad (5.8.7)$$

which means that any vertex with three distinct neutrinos is suppressed by an additional factor of $\left(\frac{m_\nu}{m_n}\right)$, as stated above.



The matrix element for $n \rightarrow \nu_j \bar{\nu}_i \nu_i$ is given by

$$M_{ij} = -\frac{G_F}{2\sqrt{2}} \left(\frac{m_\nu}{m_n}\right)^{\frac{1}{2}} \eta (1 + 2\delta_{ij}) \bar{u}_{\nu_j} \gamma^\mu \gamma^5 u_n \bar{u}_{\nu_i} \gamma_\mu \gamma^5 v_{\nu_i}. \quad (5.8.8)$$

Hence, the spin averaged amplitude squared is given by

$$\frac{1}{2} \Sigma |M|^2 = 2\eta^2 G_F^2 \left(\frac{m_\nu}{m_n}\right) (1 + 2\delta_{ij})^2 [(k \cdot q)(k' \cdot p) + (k' \cdot q)(k \cdot p)], \quad (5.8.9)$$

where the momenta are as labelled above, which gives a partial decay rate

$$\Gamma_{ij} = \frac{\eta^2 G_F^2 (1 + 2\delta_{ij}) m_\nu}{6048\pi^3} m_n^4. \quad (5.8.10)$$

If these are the only decay channels (i.e. for $m_n < 2m_e$), then the lifetime is given by

$$\tau = \frac{2048\pi^3\hbar}{5\eta^2 G_F^2 m_\nu} \frac{1}{m_n^4} \approx \eta^{-2} \left(\frac{\text{GeV}}{m_n} \right)^4 3 \text{ s}. \quad (5.8.11)$$

The important thing to note is that these decays are cosmologically important, as any decays into the neutrino or photon sector which occur after neutrino decoupling affect the neutrino-photon temperature ratio (and hence N_{eff}).

Any Portalino decays to neutrinos that occur before BBN or recombination, but after neutrino decoupling, would affect N_{eff} at these times, and such a change is tightly constrained [22, 1]. These constraints leave us with two options: the Portalinos must decay before neutrino decoupling, or after recombination. This latter possibility can be further split into two scenarios: one in which the Portalinos decay after recombination, and another in which the Portalinos don't decay within the lifetime of the universe. These three scenarios will be discussed in Sections 5.8.3, 5.8.4, and 5.8.5.

5.8.2 Portalino Decoupling

The Portalino states will drop out of thermal equilibrium after the DM states have frozen-out. The mass of the Portalino will determine when they decouple and, as we will see, this may be when they are still relativistic.

With all other dark sector states beyond the DM having decayed, the Portalino is kept in thermal equilibrium via its interactions with the SM. The leading contribution to these interactions depends on a coupling of order $\mathcal{O}(m_d/m_\psi)$ or in terms of the physical mass states $\mathcal{O}\left(\sqrt{m_\nu/m_n}\right)$. The more massive the Portalino state is, the weaker its coupling with the SM becomes.

This relationship between the Portalino mass and its coupling to the SM,

in particular to the SM leptons, determines the Portalino decoupling temperature. Portalinos are primarily held in thermal equilibrium by processes such as $en \leftrightarrow e\nu$. The rate of this process at a temperature T has the form

$$\Gamma \sim \eta^2 \left(\frac{m_\nu}{m_n} \right) G_F^2 T^2, \quad (5.8.12)$$

with decoupling temperature given by

$$T_{n,\text{decouple}} \sim 8.5 \text{ GeV} \eta^{-\frac{2}{3}} \left(\frac{m_n}{1 \text{ GeV}} \right)^{\frac{1}{3}}. \quad (5.8.13)$$

If the Portalino mass is less than a few GeV, they will tend to decouple while relativistic and a significant energy density is generated. What happens to this energy density is critical; the Portalinos do decay in this model, but the timing of these decays is the important factor.

5.8.3 The Heavy Portalino Case

One possible scenario is that the Portalinos decay before neutrino decoupling. With reference to Equation 5.8.2 (in combination with other constraints), this scenario is limited to Portalinos with masses $m_n \gtrsim 481 \text{ MeV}$. Portalinos in this mass range decouple at $T \sim \text{few GeV}$ while relativistic, and constitute a significant population after decoupling. The Portalinos then mostly decay before neutrinos decouple, according to Equation 5.8.2, and as a consequence do not impact N_{eff} in this way. Any decays after neutrino decoupling are constrained by the value of ΔN_{eff} during BBN/CMB.

The constraints coming from ΔN_{eff} during BBN/CMB and more general constraints coming from the Portalino-neutrino mixing are summarised in Figure 5.4 and described in detail below. In Figure 5.4 the model parameter space lies along the diagonal multicoloured line labelled $T_{n,\text{decouple}}(\tau)$ - in other words, this is the line parameterised by Equations 5.8.2 and 5.8.13.

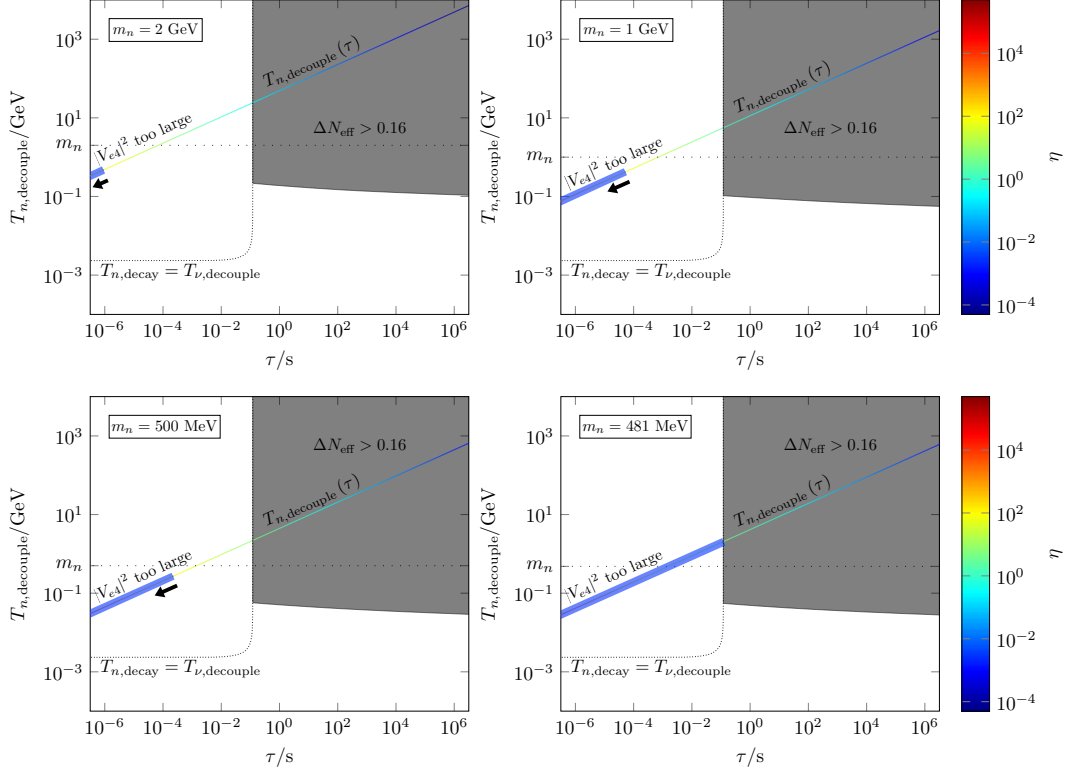


Figure 5.4: Portalino decoupling temperature against Portalino lifetime, for a range of Portalino masses. Marked on the plot are: the decoupling temperature as a function of lifetime, $T_{n,\text{decouple}}(\tau)$, parameterised by η (the enhancement/suppression of the Portalino-neutrino mixings); the line where the Portalino decay temperature $T_{n,\text{decay}}$ is equal to the neutrino decoupling temperature $T_{\nu,\text{decouple}}$, to the right of which the Portalino decays impact on the effective extra relativistic degrees of freedom N_{eff} ; and the region where the Portalino-neutrino mixing is larger than allowed by constraints as detailed in Section 5.8.3. The allowed region lies on the multicoloured line $T_{n,\text{decouple}}(\tau)$, between the blue box (where the model is ruled out by too large a Portalino-neutrino mixing), and the grey region (where the mixing is too small, and hence the Portalinos decay after neutrino decoupling).

Neutrino Heating

Neutrinos decouple from the rest of the thermal bath before electron-positron annihilation, and hence the entropy from electrons and positrons is transferred into the photons alone, raising the photon temperature relative to the neutrino temperature. In the standard case this leads to the ratio $T_\nu \approx \left(\frac{4}{11}\right)^{\frac{1}{3}} T_\gamma$ (in reality the neutrino temperature is slightly higher than this, as they have not

completely decoupled when electrons and positrons annihilate).

However, Portalinos would decay into neutrinos and charged leptons, so if the Portalinos decay after neutrino decoupling they will alter the neutrino-photon temperature ratio. A convenient way to parameterise this is as a constraint on the effective number of neutrino species N_{eff} : $\Delta N_{\text{eff}} = N_{\text{eff}} - N'_{\text{eff}}$ is constrained to be less than 0.16 at BBN [22], and less than 0.33 at recombination [1] (where $N'_{\text{eff}} = 3.046$ is the Standard Model prediction [14, 15]). N_{eff} can be defined via the relationship between the total radiation energy density and the energy density in photons, as discussed in Chapter 2:

$$\rho_r = \rho'_\gamma + \rho'_\nu + \Delta\rho \quad (5.8.14)$$

$$= \rho_\gamma \left(1 + \frac{7}{8} N_{\text{eff}} \left(\frac{4}{11} \right)^{\frac{4}{3}} \right), \quad (5.8.15)$$

where $\Delta\rho$ is the energy density due to Portalino decay products, and the $'$ superscript refers to quantities ignoring any Portalino contributions.

The form of $\Delta\rho$ depends on whether the Portalinos decouple relativistically or remain in thermal equilibrium long enough such that they freeze-out non-relativistically. If the Portalinos decouple while relativistic (and assuming they decay at a temperature $T_{n,\text{decay}} < m_n$), the energy density due to Portalino decay products at (photon thermal bath) temperatures T is given by

$$\begin{aligned} \Delta\rho(T) &= m_n n_n(T_{n,\text{decay}}) \left(\frac{T}{T_{n,\text{decay}}} \right)^4 \\ &= \frac{3m_n \zeta(3)}{2\pi^2} T_{n,\text{decouple}}^3 \left(\frac{a_{n,\text{decouple}}}{a_{n,\text{decay}}} \right)^3 \left(\frac{T}{T_{n,\text{decay}}} \right)^4, \end{aligned} \quad (5.8.16)$$

which by conservation of entropy gives

$$\frac{\Delta\rho(T)}{T^4} = \frac{3\zeta(3)}{2\pi^2} \frac{g_*(T_{n,\text{decay}})}{g_*(T_{n,\text{decouple}})} \frac{m_n}{T_{n,\text{decay}}}. \quad (5.8.17)$$

If the Portalinos decouple while non-relativistic, a Boltzmann-suppressed Portalino abundance will freeze out. The energy density will be given by

$\Delta\rho = \Omega_{n,0}^{\text{no decay}} a^{-3} \left(\frac{3H_0^2}{8\pi G} \right)$, where $\Omega_n^{\text{no decay}} h^2$ is the freeze-out abundance of Portalinos. This gives

$$\frac{\Delta\rho(T)}{T^4} = \frac{3H_0^2}{8\pi G} \frac{g_*(T)}{g_*(T_0)} \frac{\Omega_{n,0}^{\text{no decay}}}{T_0^3 T_{n,\text{decay}}}, \quad (5.8.18)$$

where the 0 subscript denotes present day values, so that e.g. T_0 is the temperature at the present day. Note that the factor $\frac{g_*(T)}{g_*(T_0)}$ will be equal to 1 after neutrino decoupling ($T < T_{\nu,\text{decouple}}$), which is the only situation in which we are interested (if Portalinos decay before neutrino decoupling, then no constraint arises from ΔN_{eff}). In Figure 5.4 we calculate $\Omega_{n,0}^{\text{no decay}} h^2$ using micrOMEGAs [262].

Assuming the Portalinos instantaneously decay at (thermal bath) temperature $T_{n,\text{decay}}$, with energy density $\Delta\rho$, they deposit energy densities $\beta\Delta\rho$ and $(1 - \beta)\Delta\rho$ into the neutrino and photon sectors respectively. The resulting change in N_{eff} reads

$$\Delta N_{\text{eff}} = \frac{15 \left(\beta \frac{8}{7} \left(\frac{11}{4} \right)^{\frac{4}{3}} - (1 - \beta) N'_{\text{eff}} \right)}{\pi^2 + 15(1 - \beta) \frac{\Delta\rho}{(T_{n,\text{decay}})^4}} \frac{\Delta\rho}{(T_{n,\text{decay}})^4}. \quad (5.8.19)$$

Figure 5.4 illustrates the constraints on the model stemming from the limit on ΔN_{eff} . As mentioned above, our model lies along the diagonal multicoloured line labelled $T_{n,\text{decouple}}(\tau)$ parameterised by the mixing enhancement η . The grey exclusion region in the figure results from the limit $\Delta N_{\text{eff}} < 0.16$, and the blue exclusion region covers the case in which the Portalino-neutrino mixing is too large (these constraints are discussed in more detail in Section 5.8.3). For simplicity, we make the conservative assumption (in the sense of erring on the side of ruling out too much parameter space rather than too little) $\beta = 1$ when producing these figures – as the Portalinos tend to decouple relativistically (in the regions of interest), their abundance is so large that $\Delta N_{\text{eff}} \gg 0.16$ whenever Portalinos decay after neutrino decoupling, regardless

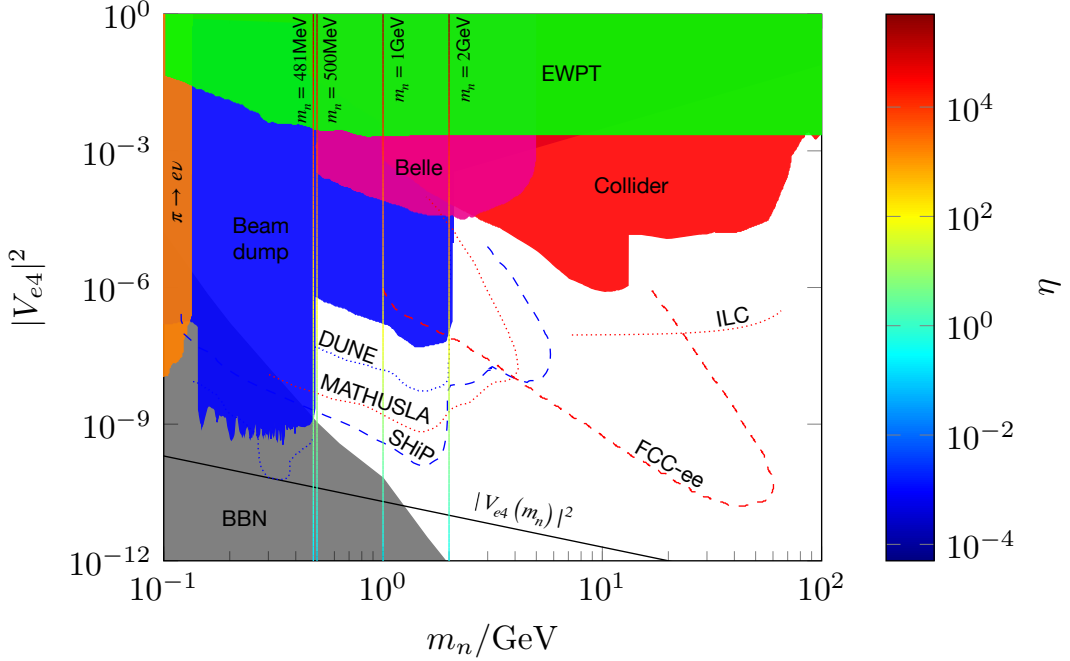


Figure 5.5: Current and future bounds on heavy Portalino mixing with the electron neutrino, combined with the constraint that the Portalino must decay before neutrino decoupling. See text for details of constraints such as ‘Collider’. The line labelled $|V_{e4}(m_n)|^2$ indicates an approximate expected size of the Portalino-neutrino mixing, $|V_{e4}(m_n)|^2 \sim m_\nu/m_n$. The four lines of $T_{n,\text{decouple}}(\tau)$ from Figure 5.4 parameterised by η (for $m_n = 481$ MeV, 500 MeV, 1 GeV and 2 GeV), projected into the m_n - $|V_{e4}|^2$ plane, are also included.

of the value of β (as long as $\beta \gtrsim 0.4$, below which ΔN_{eff} becomes negative). This assumption does change the shape of the lower edge of the grey exclusion region slightly, but this is unimportant for our purposes, given that our model doesn’t intersect with this edge.

Limits from Portalino-Neutrino Mixing

As noted in Section 5.3, the neutral lepton sector closely resembles that of a 3+1 sterile neutrino model, so many sterile neutrino searches can be reinterpreted to constrain the properties of the Portalino.

Electroweak Precision Tests: The Portalino mixing with active neutrinos can affect several electroweak observables, such as the invisible Z decay width. These effects are primarily dependent on the size of the Portalino-neutrino mixing $V_{n\nu}$, but there is some mass dependence for lower values of m_n . Global fits of sterile neutrino mixing have been performed on electroweak precision data (taken from [264] - which draws from [265, 266, 267, 268, 269]), and these bounds can be applied to the Portalino. This constraint is displayed in Figure 5.5, labelled ‘EWPT’.

Collider searches: Portalinos can be produced directly (e.g. via $e^+e^- \rightarrow n\nu$ or $pp \rightarrow W^* \rightarrow nl^\pm$) or via Z -boson decays. They could then decay into visible products, possibly with detectable displaced vertices. Searches for such decays have been carried out using data from LEP [270, 271], ATLAS [272], and CMS [273, 274, 237]. Limits have also been projected for future experiments such as MATHUSLA [275], FCC-ee [276] and ILC [276]. These constraints are displayed in Figure 5.5, labelled ‘Collider’, along with projected limits for future experiments labelled ‘MATHUSLA’, ‘FCC-ee’ and ‘ILC’.

Beam dump experiments: Portalinos with a mass of around 1 GeV tend to have a lifetime of very roughly 0.5 s, and so may decay at some distance from the production site. Visible decay products can be searched for in beam dump experiments with the detector positioned at a distance from the production site. Many such experiments have been carried out [277, 278, 279, 280, 281, 282, 283]. These constraints are displayed in Figure 5.5, labelled ‘Beam dump’, along with projected limits for future experiments labelled ‘DUNE’ [284] and ‘SHiP’ [238]. Note that CHARM and PS191 bounds have been adjusted to account for the Majorana nature of the Portalino - bounds are twice as strong in this case [285].

Meson decays: The Portalino may take part in charged meson decays such as $X^\pm \rightarrow l^\pm n$, with branching ratio proportional to $|V_{nl}|^2$. This would manifest as an additional peak in the charged meson decay spectrum. Constraints from decays such as $\pi^+ \rightarrow e^+\nu$ are compiled in [286, 264], these constraints are displayed in Figure 5.5 labelled as ‘ $\pi \rightarrow e\nu$ ’. Additionally, the Belle experiment, which searched for the decay $B \rightarrow XlN$ or $B \rightarrow lN$ followed by $N \rightarrow l\pi$ (where N is a sterile neutrino and X is a meson), would also place constraints on the neutrino-Portalino mixing [287]. This constraint is labelled ‘Belle’.

Lepton number violation in meson decays: The Majorana mass term violates lepton number. Hence, in the Portalino model lepton number violating (LNV) processes such as $K^+ \rightarrow l^+l^+\pi^-$ may take place. Many searches for LNV processes have been carried out (e.g. [279]). However, the bounds from lepton number violation are weaker than other limits and are not shown in Figure 5.5.

The combined constraints on $|V_{e4}|^2$ for Portalino masses between 0.1 GeV and 100 GeV are shown in Figure 5.5. (Note – the Portalino is not expected to mix more strongly with any particular neutrino, and so only constraints for $|V_{e4}|^2$ are shown, as these are strongest.)

These limits are also included in Figure 5.4 - they are represented by the blue exclusion regions (larger Portalino-neutrino mixing gives lower decoupling temperature/lower lifetime, which corresponds to moving left/downward on the plot).

5.8.4 Intermediate Portalino

Decreasing the mass of the Portalino (and/or decreasing η) allows for their decays to occur after recombination. This means that they don’t affect the neutrino-photon temperature ratio at recombination, and hence they evade

constraints on N_{eff} at this point, potentially opening up an additional region of parameter space. However, we will show that this set-up tends to lead to an early extra period of (Portalino) matter domination, and a universe which, at the present day temperature, has an energy density and expansion rate that is too high.

Firstly, η increases the decay rate of the Portalino. The condition that the Portalinos must decay after recombination can be recast as a condition on η :

$$\mathbf{Condition\ 1:} \quad \tau > t_{\text{recombination}} \implies \eta \lesssim 160 \left(\frac{100 \text{ keV}}{m_n} \right)^2.$$

Next, we can consider the time dependence of the expansion of the universe. Similarly to the heavy case, in this scenario the Portalino tends to decouple while relativistic and with a significant number density. If $m_n \gtrsim 100 \text{ eV}$ the energy density in Portalinos comes to dominate the universe until they decay. This allows us to place a lower limit on η given that the smaller the value of η the longer lived the Portalinos are. An increase in the Portalino lifetime increases the length of the period of early matter domination, and leads to a lower temperature (or equivalently, a larger scale factor $a(t)$) at the point that Portalinos decay. Under the assumption that $\tau > t_{\text{recombination}}$, this doesn't leave enough time to reach matter domination between Portalino decays and the point when the temperature of the universe reaches T_0 (i.e. the present day). This can be seen from the following approximation for the scale factor at matter-radiation equality (where radiation includes Portalino decay products):

$$a_{\text{MRE}} \approx 5.8 \times 10^3 \left(\frac{61.75}{g_*(T_{n,\text{decouple}})} \right)^{\frac{2}{9}} \eta^{-\frac{4}{3}} \left(\frac{100 \text{ keV}}{m_n} \right)^{\frac{7}{3}}, \quad (5.8.20)$$

where $a_{\text{MRE}} > 1$ would mean that the present day is radiation-dominated, with a higher expansion rate H_0 than observed. The condition that $a_{\text{MRE}} < 1$ (i.e. that matter-radiation equality is reached before the present day) can be translated into a constraint on η :

$$\mathbf{Condition\ 2:} \quad a_{\text{MRE}} < 1 \implies \eta \gtrsim 670 \left(\frac{61.75}{g_*(T_{n,\text{decouple}})} \right)^{\frac{1}{6}} \left(\frac{100 \text{ keV}}{m_n} \right)^{\frac{7}{4}}.$$

The final condition that must be taken into account is that $|V_{e4}|^2 < 1$ and so η cannot be too large:

$$\mathbf{Condition\ 3:} \quad |V_{e4}|^2 < 1 \implies \eta \lesssim 2.2 \times 10^3 \left(\frac{m_n}{100 \text{ keV}} \right)^{\frac{1}{2}}.$$

Conditions 1, 2 and 3 cannot be simultaneously satisfied, for any value of m_n . This is equivalent to the statement that the existence of a long-lived Portalino ($\tau > t_{\text{recombination}}$) which comes to dominate the universe inevitably leads to a current-day universe which is dominated by Portalino decay products (or Portalinos themselves), and is growing more quickly than we observe. Hence, this scenario is ruled out.

This only leaves the possibility that the initial Portalino density is so low (via low mass and/or density) that they never come to dominate the universe, which brings us on to the next section – the light Portalino.

5.8.5 Light Portalino

The final possibility is a very light ($m_n \lesssim 10 \text{ eV}$) Portalino. Similarly to the above cases, DM freezes out at a temperature $T \sim \text{few hundred GeV}$. Following this, the Portalinos decouple (possibly long) before the QCD phase transition. Again, there is still a significant population of Portalinos after decoupling. However, unlike in either of the above cases the light Portalinos never come to dominate the energy density of the universe, and tend not to decay within the lifetime of the universe. They will however contribute to ΔN_{eff} at BBN and will behave like light sterile neutrinos and will be constrained by measurements of the Cosmic Microwave Background Radiation (CMB) by Planck [1].

There are several other bounds for this scenario coming from the Portalino-neutrino mixing, e.g. those that arise from beta decay experiments (see for example [288]). However, these bounds are far weaker than the constraints from ΔN_{eff} and the current energy density of the Universe.

As the light Portalino will be relativistic until well after BBN, its contribution to the energy density at BBN will follow

$$\rho_n = \frac{7\pi^2}{120} T_n^4 = \frac{7\pi^2}{120} \left(\frac{g_{*s}(\nu, \text{decouple})}{g_{*s}(T)} \right) T^4, \quad (5.8.21)$$

where $g_{*s}(\nu, \text{decouple})$ is the number of relativistic degrees of freedom at neutrino decoupling and T is the temperature of the Universe. As above,

$$\Delta N_{\text{eff}} = \frac{120\rho_n}{7\pi^2 T_\nu^4} = \left(\frac{T_n}{T_\nu} \right)^4 = \left(\frac{g_{*s}(\nu, \text{decouple})}{g_{*s}(n, \text{decouple})} \right)^{\frac{4}{3}}.$$

Imposing $\Delta N_{\text{eff}} < 0.16$ [22] (and inserting $g_{*s}(\nu, \text{decouple}) = 43/4$), implies that $g_{*s}(n, \text{decouple}) > 42.5$, or equivalently $T_{n, \text{decouple}} \gtrsim 150$ MeV for the light Portalino. Comparing this to Equation 5.8.13 this implies

$$\eta \lesssim 0.042 (m_n/10 \text{ eV})^{\frac{1}{2}}. \quad (5.8.22)$$

The second constraint on this scenario comes from Planck's determination of cosmological parameters from measurements of the CMB anisotropies, which combines data from temperature and polarisation maps with lensing and Baryon Acoustic Oscillation (BAO) measurements. In particular, the light ($m_n < 10$ eV) Portalino is constrained by the Planck TT, TE, EE + lowE + lensing + BAO analysis limit on an effective sterile neutrino mass, m_{eff} , where $m_{\text{eff}} = \Omega_{\text{sterile}} h^2 (94.1 \text{ eV})$ is constrained to be less than 0.65 eV [1].

Applying this to our case, the light Portalino abundance reads

$$\Omega_n = \frac{4\zeta(3)GT_0^3}{\pi H_0^2} \frac{g_{*s}(T_0)}{g_{*s}(T_{n, \text{decouple}})} m_n, \quad (5.8.23)$$

where G is the gravitational constant. Hence, this limit is almost entirely a constraint on m_n alone, with a small adjustment depending on $T_{n, \text{decouple}}$.

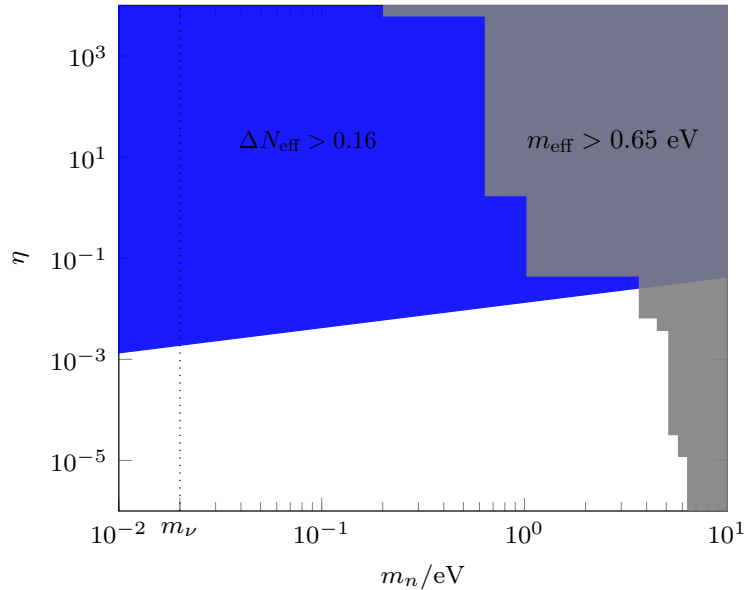


Figure 5.6: Constraints on the light Portalino scenario, with the blue region ruled out by constraints on ΔN_{eff} at BBN and the grey region ruled out by Planck’s analysis of the CMB anisotropies [1]. The vertical dashed line indicates the scale of neutrino masses and is included to highlight the limitations of the model assumption that the Portalino is more massive than the neutrinos.

For example, if the Portalinos decouple extremely early, before top quarks, $m_{\text{eff}} < 0.65 \text{ eV}$ translates to $m_n \lesssim 6.4 \text{ eV}$.

In Figure 5.6 the combined limits on the light Portalino scenario are mapped out as a function of η and m_n with the coloured regions ruled out. The blue region is ruled out due to the Portalino contributing too much to ΔN_{eff} at BBN, with the shape of the region determined by Equation 5.8.22. The grey region represents the parameter region ruled out by the Planck constraint on m_{eff} , where the stepped shape comes from the temperature dependence of g_{*S} .

5.9 Conclusions and Discussion

It seems fairly natural that if a singlet right-handed neutrino does exist (as is the case in many models of neutrino mass) then it may have interactions with the hidden sector and may play a role in DM dynamics, creating a connection

or portal between the SM and dark sectors.

In this chapter, we have expanded on the Portalino model outlined in [255] to include neutrino masses and an expanded dark sector including a DM state. A dark $U(1)$ gauge symmetry was introduced and spontaneously broken generating the dark sector masses including for the Dirac Fermion DM state whose stability is ensured via an unbroken \mathbb{Z}_3 symmetry. The observed DM abundance in this model can be generated by freeze-out via DM self-annihilations to either the Portalino states or the now massive dark sector gauge bosons. Following the freeze-out of DM, a population of Portalino states is produced. The Portalino lifetime is cosmologically relevant and as a result provides the main constraints on the properties of these states.

We have considered three qualitatively different scenarios categorised in terms of the mass of the Portalino: an intermediate case, which is not cosmologically viable; a heavy and light case, the former with allowed parameter space for a Portalino mass $m_n \gtrsim 481$ MeV and the latter viable for $m_n \lesssim 6.4$ eV provided Portalinos decouple before top quarks.

Throughout this chapter, we have only considered including one Portalino (with three heavy singlet neutrinos), but we could consider models with multiple Portalinos (and/or a different number of heavy neutrinos). We can put concrete restrictions on which configurations are viable by imposing that they must give rise to at most one massless active neutrino. In the absence of specific flavour symmetries, the number of massless states is given by $n_0 = \min(0, 3 - n_R + n_p)$ where n_R is the number of heavy neutrinos and n_p is the number of Portalino states. Hence, for a model with n_p Portalinos the number of heavy right-handed neutrinos required is at least $2 + n_p$.

The inclusion of a full neutrino flavour model was beyond the scope of this work. The details of such a flavour model will feed into the Portalino phenomenology in a more complicated way compared with the parameterisation used here in terms of η and may lead to ways to widen the allowed parameter

range found in this work.

Another variation on what has been presented here is to remove the Majorana mass term M_R . In order to generate the light active neutrino masses, the neutrino Yukawa couplings λ_ν would need to be small ($\sim 10^{-13}$). The structure of this model is significantly different: for example, the Portalino mass isn't suppressed relative to the other dark states and the Portalino-neutrino mixing is significantly suppressed. Interestingly, if the $h - \phi$ interactions were turned off or also significantly suppressed, the Portalino-neutrino mixing could be the strongest interaction between the dark and visible sectors, and could potentially lead to the freeze-in production [289, 86] of the Portalino or other dark sector states.

The Portalino can in principle provide explanations for some anomalies. For example, a decaying sterile state (which could be the heavy Portalino) has been proposed as a solution to short baseline anomalies [290, 291, 292]. An eV sterile neutrino has also been mooted as a solution to these anomalies, however the most straightforward case of an eV Portalino with sufficiently strong mixing ($V_{n\nu} \sim 0.1$) with SM neutrinos would be ruled out by cosmological constraints [290, 293].

Indirect dark matter signals in the form of highly boosted, mono-energetic Portalinos produced in Dark Matter annihilations provide a target for neutrino telescopes.

Chapter 6

Freeze-in Dark Matter in the Effective MSSM

6.1 Introduction

As discussed in Chapter 4, the Minimally Supersymmetric Standard Model (MSSM) offers a potential solution to the gauge hierarchy problem [242, 243, 294, 245, 244], a dark matter candidate [295, 296], and a framework for gauge coupling unification [297, 298, 299, 300]. As also explained there, the MSSM suffers from the ‘ μ -problem’ – the question of why the parameter μ in the superpotential, which feeds into the Higgs masses, lies around the SUSY-breaking scale M_{SUSY} . In this Chapter, we will consider the Next-to-Minimally Supersymmetric Standard Model (NMSSM or (M+1)SSM), which attempts to resolve this issue by introducing a singlet scalar S (the complex scalar component of a chiral superfield \hat{S}) which has a Yukawa coupling $\lambda SH_u H_d$. This singlet then obtains a vacuum expectation value (vev) $\langle S \rangle = v_s$, giving rise to the term $\lambda v_s H_u H_d$ and hence generating the μ term of the MSSM [301, 302].

It is curious to observe that, providing we keep the product of λv_s constant, the sizes of λ and v_s may vary. For example, one choice is the decoupling limit $\lambda \ll 1$, which leads to a model known as the ‘effective MSSM’ [302, 303]. We follow other papers in using this name, but note that it is a slight misnomer:

this scenario, while resembling the MSSM in many respects, would have a few key differences. Firstly, the singlino (the fermionic superpartner of S) can be the lightest superpartner (LSP), and hence the lightest MSSM-like neutralino would no longer be stable. It is only able to decay into the singlino, and hence its width is proportional to λ^2 . The additional scalars (one CP-even and the other CP-odd) would also freeze in, and have widths $\sim \lambda^2$, and hence decay relatively slowly. These decays can all be cosmologically interesting. The other key difference, which motivates this chapter, is that the correct relic abundance could be generated via freeze-in of the singlino, rather than (or in addition to) freeze-out of the neutralino.

In Section 6.2, we describe the model in full, and identify the mass orderings which can give rise to a possible dark matter candidate. In Section 6.3, we examine a scenario in which the singlino is the LSP and freezes-in to produce the correct relic abundance, including a discussion of the phenomenological and cosmological implications of such a scenario, and identify the region of parameter space in which experimental constraints can be satisfied. In Section 6.4 we briefly show that it is also possible, within the effective MSSM, for the dark matter to be an MSSM-like neutralino LSP produced via freeze-out, and discuss how this situation would differ from the usual MSSM.

6.2 The Effective MSSM

The NMSSM is defined as the MSSM with an additional gauge-singlet chiral superfield \hat{S} . The scale invariant superpotential reads

$$W_{H,S} = \lambda \hat{S} \left(\hat{H}_u \cdot \hat{H}_d \right) + \frac{\kappa}{3} \hat{S}^3 + \dots \quad (6.2.1)$$

where \hat{H}_u, \hat{H}_d are the up-like and down-like Higgs superfields respectively, λ and κ are dimensionless constants, and the ellipsis contains terms which include (s)fermion superfields.

There are also soft SUSY-breaking terms,

$$\begin{aligned}
-\mathcal{L}_{\text{soft}} \supset & m_{H_u}^2 |H_u|^2 + m_{H_d}^2 |H_d|^2 + m_S^2 |S|^2 \\
& + \left(\lambda A_\lambda S (H_u \cdot H_d) + \frac{\kappa}{3} A_\kappa S^3 + \text{h.c.} \right) + \dots, \tag{6.2.2}
\end{aligned}$$

where the ellipsis contains soft SUSY-breaking terms involving sfermions and gauginos.

These soft SUSY-breaking terms cause \hat{S} to obtain a vacuum expectation value v_s . A connection to the MSSM can then be made, with the term $\lambda v_s (\hat{H}_u \cdot \hat{H}_d)$ playing the role of the Higgs mass term $\mu (\hat{H}_u \cdot \hat{H}_d)$ of the MSSM superpotential.

As μ needs to be around the SUSY-breaking scale¹, the vev v_s is usually taken to be of the SUSY-breaking scale (with λ not much less than 1). However, this is not strictly phenomenologically necessary, as long as the *combination* λv_s is of the correct scale.

In this work, we consider an alternative choice that is the decoupling limit, which is related to the ‘Effective MSSM’ where $\lambda \ll 1$. In our model, we consider $\lambda \sim 10^{-12}$ in order to obtain the correct freeze-in dark matter abundance.

6.2.1 Minima of the Potential $V(H_u, H_d, S)$

The scalar potential for \hat{H}_u, \hat{H}_d and \hat{S} is slightly modified compared to the MSSM. The D -term contributions are unchanged as they all stem from gauge terms, which are not altered by the presence of a singlet,

$$-\mathcal{L}_D = \frac{1}{2g_1^2} D_B^2 + \frac{1}{2g_2^2} D_W^A D_W^A, \tag{6.2.3}$$

¹As the superfields \hat{H}_u and \hat{H}_d contain charged fermionic components (charginos), the mass μ cannot be too small, otherwise the charginos would be light, which is ruled out by collider searches. This sets $\mu \gtrsim 100$ GeV. At the same time, μ cannot be too large, otherwise the Higgs potential becomes stable at the origin and the Higgses don’t acquire vevs. This leads to a requirement that μ be smaller than approximately the SUSY-breaking scale.

where g_1 and g_2 are the $U(1)_Y$ and $SU(2)_L$ gauge couplings respectively and

$$\begin{aligned} D_B &= -g_1^2 \sum_{\phi} Y_{\phi} \phi^{\dagger} \phi \\ D_W^A &= -\frac{g_2^2}{2} \sum_{\phi \in SU(2)_L} \phi^{\dagger} \sigma^A \phi \end{aligned} \quad (6.2.4)$$

so that

$$\begin{aligned} -\mathcal{L}_D &= \frac{g_1^2 + g_2^2}{8} \left[(H_u^{\dagger} H_u)^2 + (H_d^{\dagger} H_d)^2 - 2 (H_u^{\dagger} H_u) (H_d^{\dagger} H_d) \right] \\ &\quad + \frac{g_2^2}{2} |H_u^{\dagger} H_d|^2 + \dots \end{aligned} \quad (6.2.5)$$

The F -field contributions are given by

$$\begin{aligned} -\mathcal{L}_F &= \sum_i F_i^* F_i = \sum_i \left| \frac{\partial W}{\partial \phi_i} \right|^2 \\ &= |\lambda S H_u|^2 + |\lambda S H_d|^2 + |\kappa S^2 + \lambda (H_u \cdot H_d)|^2 + \dots \end{aligned} \quad (6.2.6)$$

Combining these terms with the soft SUSY-breaking terms in Equation 6.2.2, the scalar potential for \hat{H}_u , \hat{H}_d and \hat{S} is given by

$$\begin{aligned} V(H_u, H_d, S) &= (m_{H_u}^2 + |\lambda S|^2) |H_u|^2 + (m_{H_d}^2 + |\lambda S|^2) |H_d|^2 + m_S^2 |S|^2 \\ &\quad + |\kappa S^2 + \lambda (H_u \cdot H_d)|^2 + \left(\lambda A_{\lambda} S (H_u \cdot H_d) + \frac{\kappa}{3} A_{\kappa} S^3 + \text{h.c.} \right) \\ &\quad + \frac{g_1^2 + g_2^2}{8} [|H_u|^2 - |H_d|^2]^2 + \frac{g_2^2}{2} |H_u^{\dagger} H_d|^2. \end{aligned} \quad (6.2.7)$$

As in the MSSM, the charged part of one of the Higgses H_u or H_d can be set to zero at the minimum of the potential by a gauge transformation, which then leads to the charged part of the other Higgs being equal to zero at the minimum. For the neutral components, we expand around the respective vevs as

$$H_u^0 = v_u + \frac{H_{uR} + iH_{uI}}{\sqrt{2}}, \quad H_d^0 = v_d + \frac{H_{dR} + iH_{dI}}{\sqrt{2}}, \quad S = v_s + \frac{S_R + iS_I}{\sqrt{2}}, \quad (6.2.8)$$

where the vacuum expectation values v_u and v_d can be chosen to be real and non-negative. Similarly, we can choose the singlet vev v_s , along with $\lambda, \kappa, A_\kappa$ and A_λ , to be real, with λ positive (additional constraints on the relative signs of these parameters are found from the requirement that all squared masses should be positive, details of which are outlined in Section 6.2.2). The vevs are found via minimisation of

$$\begin{aligned} V(v_u, v_d, v_s) = & (m_{H_u}^2 + \lambda^2 v_s^2) v_u^2 + (m_{H_d}^2 + \lambda^2 v_s^2) v_d^2 + m_S^2 v_s^2 \\ & + (\kappa v_s^2 - \lambda v_u v_d)^2 + 2 \left(\frac{\kappa}{3} A_\kappa v_s^3 - \lambda A_\lambda v_s v_u v_d \right) \\ & + \frac{g_1^2 + g_2^2}{8} (v_u^2 - v_d^2)^2 + \frac{g_2^2}{2} v_u^2 v_d^2. \end{aligned} \quad (6.2.9)$$

The minimisation equations are given by [302]

$$\begin{aligned} v_u \left(m_{H_u}^2 + \lambda^2 (v_s^2 + v_d^2) + \frac{g_1^2 + g_2^2}{4} (v_u^2 - v_d^2) \right) - \lambda v_d v_s (A_\lambda + \kappa v_s) &= 0, \\ v_d \left(m_{H_d}^2 + \lambda^2 (v_s^2 + v_u^2) + \frac{g_1^2 + g_2^2}{4} (v_d^2 - v_u^2) \right) - \lambda v_u v_s (A_\lambda + \kappa v_s) &= 0, \\ v_s \left(m_S^2 + \kappa A_\kappa v_s + 2\kappa^2 v_s^2 + \lambda^2 (v_u^2 + v_d^2) - 2\lambda \kappa v_u v_d \right) - \lambda v_u v_d A_\lambda &= 0. \end{aligned} \quad (6.2.10)$$

In this work, we consider $\lambda \ll 1$ and look for minima of the potential in the large v_s region. In this limit, the relevant potential terms determining v_s are

$$V(v_s) = m_S^2 v_s^2 + \frac{2\kappa}{3} A_\kappa v_s^3 + \frac{\kappa^2}{4} v_s^4, \quad (6.2.11)$$

with the minimisation condition for v_s reducing to

$$v_s \left(m_S^2 + \kappa A_\kappa v_s + 2\kappa^2 v_s^2 \right) = 0. \quad (6.2.12)$$

Provided $A_\kappa^2 > 8m_S^2$ a real non-zero vacuum expectation value for S exists but $A_\kappa^2 > 9m_S^2$ is the condition required for a global minimum [302] with

$$v_s = \frac{1}{4\kappa} \left(-A_\kappa - \text{sgn}(A_\kappa) \sqrt{A_\kappa^2 - 8m_S^2} \right). \quad (6.2.13)$$

A large v_s can be achieved if $\kappa \ll 1$. The resulting effective μ term has the form

$$\mu_{\text{eff}} = \lambda v_s = \frac{\lambda}{4\kappa} \left(-A_\kappa - \text{sgn}(A_\kappa) \sqrt{A_\kappa^2 - 8m_S^2} \right). \quad (6.2.14)$$

This is of the electro-weak scale provided $\lambda \sim \kappa$. This means that it is possible to obtain the correct scale of μ_{eff} in the effective MSSM, as long as $\kappa \sim \lambda$. Applying $\lambda, \kappa \ll 1$ in Equation 6.2.9, the potential determining v_u and v_d is reduced to

$$\begin{aligned} V(v_u, v_d) \approx & (m_{H_u}^2 + \mu_{\text{eff}}^2) v_u^2 + (m_{H_d}^2 + \mu_{\text{eff}}^2) v_d^2 - 2B_{\text{eff}} \mu_{\text{eff}} v_u v_d \\ & + \frac{g_1^2 + g_2^2}{8} (v_u^2 - v_d^2)^2 + \frac{g_2^2}{2} v_u^2 v_d^2, \end{aligned} \quad (6.2.15)$$

where $B_{\text{eff}} = A_\lambda + \frac{\kappa}{\lambda} \mu_{\text{eff}}$, and with minimisation conditions

$$\begin{aligned} v_u \left(m_{H_u}^2 + \mu_{\text{eff}}^2 + \frac{g_1^2 + g_2^2}{4} (v_u^2 - v_d^2) \right) - v_d \mu_{\text{eff}} B_{\text{eff}} &= 0, \\ v_d \left(m_{H_d}^2 + \mu_{\text{eff}}^2 + \frac{g_1^2 + g_2^2}{4} (v_d^2 - v_u^2) \right) - v_u \mu_{\text{eff}} B_{\text{eff}} &= 0. \end{aligned} \quad (6.2.16)$$

This is identical to the MSSM case (with $\mu, B \rightarrow \mu_{\text{eff}}, B_{\text{eff}}$), and so electroweak symmetry breaking can follow as in the MSSM, with the condition that $(B_{\text{eff}} \mu_{\text{eff}})^2$ must be sufficiently large to trigger symmetry breaking:

$$\left(A_\lambda + \frac{\kappa}{\lambda} \mu_{\text{eff}} \right)^2 \mu_{\text{eff}}^2 \gtrsim (\mu_{\text{eff}}^2 + m_{H_u}^2) (\mu_{\text{eff}}^2 + m_{H_d}^2). \quad (6.2.17)$$

However, $B_{\text{eff}} \mu_{\text{eff}}$ cannot be too large otherwise the potential is not bounded below for $v_u = v_d \rightarrow \infty$, leading to the condition

$$\left(A_\lambda + \frac{\kappa}{\lambda} \mu_{\text{eff}} \right) \mu_{\text{eff}} \lesssim 2 \mu_{\text{eff}}^2 + m_{H_u}^2 + m_{H_d}^2. \quad (6.2.18)$$

6.2.2 Effective MSSM Spectrum

The spectrum of the mass eigenstates arising from H_u and H_d after EWSB is for the most part unchanged compared with the MSSM, where H_u and H_d together contain four neutral scalars (two CP-even and two CP-odd) and two charged scalars. One CP-odd scalar and one charged scalar become Goldstone modes, and are absorbed as the longitudinal modes of the Z and W^\pm bosons respectively. This leaves two CP-even scalars, h and H , with h corresponding to the Standard Model Higgs, along with a CP-odd scalar A and a charged scalar H^\pm . The masses and mixings of these states are the same as in the MSSM (as discussed in Section 4.7, or see for example [248]) as the mixing with the singlet states will be $\mathcal{O}(\lambda)$ and can be neglected.²

6.2.3 Higgs and Singlino Sector

The tree level Higgs mass matrices are obtained by expanding the full scalar potential Equation 6.2.9 around v_u , v_d and v_s , following Equation 6.2.8. After the elimination of $m_{H_d}^2$, $m_{H_u}^2$, and m_S^2 , the CP-odd Higgs mass matrix is found by rotating the CP-odd Higgs states into the basis (P, G, S_I) , where $P = \cos \beta H_{uI} + \sin \beta H_{dI}$ and G is the Goldstone mode [302]. Dropping the Goldstone mode, the mass matrix \mathcal{M}_O^2 in the basis (P, S_I) has the elements

$$\begin{aligned}\mathcal{M}_{O,11}^2 &= \frac{2\mu_{\text{eff}} B_{\text{eff}}}{\sin 2\beta}, \\ \mathcal{M}_{O,22}^2 &= \lambda^2 (B_{\text{eff}} + 3\frac{\kappa}{\lambda}\mu_{\text{eff}}) \frac{v_u v_d}{\mu_{\text{eff}}} - 3\frac{\kappa}{\lambda}\mu_{\text{eff}} A_\kappa, \\ \mathcal{M}_{O,12}^2 &= \lambda (A_\lambda - 2\frac{\kappa}{\lambda}\mu_{\text{eff}}) v.\end{aligned}\tag{6.2.19}$$

For $\lambda \ll 1$ the tree-level masses are given by

$$m_{S_1}^2 \approx -\left(3\frac{\kappa}{\lambda}\mu_{\text{eff}} A_\kappa\right),$$

²This does of course mean that in this model the tree-level $\sim \lambda m_Z$ correction to the Standard Model Higgs mass found in the NMSSM is now negligible and removes one of the motivations for introducing a singlet to the MSSM.

$$m_A^2 \approx \frac{2\mu_{\text{eff}} B_{\text{eff}}}{\sin 2\beta} = \frac{2\mu_{\text{eff}} (A_\lambda + \frac{\kappa}{\lambda}\mu_{\text{eff}})}{\sin 2\beta}, \quad (6.2.20)$$

where we have defined S_1 as the mostly-singlet CP-odd mass eigenstate and A as the mostly-MSSM-like mass eigenstate. We note an explicit dependence on the ratio κ/λ in m_A^2 . This is important as this ratio will be constrained, along with the relative sizes of A_λ and μ , by collider limits on the mass of m_A .

The mass mixing matrix for the CP-even mass matrix \mathcal{M}_E^2 in the basis (H_{dR}, H_{uR}, S_R) has the form

$$\begin{aligned} \mathcal{M}_{E,11}^2 &= \frac{g_1^2 + g_2^2}{2} v_d^2 + (\mu_{\text{eff}} B_{\text{eff}}) \tan \beta, \\ \mathcal{M}_{E,22}^2 &= \frac{g_1^2 + g_2^2}{2} v_u^2 + (\mu_{\text{eff}} B_{\text{eff}}) / \tan \beta, \\ \mathcal{M}_{E,33}^2 &= \lambda A_\lambda \frac{v_u v_d}{v_s} + \frac{\kappa}{\lambda} \mu_{\text{eff}} (A_\kappa + 4 \frac{\kappa}{\lambda} \mu_{\text{eff}}), \\ \mathcal{M}_{E,12}^2 &= (2\lambda^2 - \frac{g_1^2 + g_2^2}{2}) v_u v_d - \mu_{\text{eff}} B_{\text{eff}}, \\ \mathcal{M}_{E,13}^2 &= \lambda (2\mu_{\text{eff}} v_d - (B_{\text{eff}} + \frac{\kappa}{\lambda} \mu_{\text{eff}}) v_u), \\ \mathcal{M}_{E,23}^2 &= \lambda (2\mu_{\text{eff}} v_u - (B_{\text{eff}} + \frac{\kappa}{\lambda} \mu_{\text{eff}}) v_d). \end{aligned} \quad (6.2.21)$$

It is noted that for fixed μ there is no λ dependence in the first two diagonal components with the mixing of the two Higgs states H_{uR} and H_{dR} with S_R appearing at first order in the suppressed coupling, λ , meaning that the mass spectrum for the MSSM-like states will follow the MSSM up to order λ^2 corrections, which for this work will be smaller than the 1-loop (and higher order) corrections. Defining S_2 as the mostly-singlet CP-even mass eigenstate, it is straightforward to read off its mass from the $(3, 3)$ component as

$$m_{S_2}^2 \approx 4 \left(\frac{\kappa}{\lambda} \right)^2 \mu_{\text{eff}}^2 + \frac{\kappa}{\lambda} \mu_{\text{eff}} A_\kappa.$$

Finally, the form of the charged Higgs mass is identical to that in the MSSM, namely $m_{H^\pm}^2 = m_A^2 + m_W^2$, where m_W is the SM W boson mass.

The singlet superfield also contains a Weyl fermion, \tilde{S} . The relevant mass terms arising from the superpotential for the singlino are

$$\mathcal{L} \supset -\kappa S \left(\tilde{S}\tilde{S} \right) - \lambda \left(\tilde{S}\tilde{H}_u \cdot H_d + H_u \cdot \tilde{H}_d\tilde{S} \right) + \text{h.c.} \quad (6.2.22)$$

which gives the following mass term after the scalars gain vevs:

$$\mathcal{L} \supset -\frac{\kappa}{\lambda}\mu_{\text{eff}}\tilde{S}\tilde{S} - \frac{\kappa}{\lambda}\mu_{\text{eff}}\tilde{\tilde{S}}\tilde{\tilde{S}} + \dots \quad (6.2.23)$$

where the ellipses represent the suppressed mixing terms with \tilde{H}_u and \tilde{H}_d appearing in Equation 6.2.22, which are important in determining the detailed mixing and resulting interactions for the extended neutralino sector. These terms however represent very small corrections to the tree-level mass of the mostly-singlet state. In analogy with the MSSM neutralinos we recast this as a Majorana fermion, which we call the singlino, χ_s . The tree-level mass of the singlino has the form

$$m_{\chi_s} = 2\frac{\kappa}{\lambda}\mu_{\text{eff}}. \quad (6.2.24)$$

6.2.4 Dark Matter Phenomenology Overview

The dark matter phenomenology of the model depends on the mass ordering of the supersymmetric states. There are two possible dark matter candidates, the first is where the singlino χ_s is the LSP and the second is where the lightest MSSM neutralino, call it χ_1 , is the LSP. In this work, we will focus primarily on the singlino case.

For both candidates we may expect that the mechanism responsible for generating the dominant contribution to the dark matter relic density is either freeze-in of the singlino, or freeze-out of the neutralino, leading to four possible scenarios [86].

The first has a singlino LSP, with the dominant contribution of the relic abundance generated via freeze-in of the singlino. The freeze-out of the neutralino still occurs, but generates a sub-dominant relic neutralino abundance,

which then decays to the singlino.

The second scenario again has the singlino as the LSP, but this time with freeze-in contributing a sub-dominant component of the required relic abundance. The dominant contribution comes from the freeze-out of the lightest neutralino, which subsequently decays to the singlino, boosting its abundance to the required value.

The third scenario is close to the vanilla MSSM scenario, with the lightest neutralino as the LSP. The dominant contribution comes from freeze-out of the neutralino, but with a sub-dominant contribution from the freeze-in and subsequent decay of the singlino. This is a realisation of the scenario outlined in [304].

The fourth scenario has a neutralino LSP with the dominant contribution to its relic abundance coming from the freeze-in and subsequent decay of the singlino, with the freeze-out abundance of the neutralinos contributing a sub-dominant component.

In all four scenarios, there are some additional features that require consideration. The first is related to the decay of the NLSP abundance into the LSP. In all cases, the coupling λ is suppressed in order for the freeze-in abundance of the singlino to either mostly recreate the relic abundance or to produce a sub-dominant component. In either case, there is an upper limit of $\lambda, \kappa \lesssim 10^{-11}$. The coupling λ determines the decay width of the NLSP in all scenarios, leading to long-lived states. A significant abundance of late decaying states may impact BBN (see for example [19, 20, 21, 23]) and provides constraints on the scenarios considered.

Further constraints on these scenarios arise due to the freeze-in production of the singlet scalar states, S_1 and S_2 . These states are unstable, but their decay rates are suppressed by either λ or κ and as a result are long-lived. Just like the NLSP, the lifetime of the two singlet scalars states could be long enough for BBN to play a role in constraining the model.

Depending on the mass spectrum, the singlet scalars may also decay into a pair of LSPs or, via the mixing with the MSSM Higgs states, into SM states such as (heavy) quark pairs. If it is possible to decay into a pair of LSPs then the topping up of the abundance of the LSP needs to be taken into account.

In Section 6.3 we examine the first scenario with singlino LSP dominantly produced by freeze-in in detail, which is the focus of this work. We also show in Section 6.3 that scenario two, where the singlino LSP abundance is mostly generated via the freeze-out and decay of the neutralino NLSP, is ruled out. We outline the neutralino LSP scenario in Section 6.4 and highlight the challenges for these scenarios. Even though these scenarios are theoretically possible in this framework, scenario three is essentially a more constrained version of the standard MSSM with neutralino dark matter.

6.3 Singlino(-like) Dark Matter

We focus first on scenario one, in which the singlino is the LSP and dark matter candidate whose abundance is dominantly produced by freeze-in. We are interested primarily in the semi-decoupled sector, in particular the dependence of the model on the NMSSM specific parameters $\lambda, \kappa, A_\lambda$, and A_κ . We fix the MSSM SUSY parameters according to the benchmarks outlined in [305, 306], where the benchmarks can generate the correct Higgs mass and evade current bounds on squark masses.

The chosen benchmark model specifies a common soft SUSY-breaking mass $M_{\bar{f}} = 2 \text{ TeV}$ for first and second generation sfermions, with the corresponding Higgs-sfermion trilinear scalar interaction terms for the first two generation $A_{\bar{f}}$ set to zero. The remaining parameters are fixed as

$$\begin{aligned} M_{Q,U,D_3} &= 1.5 \text{ TeV}, & M_{L,E_3} &= 2 \text{ TeV} \\ M_1 &= M_2 = 1 \text{ TeV}, & M_3 &= 2.5 \text{ TeV} \\ \mu &= 1 \text{ TeV}, & X_t &= A_t - \mu \cot \beta = 2.8 \text{ TeV} \end{aligned}$$

$$A_b = A_\tau = A_t, \quad \tan \beta = 8.5, \quad (6.3.1)$$

where M_{Q,U,D_3}, M_{L,E_3} are the soft masses of the third generation sfermions, $M_{1,2,3}$ are the masses of the gauginos, $A_{b,\tau,t}$ are the trilinear Higgs-sfermion couplings for the third generation, and the parameter X_t enters the left-right mixing term in the stop mass matrix and feeds into the correction to the SM-like Higgs mass. For brevity, we have relabelled $\mu_{\text{eff}} = \mu$.

As we will discuss in Section 6.3.3, in this benchmark we would like $\tan \beta$ as small as possible to satisfy constraints from big bang nucleosynthesis. However, the Higgs mass is proportional to $\cos^2 2\beta$ and so we require $\tan \beta \gtrsim 8.5$ in order to obtain a large enough Higgs mass. This explains why we have taken $\tan \beta = 8.5$.

The benchmark parameter values chosen lead to an NLSP neutralino, χ_1 , with mass $m_{\chi_1} = 939$ GeV, and a freeze-out abundance, as calculated using micrOMEGAs [262], of $\Omega_{\chi_1} h^2 = 5.75 \times 10^{-2}$, which is a factor of two below the measured dark matter abundance. The NLSP in this scenario is, however, unstable, and will decay into the singlino dark matter state, with decay rate determined by the small coupling λ , contributing an additional $\Delta\Omega_{\chi_s} h^2 = \Omega_{\chi_1} h^2 m_{\chi_s}/m_{\chi_1}$ to the singlino relic abundance, whose final relic abundance is then

$$\Omega_{\chi_s} h^2 = \Omega_{\chi_s}^{\text{FI}} h^2 + \frac{m_{\chi_s}}{m_{\chi_1}} \Omega_{\chi_1} h^2, \quad (6.3.2)$$

where $\Omega_{\chi_s}^{\text{FI}} h^2$ is the abundance of singlino dark matter produced via freeze-in. The choice of this benchmark is not critical to the analysis, beyond that the NLSP freeze-out abundance should generate a sub-dominant contribution to the singlino abundance. If the ratio of the masses of the NLSP and singlino is large, then the freeze-out abundance of NLSP can in fact be a little higher than produced by this benchmark, with the final DM abundance still being dominantly determined by the freeze-in of the singlino.

Depending on the mass of the singlino, the NLSPs decay dominantly via $\chi_1 \rightarrow h\chi_s, H\chi_s, A\chi_s$ and $Z\chi_s$. All of these decays will have large hadronic branching fractions in addition to producing radiation, potentially leading to changes in primordial abundances produced at BBN if the NLSP decays during that epoch.

6.3.1 Freeze-In Abundances

In this scenario, the freeze-in abundance of the singlino will form the dominant contribution to the final dark matter density, however it is not the only particle that freezes-in. Both the CP-odd and CP-even mostly singlet scalars will also freeze-in, generating a potentially significant energy density in both states that will decay back into the Standard Model.

The parameter λ plays a critical role in determining both the three singlet field abundances and the lifetimes of S_1 , S_2 , and the NLSP, χ_1 . The abundances of the singlet particles scale as λ^2 , while the lifetimes of the scalars, along with that of the NLSP, scale as λ^{-2} . The fact that both the abundances and the lifetimes are determined by one parameter means that limits on the lifetimes of the three decaying states, coming from BBN, can be used to constrain the model.

We numerically compute the freeze-in abundances of χ_s, S_1 and S_2 using micrOMEGAs version 5.2.8 [262] along with NMSSMtools [307]. micrOMEGAs will calculate the freeze-in abundance for the LSP by assuming that all frozen-in states will decay down to the lightest FIMP state. This calculation is very slow (running a single point in parameter space takes approximately 30 minutes), so we chose to scan over limited regions of the parameter space. Though slow, calculating the freeze-in abundance of the singlino is straightforward, as it is the only stable FIMP state in the model. Calculating the abundance of the mostly-singlet scalars is more complicated but can be

done by declaring that they are both FIMP states possessing R-parity, meaning micrOMEGAs will assume that their freeze-in abundances will decay down to the singlino LSP state. Although this produces the incorrect abundance for the singlino, micrOMEGAs outputs the leading processes that contribute to the final LSP abundance, which includes the processes freezing-in S_1 and S_2 , and hence their freeze-in abundances can be computed via an appropriate re-scaling.

For the parameter region of interest, the leading freeze-in processes in the production of the singlino are the decay of the NLSP neutralino, the co-annihilation of charginos with a Z , following $\chi_i^- Z \rightarrow W^+ \chi_s$, and co-annihilation with a b quark following $\chi_i^- b \rightarrow t \chi_1$.³ The number of processes that contribute to the freeze-in abundance is very large, with many contributing at the percent level.

The freeze-in abundances of the scalar states, S_i , are produced by reactions of the type $q'\bar{q} \rightarrow W^\pm S_i$, $W^\pm q \rightarrow q S_i$, $ZW^\pm \rightarrow W^\pm S_i$, $t\bar{t} \rightarrow G S_i$ (where G is the SM gluon), and, at a very suppressed level, the decays of the NLSP, $\chi_1 \rightarrow \chi_s S_i$. The relative sizes of the contributions of these channels depend on the spectrum.

In addition to the decaying NLSP topping up the singlino abundance, all three of the late decaying states will lead to late-time entropy production and as a result can dilute the singlino DM relic density assuming that these decays occur after the singlinos have frozen-in (as they do in this scenario). However, this effect is extremely small (the energy density of the long-lived particles is very small relative to the overall energy density in radiation) and can be safely ignored. To confirm this, the dilution can be calculated by determining by the

³Care must be taken around the calculation of the process $\chi_i^- b \rightarrow t \chi_1^0$, which in one diagram proceeds via a t-channel exchange of a W boson. micrOMEGAs does not include thermal masses in its freeze-in calculations. The cross-section of the t-channel W process without including a thermal mass for the W is constant at high energies and can lead to an enhanced freeze-in production at high temperatures. To resolve this issue, a cut on the integration angle range can be applied that simulates the effect of a thermal W mass.

ratio of entropy deposited by the decays compared to the overall entropy:

$$\frac{\Delta s}{v_s} \approx \left(1 + \frac{4}{3} Y_i \left(\frac{m_i}{T_{\text{decay}}}\right)\right)^{\frac{3}{4}} - 1 \quad (6.3.3)$$

As we will discuss in Section 6.3.2, the yield Y_i and the decay temperature T_{decay} (or equivalently, the lifetime τ_i) are constrained by big bang nucleosynthesis (e.g. see Figure 6.1 and the surrounding discussion). We can take some representative values of Y_i and T_{decay} which arise in the model, e.g. $m_i Y_i \sim 1 \times 10^{-10}$ GeV and $\tau \sim 100$ s (so that $T_{\text{decay}} \sim 0.1$ MeV) for which this dilution effect is $\sim 10^{-6}$. For more extreme values, such as $m_i Y_i \sim 1 \times 10^{-8}$ GeV and $\tau \sim 1$ s (so that $T_{\text{decay}} \sim 1$ MeV), the dilution effect is $\sim 10^{-5}$, so in all cases, this effect can be neglected.

6.3.2 Constraining the Singlino LSP Scenario

In this section, the constraints on the singlino LSP are detailed. The leading constraint on the bulk of parameter space comes from the requirement that the long-lived states do not decay with significant abundances during BBN. A further important constraint comes from the MSSM Higgs states' dependencies on the NMSSM-like parameters κ and λ , or, more precisely, the ratio κ/λ . Even though the parameters λ and κ are suppressed, their ratio feeds into the mass of the CP-odd MSSM Higgs state A . Limits on the size of m_A thus lead to constraints on the relative size of κ and λ . This ratio also feeds into the conditions for successful electroweak symmetry breaking, and is as a result further constrained.

Constraints from Big Bang Nucleosynthesis

The decays of the three long-lived particles (the mostly-singlet CP-even and -odd scalars, and the NLSP) can impact the dynamics of BBN if a large enough abundance is produced, and they are sufficiently long-lived, particularly if their decays produce hadrons or significant radiation.

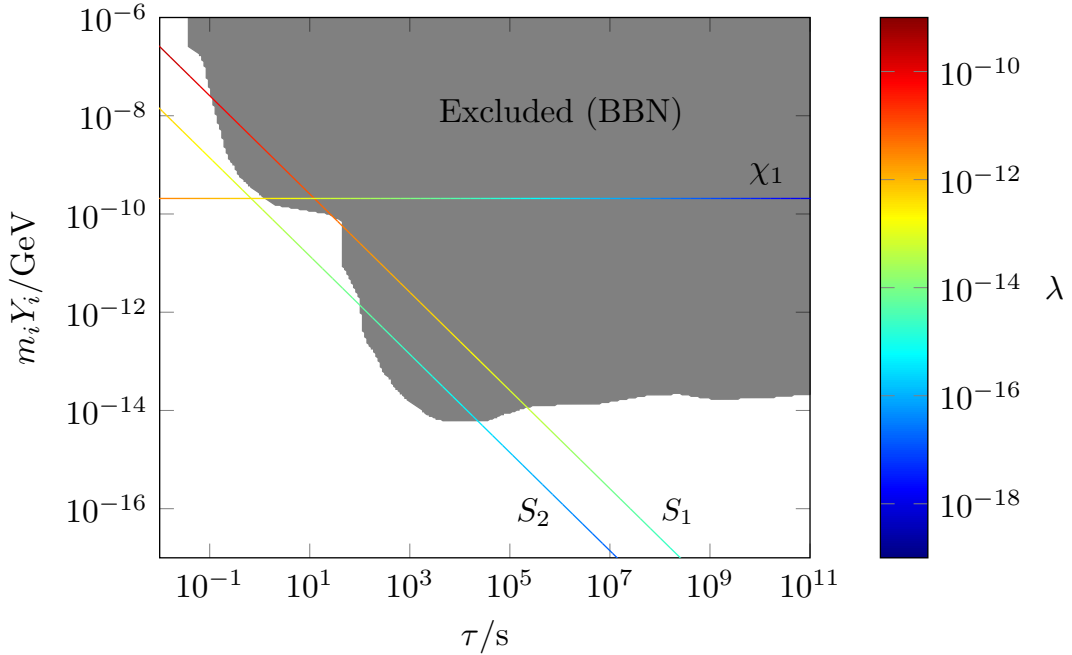


Figure 6.1: This plot illustrates how the lifetimes and abundances of the three long-lived particles vary with λ , for κ/λ (and all other parameters) fixed. As described in the text, we take the constraints from BBN on a particle of mass 30 GeV decaying to $\bar{b}b$, which gives a conservative bound. This limit is indicated in grey. Although these constraints assume only a single particle decaying, this is a reasonable assumption for our purposes, as explained in the text. As can be seen, the NLSP lifetime scales as λ^{-2} , while the abundance does not depend on λ , so BBN constraints on the NLSP provide a simple lower bound on λ . The singlet scalar lifetimes also scale as λ^{-2} , but their abundances scale as λ^2 . This means that BBN constraints on the scalars don't give rise to a simple upper or lower limit on λ : when λ is very small, the scalar abundances are very small, and so they don't affect BBN; when λ is very large the scalar lifetimes are very short and so again they don't affect BBN. Between these two extremes, some values of λ are ruled out, as shown.

The primary decay channels for the CP-odd scalar are $S_1 \rightarrow b\bar{b}$ and $S_1 \rightarrow \tau^+\tau^-$, while the CP-even scalar can decay via a variety of channels, but the dominant channels are $S_2 \rightarrow b\bar{b}$, $S_2 \rightarrow W^+W^-$, $S_2 \rightarrow hh$ and $S_2 \rightarrow ZZ$ for our benchmark parameter values.

Following [23], we apply limits on the relic abundance of the decaying particle as a function of their lifetimes. We model the decays of all long-lived states as $X \rightarrow \bar{b}b$ to gain a conservative bound (in the sense of erring on

the side of ruling out too much parameter space rather than too little) given that decays to $\bar{b}b$ yield the most stringent limits (of the channels relevant to our model). Additionally, we take the limits for a decaying particle with mass $m_i = 30 \text{ GeV}$ - this is a lower limit for the decaying particles in our model, and hence this limit gives a conservative bound, as lighter decaying particles are more tightly constrained. This is because the number of hadrons produced in hadronisation goes like $\sim m_i^{0.3}$ and so the limit on $m_i Y_i$ increases with increasing m_i : $m_i Y_i < k(\tau, m_i) \sim m^{0.7} k'(\tau)$ [23]. These limits are taken from the upper-right of Figure 12 in [23] (which also illustrates the point that the decay described above is the most tightly constrained of the relevant channels, and so the limit we consider gives a conservative bound).

In Figure 6.1, the abundances versus lifetimes for all three decaying particles are plotted as a function of the coupling λ , along with the excluded region due to BBN. We set $A_\lambda = 1 \text{ GeV}$, $A_\kappa = -34 \text{ GeV}$ and fix κ/λ to illustrate the behaviour with the colour spectrum on each of the lines representing the size of λ .

The constraints from the NLSP decays are relatively straightforward for fixed κ/λ . The NLSP abundance is generated through freeze-out and hence is unaffected by the size of λ , while, as mentioned above, its lifetime scales like λ^{-2} (as all of its decay channels involve the feebly coupled singlino). Requiring that the NLSP decays before BBN means that we apply a lower bound on λ , if all else is fixed. If the lower bound is too large to produce the correct freeze-in abundance of singlinos, then the point in parameter space is ruled out.

As κ/λ increases, the mass of the singlino increases, reducing the number of available decay channels for the NLSP, and increasing the lifetime of the NLSP. If we applied that to the horizontal line in Figure 6.1, the effect would be to shift the colour spectrum representing the value of λ to the right, moving the lower bound to larger values of λ .

The constraints from the singlet scalars are slightly more complicated, as

their lifetimes scale like λ^{-2} , but their abundances scale like λ^2 (for fixed κ/λ). Hence, as λ increases, the lifetime of the scalars decrease but, at the same time, increasing λ increases the freeze-in abundance of the scalar. This explains the direction of the lines for S_1 and S_2 in Figure 6.1, and why increasing λ moves us up and left along the lines. Given the shape of the excluded region due to BBN, for our chosen parameter values, we find that certain ranges of λ are excluded or more positively put, certain ranges of λ are allowed as illustrated in the figure.

In creating the plot in Figure 6.1 we make the approximation of considering the effect of each decaying particle on BBN separately, that is, we do not combine their effects. This is reasonable for the parameter values we choose, given the dependence on λ of the lifetimes of the three particles. That is, there is no point in the parameter space we consider where BBN is unaffected by each of the decaying states taken individually but when combined they produce an effect that is ruled out by BBN.

It is important to note that achieving the correct freeze-in abundance requires a specific λ coupling (if all else is fixed). For our chosen point, this is of order $\lambda \sim 10^{-12}$. As can be seen from Figure 6.1, for a coupling of this size the NLSP and the CP-even singlet scalar will tend to decay far before they would have any effect on BBN. The CP-odd singlet will decay late enough to give the leading constraint on the allowed value of λ .

Using Figure 6.1 we can make some comments about the viability of scenario two. Scenario two still has the singlino as the LSP, but the dominant contribution to the DM relic abundance comes from the freeze-out and decay of the neutralino NLSP, with the freeze-in abundance of singlinos being subdominant. Assuming an MSSM benchmark such that the neutralino NLSP abundance is large enough to achieve this, the effect in Figure 6.1 would be to move the horizontal neutralino line up. Due to the shape of the BBN excluded region, this would moderately increase the lower bound on λ . However, as we

are considering a sub-dominant freeze-in abundance this requires an even more suppressed coupling λ , increasing the lifetime of the NLSP, meaning that the model would live more towards the blue end of the χ_1 line and hence will be ruled out by BBN.

We may still expect constraints from the decays of S_1 and S_2 , but these will become less important for smaller λ , as their abundances decrease and potentially fall below the BBN excluded region in Figure 6.1. Scenario two however will be ruled out by the NLSP decays.

Constraints from the Higgs Sector

To examine the model in more detail and, in particular, to evaluate whether there are regions of parameter space that produce the correct singlino abundance, we will now vary both κ and λ and hence allow the ratio κ/λ to vary.

The ratio κ/λ feeds in to the MSSM CP-odd Higgs mass as

$$m_A^2 = \frac{2\mu (A_\lambda + \frac{\kappa}{\lambda}\mu)}{\sin 2\beta} + \delta m_A^2, \quad (6.3.4)$$

where δm_A^2 represents higher order corrections, which for our benchmark parameter values tends to be moderately large and negative. Limits in the $(m_A, \tan \beta)$ plane (see for example Figure 1 of [305]) derived from searches for additional Higgs bosons or the requirement that the lightest CP-even Higgs has predicted mass and couplings compatible with observation determines a lower limit for m_A for a given value of $\tan \beta$.

With fixed values of μ and A_λ , the lower limit on m_A will translate into a lower limit on κ/λ . For the chosen MSSM benchmark, we have taken $\tan \beta = 8.5$, which gives a lower limit of $m_A > 610$ GeV, leading to the limit on κ/λ calculated using micrOMEGAs [262] and NMSSMTools [307]

$$\frac{\kappa}{\lambda} \gtrsim 0.078. \quad (6.3.5)$$

The limit on m_A becomes more stringent as $\tan \beta$ is increased (as can be seen in Figure 1 of [305]) with the leading constraint in this region of

parameter space coming from searches for H/A decays to $\tau^+\tau^-$. Hence, if $\tan\beta$ is increased, the lower bound on κ/λ also increases, and the available parameter space shrinks. This explains why we are interested in a value of $\tan\beta$ which is as small as possible, as mentioned in Section 6.3.

Constraints from the requirement that the model allows for successful Electroweak Symmetry Breaking are also included in our analysis. For the benchmark point we consider, we find a limit

$$\frac{\kappa}{\lambda} \gtrsim 0.035. \quad (6.3.6)$$

This particular value of κ/λ gives $m_A^2 = 0$, with a smaller value of the ratio predicting $m_A^2 < 0$ indicating that the vacuum described by v_u, v_d and v_s is no longer the global minimum.

Lastly, it is required that in this scenario, the singlino is the LSP. Increasing the ratio κ/λ increases the mass of the singlino, whose mass at tree-level is $m_{\chi_s} = 2\kappa\mu/\lambda$. For the chosen benchmark point, detailed in Equation 6.3.1 the NLSP has a mass of 939 GeV leading to a limit of $\kappa/\lambda \lesssim 0.47$.

6.3.3 Results

In Figure 6.2 we plot the constraints on the singlino DM scenario as a function of κ and λ using micrOMEGAs [262]. We use the benchmark for the MSSM parameters as listed in Equation 6.3.1. Additionally, we set $A_\lambda = 1$ GeV and $A_\kappa = -34$ GeV.

The solid black line indicates the contour in the κ, λ where the correct relic abundance for the singlino is achieved. The abundance is made up of two components: the dominant contribution from the directly frozen-in singlinos and a sub-dominant contribution from the freeze-out and decay of the neutralino NLSP.

In the top left corner, the grey exclusion region corresponds to where $\kappa/\lambda > 0.47$ and so the singlino is no longer the LSP. This region is labelled ‘‘Singlino

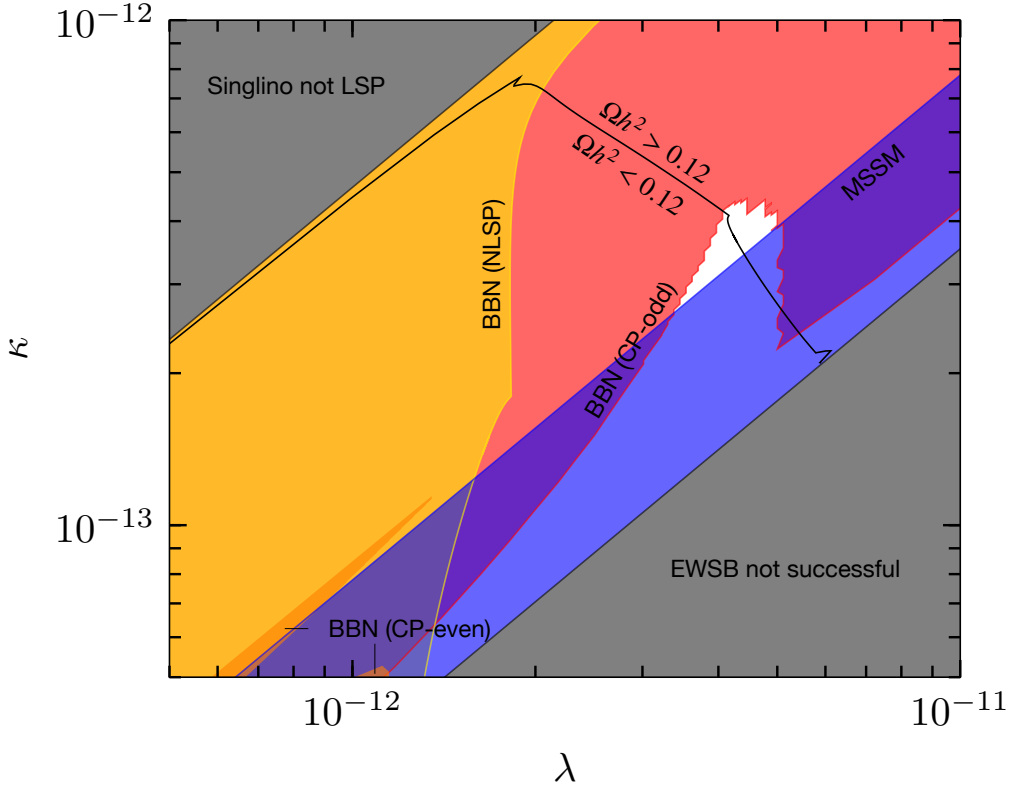


Figure 6.2: This plot shows the allowed region in the $\kappa - \lambda$ parameter space, within the M_h^{125} benchmark (Equation 6.3.1 with NMSSM parameter values $A_\kappa = -34$ GeV and $A_\lambda = 1$ GeV). The solid black contour represents parameter points with the correct DM relic abundance. The regions ruled out by long-lived particle decays are shown labelled "BBN (NLSP/CP-odd/even)" and are coloured yellow, red and orange respectively. The blue region labelled "MSSM" is ruled out by limits on MSSM Higgs masses. In the bottom right grey region labelled "EWSB not successful" there is no EWSB and in the top left grey area labelled "Singlino not LSP" the neutralino is the LSP. See text for details.

not LSP".

In the bottom right-hand corner, the grey region labelled "EWSB not successful" represents parameter values for which the desired vacuum structure is no longer achieved, the upper left boundary of which is given by $\kappa/\lambda = 0.035$. The blue strip labelled "MSSM" is excluded due to limits in the MSSM Higgs states parameterised as $m_A > 610$ GeV as discussed above. For this region of parameter space, the dominant constraint comes from ensuring that the

lightest neutral Higgs boson is sufficiently heavy to match observations. The red, yellow and orange regions are excluded due to constraints coming from BBN. The red region is ruled out due to the decay of the frozen-in CP-odd scalar state S_1 , the yellow region is ruled out due to the decays of the neutralino NLSPs and the small orange regions are ruled out due to the decays of the frozen-in CP-even scalar state, S_2 .

There is a kink in the dark matter abundance line just before it intersects with the BBN (CP-odd) constraint region. This corresponds to the (κ/λ) threshold at which $m_{\chi_1} = m_{\chi_s} + m_A (= m_{\chi_s} + m_H)$, above which the NLSP's only significant decay channels are into a singlino plus a Higgs or Z boson - all other channels are very suppressed, such as the decays into a singlino plus a singlet scalar which are suppressed by an additional factor of λ^2 . As κ/λ increases towards this threshold, fewer decay channels are available and the NLSP width decreases more rapidly, while as κ/λ increases beyond this threshold there are no more significant decay channels to turn off (until the singlino mass approaches the NLSP mass) and so the NLSP width decreases less rapidly. This affects the behaviour of the singlino freeze-in abundance: as κ/λ increases towards this threshold, the rapid decrease in NLSP width means that the freeze-in abundance increases more gradually (corresponding to a steeper slope in the $\kappa - \lambda$ plane, as an increase in κ/λ - i.e. a move upwards on the plot - requires a smaller decrease in λ - i.e. a smaller move leftwards on the plot - to offset it); while above the threshold the freeze-in abundance increases more rapidly with increasing κ/λ (corresponding to a shallower slope in the $\kappa - \lambda$ plane), leading to the kink behaviour observed.

This scenario requires approximately $19 \text{ GeV} < -A_\kappa < 52 \text{ GeV}$ and $-10 \text{ GeV} < A_\lambda < 8 \text{ GeV}$.

6.4 Neutralino Dark Matter

We next consider the scenarios where the neutralino is the LSP. These two scenarios are less motivated in the context of this work. For example, this case is much more similar to the standard MSSM with the neutralino as the dark matter, but with addition of the frozen-in unstable states S_1, S_2 and χ_s . Once all the frozen-in singlet particles have decayed, they play no further role in the model, for example at colliders. The MSSM with neutralino DM is well studied and, due to the lack of observation at direct detection or collider experiments, well constrained [308, 309, 310, 311, 312, 313].

The additional particles further constrain the available parameter space, in two ways: firstly, the singlino decays top up the neutralino relic abundance. This tightens the upper bound on the neutralino relic abundance, hence requiring a larger than “standard” freeze-out annihilation cross-section. This can in some cases be something desirable (see e.g. [304]) as it can boost indirect detection signals, but at the same time the model can run into issues with limits from direct detection depending on how the annihilation rate is increased. Secondly, it introduces new constraints stemming from the impact that the singlet particles’ decays can have on BBN.

Due to the similarity of the scenario to the well-studied MSSM, we do not perform a scan of the available parameter space, but rather note that this situation is possible, and effective MSSM models with this mass ordering can satisfy all experimental constraints. For example, drawing on the best-fit point from [309] we take MSSM parameters $M_{\tilde{f}} = 152.35$ GeV for first and second generation sfermions, set corresponding Higgs-sfermion interaction terms $A_{\tilde{f}}$ to zero; and remaining parameters

$$\begin{aligned} M_{Q,U,D_3} &= 2234.41 \text{ GeV}, & M_{L_3} &= 1995.54 \text{ GeV}, & M_{E_3} &= 1250.89 \text{ GeV} \\ M_1 &= -136.09 \text{ GeV}, & M_2 &= 149.98 \text{ GeV}, & M_3 &= 2000.09 \text{ GeV} \end{aligned}$$

$$\mu = -778.01 \text{ TeV}, \quad A_b = A_\tau = 6396.91 \text{ GeV}, \quad A_t = 2380.81 \text{ GeV},$$

along with $\tan \beta = 17.81$, and NMSSM values $A_\lambda = 410 \text{ GeV}$, $A_\kappa = 10 \text{ GeV}$, $\lambda = 2.74 \times 10^{-12}$, and $\kappa = 1.67 \times 10^{-12}$. We find that all experimental constraints can be satisfied for this benchmark.

6.4.1 Phenomenology

In this case, we again have four particles of interest, however their roles are altered compared to the case where the singlino is the LSP. The lightest MSSM neutralino is now the dark matter candidate, and the dominant part of its relic density is produced via freeze-out. The singlino will freeze-in and then decay to the neutralino LSP after it has frozen-out, topping up its abundance.

The additional scalars also freeze-in, but then decay to SM particles. This can slightly dilute the relic density, if the decays occur after the neutralinos have frozen out, however this effect is extremely small as it was in the singlino DM case above.

With the parameter values specified above, the neutralino LSP has a mass $\approx 134 \text{ GeV}$ with a freeze-out abundance of $\Omega h^2 = 5.17 \times 10^{-2}$, which is around a factor of 2 down on the required value from observation.

With particular choices of λ and κ , such as those specified above, the required freeze-in abundance of singlinos can be found that tops up the neutralino DM relic density. The choices of λ and κ will then determine the freeze-in abundances of S_1 and S_2 , as well as the lifetimes of all three frozen-in states.

In analogy with the singlino LSP case, the decay of the three long-lived particles can interfere with BBN if a large enough abundance is produced, and they are sufficiently long-lived.

Figure 6.3 illustrates how the particle lifetimes and abundances vary with λ for fixed κ/λ . We again indicate the region ruled out by BBN constraints on the decaying particles.

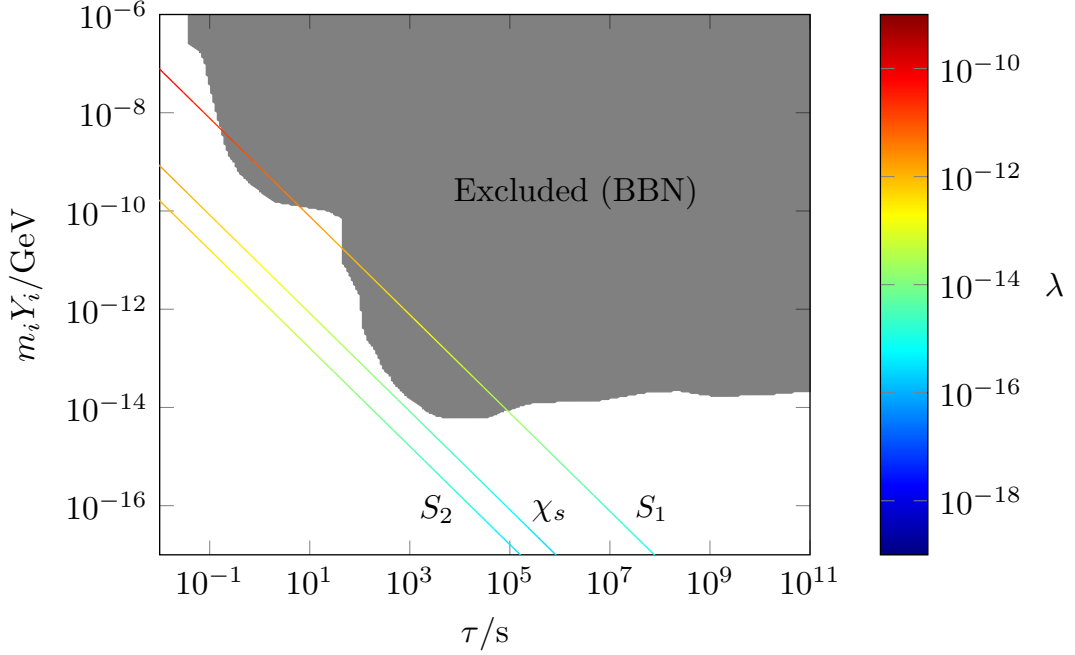


Figure 6.3: This plot illustrates how the lifetimes and abundances of the three long-lived singlet particles vary with λ , for $\frac{\kappa}{\lambda}$ (and all other parameters) fixed, in the case where a neutralino is the LSP. The constraints from BBN on a particle (of mass 30 GeV) decaying to $\bar{b}b$ is also indicated in grey. As described in the text, this choice of limit gives a conservative bound. Although these limits assume only a single particle decaying, this is a reasonable assumption for our purposes, as explained in the text.

As can be seen from Figure 6.3, for almost all values of λ the CP-odd scalar is the only particle which crosses the excluded region.

As opposed to the case where the singlino is the LSP, the BBN constraints don't give rise to a lower limit on λ . This is unsurprising - in this case, as $\lambda \rightarrow 0$, the singlet particles have extremely small abundances and essentially no impact on the model.

We find that setting $\lambda = 2.74 \times 10^{-12}$, $\kappa = 1.67 \times 10^{-12}$ generates a singlino with mass $m_{\chi_s} \approx 945$ GeV with a freeze-in abundance of $\Omega h^2 \approx 0.48$. The additional neutralino abundance this generates once the singlino decays is $\Delta\Omega h^2 = 0.48 m_{\chi_1} / m_{\chi_s} = 6.8 \times 10^{-2}$, which is enough to top up the neutralino abundance to the required value.

In reference to Figure 6.3, the only possible BBN constraint comes from

the decays of S_1 . For these values of λ and κ , the CP-odd scalar mass is $m_{S_1} \approx 119 \text{ GeV}$ and has a frozen-in abundance $\Omega h^2 = 0.034$, equivalent to a yield of $m_{S_1} Y_{CP\text{-}odd} = 1.22 \times 10^{-10}$) with a lifetime of $\tau_{S_1} \approx 6.3 \text{ s}$. This places the model point just below the BBN exclusion region.

Pushing this scenario further, we can look for MSSM parameter values where the freeze-in abundance of the neutralino is further suppressed and the dominant contribution to the abundance comes from freeze-out and decay. The main challenge with such a scenario is finding neutralino DM that has such a large freeze-out annihilation rate to suppress the freeze-out abundance whilst avoiding constraints from direct and indirect detection.

Moving the scenario in the opposite direction, we can reduce the freeze-in abundance of the singlino by decreasing λ leaving neutralino freeze-out to explain the observed DM abundance. Provided λ is sufficiently small, the very long-lived states S_1, S_2 and χ_S have abundances that are too small to effect BBN. The motivation for such a scenario is however difficult to imagine.

6.5 Conclusion

In this chapter, we have considered how the ‘effective MSSM’ can give rise to cosmologically viable models. We have found that it is possible for the singlino to be the LSP, and that in this case the correct dark matter abundance can be produced via a combination of freeze-in and freeze-out. This can be done while satisfying constraints from big bang nucleosynthesis and collider experiments, but only for very specific values of the parameters. It is worth pointing out that in this case, the direct detection limits have been bypassed, at the cost of introducing cosmological constraints due to the additional long-lived particles.

We have also found that the effective MSSM can also produce a viable dark matter candidate in the case where the singlino is not the LSP, via a frozen-out neutralino. However, this scenario is generally very similar to the usual

MSSM case with frozen-out neutralino DM but with additional dark matter from singlino decays, which brings the model closer to being ruled out by direct detection limits, and additional long-lived particles, which further reduce the parameter space. For this reason, along with the fact that the MSSM is already well-studied, we have not performed a full scan of the available parameter space, but rather consider this a demonstration of possibility.

Chapter 7

Conclusion

In this thesis, we have discussed various aspects of cosmology and particle physics. We have explored two different classes of dark matter model, each with an isolated dark sector containing a dark matter candidate which only has very weak or indirect interactions with the Standard Model particles.

After Chapters 2, 3 and 4 covering cosmology and its relevance to particle physics, dark matter, and supersymmetry respectively, we explored the first class of these dark matter models in Chapter 5. This discussed models based around a ‘Portalino’ framework, i.e. models which contain right-handed neutrinos ν_R which couple to the Standard Model neutrinos via a coupling with the left-handed leptons and the Higgs, $\lambda_\nu LH$, which gives rise to a mixing between ν_R and ν_L after electroweak symmetry breaking, with a similar symmetry-breaking process occurring in the dark sector, leading to a mixing between ν_R and the ‘Portalino’ in the dark sector, which is an analogue to the Standard Model neutrinos. We considered Portalino-based models which included a Majorana mass for the right-handed neutrinos in order to produce neutrino masses of the correct size. We found that the correct dark matter density can be produced in a model of this type, with the dark matter particle freezing-out via annihilations to Portalinos. We showed that these Portalinos tend to be relatively long-lived, and their decays can give rise to a dominant constraint on the model. We considered a wide range of Portalino masses

$0.02 \text{ eV} \lesssim m_n \lesssim \text{TeV}$, and showed that these fall into three qualitatively different scenarios: the ‘heavy’, ‘intermediate’ and ‘light’ cases. In the heavy case, the Portalinos are constrained by the requirement that they decay before neutrinos decouple, along with constraints arising from the mixing between the Portalinos and neutrinos. The intermediate case contains Portalinos which decay after recombination, however we showed that it is inconsistent with cosmological constraints. The light case is characterised by Portalinos which don’t decay within the lifetime of the universe, and is constrained by its impact on BBN and the CMBR. These models may be probed in future, such as via indirect dark matter signals in the form of highly boosted, mono-energetic Portalinos produced in Dark Matter annihilations, which may provide a target for current and future neutrino telescopes.

Following this, in Chapter 6, we investigated how the correct dark matter abundance can arise in the ‘effective MSSM’, which is similar to the MSSM but with an additional extremely weakly coupled singlet superfield, which provides the Higgs mass term μ . This feeble coupling leads to freeze-in production of the singlet particles, along with long lifetimes for the singlet scalars and the next-to-lightest superpartner (NLSP). We explored two possibilities: that the singlino (the singlet fermion) is the LSP and hence the dark matter candidate; or that one of the MSSM-like neutralinos is the LSP, with a particular interest in the first possibility. In the singlino-LSP case, the dark matter abundance is primarily produced via freeze-in of the singlino, which is then topped up by decays of the frozen-out NLSP. This case resembles the MSSM in many ways, with two key differences: firstly, the decays of the NLSP and singlet scalars effect big bang nucleosynthesis, and so are tightly constrained. Secondly, due to the frozen-out neutralinos decaying to singlinos, this set-up can evade direct detection constraints. We then discussed the case where an MSSM-like neutralino is the LSP, however we highlighted that this case is of less interest due to enhanced constraints from direct detection, alongside additional constraints

from big bang nucleosynthesis.

In each of the models we considered, we focused on scenarios in which the dark matter is isolated from the visible sector. This can reduce the strength of direct detection and collider constraints on the model, but also gives rise to long-lived particles in the theory. The behaviour and decays of these particles can be cosmologically important, leading to stringent cosmological constraints, and possibly leading to characteristic indirect signals. These long-lived particles could possibly also be detected via distinctive displaced vertex signals in collider experiments.

These models illustrate the strength of leveraging cosmology and particle physics together to gain an understanding of the nature and origin of dark matter.

Bibliography

- [1] N. Aghanim et al. Planck 2018 results. VI. Cosmological parameters. *Astron. Astrophys.*, 641:A6, 2020.
- [2] Scott Dodelson. *Modern Cosmology*. Academic Press, Amsterdam, 2003.
- [3] Edward W. Kolb and Michael S. Turner. *The Early Universe*, volume 69. Westview Press, 1990.
- [4] Alan H. Guth. The Inflationary Universe: A Possible Solution to the Horizon and Flatness Problems. *Phys. Rev. D*, 23:347–356, 1981.
- [5] K. Sato. First Order Phase Transition of a Vacuum and Expansion of the Universe. *Mon. Not. Roy. Astron. Soc.*, 195:467–479, 1981.
- [6] Alexei A. Starobinsky. A New Type of Isotropic Cosmological Models Without Singularity. *Phys. Lett. B*, 91:99–102, 1980.
- [7] Andrei D. Linde. A New Inflationary Universe Scenario: A Possible Solution of the Horizon, Flatness, Homogeneity, Isotropy and Primordial Monopole Problems. *Phys. Lett. B*, 108:389–393, 1982.
- [8] Andreas Albrecht and Paul J. Steinhardt. Cosmology for Grand Unified Theories with Radiatively Induced Symmetry Breaking. *Phys. Rev. Lett.*, 48:1220–1223, 1982.
- [9] Andrei D. Linde. Chaotic Inflation. *Phys. Lett. B*, 129:177–181, 1983.
- [10] D. N. Spergel et al. Wilkinson Microwave Anisotropy Probe (WMAP) three year results: implications for cosmology. *Astrophys. J. Suppl.*, 170:377, 2007.

- [11] N. Aghanim et al. Planck 2018 results. I. Overview and the cosmological legacy of Planck. *Astron. Astrophys.*, 641:A1, 2020.
- [12] Adam G. Riess et al. Observational evidence from supernovae for an accelerating universe and a cosmological constant. *Astron. J.*, 116:1009–1038, 1998.
- [13] S. Perlmutter et al. Measurements of Ω and Λ from 42 high redshift supernovae. *Astrophys. J.*, 517:565–586, 1999.
- [14] Gianpiero Mangano, Gennaro Miele, Sergio Pastor, Teguyayco Pinto, Ofelia Pisanti, and Pasquale D. Serpico. Relic neutrino decoupling including flavor oscillations. *Nucl. Phys. B*, 729:221–234, 2005.
- [15] Pablo F. de Salas and Sergio Pastor. Relic neutrino decoupling with flavour oscillations revisited. *JCAP*, 07:051, 2016.
- [16] K. Enqvist, K. Kainulainen, and V. Semikoz. Neutrino annihilation in hot plasma. *Nucl. Phys. B*, 374:392–404, 1992.
- [17] K. N. Abazajian et al. Neutrino Physics from the Cosmic Microwave Background and Large Scale Structure. *Astropart. Phys.*, 63:66–80, 2015.
- [18] Céline Boehm, Matthew J. Dolan, and Christopher McCabe. A Lower Bound on the Mass of Cold Thermal Dark Matter from Planck. *JCAP*, 08:041, 2013.
- [19] Karsten Jedamzik. Big bang nucleosynthesis constraints on hadronically and electromagnetically decaying relic neutral particles. *Phys. Rev. D*, 74:103509, 2006.
- [20] Sean Bailly, Karsten Jedamzik, and Gilbert Moulta. Gravitino Dark Matter and the Cosmic Lithium Abundances. *Phys. Rev. D*, 80:063509, 2009.

- [21] Sean Baily. Gravitino dark matter and the lithium primordial abundance within a pre-BBN modified expansion. *JCAP*, 03:022, 2011.
- [22] Brian D. Fields, Keith A. Olive, Tsung-Han Yeh, and Charles Young. Big-Bang Nucleosynthesis After Planck. *JCAP*, 03:010, 2020.
- [23] Masahiro Kawasaki, Kazunori Kohri, Takeo Moroi, and Yoshitaro Takaesu. Revisiting Big-Bang Nucleosynthesis Constraints on Long-Lived Decaying Particles. *Phys. Rev. D*, 97(2):023502, 2018.
- [24] R. L. Workman. Review of Particle Physics. *PTEP*, 2022:083C01, 2022.
- [25] Andreas Goudelis, Maxim Pospelov, and Josef Pradler. Light Particle Solution to the Cosmic Lithium Problem. *Phys. Rev. Lett.*, 116(21):211303, 2016.
- [26] P. D. O'Malley, D. W. Bardayan, A. S. Adekola, S. Ahn, K. Y. Chae, J. A. Cizewski, S. Graves, M. E. Howard, K. L. Jones, R. L. Kozub, L. Lindhardt, M. Matos, B. M. Moazen, C. D. Nesaraja, S. D. Pain, W. A. Peters, S. T. Pittman, K. T. Schmitt, J. F. Shriner, M. S. Smith, I. Spassova, S. Y. Strauss, and J. L. Wheeler. Search for a resonant enhancement of the ${}^7\text{be} + d$ reaction and primordial ${}^7\text{li}$ abundances. *Phys. Rev. C*, 84:042801, Oct 2011.
- [27] F. Hammache et al. Search for new resonant states in ${}^{10}\text{C}$ and ${}^{11}\text{C}$ and their impact on the cosmological lithium problem. *Phys. Rev. C*, 88(6):062802, 2013.
- [28] Mark W. Paris, Gerald M. Hale, Anna C. Hayes-Sterbenz, and Gerard Jungman. R-matrix analysis of reactions in the 9B compound system. *Nucl. Data Sheets*, 120:184–187, 2014.

- [29] S. Q. Hou, J. J. He, A. Parikh, D. Kahl, C. A. Bertulani, T. Kajino, G. J. Mathews, and G. Zhao. Non-extensive Statistics to the Cosmological Lithium Problem. *Astrophys. J.*, 834(2):165, 2017.
- [30] L. Sbordone et al. The metal-poor end of the Spite plateau. 1: Stellar parameters, metallicities and lithium abundances. *Astron. Astrophys.*, 522:A26, 2010.
- [31] Olivier Richard, Georges Michaud, and Jacques Richer. Implications of WMAP observations on Li abundance and stellar evolution models. *Astrophys. J.*, 619:538–548, 2005.
- [32] Brian D. Fields. The primordial lithium problem. *Ann. Rev. Nucl. Part. Sci.*, 61:47–68, 2011.
- [33] John D. Barrow. Observational Limits on the Time Evolution of Extra Spatial Dimensions. *Phys. Rev. D*, 35:1805–1810, 1987.
- [34] Bruce A. Campbell and Keith A. Olive. Nucleosynthesis and the time dependence of fundamental couplings. *Phys. Lett. B*, 345:429–434, 1995.
- [35] L. Bergstrom, S. Iguri, and H. Rubinstein. Constraints on the variation of the fine structure constant from big bang nucleosynthesis. *Phys. Rev. D*, 60:045005, 1999.
- [36] J. C. Berengut, E. Epelbaum, V. V. Flambaum, C. Hanhart, U. G. Meissner, J. Nebreda, and J. R. Pelaez. Varying the light quark mass: impact on the nuclear force and Big Bang nucleosynthesis. *Phys. Rev. D*, 87(8):085018, 2013.
- [37] Alain Coc, Nelson J. Nunes, Keith A. Olive, Jean-Philippe Uzan, and Elisabeth Vangioni. Coupled Variations of Fundamental Couplings and Primordial Nucleosynthesis. *Phys. Rev. D*, 76:023511, 2007.

- [38] V. V. Flambaum and E. V. Shuryak. Limits on cosmological variation of strong interaction and quark masses from big bang nucleosynthesis, cosmic, laboratory and Oklo data. *Phys. Rev. D*, 65:103503, 2002.
- [39] C. J. A. P. Martins. Primordial nucleosynthesis with varying fundamental constants: Degeneracies with cosmological parameters. *Astron. Astrophys.*, 646:A47, 2021.
- [40] Wayne Hu and Scott Dodelson. Cosmic Microwave Background Anisotropies. *Ann. Rev. Astron. Astrophys.*, 40:171–216, 2002.
- [41] Zhen Hou, Ryan Keisler, Lloyd Knox, Marius Millea, and Christian Reichardt. How Massless Neutrinos Affect the Cosmic Microwave Background Damping Tail. *Phys. Rev. D*, 87:083008, 2013.
- [42] Sergei Bashinsky and Uros Seljak. Neutrino perturbations in CMB anisotropy and matter clustering. *Phys. Rev. D*, 69:083002, 2004.
- [43] Daniel Baumann, Daniel Green, Joel Meyers, and Benjamin Wallisch. Phases of New Physics in the CMB. *JCAP*, 01:007, 2016.
- [44] F. Zwicky. Die Rotverschiebung von extragalaktischen Nebeln. *Helv. Phys. Acta*, 6:110–127, 1933.
- [45] K. C. Freeman. On the disks of spiral and SO Galaxies. *Astrophys. J.*, 160:811, 1970.
- [46] Vera C. Rubin and W. Kent Ford, Jr. Rotation of the Andromeda Nebula from a Spectroscopic Survey of Emission Regions. *Astrophys. J.*, 159:379–403, 1970.
- [47] V. C. Rubin, N. Thonnard, and W. K. Ford, Jr. Rotational properties of 21 SC galaxies with a large range of luminosities and radii, from NGC

- 4605 /R = 4kpc/ to UGC 2885 /R = 122 kpc/. *Astrophys. J.*, 238:471, 1980.
- [48] M. Milgrom. A Modification of the Newtonian dynamics as a possible alternative to the hidden mass hypothesis. *Astrophys. J.*, 270:365–370, 1983.
- [49] Maxim Markevitch, A. H. Gonzalez, D. Clowe, A. Vikhlinin, L. David, W. Forman, C. Jones, S. Murray, and W. Tucker. Direct constraints on the dark matter self-interaction cross-section from the merging galaxy cluster 1E0657-56. *Astrophys. J.*, 606:819–824, 2004.
- [50] Douglas Clowe, Marusa Bradac, Anthony H. Gonzalez, Maxim Markevitch, Scott W. Randall, Christine Jones, and Dennis Zaritsky. A direct empirical proof of the existence of dark matter. *Astrophys. J. Lett.*, 648:L109–L113, 2006.
- [51] M. Markevitch, A. H. Gonzalez, L. David, A. Vikhlinin, S. Murray, W. Forman, C. Jones, and W. Tucker. A Textbook example of a bow shock in the merging galaxy cluster 1E0657-56. *Astrophys. J. Lett.*, 567:L27, 2002.
- [52] S. W. Allen, R. W. Schmidt, H. Ebeling, A. C. Fabian, and L. van Speybroeck. Constraints on dark energy from Chandra observations of the largest relaxed galaxy clusters. *Mon. Not. Roy. Astron. Soc.*, 353:457, 2004.
- [53] Alexey Vikhlinin, A. Kravtsov, W. Forman, C. Jones, M. Markevitch, S. S. Murray, and L. Van Speybroeck. Chandra sample of nearby relaxed galaxy clusters: Mass, gas fraction, and mass-temperature relation. *Astrophys. J.*, 640:691–709, 2006.

- [54] Ignacio Ferreras, Mairi Sakellariadou, and Muhammad Furqaan Yusaf. The necessity of dark matter in MOND within galactic scales. *Phys. Rev. Lett.*, 100:031302, 2008.
- [55] David Harvey, Richard Massey, Thomas Kitching, Andy Taylor, and Eric Tittley. The non-gravitational interactions of dark matter in colliding galaxy clusters. *Science*, 347:1462–1465, 2015.
- [56] Marusa Bradac, Steven W. Allen, Tommaso Treu, Harald Ebeling, Richard Massey, R. Glenn Morris, Anja von der Linden, and Douglas Applegate. Revealing the properties of dark matter in the merging cluster MACSJ0025.4-1222. *Astrophys. J.*, 687:959, 2008.
- [57] G. Efstathiou and J. Silk. The Formation of Galaxies. *Fund. Cosmic Phys.*, 9:1–138, November 1983.
- [58] N. Vittorio and J. Silk. Fine-scale anisotropy of the cosmic microwave background in a universe dominated by cold dark matter. *Astrophys. J. Lett.*, 285:L39–L43, 1984.
- [59] G. Efstathiou, J. R. Bond, and Simon D. M. White. COBE Background radiation anisotropies and large scale structure in the universe. *Mon. Not. Roy. Astron. Soc.*, 258:1–6, 1992.
- [60] S. D. M. White, C. S. Frenk, and M. Davis. Clustering in a neutrino-dominated universe. *Astrophys. J.*, 274:L1–L5, November 1983.
- [61] Ya. B. Zel’dovich. Fragmentation of a homogeneous medium under the action of gravitation. *Astron. Astrophys.*, 5:84, 1970.
- [62] J. R. Bond and A. S. Szalay. The collisionless damping of density fluctuations in an expanding universe. *Astrophys. J.*, 274:443–468, November 1983.

- [63] J. R. Bond, A. S. Szalay, and Michael S. Turner. Formation of Galaxies in a Gravitino Dominated Universe. *Phys. Rev. Lett.*, 48:1636, 1982.
- [64] Scott Dodelson and Lawrence M. Widrow. Sterile-neutrinos as dark matter. *Phys. Rev. Lett.*, 72:17–20, 1994.
- [65] Julio F. Navarro, Carlos S. Frenk, and Simon D. M. White. The Structure of cold dark matter halos. *Astrophys. J.*, 462:563–575, 1996.
- [66] B. Moore. Evidence against dissipationless dark matter from observations of galaxy haloes. *Nature*, 370:629, 1994.
- [67] Michael Boylan-Kolchin, James S. Bullock, and Manoj Kaplinghat. Too big to fail? The puzzling darkness of massive Milky Way subhaloes. *Mon. Not. Roy. Astron. Soc.*, 415:L40, 2011.
- [68] Michael Boylan-Kolchin, James S. Bullock, and Manoj Kaplinghat. The Milky Way’s bright satellites as an apparent failure of LCDM. *Mon. Not. Roy. Astron. Soc.*, 422:1203–1218, 2012.
- [69] G Kauffmann, Simon D. M. White, and B. Guiderdoni. The Formation and Evolution of Galaxies Within Merging Dark Matter Haloes. *Mon. Not. Roy. Astron. Soc.*, 264:201, 1993.
- [70] Anatoly A. Klypin, Andrey V. Kravtsov, Octavio Valenzuela, and Francisco Prada. Where are the missing Galactic satellites? *Astrophys. J.*, 522:82–92, 1999.
- [71] B. Moore, S. Ghigna, F. Governato, G. Lake, Thomas R. Quinn, J. Stadel, and P. Tozzi. Dark matter substructure within galactic halos. *Astrophys. J. Lett.*, 524:L19–L22, 1999.
- [72] Mark R. Lovell, Vincent Eke, Carlos S. Frenk, Liang Gao, Adrian Jenkins, Tom Theuns, Jie Wang, D. M. White, Alexey Boyarsky, and Oleg

- Ruchayskiy. The Haloes of Bright Satellite Galaxies in a Warm Dark Matter Universe. *Mon. Not. Roy. Astron. Soc.*, 420:2318–2324, 2012.
- [73] Mark R. Lovell, Carlos S. Frenk, Vincent R. Eke, Adrian Jenkins, Liang Gao, and Tom Theuns. The properties of warm dark matter haloes. *Mon. Not. Roy. Astron. Soc.*, 439:300–317, 2014.
- [74] Shunsaku Horiuchi, Brandon Bozek, Kevork N. Abazajian, Michael Boylan-Kolchin, James S. Bullock, Shea Garrison-Kimmel, and Jose Onorbe. Properties of resonantly produced sterile neutrino dark matter subhaloes. *Mon. Not. Roy. Astron. Soc.*, 456(4):4346–4353, 2016.
- [75] Julio F. Navarro, Vincent R. Eke, and Carlos S. Frenk. The cores of dwarf galaxy halos. *Mon. Not. Roy. Astron. Soc.*, 283:L72–L78, 1996.
- [76] Fabio Governato et al. At the heart of the matter: the origin of bulgeless dwarf galaxies and Dark Matter cores. *Nature*, 463:203–206, 2010.
- [77] Sean Tulin and Hai-Bo Yu. Dark Matter Self-interactions and Small Scale Structure. *Phys. Rept.*, 730:1–57, 2018.
- [78] K. N. Abazajian et al. Light Sterile Neutrinos: A White Paper. 4 2012.
- [79] Thomas Appelquist, Hsin-Chia Cheng, and Bogdan A. Dobrescu. Bounds on universal extra dimensions. *Phys. Rev. D*, 64:035002, 2001.
- [80] G. Belanger, M. Kakizaki, and A. Pukhov. Dark matter in UED: The Role of the second KK level. *JCAP*, 02:009, 2011.
- [81] Nicolas Deutschmann, Thomas Flacke, and Jong Soo Kim. Current LHC Constraints on Minimal Universal Extra Dimensions. *Phys. Lett. B*, 771:515–520, 2017.

- [82] Jyotiranjana Beuria, Asesh Krishna Datta, Dipsikha Debnath, and Konstantin T. Matchev. LHC Collider Phenomenology of Minimal Universal Extra Dimensions. *Comput. Phys. Commun.*, 226:187–205, 2018.
- [83] Jay Hubisz and Patrick Meade. Phenomenology of the littlest Higgs with T-parity. *Phys. Rev. D*, 71:035016, 2005.
- [84] Andreas Birkedal, Andrew Noble, Maxim Perelstein, and Andrew Spray. Little Higgs dark matter. *Phys. Rev. D*, 74:035002, 2006.
- [85] Brando Bellazzini, Csaba Csáki, and Javi Serra. Composite Higgses. *Eur. Phys. J. C*, 74(5):2766, 2014.
- [86] Lawrence J. Hall, Karsten Jedamzik, John March-Russell, and Stephen M. West. Freeze-In Production of FIMP Dark Matter. *JHEP*, 03:080, 2010.
- [87] Jonathan L. Feng, Arvind Rajaraman, and Fumihiro Takayama. Superweakly interacting massive particles. *Phys. Rev. Lett.*, 91:011302, 2003.
- [88] Edward W. Kolb, Daniel J. H. Chung, and Antonio Riotto. WIMPzillas! *AIP Conf. Proc.*, 484(1):91–105, 1999.
- [89] Jihn E. Kim and Gianpaolo Carosi. Axions and the Strong CP Problem. *Rev. Mod. Phys.*, 82:557–602, 2010. [Erratum: *Rev. Mod. Phys.* 91, 049902 (2019)].
- [90] C. Abel et al. Measurement of the Permanent Electric Dipole Moment of the Neutron. *Phys. Rev. Lett.*, 124(8):081803, 2020.
- [91] Jihn E. Kim. Weak Interaction Singlet and Strong CP Invariance. *Phys. Rev. Lett.*, 43:103, 1979.

- [92] Mikhail A. Shifman, A. I. Vainshtein, and Valentin I. Zakharov. Can Confinement Ensure Natural CP Invariance of Strong Interactions? *Nucl. Phys. B*, 166:493–506, 1980.
- [93] Michael Dine, Willy Fischler, and Mark Srednicki. A Simple Solution to the Strong CP Problem with a Harmless Axion. *Phys. Lett. B*, 104:199–202, 1981.
- [94] Georg G. Raffelt. Astrophysical axion bounds. *Lect. Notes Phys.*, 741:51–71, 2008.
- [95] John Preskill, Mark B. Wise, and Frank Wilczek. Cosmology of the Invisible Axion. *Phys. Lett. B*, 120:127–132, 1983.
- [96] Kyu Jung Bae, Ji-Haeng Huh, and Jihn E. Kim. Update of axion CDM energy. *JCAP*, 09:005, 2008.
- [97] S. S. Gershtein and Ya. B. Zeldovich. Rest Mass of Muonic Neutrino and Cosmology. *JETP Lett.*, 4:120–122, 1966.
- [98] M. Aker et al. Direct neutrino-mass measurement with sub-electronvolt sensitivity. *Nature Phys.*, 18(2):160–166, 2022.
- [99] R. E. Shrock. New Tests For, and Bounds On, Neutrino Masses and Lepton Mixing. *Phys. Lett. B*, 96:159–164, 1980.
- [100] Q. R. Ahmad et al. Measurement of the rate of $\nu_e + d \rightarrow p + p + e^-$ interactions produced by ^8B solar neutrinos at the Sudbury Neutrino Observatory. *Phys. Rev. Lett.*, 87:071301, 2001.
- [101] Maria Concepcion Gonzalez-Garcia, Michele Maltoni, and Thomas Schwetz. NuFIT: Three-Flavour Global Analyses of Neutrino Oscillation Experiments. *Universe*, 7(12):459, 2021.

- [102] Y. Fukuda et al. Evidence for oscillation of atmospheric neutrinos. *Phys. Rev. Lett.*, 81:1562–1567, 1998.
- [103] Tsutomu Yanagida. Horizontal Symmetry and Masses of Neutrinos. *Prog. Theor. Phys.*, 64:1103, 1980.
- [104] J. Schechter and J. W. F. Valle. Neutrino Masses in $SU(2) \times U(1)$ Theories. *Phys. Rev. D*, 22:2227, 1980.
- [105] Esra Bulbul, Maxim Markevitch, Adam Foster, Randall K. Smith, Michael Loewenstein, and Scott W. Randall. Detection of An Unidentified Emission Line in the Stacked X-ray spectrum of Galaxy Clusters. *Astrophys. J.*, 789:13, 2014.
- [106] Alexey Boyarsky, Oleg Ruchayskiy, Dmytro Iakubovskiy, and Jeroen Franse. Unidentified Line in X-Ray Spectra of the Andromeda Galaxy and Perseus Galaxy Cluster. *Phys. Rev. Lett.*, 113:251301, 2014.
- [107] D. Malyshev, A. Neronov, and D. Eckert. Constraints on 3.55 keV line emission from stacked observations of dwarf spheroidal galaxies. *Phys. Rev. D*, 90:103506, 2014.
- [108] Kerstin Perez, Kenny C. Y. Ng, John F. Beacom, Cora Hersh, Shunsaku Horiuchi, and Roman Krivonos. Almost closing the ν MSM sterile neutrino dark matter window with NuSTAR. *Phys. Rev. D*, 95(12):123002, 2017.
- [109] Christopher Dessert, Nicholas L. Rodd, and Benjamin R. Safdi. The dark matter interpretation of the 3.5-keV line is inconsistent with blank-sky observations. *Science*, 367(6485):1465–1467, 2020.
- [110] E. O. Nadler et al. Milky Way Satellite Census. III. Constraints on Dark Matter Properties from Observations of Milky Way Satellite Galaxies. *Phys. Rev. Lett.*, 126:091101, 2021.

- [111] John March-Russell, Hannah Tillim, and Stephen M. West. Reproductive freeze-in of self-interacting dark matter. *Phys. Rev. D*, 102(8):083018, 2020.
- [112] Clifford Cheung, Gilly Elor, Lawrence J. Hall, and Piyush Kumar. Origins of Hidden Sector Dark Matter I: Cosmology. *JHEP*, 03:042, 2011.
- [113] Robert M. Schabinger and James D. Wells. A Minimal spontaneously broken hidden sector and its impact on Higgs boson physics at the large hadron collider. *Phys. Rev. D*, 72:093007, 2005.
- [114] Brian Patt and Frank Wilczek. Higgs-field portal into hidden sectors. 5 2006.
- [115] John March-Russell, Stephen M. West, Daniel Cumberbatch, and Dan Hooper. Heavy Dark Matter Through the Higgs Portal. *JHEP*, 07:058, 2008.
- [116] Oleg Lebedev. The Higgs portal to cosmology. *Prog. Part. Nucl. Phys.*, 120:103881, 2021.
- [117] Adam Falkowski, Jose Juknevič, and Jessie Shelton. Dark Matter Through the Neutrino Portal. 8 2009.
- [118] Adam Falkowski, Christian Gross, and Oleg Lebedev. A second Higgs from the Higgs portal. *JHEP*, 05:057, 2015.
- [119] Manfred Lindner, Alexander Merle, and Viviana Niro. Enhancing Dark Matter Annihilation into Neutrinos. *Phys. Rev. D*, 82:123529, 2010.
- [120] Vannia Gonzalez Macias and Jose Wudka. Effective theories for Dark Matter interactions and the neutrino portal paradigm. *JHEP*, 07:161, 2015.

- [121] M. Blennow, E. Fernandez-Martinez, A. Olivares-Del Campo, S. Pascoli, S. Rosauero-Alcaraz, and A.V. Titov. Neutrino Portals to Dark Matter. *Eur. Phys. J. C*, 79(7):555, 2019.
- [122] Bob Holdom. Two U(1)'s and Epsilon Charge Shifts. *Phys. Lett. B*, 166:196–198, 1986.
- [123] Keith R. Dienes, Christopher F. Kolda, and John March-Russell. Kinetic mixing and the supersymmetric gauge hierarchy. *Nucl. Phys. B*, 492:104–118, 1997.
- [124] F. Del Aguila. The Physics of z-prime bosons. *Acta Phys. Polon. B*, 25:1317–1336, 1994.
- [125] K. S. Babu, Christopher F. Kolda, and John March-Russell. Leptophobic U(1) s and the R(b) - R(c) crisis. *Phys. Rev. D*, 54:4635–4647, 1996.
- [126] Yasunori Nomura and Jesse Thaler. Dark Matter through the Axion Portal. *Phys. Rev. D*, 79:075008, 2009.
- [127] Junichi Yokoyama. Formation of MACHO primordial black holes in inflationary cosmology. *Astron. Astrophys.*, 318:673, 1997.
- [128] Paul H. Frampton, Masahiro Kawasaki, Fuminobu Takahashi, and Tsutomu T. Yanagida. Primordial Black Holes as All Dark Matter. *JCAP*, 04:023, 2010.
- [129] Bohdan Paczynski. Gravitational microlensing by the galactic halo. *Astrophys. J.*, 304:1–5, 1986.
- [130] C. Alcock et al. The MACHO project: Microlensing results from 5.7 years of LMC observations. *Astrophys. J.*, 542:281–307, 2000.

- [131] P. Tisserand et al. Limits on the Macho Content of the Galactic Halo from the EROS-2 Survey of the Magellanic Clouds. *Astron. Astrophys.*, 469:387–404, 2007.
- [132] B. P. Abbott et al. Observation of Gravitational Waves from a Binary Black Hole Merger. *Phys. Rev. Lett.*, 116(6):061102, 2016.
- [133] Simeon Bird, Ilias Cholis, Julian B. Muñoz, Yacine Ali-Haïmoud, Marc Kamionkowski, Ely D. Kovetz, Alvise Raccanelli, and Adam G. Riess. Did LIGO detect dark matter? *Phys. Rev. Lett.*, 116(20):201301, 2016.
- [134] Misao Sasaki, Teruaki Suyama, Takahiro Tanaka, and Shuichiro Yokoyama. Primordial Black Hole Scenario for the Gravitational-Wave Event GW150914. *Phys. Rev. Lett.*, 117(6):061101, 2016. [Erratum: *Phys.Rev.Lett.* 121, 059901 (2018)].
- [135] Bernard Carr, Kazunori Kohri, Yuuiti Sendouda, and Jun’ichi Yokoyama. Constraints on primordial black holes. *Rept. Prog. Phys.*, 84(11):116902, 2021.
- [136] Mark Hindmarsh, Russell Kirk, and Stephen M. West. Dark Matter from Decaying Topological Defects. *JCAP*, 03:037, 2014.
- [137] Gerard Jungman, Marc Kamionkowski, and Kim Griest. Supersymmetric dark matter. *Phys. Rept.*, 267:195–373, 1996.
- [138] Kim Griest and David Seckel. Three exceptions in the calculation of relic abundances. *Phys. Rev. D*, 43:3191–3203, 1991.
- [139] Joseph Silk, Keith A. Olive, and Mark Srednicki. The Photino, the Sun and High-Energy Neutrinos. *Phys. Rev. Lett.*, 55:257–259, 1985.

- [140] Lawrence M. Krauss, Mark Srednicki, and Frank Wilczek. Solar System Constraints and Signatures for Dark Matter Candidates. *Phys. Rev. D*, 33:2079–2083, 1986.
- [141] Alain Bouquet, Pierre Salati, and Joseph Silk. γ -Ray Lines as a Probe for a Cold Dark Matter Halo. *Phys. Rev. D*, 40:3168, 1989.
- [142] Mark W. Goodman and Edward Witten. Detectability of Certain Dark Matter Candidates. *Phys. Rev. D*, 31:3059, 1985.
- [143] Andriy Kurylov and Marc Kamionkowski. Generalized analysis of weakly interacting massive particle searches. *Phys. Rev. D*, 69:063503, 2004.
- [144] P. Sikivie. Experimental Tests of the Invisible Axion. *Phys. Rev. Lett.*, 51:1415–1417, 1983. [Erratum: *Phys.Rev.Lett.* 52, 695 (1984)].
- [145] R. Khatiwada et al. Axion Dark Matter Experiment: Detailed design and operations. *Rev. Sci. Instrum.*, 92(12):124502, 2021.
- [146] J. Aalbers et al. First Dark Matter Search Results from the LUX-ZEPLIN (LZ) Experiment. 7 2022.
- [147] Yue Meng et al. Dark Matter Search Results from the PandaX-4T Commissioning Run. *Phys. Rev. Lett.*, 127(26):261802, 2021.
- [148] E. Aprile et al. Dark Matter Search Results from a One Ton-Year Exposure of XENON1T. *Phys. Rev. Lett.*, 121(11):111302, 2018.
- [149] D. S. Akerib et al. Results from a search for dark matter in the complete LUX exposure. *Phys. Rev. Lett.*, 118(2):021303, 2017.
- [150] P. A. Amaudruz et al. First results from the DEAP-3600 dark matter search with argon at SNOLAB. *Phys. Rev. Lett.*, 121(7):071801, 2018.

- [151] I. Wasserman. Possibility of Detecting Heavy Neutral Fermions in the Galaxy. *Phys. Rev. D*, 33:2071–2078, 1986.
- [152] E. Armengaud et al. Searching for low-mass dark matter particles with a massive Ge bolometer operated above-ground. *Phys. Rev. D*, 99(8):082003, 2019.
- [153] P. R. Scovell et al. Low Background Gamma Spectroscopy at the Boulby Underground Laboratory. *Astropart. Phys.*, 97:160–173, 2018.
- [154] Brianna J. Mount et al. Black Hills State University Underground Campus. *Appl. Radiat. Isot.*, 126:130–133, 2017.
- [155] Toby Falk, Andrew Ferstl, and Keith A. Olive. Variations of the neutralino elastic cross-section with CP violating phases. *Astropart. Phys.*, 13:301–316, 2000.
- [156] John Ellis, Natsumi Nagata, and Keith A. Olive. Uncertainties in WIMP Dark Matter Scattering Revisited. *Eur. Phys. J. C*, 78(7):569, 2018.
- [157] Mikhail A. Shifman, A. I. Vainshtein, and Valentin I. Zakharov. Remarks on Higgs Boson Interactions with Nucleons. *Phys. Lett. B*, 78:443–446, 1978.
- [158] John R. Ellis, Andrew Ferstl, and Keith A. Olive. Reevaluation of the elastic scattering of supersymmetric dark matter. *Phys. Lett. B*, 481:304–314, 2000.
- [159] C. Patrignani et al. Review of Particle Physics. *Chin. Phys. C*, 40(10):100001, 2016.
- [160] E. A. Bagnaschi et al. Supersymmetric Dark Matter after LHC Run 1. *Eur. Phys. J. C*, 75:500, 2015.

- [161] Torsten Bringmann et al. DarkBit: A GAMBIT module for computing dark matter observables and likelihoods. *Eur. Phys. J. C*, 77(12):831, 2017.
- [162] R. Bernabei et al. First results from DAMA/LIBRA and the combined results with DAMA/NaI. *Eur. Phys. J. C*, 56:333–355, 2008.
- [163] R. Bernabei et al. New results from DAMA/LIBRA. *Eur. Phys. J. C*, 67:39–49, 2010.
- [164] R. Bernabei et al. The dark matter: DAMA/LIBRA and its perspectives. In *16th Marcel Grossmann Meeting on Recent Developments in Theoretical and Experimental General Relativity, Astrophysics and Relativistic Field Theories*, 10 2021.
- [165] C. E. Aalseth et al. Results from a Search for Light-Mass Dark Matter with a P-type Point Contact Germanium Detector. *Phys. Rev. Lett.*, 106:131301, 2011.
- [166] C. E. Aalseth et al. Search for an Annual Modulation in a P-type Point Contact Germanium Dark Matter Detector. *Phys. Rev. Lett.*, 107:141301, 2011.
- [167] R. Agnese et al. Silicon Detector Dark Matter Results from the Final Exposure of CDMS II. *Phys. Rev. Lett.*, 111(25):251301, 2013.
- [168] G. Angloher et al. Results from 730 kg days of the CRESST-II Dark Matter Search. *Eur. Phys. J. C*, 72:1971, 2012.
- [169] Laura Baudis. WIMP Dark Matter Direct-Detection Searches in Noble Gases. *Phys. Dark Univ.*, 4:50–59, 2014.
- [170] J. Amaré et al. Annual modulation results from three-year exposure of ANAIS-112. *J. Phys. Conf. Ser.*, 2156(1):012024, 2021.

- [171] G. Adhikari et al. Three-year annual modulation search with COSINE-100. 11 2021.
- [172] G. Adhikari et al. An induced annual modulation signature in COSINE-100 data by DAMA/LIBRA’s analysis method. 8 2022.
- [173] E. Aprile et al. Excess electronic recoil events in XENON1T. *Phys. Rev. D*, 102(7):072004, 2020.
- [174] K. van Bibber, P. M. McIntyre, D. E. Morris, and G. G. Raffelt. A Practical Laboratory Detector for Solar Axions. *Phys. Rev. D*, 39:2089, 1989.
- [175] Shigetaka Moriyama. A Proposal to search for a monochromatic component of solar axions using Fe-57. *Phys. Rev. Lett.*, 75:3222–3225, 1995.
- [176] Luca Di Luzio, Marco Fedele, Maurizio Giannotti, Federico Mescia, and Enrico Nardi. Solar axions cannot explain the XENON1T excess. *Phys. Rev. Lett.*, 125(13):131804, 2020.
- [177] Itay M. Bloch, Andrea Caputo, Rouven Essig, Diego Redigolo, Mukul Sholapurkar, and Tomer Volansky. Exploring new physics with O(keV) electron recoils in direct detection experiments. *JHEP*, 01:178, 2021.
- [178] Fuminobu Takahashi, Masaki Yamada, and Wen Yin. XENON1T Excess from Anomaly-Free Axionlike Dark Matter and Its Implications for Stellar Cooling Anomaly. *Phys. Rev. Lett.*, 125(16):161801, 2020.
- [179] Alejandro H. Córscico, Leandro G. Althaus, Marcelo M. Miller Bertolami, S. O. Kepler, and Enrique García-Berro. Constraining the neutrino magnetic dipole moment from white dwarf pulsations. *JCAP*, 08:054, 2014.
- [180] Santiago Arceo Díaz, Klaus-Peter Schröder, Kai Zuber, Dennis Jack, and Elena Elsa Bricio Barrios. Constraint on the axion-electron coupling

constant and the neutrino magnetic dipole moment by using the tip-RGB luminosity of fifty globular clusters. 10 2019.

- [181] Kristjan Kannike, Martti Raidal, Hardi Veermäe, Alessandro Strumia, and Daniele Teresi. Dark Matter and the XENON1T electron recoil excess. *Phys. Rev. D*, 102(9):095002, 2020.
- [182] Bartosz Fornal, Pearl Sandick, Jing Shu, Meng Su, and Yue Zhao. Boosted Dark Matter Interpretation of the XENON1T Excess. *Phys. Rev. Lett.*, 125(16):161804, 2020.
- [183] Celine Boehm, David G. Cerdeno, Malcolm Fairbairn, Pedro A. N. Machado, and Aaron C. Vincent. Light new physics in XENON1T. *Phys. Rev. D*, 102:115013, 2020.
- [184] E. Aprile et al. Search for New Physics in Electronic Recoil Data from XENONnT. *Phys. Rev. Lett.*, 129(16):161805, 2022.
- [185] T. C. Weekes et al. Observation of TeV gamma rays from the Crab nebula using the atmospheric Cerenkov imaging technique. *Astrophys. J.*, 342:379–395, 1989.
- [186] M. Ackermann et al. Searching for Dark Matter Annihilation from Milky Way Dwarf Spheroidal Galaxies with Six Years of Fermi Large Area Telescope Data. *Phys. Rev. Lett.*, 115(23):231301, 2015.
- [187] A. Abramowski et al. Search for a Dark Matter annihilation signal from the Galactic Center halo with H.E.S.S. *Phys. Rev. Lett.*, 106:161301, 2011.
- [188] H. Abdalla et al. Sensitivity of the Cherenkov Telescope Array for probing cosmology and fundamental physics with gamma-ray propagation. *JCAP*, 02:048, 2021.

- [189] P. A. Cerenkov. Visible radiation produced by electrons moving in a medium with velocities exceeding that of light. *Phys. Rev.*, 52:378–379, 1937.
- [190] W. C. Haxton. The Nuclear Response of Water Cherenkov Detectors to Supernova and Solar Neutrinos. *Phys. Rev. D*, 36:2283, 1987.
- [191] Rasha Abbasi et al. Indirect search for dark matter in the Galactic Centre with IceCube. *PoS, ICRC2021:524*, 2021.
- [192] K. Abe et al. Indirect search for dark matter from the Galactic Center and halo with the Super-Kamiokande detector. *Phys. Rev. D*, 102(7):072002, 2020.
- [193] A. Albert et al. Search for secluded dark matter towards the Galactic Centre with the ANTARES neutrino telescope. *JCAP*, 06(06):028, 2022.
- [194] Lars Bergstrom, Torsten Bringmann, Ilias Cholis, Dan Hooper, and Christoph Weniger. New Limits on Dark Matter Annihilation from AMS Cosmic Ray Positron Data. *Phys. Rev. Lett.*, 111:171101, 2013.
- [195] Aous A. Abdo et al. Measurement of the Cosmic Ray e^+ plus e^- spectrum from 20 GeV to 1 TeV with the Fermi Large Area Telescope. *Phys. Rev. Lett.*, 102:181101, 2009.
- [196] J. Chang et al. An excess of cosmic ray electrons at energies of 300-800 GeV. *Nature*, 456:362–365, 2008.
- [197] F. Aharonian et al. Probing the ATIC peak in the cosmic-ray electron spectrum with H.E.S.S. *Astron. Astrophys.*, 508:561, 2009.
- [198] A. W. Strong, I. V. Moskalenko, T. A. Porter, G. Johannesson, E. Orlando, and S. W. Digel. The GALPROP Cosmic-Ray Propagation Code. 7 2009.

- [199] Oscar Adriani et al. An anomalous positron abundance in cosmic rays with energies 1.5-100 GeV. *Nature*, 458:607–609, 2009.
- [200] Gaëlle Giesen, Mathieu Boudaud, Yoann Génolini, Vivian Poulin, Marco Cirelli, Pierre Salati, and Pasquale D. Serpico. AMS-02 antiprotons, at last! Secondary astrophysical component and immediate implications for Dark Matter. *JCAP*, 09:023, 2015.
- [201] S. D. Hunter et al. EGRET observations of the diffuse gamma-ray emission from the galactic plane. *Astrophys. J.*, 481:205–240, 1997.
- [202] Christoph Weniger. A Tentative Gamma-Ray Line from Dark Matter Annihilation at the Fermi Large Area Telescope. *JCAP*, 08:007, 2012.
- [203] Celine Boehm, Dan Hooper, Joseph Silk, Michel Casse, and Jacques Paul. MeV dark matter: Has it been detected? *Phys. Rev. Lett.*, 92:101301, 2004.
- [204] Meng Su and Douglas P. Finkbeiner. Strong Evidence for Gamma-ray Line Emission from the Inner Galaxy. 6 2012.
- [205] Douglas P. Finkbeiner. WMAP microwave emission interpreted as dark matter annihilation in the inner galaxy. 9 2004.
- [206] Dan Hooper, Douglas P. Finkbeiner, and Gregory Dobler. Possible evidence for dark matter annihilations from the excess microwave emission around the center of the Galaxy seen by the Wilkinson Microwave Anisotropy Probe. *Phys. Rev. D*, 76:083012, 2007.
- [207] F. W. Stecker, S. D. Hunter, and D. A. Kniffen. The Likely Cause of the EGRET GeV Anomaly and its Implications. *Astropart. Phys.*, 29:25–29, 2008.

- [208] Dan Hooper, Pasquale Blasi, and Pasquale Dario Serpico. Pulsars as the Sources of High Energy Cosmic Ray Positrons. *JCAP*, 01:025, 2009.
- [209] Stefano Profumo. Dissecting cosmic-ray electron-positron data with Occam’s Razor: the role of known Pulsars. *Central Eur. J. Phys.*, 10:1–31, 2011.
- [210] Gregory Dobler. A Last Look at the Microwave Haze/Bubbles with WMAP. *Astrophys. J.*, 750:17, 2012.
- [211] Gregory Dobler. Identifying the Radio Bubble Nature of the Microwave Haze. *Astrophys. J. Lett.*, 760:L8, 2012.
- [212] M. Ackermann et al. Search for Gamma-ray Spectral Lines with the Fermi Large Area Telescope and Dark Matter Implications. *Phys. Rev. D*, 88:082002, 2013.
- [213] Lisa Goodenough and Dan Hooper. Possible Evidence For Dark Matter Annihilation In The Inner Milky Way From The Fermi Gamma Ray Space Telescope. 10 2009.
- [214] Dan Hooper and Lisa Goodenough. Dark Matter Annihilation in The Galactic Center As Seen by the Fermi Gamma Ray Space Telescope. *Phys. Lett. B*, 697:412–428, 2011.
- [215] Dan Hooper and Tim Linden. On The Origin Of The Gamma Rays From The Galactic Center. *Phys. Rev. D*, 84:123005, 2011.
- [216] Kevork N. Abazajian and Manoj Kaplinghat. Detection of a Gamma-Ray Source in the Galactic Center Consistent with Extended Emission from Dark Matter Annihilation and Concentrated Astrophysical Emission. *Phys. Rev. D*, 86:083511, 2012. [Erratum: *Phys.Rev.D* 87, 129902 (2013)].

- [217] Dan Hooper and Tracy R. Slatyer. Two Emission Mechanisms in the Fermi Bubbles: A Possible Signal of Annihilating Dark Matter. *Phys. Dark Univ.*, 2:118–138, 2013.
- [218] Chris Gordon and Oscar Macias. Dark Matter and Pulsar Model Constraints from Galactic Center Fermi-LAT Gamma Ray Observations. *Phys. Rev. D*, 88(8):083521, 2013. [Erratum: *Phys.Rev.D* 89, 049901 (2014)].
- [219] Kevork N. Abazajian, Nicolas Canac, Shunsaku Horiuchi, and Manoj Kaplinghat. Astrophysical and Dark Matter Interpretations of Extended Gamma-Ray Emission from the Galactic Center. *Phys. Rev. D*, 90(2):023526, 2014.
- [220] Tansu Daylan, Douglas P. Finkbeiner, Dan Hooper, Tim Linden, Stephen K. N. Portillo, Nicholas L. Rodd, and Tracy R. Slatyer. The characterization of the gamma-ray signal from the central Milky Way: A case for annihilating dark matter. *Phys. Dark Univ.*, 12:1–23, 2016.
- [221] M. Ackermann et al. The Fermi Galactic Center GeV Excess and Implications for Dark Matter. *Astrophys. J.*, 840(1):43, 2017.
- [222] Simona Murgia. The Fermi–LAT Galactic Center Excess: Evidence of Annihilating Dark Matter? *Ann. Rev. Nucl. Part. Sci.*, 70:455–483, 2020.
- [223] Eric Carlson and Stefano Profumo. Cosmic Ray Protons in the Inner Galaxy and the Galactic Center Gamma-Ray Excess. *Phys. Rev. D*, 90(2):023015, 2014.
- [224] Jovana Petrović, Pasquale Dario Serpico, and Gabrijela Zaharijaš. Galactic Center gamma-ray ”excess” from an active past of the Galactic Centre? *JCAP*, 10:052, 2014.

- [225] Kevork N. Abazajian. The Consistency of Fermi-LAT Observations of the Galactic Center with a Millisecond Pulsar Population in the Central Stellar Cluster. *JCAP*, 03:010, 2011.
- [226] Qiang Yuan and Bing Zhang. Millisecond pulsar interpretation of the Galactic center gamma-ray excess. *JHEAp*, 3-4:1–8, 2014.
- [227] Patrick J. Fox, Roni Harnik, Joachim Kopp, and Yuhsin Tsai. Missing Energy Signatures of Dark Matter at the LHC. *Phys. Rev. D*, 85:056011, 2012.
- [228] Oliver Buchmueller, Caterina Doglioni, and Lian Tao Wang. Search for dark matter at colliders. *Nature Phys.*, 13(3):217–223, 2017.
- [229] Jessica Goodman and William Shepherd. LHC Bounds on UV-Complete Models of Dark Matter. 11 2011.
- [230] Mads T. Frandsen, Felix Kahlhoefer, Anthony Preston, Subir Sarkar, and Kai Schmidt-Hoberg. LHC and Tevatron Bounds on the Dark Matter Direct Detection Cross-Section for Vector Mediators. *JHEP*, 07:123, 2012.
- [231] Haipeng An, Ran Huo, and Lian-Tao Wang. Searching for Low Mass Dark Portal at the LHC. *Phys. Dark Univ.*, 2:50–57, 2013.
- [232] Georges Aad et al. Constraints on new phenomena via Higgs boson couplings and invisible decays with the ATLAS detector. *JHEP*, 11:206, 2015.
- [233] Vardan Khachatryan et al. Searches for invisible decays of the Higgs boson in pp collisions at $\sqrt{s} = 7, 8, \text{ and } 13$ TeV. *JHEP*, 02:135, 2017.

- [234] Rouven Essig, Philip Schuster, and Natalia Toro. Probing Dark Forces and Light Hidden Sectors at Low-Energy e^+e^- Colliders. *Phys. Rev. D*, 80:015003, 2009.
- [235] Clifford Cheung, Gilly Elor, Lawrence J. Hall, and Piyush Kumar. Origins of Hidden Sector Dark Matter II: Collider Physics. *JHEP*, 03:085, 2011.
- [236] Lorenzo Calibbi, Francesco D’Eramo, Sam Junius, Laura Lopez-Honorez, and Alberto Mariotti. Displaced new physics at colliders and the early universe before its first second. 2 2021.
- [237] Armen Tumasyan et al. Search for long-lived heavy neutral leptons with displaced vertices in proton-proton collisions at $\sqrt{s} = 13$ TeV. *JHEP*, 07:081, 2022.
- [238] C. Ahdida et al. Sensitivity of the SHiP experiment to Heavy Neutral Leptons. *JHEP*, 04:077, 2019.
- [239] Jonathan L. Feng. Collider Physics and Cosmology. *Class. Quant. Grav.*, 25:114003, 2008.
- [240] Gian Francesco Giudice, Ben Gripaios, and Rakhi Mahbubani. Counting dark matter particles in LHC events. *Phys. Rev. D*, 85:075019, 2012.
- [241] Gerard ’t Hooft. Naturalness, chiral symmetry, and spontaneous chiral symmetry breaking. *NATO Sci. Ser. B*, 59:135–157, 1980.
- [242] Edward Witten. Dynamical Breaking of Supersymmetry. *Nucl. Phys. B*, 188:513, 1981.
- [243] Savvas Dimopoulos and Howard Georgi. Softly Broken Supersymmetry and SU(5). *Nucl. Phys. B*, 193:150–162, 1981.

- [244] N. Sakai. Naturalness in Supersymmetric Guts. *Z. Phys. C*, 11:153, 1981.
- [245] Romesh K. Kaul and Parthasarathi Majumdar. Cancellation of Quadratically Divergent Mass Corrections in Globally Supersymmetric Spontaneously Broken Gauge Theories. *Nucl. Phys. B*, 199:36, 1982.
- [246] H. Georgi and S. L. Glashow. Unity of All Elementary Particle Forces. *Phys. Rev. Lett.*, 32:438–441, 1974.
- [247] A. J. Buras, John R. Ellis, M. K. Gaillard, and Dimitri V. Nanopoulos. Aspects of the Grand Unification of Strong, Weak and Electromagnetic Interactions. *Nucl. Phys. B*, 135:66–92, 1978.
- [248] Stephen P. Martin. A Supersymmetry primer. *Adv. Ser. Direct. High Energy Phys.*, 18:1–98, 1998.
- [249] J. Wess and B. Zumino. Supergauge Transformations in Four-Dimensions. *Nucl. Phys. B*, 70:39–50, 1974.
- [250] S. Heinemeyer, W. Hollik, and G. Weiglein. The Masses of the neutral CP - even Higgs bosons in the MSSM: Accurate analysis at the two loop level. *Eur. Phys. J. C*, 9:343–366, 1999.
- [251] S. Heinemeyer, W. Hollik, and G. Weiglein. Precise prediction for the mass of the lightest Higgs boson in the MSSM. *Phys. Lett. B*, 440:296–304, 1998.
- [252] S. Heinemeyer, W. Hollik, and G. Weiglein. QCD corrections to the masses of the neutral CP - even Higgs bosons in the MSSM. *Phys. Rev. D*, 58:091701, 1998.
- [253] G. F. Giudice and A. Masiero. A Natural Solution to the mu Problem in Supergravity Theories. *Phys. Lett. B*, 206:480–484, 1988.

- [254] Mikolaj Misiak, Stefan Pokorski, and Janusz Rosiek. Supersymmetry and FCNC effects. *Adv. Ser. Direct. High Energy Phys.*, 15:795–828, 1998.
- [255] Martin Schmaltz and Neal Weiner. A Portalino to the Dark Sector. *JHEP*, 02:105, 2019.
- [256] A. G. Dias, C. A. de S. Pires, P. S. Rodrigues da Silva, and A. Sampieri. A Simple Realization of the Inverse Seesaw Mechanism. *Phys. Rev. D*, 86:035007, 2012.
- [257] Di Liu and Neal Weiner. A Portalino to the Twin Sector. 5 2019.
- [258] Tony Gherghetta, Jörn Kersten, Keith Olive, and Maxim Pospelov. Evaluating the price of tiny kinetic mixing. *Phys. Rev. D*, 100(9):095001, 2019.
- [259] Stephen Parke and Mark Ross-Lonergan. Unitarity and the three flavor neutrino mixing matrix. *Phys. Rev. D*, 93(11):113009, 2016.
- [260] Ivan Esteban, M.C. Gonzalez-Garcia, Michele Maltoni, Thomas Schwetz, and Albert Zhou. The fate of hints: updated global analysis of three-flavor neutrino oscillations. *JHEP*, 09:178, 2020.
- [261] Stephen F. King. Models of Neutrino Mass, Mixing and CP Violation. *J. Phys. G*, 42:123001, 2015.
- [262] Geneviève Bélanger, Fawzi Boudjema, Andreas Goudelis, Alexander Pukhov, and Bryan Zaldivar. micrOMEGAs5.0 : Freeze-in. *Comput. Phys. Commun.*, 231:173–186, 2018.
- [263] Alexander Belyaev, Neil D. Christensen, and Alexander Pukhov. CalcHEP 3.4 for collider physics within and beyond the Standard Model. *Comput. Phys. Commun.*, 184:1729–1769, 2013.

- [264] Frank F. Deppisch, P. S. Bhupal Dev, and Apostolos Pilaftsis. Neutrinos and Collider Physics. *New J. Phys.*, 17(7):075019, 2015.
- [265] F. del Aguila, J. de Blas, and M. Perez-Victoria. Effects of new leptons in Electroweak Precision Data. *Phys. Rev. D*, 78:013010, 2008.
- [266] E. Akhmedov, A. Kartavtsev, M. Lindner, L. Michaels, and J. Smirnov. Improving Electro-Weak Fits with TeV-scale Sterile Neutrinos. *JHEP*, 05:081, 2013.
- [267] Lorenzo Basso, Oliver Fischer, and Jochum J. van der Bij. Precision tests of unitarity in leptonic mixing. *EPL*, 105(1):11001, 2014.
- [268] J. de Blas. Electroweak limits on physics beyond the Standard Model. *EPJ Web Conf.*, 60:19008, 2013.
- [269] Stefan Antusch and Oliver Fischer. Testing sterile neutrino extensions of the Standard Model at future lepton colliders. *JHEP*, 05:053, 2015.
- [270] O. Adriani et al. Search for isosinglet neutral heavy leptons in Z^0 decays. *Phys. Lett. B*, 295:371–382, 1992.
- [271] P. Abreu et al. Search for neutral heavy leptons produced in Z decays. *Z. Phys. C*, 74:57–71, 1997. [Erratum: *Z.Phys.C* 75, 580 (1997)].
- [272] Georges Aad et al. Search for heavy neutral leptons in decays of W bosons produced in 13 TeV pp collisions using prompt and displaced signatures with the ATLAS detector. *JHEP*, 10:265, 2019.
- [273] Albert M Sirunyan et al. Search for heavy Majorana neutrinos in same-sign dilepton channels in proton-proton collisions at $\sqrt{s} = 13$ TeV. *JHEP*, 01:122, 2019.

- [274] Albert M Sirunyan et al. Search for heavy neutral leptons in events with three charged leptons in proton-proton collisions at $\sqrt{s} = 13$ TeV. *Phys. Rev. Lett.*, 120(22):221801, 2018.
- [275] David Curtin et al. Long-Lived Particles at the Energy Frontier: The MATHUSLA Physics Case. *Rept. Prog. Phys.*, 82(11):116201, 2019.
- [276] Stefan Antusch, Eros Cazzato, Marco Drewes, Oliver Fischer, Bjorn Garbrecht, Dario Gueter, and Juraj Klarić. Probing Leptogenesis at Future Colliders. *JHEP*, 09:124, 2018.
- [277] P. Astier et al. Search for heavy neutrinos mixing with tau neutrinos. *Phys. Lett. B*, 506:27–38, 2001.
- [278] Oleg Ruchayskiy and Artem Ivashko. Experimental bounds on sterile neutrino mixing angles. *JHEP*, 06:100, 2012.
- [279] Anupama Atre, Tao Han, Silvia Pascoli, and Bin Zhang. The Search for Heavy Majorana Neutrinos. *JHEP*, 05:030, 2009.
- [280] Gabriel Lopez Castro and Nestor Quintero. Bounding resonant Majorana neutrinos from four-body B and D decays. *Phys. Rev. D*, 87:077901, 2013.
- [281] Han Yuan, Tianhong Wang, Guo-Li Wang, Wan-Li Ju, and Jin-Mei Zhang. Lepton-number violating four-body decays of heavy mesons. *JHEP*, 08:066, 2013.
- [282] Ying Wang, Shou-Shan Bao, Zuo-Hong Li, Nan Zhu, and Zong-Guo Si. Study Majorana Neutrino Contribution to B-meson Semi-leptonic Rare Decays. *Phys. Lett. B*, 736:428–432, 2014.
- [283] Roel Aaij et al. Search for Majorana neutrinos in $B^- \rightarrow \pi^+ \mu^- \mu^-$ decays. *Phys. Rev. Lett.*, 112(13):131802, 2014.

- [284] C. Adams et al. The Long-Baseline Neutrino Experiment: Exploring Fundamental Symmetries of the Universe. In *Snowmass 2013: Workshop on Energy Frontier*, 7 2013.
- [285] M. Anelli et al. A facility to Search for Hidden Particles (SHiP) at the CERN SPS. 4 2015.
- [286] D. A. Bryman and R. Shrock. Improved Constraints on Sterile Neutrinos in the MeV to GeV Mass Range. *Phys. Rev. D*, 100(5):053006, 2019.
- [287] D. Liventsev et al. Search for heavy neutrinos at Belle. *Phys. Rev. D*, 87(7):071102, 2013. [Erratum: *Phys.Rev.D* 95, 099903 (2017)].
- [288] André de Gouvêa and Andrew Kobach. Global Constraints on a Heavy Neutrino. *Phys. Rev. D*, 93(3):033005, 2016.
- [289] John McDonald. Gauge singlet scalars as cold dark matter. *Phys. Rev. D*, 50:3637–3649, 1994.
- [290] A.A. Aguilar-Arevalo et al. Significant Excess of ElectronLike Events in the MiniBooNE Short-Baseline Neutrino Experiment. *Phys. Rev. Lett.*, 121(22):221801, 2018.
- [291] A. Aguilar-Arevalo et al. Evidence for neutrino oscillations from the observation of $\bar{\nu}_e$ appearance in a $\bar{\nu}_\mu$ beam. *Phys. Rev. D*, 64:112007, 2001.
- [292] Oliver Fischer, Álvaro Hernández-Cabezudo, and Thomas Schwetz. Explaining the MiniBooNE excess by a decaying sterile neutrino with mass in the 250 MeV range. *Phys. Rev. D*, 101(7):075045, 2020.
- [293] Jan Hamann, Steen Hannestad, Georg G. Raffelt, and Yvonne Y. Y. Wong. Sterile neutrinos with eV masses in cosmology: How disfavoured exactly? *JCAP*, 09:034, 2011.

- [294] Edward Witten. Mass Hierarchies in Supersymmetric Theories. *Phys. Lett. B*, 105:267, 1981.
- [295] Heinz Pagels and Joel R. Primack. Supersymmetry, Cosmology and New TeV Physics. *Phys. Rev. Lett.*, 48:223, 1982.
- [296] H. Goldberg. Constraint on the Photino Mass from Cosmology. *Phys. Rev. Lett.*, 50:1419, 1983. [Erratum: *Phys.Rev.Lett.* 103, 099905 (2009)].
- [297] John R. Ellis, S. Kelley, and Dimitri V. Nanopoulos. Probing the desert using gauge coupling unification. *Phys. Lett. B*, 260:131–137, 1991.
- [298] C. Giunti, C. W. Kim, and U. W. Lee. Running coupling constants and grand unification models. *Mod. Phys. Lett. A*, 6:1745–1755, 1991.
- [299] Ugo Amaldi, Wim de Boer, and Hermann Furstenau. Comparison of grand unified theories with electroweak and strong coupling constants measured at LEP. *Phys. Lett. B*, 260:447–455, 1991.
- [300] Paul Langacker and Ming-xing Luo. Implications of precision electroweak experiments for M_t , ρ_0 , $\sin^2 \theta_W$ and grand unification. *Phys. Rev. D*, 44:817–822, 1991.
- [301] U. Ellwanger, Michel Rausch de Traubenberg, and Carlos A. Savoy. Phenomenology of supersymmetric models with a singlet. *Nucl. Phys. B*, 492:21–50, 1997.
- [302] Ulrich Ellwanger, Cyril Hugonie, and Ana M. Teixeira. The Next-to-Minimal Supersymmetric Standard Model. *Phys. Rept.*, 496:1–77, 2010.
- [303] C. T. Potter. Natural NMSSM with a Light Singlet Higgs and Singlino LSP. *Eur. Phys. J. C*, 76(1):44, 2016.

- [304] Andrew J. Williams, Celine Boehm, Stephen M. West, and Daniel Albornoz Vasquez. Regenerating WIMPs in the Light of Direct and Indirect Detection. *Phys. Rev. D*, 86:055018, 2012.
- [305] Emanuele Bagnaschi et al. MSSM Higgs Boson Searches at the LHC: Benchmark Scenarios for Run 2 and Beyond. *Eur. Phys. J. C*, 79(7):617, 2019.
- [306] Emanuele Angelo Bagnaschi, Sven Heinemeyer, Stefan Liebler, Pietro Slavich, and Michael Spira. Benchmark Scenarios for MSSM Higgs Boson Searches at the LHC. *LHCHWG-2021-001*, 2021.
- [307] Ulrich Ellwanger and Cyril Hugonie. NMHDECAY 2.0: An Updated program for sparticle masses, Higgs masses, couplings and decay widths in the NMSSM. *Comput. Phys. Commun.*, 175:290–303, 2006.
- [308] E. Bagnaschi et al. Likelihood Analysis of the pMSSM11 in Light of LHC 13-TeV Data. *Eur. Phys. J. C*, 78(3):256, 2018.
- [309] C. Strege, G. Bertone, G. J. Besjes, S. Caron, R. Ruiz de Austri, A. Strubig, and R. Trotta. Profile likelihood maps of a 15-dimensional MSSM. *JHEP*, 09:081, 2014.
- [310] Clifford Cheung, Lawrence J. Hall, David Pinner, and Joshua T. Ruderman. Prospects and Blind Spots for Neutralino Dark Matter. *JHEP*, 05:100, 2013.
- [311] J. C. Costa et al. Likelihood Analysis of the Sub-GUT MSSM in Light of LHC 13-TeV Data. *Eur. Phys. J. C*, 78(2):158, 2018.
- [312] Peter Athron. SUSY Global Fits. In *5th Large Hadron Collider Physics Conference*, 8 2017.

- [313] Peter Athron et al. Combined collider constraints on neutralinos and charginos. *Eur. Phys. J. C*, 79(5):395, 2019.